

KØBENHAVNS UNIVERSITET
UNIVERSITY OF COPENHAGEN



A HADRONIC CALORIMETER FOR ALICE

Master Thesis

Written by:

Laura Marie Dufke

Niels Bohr Institute

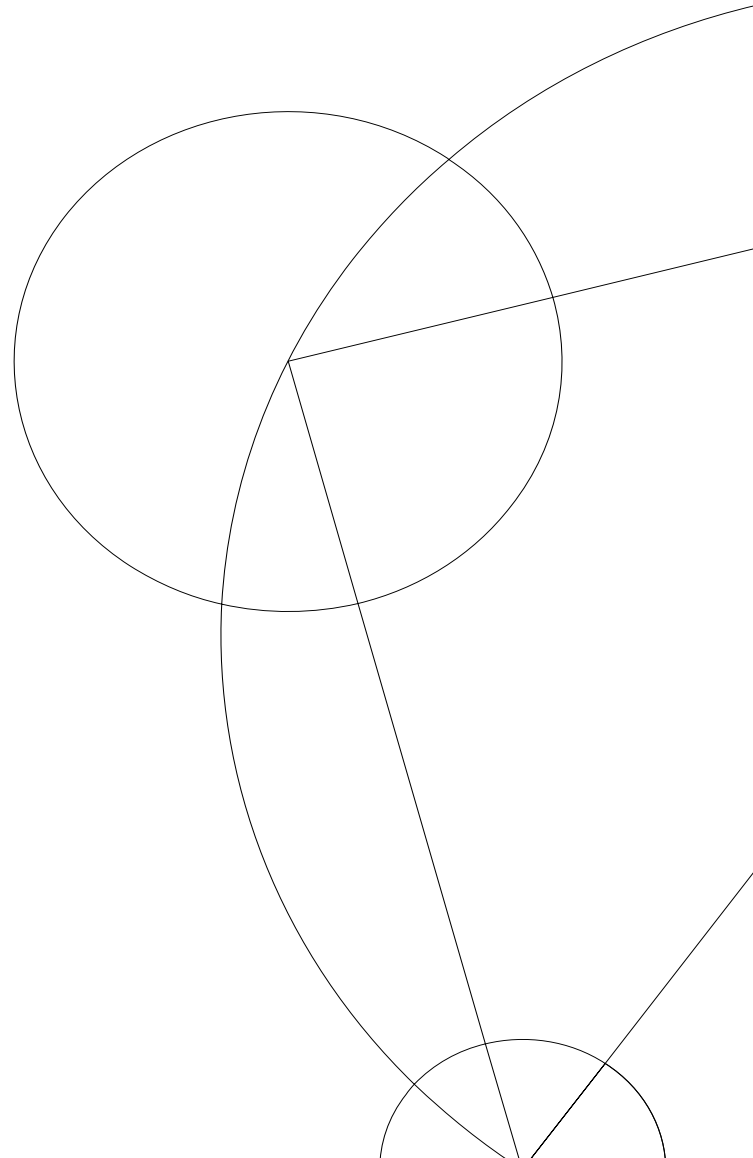
University of Copenhagen

Academic Advisor:

Professor, Ian Bearden

Niels Bohr Institute

University of Copenhagen



Abstract

In 2020 The ALICE Collaboration proposed to add a forward electromagnetic and hadronic calorimeter (FoCal) as an upgrade to the ALICE experiment. The first prototype for the hadronic calorimeter (FoCal-H) was tested in September 2021. These tests showed to be a promising starting point, even though issues with the readout system appeared. Throughout the rest of 2021, the FoCal-H first prototype was tested in a number of ways to pin-point which parameters needed to be optimized, and in which way this could be done. In particular, these tests focused on fully characterizing light propagation through the scintillating fibers, specifically the amount of optical crosstalk between the silicon photomultipliers (SiPMs). The results of this, as well as multiple other studies, were used to optimize the design for the FoCal-H second prototype, which was constructed in the summer of 2022. The FoCal-H second prototype was tested in the fall of 2022, at the SPS beamline at CERN, at energies from 60 to 350 GeV. The results of these tests have been examined and compared with simulations, to test the technical performance of the prototype.

This thesis revolves around characterizing the performance of the FoCal-H calorimeter components as well as analyzing the November 2022 SPS H2 testbeam data. Simulations corresponding to the test-beam detector setup was performed in order to compare and estimate the FoCal-H second prototype's technical performance.

The performance characteristics of the FoCal-H calorimeter components, were studied with the aim of optimizing the design for a future prototype or the final design of FoCal-H. These studies focused on optical crosstalk measurements between the SiPMs, the cutting technique used on the scintillating fibers, and the ratio between the passive and active material of the FoCal-H calorimeter.

Optical crosstalk between the SiPMs was found to be an issue for both the central 7x7 SiPM calorimeter module and the outer 5x5 SiPM calorimeter modules, due to the compact design leading to a small distance between the SiPMs, as well as the wide scattering of photons from the scintillating fibers. The study of the cutting techniques for the scintillating fibers found that optical crosstalk between the SiPMs, could be reduced significantly by cutting the scintillating fibers with a technique using optical glue and a diamond blade. The study of the ratio between the passive and active material of the FoCal-H calorimeter, found that by reducing the inner diameter of the copper-tubes, thus reducing the size of the scintillating fibers, the energy resolution and the response linearity across a large range of beam energies could be improved.

The analysis of the November 2022 SPS H2 testbeam data, as well as the analysis of the corresponding simulations, focused on a number of studies related to the source of response peaks, energy resolution, lateral shower containment, and examination of the intersections between calorimeter modules by performing a position scan. The investigation of these studies, lead to comparisons between the testbeam data and the simulations, to estimate the FoCal-H second prototype's technical performance. The comparison studies found that the energy resolution of the testbeam data was better than the one from the simulation. In light of this result, multiple studies were performed in order to point out any potential reason. These studies included the use of physics list in the simulations, and saturation in simulations and/or in the testbeam data. A reason for this unexpected result of the energy resolution was not found, but potential other studies were suggested.

Contents

1	Introduction	1
2	CERN facilities and experiments	2
2.1	Particle accelerators	2
2.2	ALICE (A Large Ion Collider Experiment)	4
2.2.1	The central region	6
2.2.2	The forward region	7
2.2.3	The Muon spectrometer	8
3	FoCal physics goals	8
3.1	Measure the gluon density in protons and lead nuclei and quantify its nuclear modification at small x and Q^2	9
3.2	Explore the physical origin of shadowing effects	11
3.3	Jet quenching at forward rapidity in Pb–Pb collisions	11
3.4	Origin of long-range flow-like correlations in p-p and p–Pb collisions	12
4	Calorimeter physics	13
4.1	Homogeneous and Sampling Calorimeters	14
4.2	Electromagnetic calorimeter	15
4.3	Hadronic calorimeter	17
5	Forward Calorimeter (FoCal)	19
5.1	FoCal-E	19
5.2	FoCal-H	20
5.2.1	FoCal-H first prototype	21
5.2.2	FoCal-H second prototype	22
6	Performance study of calorimeter components	26
6.1	Optical crosstalk	26
6.1.1	Central 7x7 SiPM module	28
6.1.2	Outer 5x5 SiPM modules	30
6.2	Scintillating fibers	34
6.2.1	Cutting techniques of scintillating fibers	34
6.2.2	Rolled scalpel cut	35
6.2.3	Rolled scalpel and polished cut	38
6.2.4	Optical glue and diamond blade cut	38
6.3	Collector plate material	42
7	November 2022 SPS H2 testbeam setup	44
7.1	Testbeam prototype setup	44
8	Data analysis of the November 2022 SPS H2 testbeam	47
8.1	Testbeam data - November 2022 SPS H2	47
8.1.1	FoCal detector setup	48
8.2	Simulation data - November 2022 SPS H2	55

8.2.1	Comparison between updates in simulations	55
8.2.2	Beam shape and size	56
8.2.3	FoCal detector setup	59
8.2.4	Shower containment	68
8.2.5	Position scan	70
8.3	Comparison between testbeam data and simulation data	75
8.3.1	Energy calibration	75
8.3.2	Energy resolution	79
8.3.3	Punch through peak	83
9	FoCal-H third prototype	89
9.1	FoCal detector setup	89
9.2	Energy resolution	91
9.2.1	Compensation	93
9.2.2	Shower containment	97
10	Conclusion	99
11	Appendix	101
11.1	FoCal-H first prototype	101
11.2	Optical crosstalk	102
11.2.1	Central 7x7 SiPM module (Module 5)	103
11.2.2	Outer 5x5 SiPM modules	106
11.3	Cutting techniques of scintillating fibers	123
11.4	Simulation - November 2022 SPS H2	124
11.4.1	Comparison between updates in simulations	124
11.4.2	Simulations including FoCal-E physics list comparison	126
11.4.3	Simulations including and excluding FoCal-E	126
11.4.4	Comparison between simulation physics lists	127
11.4.5	Shower containment	129
11.4.6	Position scan	131
11.4.7	Spatial energy distribution	136
11.5	Comparison between testbeam data and simulation data	138
11.5.1	Difference between Gaussian and Crystal Ball function fit	138
11.5.2	Calibrated total charge	139
11.5.3	Saturation	140
11.5.4	Punch through peak	141
11.5.5	Rotation of FoCal-H	144
11.6	FoCal-H third prototype	145
11.6.1	Compensation	146
11.6.2	Shower containment	150

1 Introduction

In the summer of 2020 the ALICE (A Large Ion Collider Experiment) collaboration proposed to add a forward calorimeter as an upgrade to the ALICE experiment. This Forward Calorimeter (FoCal) consists of an electromagnetic calorimeter (FoCal-E) and a hadronic calorimeter (FoCal-H), placed at pseudorapidity $3.4 < \eta < 5.8$, in ALICE's forward A region, right beside the compensator magnet. With FoCal as an upgrade to the ALICE experiment, four main physics goals are to be explored. These four physics goals are [1]:

- Measure the gluon density in protons and lead nuclei and quantify its nuclear modification at small x and Q^2 .
- Explore the physical origin of shadowing effects.
- Investigate the origin of long-range flow correlations in pp and p-Pb collisions
- Explore jet quenching at forward rapidity in Pb-Pb collisions

Along with these four physics goals, information about the identification of isolated photons at forward rapidity in p-p and p-Pb collisions can be extracted. FoCal will as an upgrade to the ALICE experiment provide direct information about partons, in the prospect to describe the initial stages of the universe, which possible can be described by the theory of Color Glass Condensate [1]. A detailed description of the four FoCal physics goals can be found in section 3.

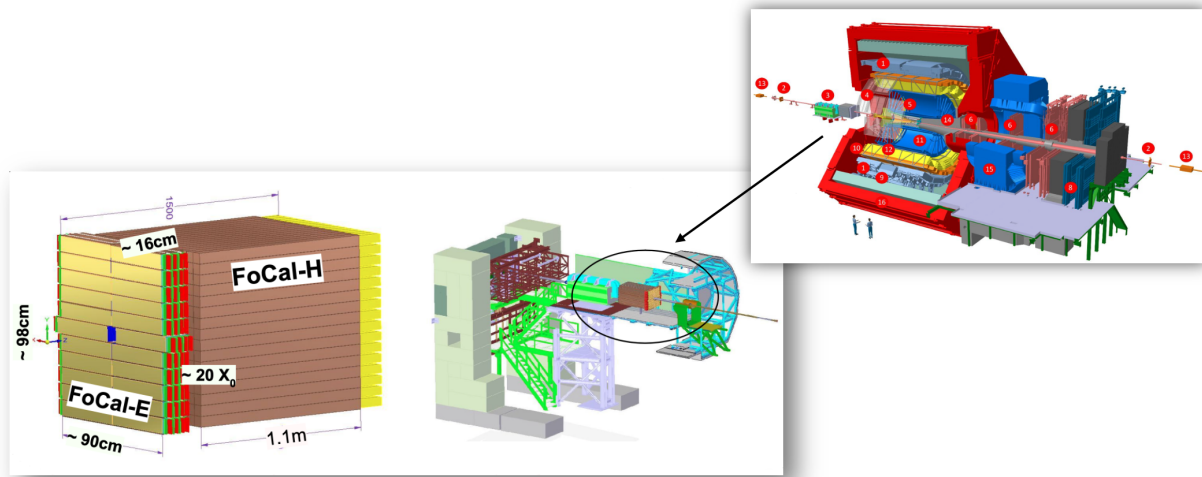


Figure 1: The figure shows a proposed design as well as the placement of the forward calorimeter (FoCal) in ALICE. The hadronic calorimeter (FoCal-H) is positioned closest to the compensator magnet, whereas the electromagnetic calorimeter (FoCal-E) is placed in front of FoCal-H, closest to the interaction point [4].

From 2020 and onward, the ALICE group at the Niels Bohr Institute at University of Copenhagen has been one of the groups responsible for constructing and testing components of the FoCal-H first and second prototype, as well as analyzing data and generating simulations.

The FoCal-H first prototype was constructed in September 2021 and was tested in testbeam later in the

same month, to see if the conceptual ideas of the design were valid. These tests provided a preliminary indication of how the final detector might perform and led to the design and construction of the FoCal-H second prototype. In the summer of 2022, I helped design, construct, and perform a number of technical tests on the FoCal-H second prototype. Later that summer, as well as in the fall, the FoCal-H second prototype was tested in testbeam, at the PS and SPS beamlines. The data from the testbeam in the fall of 2022 (November 2022 SPS H2) is the foundation for this thesis.

This thesis focus on characterizing the performance of the FoCal-H calorimeter components as well as analyzing the November 2022 SPS H2 testbeam data. Simulations corresponding to the testbeam detector setup was performed in order to compare and estimate the FoCal-H second prototype's technical performance.

The performance characteristics of the FoCal-H calorimeter components were studied in order to optimize the design for a future prototype or the final design of FoCal-H. These studies focus on optical crosstalk measurements between the SiPMs, the cutting technique of the scintillating fibers, and the ratio between the passive and active material of the FoCal-H calorimeter.

The analysis of the November 2022 SPS H2 testbeam data, as well as the analysis of the corresponding simulations, focus on a number of studies related to the source of response peaks, energy resolution, lateral shower containment, and examination of the intersections between calorimeter modules by performing a position scan. The investigations of these studies, lead to comparisons between the testbeam data and the simulations, to estimate the FoCal-H second prototype's technical performance.

Sections of this thesis will be used as a primary source for the ALICE Forward Calorimeter Technical Design Report (TDR), which will be submitted to the ALICE collaboration in the summer of 2023.

2 CERN facilities and experiments

This section will briefly go through the CERN facilities and the experiments located at CERN. The aim is to provide the necessary information on the connection between the accelerator rings and the experiments to get a understanding of the testbeam facility and data taken with FoCal, as well as the future location of the detector.

2.1 Particle accelerators

CERN (European Organization for Nuclear Research) is an organization established in 1954, which has the mission to "*uncover what the universe is made of and how it works*" [2]. CERN explores this mission using various sizes and shapes of particle accelerators, which accelerate particles and nuclei up to nearly the speed of light, where they collide and the produced particles and physics processes are studied.

CERN has two small accelerators that provide particles and nuclei for experiments, namely LINAC 3 and LINAC 4 (linear accelerator 3 and 4). Depending on the study of either protons or heavy ions, the acceleration process starts in these two different accelerators. However, some of the larger accelerators are used for both protons and heavy ions.

In LINAC 3, low-energy heavy ions are generated. Until now, LINAC 3 has been able to generate lead (Pb) and xenon (Xe) ions. The heavy ions are produced by taking for instance a piece of pure Pb, which is

vaporized into a smaller number of atoms at around 500 C° . After this procedure, the atoms are stripped of electrons, by the use of an electric current, creating the heavy ions, with an energy of around 4 MeV [7, p.58]. The heavy ions are injected into LEIR (Low Energy Ion Ring) through beam lines. LEIR receives the heavy ions in long pulses and transforms them into bunches. During this procedure the heavy ions are accelerated to an energy of 72 MeV [6], and will then be injected into the larger accelerators that are used for both protons and heavy ions.

In LINAC 4, negative hydrogen ions are generated and accelerated up to 160 MeV before getting injected into the PSB (Proton Synchrotron Booster). In the PSB beam-line, the electrons are removed from the hydrogen atoms using an electric current, leaving the nucleus with a single proton. These protons are in the PSB accelerated up to an energy of 2 GeV , before getting injected into the larger accelerators.

After being accelerated in the smaller accelerators, the protons and/or heavy ions, are injected into the PS (Proton Synchrotron) circular accelerator. The PS accelerator has two purposes, it functions as an injector to a larger accelerator, but it also functions as a testbeam facility for various experiments¹. In the PS, the protons and/or heavy ions can be accelerated up to an energy of 26 GeV , before getting injected into the larger circular accelerator SPS (Super Proton Synchrotron) [8]. The protons and/or heavy ions in the SPS are accelerated up to an energy of 450 GeV . As for the PS accelerator, the SPS accelerator has multiple purposes, one of them being a testbeam facility for various experiments² [9]. Another purpose of the SPS accelerator is to serve as an injector of high-energy protons and/or heavy ions into the LHC (Large Ion collider), which is a 26.7 km long circular accelerator. The protons and/or heavy ions are then transferred into two beam lines, one where they move clockwise and another where they move anti-clockwise. The protons and/or heavy ions in the two LHC beamlines are accelerated up to their maximum energy, and then collided with each other.

LHC has so far been able to collide protons with a center-of-mass energy of 13.7 TeV , lead ions at 5.36 TeV and xenon ions at 5.44 TeV per colliding nucleon pair. These high energies are possible to reach, because of the different types of magnets placed around the LHC beampipes. The LHC has 1232 dipole magnets, each 15 meters in length, and 392 quadrupole magnets, which have a length of $5\text{-}7\text{ meters}$. The dipole magnets bend the beam to the desired position depending on the particle or ion, as well as the energy it has. The quadrupole focuses the beam in the LHC beampipe, which is an important role in colliding the protons and/or heavy ions [10].

¹The PS testbeam facility, beam-line T9, and T10 are used for some of the FoCal testings, e.g performance test of the FoCal-H first and second prototype.

²The SPS testbeam facility, beam-line H6, and H2 are used for some of the FoCal testings, e.g the fall 2022 testbeam of the FoCal-H second prototype.

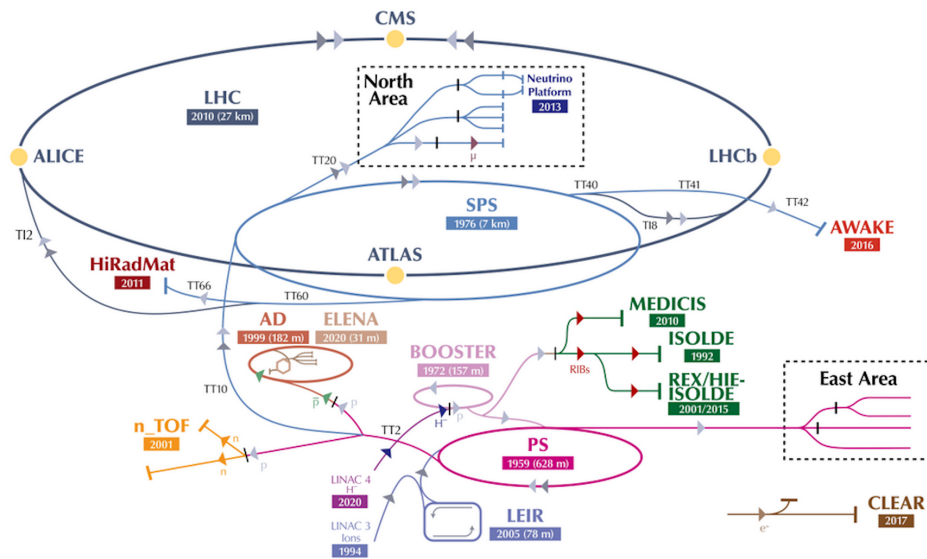


Figure 2: The figure shows the CERN accelerator complex and how the different accelerators and experiments are connected [5] to each other. The figure lists all the accelerators and experiments by their acronym [3].

The accelerators and experiments described in this overview of the CERN facility constitute only a fraction of the operating accelerators and experiments at CERN in 2023. However, the remaining accelerators and experiments are not important in regards to this thesis. An illustration of the CERN facility can be seen in figure 2 above.

2.2 ALICE (A Large Ion Collider Experiment)

The collisions between the protons and/or heavy ions happen in four collision points in the LHC. In these collision points, four major experiments are placed, ALICE (A Large Ion Collider Experiment), ATLAS (A Toroidal LHC Apparatus), CMS (Compact Muon Solenoid), and LHCb (LHC-beauty).

The general purpose of ATLAS and CMS is to investigate a wide range of physics, from the Standard Model to the Higgs Boson, in the search for extra dimensions and particles that could explain dark matter. However, ATLAS and CMS have different technical solutions and detector designs, in order to achieve these goals. LHCb's general purpose is to investigate the difference between anti-matter and matter. LHCb does this by studying the beauty/bottom(b)-quark [7, p.58-59] This thesis, however, concentrates on ALICE, and will therefore not go into further details about the other experiments at the LHC.

ALICE's general purpose is to investigate heavy ion and proton collisions, as well as the physics processes occurring when colliding these. ALICE focuses on the physics of strongly interacting matter at extreme energy densities, such as Quark Gluon Plasma (QGP), hence also Quantum chromodynamics (QCD).

Ordinary matter as we know it today is made of atoms, with an atomic nucleus consisting of protons and neutrons, surrounded by a cloud of electrons. The protons and neutrons belong to a particle group called hadrons. Hadrons are made of quarks bound together by their force carrier, called gluons, and have never been observed to be free. However, when colliding heavy ions in the LHC, temperatures of

around 100.000 times hotter than our sun can be reached. The LHC can therefore, recreate similar conditions to those that were present after the Big Bang. Due to these extremely high energies and densities, the quarks inside the hadrons get freed from their bond with the gluons. This phase is what is called the Quark Gluon Plasma (QGP), and the properties of the QGP is one of the crucial areas which needs to be investigated in the search for answers to describing the theory of quantum chromodynamics (QCD). ALICE has studied the evolution of the QGP for many years now. As it expands, the temperature decreases, and the particles as we know them today get created. The time has now come to investigate the stages, which took place before the QGP. One theory describing these stages is called Color-Glass Condensate (CGC). A physics process which can be described by CGC, will be described in detail in section 3. Before that, a brief description will be given of ALICE, and its detectors and components. An illustration of ALICE and the can be seen in figure 3.

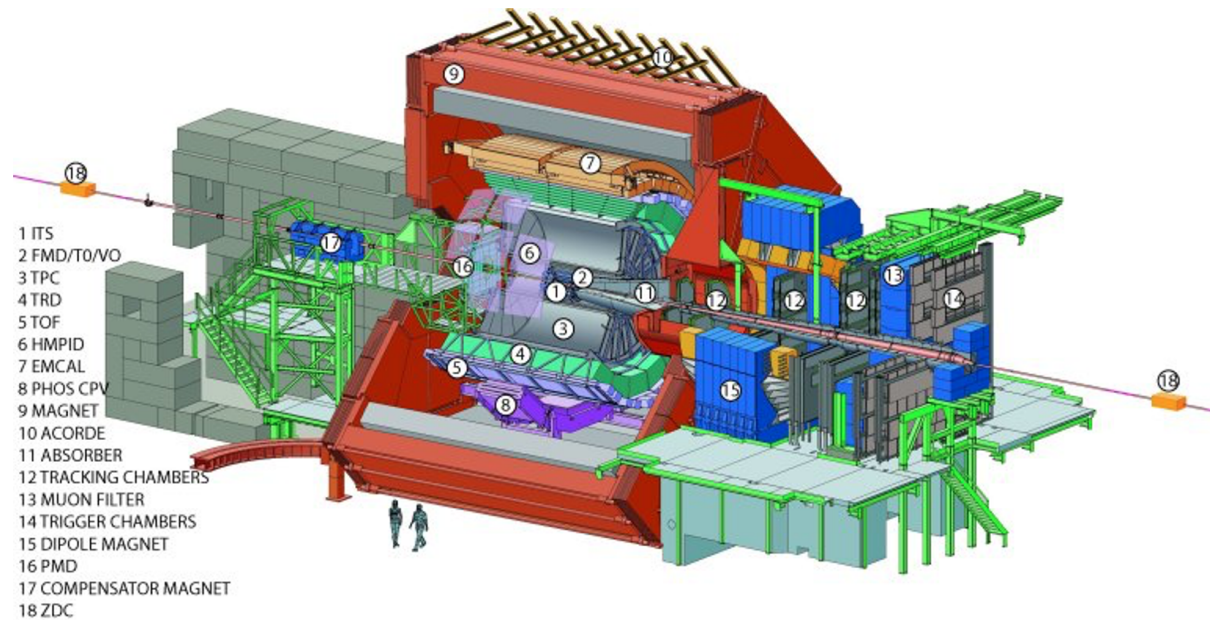


Figure 3: The figure shows a sketch of ALICE (A Large Ion Collider Experiment). All 18 detectors and components are labeled with a number and listed by their acronym.

ALICE consists of 18 different detection systems, which are placed inside a large solenoid magnet inherited from the former LEP experiment L3. The experimental structure has a length of 26 m, a height of 16 m, and a width of 16 m and weighs approximately 10.000 tons. Each of the 18 sub-detectors has its own specification in terms of technology choice and design constraints, in order to collect relevant information about particle properties to fulfill the ALICE experiment's general physics purpose. This information could for instance be the mass, charge, and velocity of the particles. The relevant information is gathered by having a variety of different types of particle detectors [7].

ALICE is built up in detector layers from the collision point and out, starting from the ITS (Inner Tracking System) to the ZDC (Zero Degree Calorimeter). The detectors can be split into three regions, the central region, the forward region, and the muon spectrometer. The detectors in ALICE will be presented in this section, but not all detector specifications will be described in detail, due to the focus of this thesis.

This thesis revolves around a new calorimeter, which is to be placed in ALICE. This new detector is called FoCal and will be placed right beside the compensator magnet. Through the thesis, an understanding

of FoCal will be established, as well as an understanding of what FoCal can contribute to the whole detector system in ALICE.

2.2.1 The central region

The central region concentrates around the collision point and covers the direction perpendicular to the beam from $|\eta| < 0.9$. The main focus of the detectors in the central region is to measure the momentum and identity of particles produced in the region. The central region is very important, in the sense that it is here the first measurements are taken, after the particles escape from the primordial matter, being QGP.

The first detector that the particles encounter, when they transverse the detector layers outwards, is the **ITS** (Inner Tracking System). The ITS is constructed of three detection layers covering the total azimuth angle. The ITS's different layers provide information about the multiplicity of the collision, the vertex location, particle identification, and track reconstruction [11].

The second detector is the **TPC** (Time Projection Chamber), which is a large gas detector providing tracking and particle identification. The detector works by having charged particles transverse the volume of the gas, where they ionize the gas and the electrons drift toward the readout planes. Particle identification in the TPC is done by using the energy loss of particles in the gas [12].

The third detector is the **TRD** (Transition Radiation Detector). As the name indicates, the TRD works by having a charged particle that crosses over the boundary between two materials with different dielectric constants emitting radiation. The amount of radiation emitted will depend on different types of particles. Thus, the TRD provides information about the particles' identity [13].

The fourth detector is the **TOF** (Time Of Flight). TOF provides information of the velocity of charged particles, by measuring the flight time for a specified distance. Using the momentum, p , and the trajectory length, l , known from the three previously mentioned detectors, the different particles' mass can be calculated, from the time of flight [14]:

$$m = p \cdot \sqrt{\frac{t^2}{l^2} - 1}$$

These four detectors are part of the area closest to the interaction point.

To help collect the information in the innermost central region, there are three additional detectors. The first of these is the **HMPID** (High Momentum Particle Identification Detector). The main goal of HMPID is to identify particle types with high momentum, by using the phenomena of Cherenkov radiation. When a charged particle travels through a medium with a greater velocity than light is able to travel within that medium, Cherenkov radiation is emitted. This radiation is emitted as waves with an angle depending on the trajectory, and hence velocity, of the particles. So by determining the opening angle of the wave, the velocity of the particles, relative to the velocity of the light in the medium can be determined by [15]:

$$\cos(\theta_c) = \frac{1}{\beta \cdot n} = \frac{v}{c} \cdot n$$

where v is the velocity of the charged particle, c is the speed of light, and n is the refractive index of the medium.

The second detector is the **EMCAL** (Electromagnetic Calorimeter), which measures the transverse energy and transverse momentum (p_T) of particles. EMCAL is a sampling calorimeter, that has a passive

material made of lead and an active material made of scintillating wavelength shifters. EMCAL is built in a cylindrical geometry and has as its main goal to study energetic particles and the correlations between particles. These particles are photons, electrons, neutral pions, and jets of particles. [16].

The third detector, and last in the central region, is the **PHOS** (Photon Spectrometer), which is a high-resolution electromagnetic calorimeter made of lead-tungsten crystals. PHOS is placed at the bottom of ALICE, very close to the interaction point. The position of the detector is important for its purpose, which is to study the thermal and dynamical properties of the initial stage of the collision, by studying the photons that emerge from the collision [17].

The detectors in the central region are all placed inside a large solenoid **Magnet**, with the purpose is to keep a uniform magnetic field inside the magnet. A uniform magnetic field is important for a lot of the detectors placed in the central region. Placed on top of the ALICE magnet is **ACORDE** (ALICE Cosmic Rays Detector), which detects the arrival of cosmic ray showers coming from high-energy cosmic muons. ACORDE is built from 60 scintillator modules located perpendicular to the beam axis and can be configured to trigger on either single or multiple muon events [18].

2.2.2 The forward region

In the forward region, with small angles relative to the beam pipe, three detectors are placed as one system. The first one is the **FMD** (Forward Multiplicity Detector). The key role of the FMD is to measure the number of charged particles at forward angles. The FMD consist of 5 rings placed around the beam-pipe, which are split into two parts positioned at the A and C-side of ALICE. The FMD covers pseudorapidities $-3.4 < \eta < -1.7$ and $1.7 < \eta < 5.0$.

The second detector is the **T0**, which is a high-resolution timing detector, used to time the collision. The information from the T0 detector is used in TOF to identify particles. The T0 detector is split into two parts placed at the A and C-side of ALICE. Both sides of the T0 are built from 12 cylindrical Cherenkov counters, which are placed closely around the beam pipe to maximize the trigger efficiency.

Finally, the third forward detector in this three part detector system, is the **V0**. The V0 detector is also split into two parts, placed on the A and C-side respectively. It consists of two arrays of segmented oscillator counters, which sum the multiplicity, thereby providing the necessary information to identify the centrality of a collision. Moreover, the V0 is also used as a minimum bias trigger, but also as the source to reject the beam-gas background [7, p.61].

In addition to these three detectors, the forward region also includes the **ZDC** (Zero Degree Calorimeter) which helps the T0 and the V0 characterize the collision. The ZDC detector is a sampling calorimeter built of quartz and silica optical fibers. The ZDC detector consists of two identical sets of calorimeters located on both sides of the interaction point. One of these calorimeters focus on detecting protons, while the other detects neutrons. As indicated by the name of the detector, some of the ZDC detector is placed at zero degrees with respect to the beam pipe. The focus of the ZDC detector is to determine the overlap region of the two colliding nuclei [19].

Moreover, the last detector in the forward region is the **PMD** (Photon Multiplicity Detector), which is mounted on the door of the large solenoid magnet. As the name indicates, The PMD measures the multiplicity and the spatial distribution of photons event by event. This focus of study makes it possible to determine the shapes and fluctuations of events. The PMD can be used to provide estimates of the transverse electromagnetic energy for particle events [21].

The final component in the forward region is the **Compensator Magnet**, whose role is to compensate for the deflection of the trajectory of the particles in the beampipe. The particles will be slightly deflected when traveling past the dipole magnet in the muon spectrometer, due to the magnetic field in the magnet. This needs to be corrected, before the particles reach the collision point. The particle coming from the opposite beampipe will experience the same deflection from the compensator magnet, where the dipole magnet will correct for this.

2.2.3 The Muon spectrometer

A collection of five detectors constituting the Muon spectrometer are placed on the opposite region of the detectors described in 2.2.2. The Muon spectrometer's role is to study the variety of heavy quarkonia (a flavorless meson constituting a heavy quark and its own anti-quark) by studying their decay into muons.

The first detector the particles encounter when reaching the muon spectrometer is **The Front Absorber**, which among other things focuses on suppressing all particles coming from the interaction point, except the muons. In addition, the absorber has a crucial role in reducing the low-energy background from secondary interactions to the tracking and trigger chambers coming right behind the absorber.

The second and third detector the muons will transverse is a set of **Tracking Chambers**, placed on either side of a **Dipole Magnet**. The tracking chambers together with the dipole magnet determine the momenta of the muons transversing the detectors. The momentum for each muon is determined by tracking the muons in a magnetic field generated by the magnet, which is positioned so that the magnetic field is perpendicular to the beamline. The fourth detector is the **Muon Filter**, which provides the transverse momentum of each muon passing through the filter. The last detector in the muon spectrometer is the **The Trigger System**. The trigger system is placed right behind the muon filter, and has the focus to study heavy-quark resonance decays. The trigger system consists of two sections, each section having two resistive plate chambers. With these chambers and the electronics, a timing resolution of around 2 ns can be obtained. This is used, among other things, to identify bunch crossings in the spectrometer [20].

3 FoCal physics goals

As mentioned in section 1, FoCal has four main physics goals, which are to be investigated after the instalment in ALICE in 2027/2028. The focus of the four physics goals are important topics, which are to be investigated in order to gain knowledge about initial stages of the universe. However, the reason why a detector equivalent to FoCal is needed to answer these questions, is as important to understand as the physics goals themselves.

FoCal is a forward calorimeter, which means that the intended placement in ALICE is in the forward region, at pseudorapidity of $3.4 < \eta < 5.8$, also called high-rapidity. This means that FoCal investigates physics in the small x regime, thus, directly relating to the physics goal "*Measure the gluon density in protons and lead nuclei and quantify its nuclear modification at small x and Q^2* ". With this forward region, other physics goals such as "*Jet quenching at forward rapidity in Pb–Pb collisions*", and "*Physical origin of shadowing effects*" can also be studied, since these phenomena occur in the small x regime.

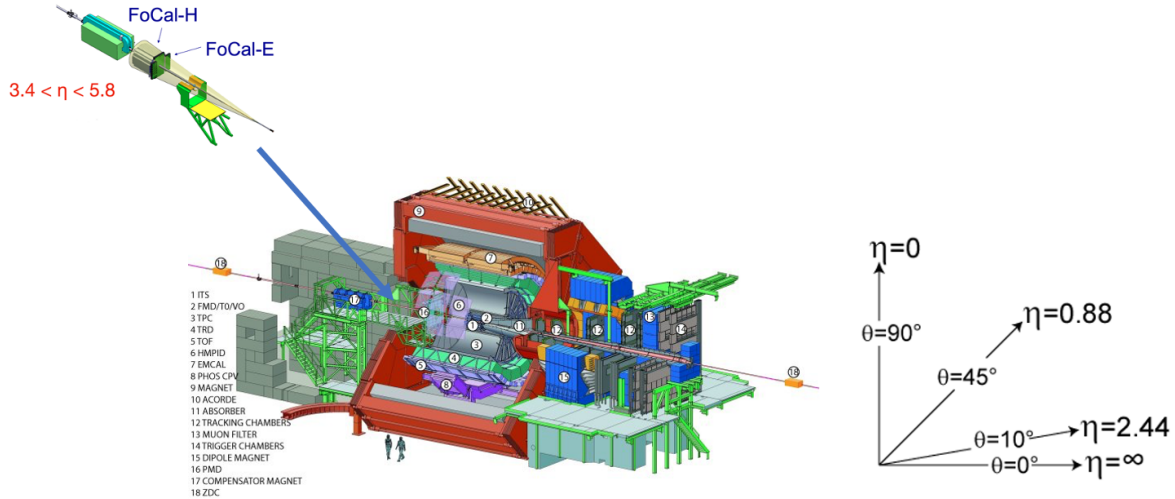


Figure 4: The left-side figure shows a sketch of ALICE, and indicates the forward placement of FoCal in ALICE [4]. The right-side figure shows a description of the rapidity in terms of degrees with respect to the beam-pipe [23].

The position in the forward region, means that incoming particles from the collision point are high-energy particles. This leads to why FoCal has been chosen to be constructed as a calorimeter. Calorimeters are built as dense particle detectors, which means they have the ability to absorb high-energy particles. There exist multiple types of calorimeters, depending on the material, number of materials and the sampling method. These different types of calorimeters will be described in section 4. The specific type of calorimeter for FoCal is determined based on the placement of FoCal in ALICE. FoCal is constructed as a scintillating light sampling calorimeter, due to the placement right beside the compensator magnet. The signal type is specifically chosen to avoid possible effects coming from the magnetic field, which means that signal types such as an electric charge type calorimeter is excluded.

The reasoning behind the four main FoCal physics goals will be described in further detail in this section. This is done in order to understand, which phenomena FoCal can contribute information and maybe explanations to.

3.1 Measure the gluon density in protons and lead nuclei and quantify its nuclear modification at small x and Q^2

The sub-structure of protons and nuclei is characterized in terms of parton distribution functions (PDFs). The PDFs are determined from high-energy scattering experiments, and are used to absorb divergences in non-perturbative QCD physics. Various phenomena in non-perturbative QCD are not currently well understood, e.g. the hadronic sub-structure of protons and nuclei, since theoretical predictions cannot be performed. This is why some elements, such elements as the PDFs, are predicted in experiments. These experiments are usually deep inelastic scattering experiments. Through these scattering experiments it becomes possible to estimate the quark and gluon (partons) contribution in e.g. protons [1]. The procedure of estimating the PDFs is currently done from the Björken parameter x , which describes the momentum fraction of the partons of the total momentum of the e.g. proton. The Björken parameter x is

given by [22, p.201-214]:

$$x = \frac{Q^2}{2Mc^2\nu}$$

where Q^2 is the squared four-momentum transfer, ν the energy transfer and M the nucleon mass. At small values of x , the partons only carry a small fraction of the total momentum of the proton. At x -values around 1/3 one can determine the building blocks of the protons to be 2/3 u-quarks and 1/3 d-quark, as seen in figure 5. These quarks in the proton are called valence quarks. If one goes toward smaller values of x , one finds that other types of quarks also contribute to the total momentum of the proton. This contribution of quarks for small x are called sea quarks. Together with the increasing contribution from the quarks, the contribution from gluons increases for small values of x . Experiments show that the density of gluons increase dramatically towards small x and large values of Q^2 . The increase of the gluon density stems from multiple factors, one factor coming from binding the quarks together, which means that for small values of x more quarks get created from the vacuum, resulting in several gluons to bind these sea quarks together. Another factor is that the gluons can interact with themselves, which can lead to gluon fusion, and fission. The current theory predicts that the increase of the gluon density should not continue linearly for small enough values of x . However, the evolution of the gluon density in e.g. protons and nuclei should reach a point where non-linear effects are present, limiting the value of the PDFs. One explanation of this phenomenon is called gluon saturation. Gluon saturation has not yet been confirmed by experiments, but is predicted by theories. One of these theories are called Color Glass Condensate (CGC) [1] [22].

The examination of the gluons' density at small x and Q^2 in protons and lead nuclei, is one of the focus points of FoCal [1], due to its forward placement in ALICE, leading to investigation in small values of x .

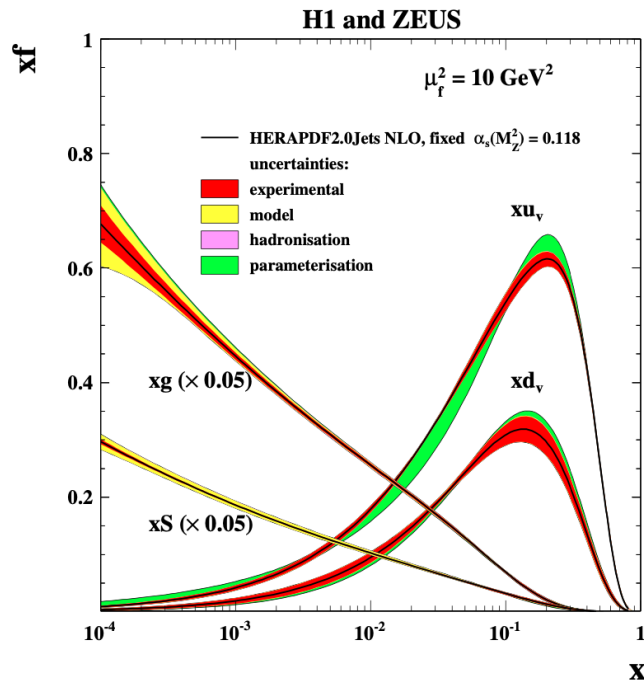


Figure 5: The figure shows a plot of the estimated PDFs from the experiment from HERAPDF 2.0 data. The PDFs are determined from charm data, jet data and low energy data as well as the HERA-I and II high energy inclusive data [1].

3.2 Explore the physical origin of shadowing effects

Shadowing effects are another possible explanation to the non-linear effects limiting the PDFs. Global fits to the PDFs from the measurements of the deep inelastic scattering experiments indicate that the gluon density at small values of x , should be smaller in e.g. lead nuclei than it should be for e.g. a free proton. It is the magnitude of this suppression, which is called shadowing effects [1].

In the region of small values of x a systematic reduction of the nuclear structure function, F_2 is observed. The nuclear structure function is usually defined through the ratio of the nuclear structure function per nucleon divided by the nucleon structure function [26]:

$$R_{F_2}^A(x, Q^2) = \frac{F_2^A(x, Q^2)}{A \cdot F_2^{\text{nucleon}}(x, Q^2)}$$

where A is the nuclear mass number. At $x < 0.1$ shadowing can be used to describe the gluon density in protons and nuclei. The shadowing effect increases as x decreases, where the smallest value of x , can be used to describe the saturation of the density of gluons. The shadowing increases with A , and decreases with increasing values of Q^2 [26].

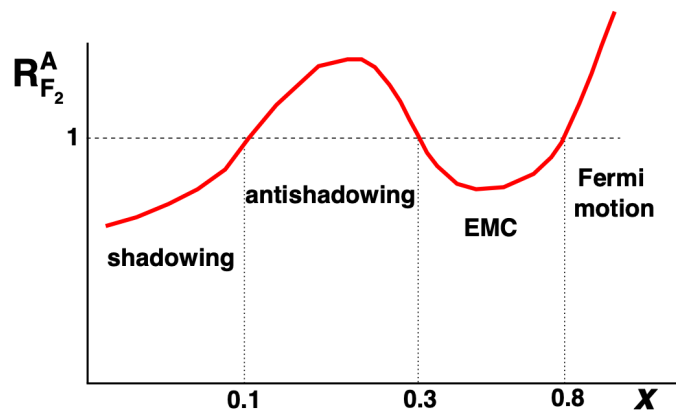


Figure 6: The figure shows the region of small x , where shadowing effects are present [26].

The examination of the origin of shadowing effects at small x and Q^2 in protons and lead nuclei, are one of the focus points of FoCal [1], again due to its forward placement in ALICE, leading to investigation in small values of x .

3.3 Jet quenching at forward rapidity in Pb–Pb collisions

A jet is a collection of high-energy elementary particles that emerges from a collision of ultra-high-energy particles. Jets are produced in collisions by quantum chromodynamic (QCD) hard scattering processes, where quarks and gluons with high transverse momentum ($p_T = \sqrt{p_x^2 + p_y^2}$) collides and combines. In these collisions, where the jets are produced, an extremely hot and dense medium is created (QGP), and it is in the interaction between the jet and this medium that the phenomena jet quenching occurs. In the collision and in the creation of particles, it is seen that two back-to-back jets are created, i.e. jets that travel in opposite directions. These two jets are called the leading and sub-leading jet. In the creation of the back-to-back jets, one of the jets can interact strongly with the medium of the QGP, leading to a

significant energy reduction of the jet (sub-leading jet). This energy reduction of the jet is what is called jet quenching. Jet quenching, is one of the proofs which have been used to establish the existence of the QGP. The jet's interaction with the QGP medium, can provide information of the properties of the medium, and thus some of the early stages of the universe [25].

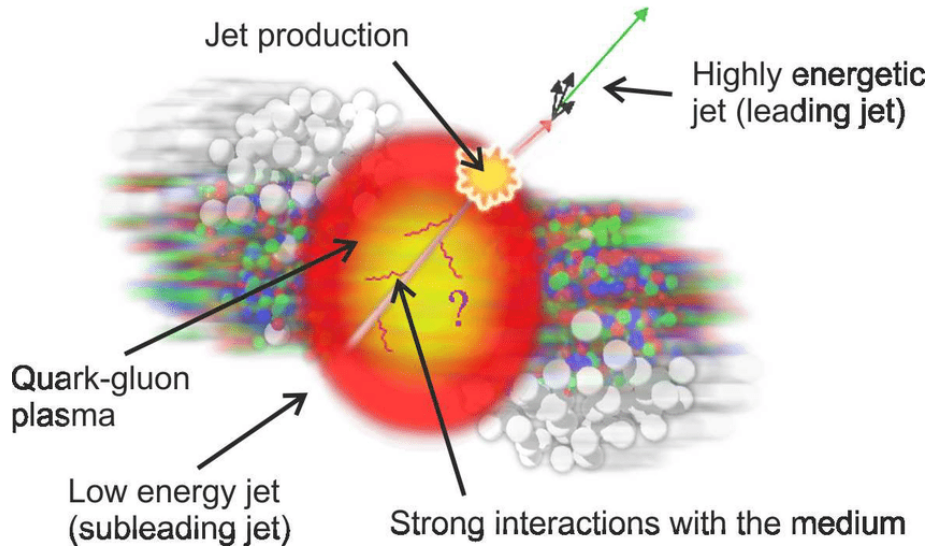


Figure 7: The figure shows a sketch of the jet quenching phenomenon during heavy ion collision [24].

The current theory is that jet quenching occurs both in p-p, p-Pb and Pb-Pb collision, but has so far only been observed in Pb-Pb collisions due to the larger number of particles being produced in these collisions, resulting in larger area of QGP that the jet can interact with. It is in these collisions and at forward rapidity, that FoCal is intended to provide information about jet quenching. The search for jet quenching in small systems, i.e. p-p and p-Pb, is active research.

3.4 Origin of long-range flow-like correlations in p-p and p-Pb collisions

In the collision of heavy ions in the LHC, the medium QGP is created. So far, QGP has not been confirmed in p-p or p-Pb collisions, but is actively being investigated. The description of the properties and the evolution of the QGP is given by the theory called hydrodynamic and can be studied by using flow observable. Flow can be studied in various systems e.g. in large systems Pb-Pb, or in small systems e.g. p-p or p-Pb.

In the stage before the collision, when the proton or heavy ion are accelerated up to nearly the speed of light, such things as length contraction occurs, and the spherical heavy ion will appear as flat disks. The centrality of the collision is determined from a parameter called the impact parameter, which can be determined by examining the number of nucleons that interact with each other. The interacting nucleons are called participants, and the non-interacting nucleons are called spectators. The ratio of participants to spectators determine the shape of the QGP. A ratio close to 1 would lead to a close to spherical shape of the medium, whereas a ratio further from 1 would lead to an almond shape. In the latter of the two cases, the pressure gradient of the QGP medium is non-uniform, which leads to a larger expansion in one direction. The asymmetric expansion of the QGP medium together with the strong interaction

between the hadrons in the medium, leads to observations where the emitted particles tend to go in one direction [25].

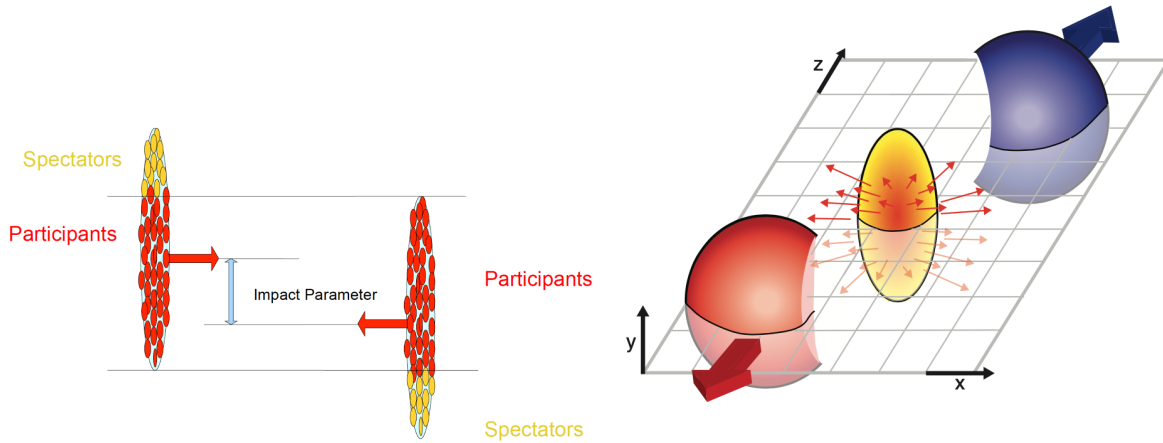


Figure 8: The left-side figure shows a sketch of the flat disk of nucleons, where the participants, spectators and impact parameter is indicated. The right-side figure shows the expansion of the almond shaped QGP medium [25].

The QGP medium cannot be measured, due to its fast expansion. However, the distribution of the emitted particles can be measured with the detectors in ALICE, and these measurements can be used to determine properties of the QGP. Fluctuations in these measurements will occur, since the distribution of the quarks and gluons that the nucleons consist of will differ, which yield a number of different outcomes. With these fluctuations a contribution of, so-called non-flow, needs to be removed since it acts as a noise in the measurement. Non-flow can e.g. be jets and decay products from the particles from the QGP medium. One of the processes used to remove non-flow and to investigate flow, is called long-range. The non-flow can e.g. be removed by demanding data from a large gap in pseudorapidity, which one can get from taking data from two different detectors. FoCal can be used as one of these detectors in the study of flow correlations in small system as collisions of p-p and p-Pb³.

4 Calorimeter physics

In particle physics, calorimeters are used to measure the deposited energy of the particles that interact with the experimental setup. In a calorimeter, the particles are fully absorbed and their energy is converted into a measurable signal. This signal serves as a measurement of the incident particle's energy. When the particle interacts with the calorimeter, it starts a particle shower, where the energy progressively decreases as the shower transverse the detector. The interaction with the calorimeter can either occur via the electromagnetic force or the strong force.

Calorimeters can have two types of structure. They either have a homogeneous structure or a sampling structure depending on the number of different materials and the type of material they are constructed of.

³Other methods are also used to study long-range flow correlations, but these does not correlate with this FoCal physics goal.

4.1 Homogeneous and Sampling Calorimeters

A homogeneous calorimeter is, as the name indicates, constructed of one material, called the active material. In a homogeneous calorimeter, the active material acts both as absorber of the incident particle, but also as the signal generator which gives a detectable signal.

Homogeneous calorimeters are used in experiments to detect three types of signals, namely scintillation light, cherenkov light, or an electric signal. Depending on what the calorimeter should detect, the active material differs.

For the case of scintillation light, $PbWO_4$ crystals are often applied. A calorimeter of this kind has been used in the experiment CMS at CERN. These crystals are among the dense materials producing scintillation light. However, one can also use liquefied noble gases to study scintillation light. If one instead wants to study cherenkov light, the most common material is lead glass, where other materials can be mixed in, for example, the material, PbF_2 . Depending on the mixed-in materials, the cost of the calorimeter goes up. The last type of signal detectable in homogeneous calorimeters is the electric signal. Homogeneous calorimeters which produce electric signals are made of silicon and germanium crystals. For this kind of calorimeter, an electron-hole pair is produced in the material valence band and in the conduction band, which gives rise to the electrical signal [27, p. 10].

Due to their relatively low cost, homogeneous calorimeters are often used in large-scale experiments which need to cover a large area. Such experiments could be neutrino and astroparticle physics experiments since large volumes are needed to detect rare events⁴. The energy resolution of a homogeneous calorimeter is often relatively good since the particles do not pass through different layers of material.

The other type of calorimeter is a sampling calorimeter, which is constructed of two types of material, an active and a passive material. The active material (e.g. a scintillator) is the signal-generating material and the passive material (e.g. copper) is the absorption material. The ratio between the active material and the passive material determines the sampling fraction of the calorimeter, given by:

$$f_{Sampling} = \frac{E_{MIP}(active)}{E_{MIP}(active) + E_{MIP}(passive)} \quad (1)$$

Where $E_{MIP}(active)$ is the deposited energy by an incident minimum-ionizing particle (MIP) in the active material, whereas $E_{MIP}(passive)$ is the corresponding deposited energy in the passive material.

Sampling calorimeters are usually used in connection with high-energy particle colliders. The energy resolution of a sampling calorimeter is usually worse in comparison to homogeneous calorimeters, but sampling calorimeters have the advantage that they can easily be segmented. Sampling calorimeters are therefore a better solution in regard to spatial resolution and thus particle identification.

Sampling calorimeters are categorized with respect to the active material. Hence, there exist four types of categories within sampling calorimeters: scintillation, gas, solid-state, and liquid calorimeters. As for the case of the homogeneous calorimeter, the signal from scintillation calorimeters is generated in the form of light in the UV or visible spectra. For the remaining three cases, the signal is an electric charge [28]. The electrical charge type calorimeters will not be described due to the focus of this thesis.

Scintillation materials come in many shapes and sizes, which makes them advantageous in the construction of sampling calorimeters. Most scintillating materials used in sampling calorimeters are constructed from a core (e.g. glass or polystyrene) with a cladding material around the core. The cladding has a lower

⁴I will not go into further detail with homogeneous calorimeters since the calorimeter investigated in this thesis is a sampling calorimeter.

index of refraction than the core of the scintillator. This is required for the photons to be transported along the scintillator, to where the readout is placed. The photons inside the scintillator is therefore traveling near the critical angle, which is defined as [29]:

$$\theta_{cr} = \arcsin\left(\frac{n_{clad}}{n_{core}}\right)$$

where n_{clad} and n_{core} is the refractive index of the cladding material and core, respectively. The photons in the scintillator is generated under excitation from high-energy particles in particle showers in the calorimeter. A benefit of using scintillation light is that it functions as both the generator of the photons and the transport to the readout of the calorimeter [29]. An example of such a scintillating material could be scintillating fibers.

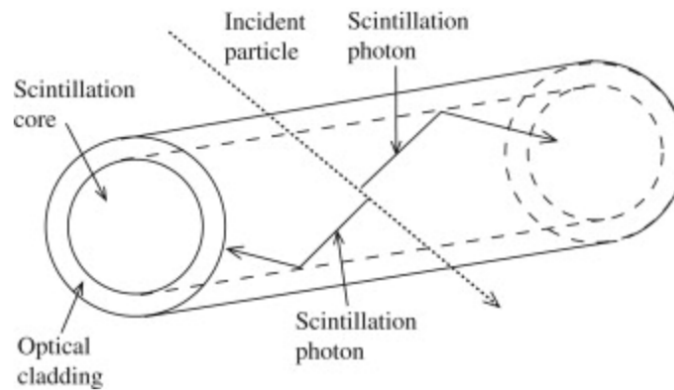


Figure 9: The figure shows the construction of a scintillating fiber, as well as the photons generated inside the fiber [36].

The most commonly used passive materials are lead, iron, and copper [28]. The choice of passive material often comes down to the cost to efficiency of the material. Depending on the generated signal, the construction of the passive and active layers and the interplay between the materials also plays a role. A sampling calorimeter can either have transverse (spaghetti calorimeter) or longitudinal (sandwich calorimeter) segments⁵.

4.2 Electromagnetic calorimeter

The purpose of an electromagnetic calorimeter is to measure the deposited energy of electrons, positrons, photons, and π^0 as they transverse the material of a calorimeter. An electromagnetic calorimeter therefore studies particle showers produced by particles that interact electromagnetically. The deposited energy in an electromagnetic shower increases with increasing shower depth. As the electromagnetic shower develops, the energy of the particles decreases, until a threshold is reached. This threshold is called a shower maximum [29, p.53].

Electromagnetic showers differ depending on the type of particle that enters the calorimeter. An example of a shower development induced by electrons or photons can be seen in figure 10.

⁵An example of these two constructions will be given in section 5.

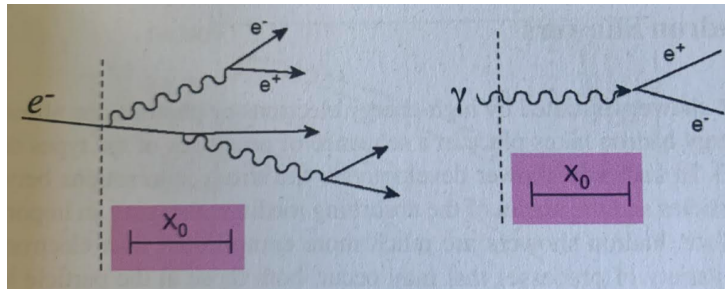


Figure 10: The figure shows two different electromagnetic showers induced by either an electron (left) or a photon (right) when transversing the passive material of a calorimeter [29, p.55].

An electromagnetic shower started by an electron or positron has two different ways through which it loses its energy, when interacting with the passive material. These are ionization of atoms and Bremsstrahlung. Ionization of atoms happens when a charged particle transverse matter (e.g. the passive material of the calorimeter). In this process the charged particle ionizes the atom, which either gains or lose an electron. In the process of Bremsstrahlung, the electron/positron losses energy by radiating photons due to Coulomb interactions with the electric field from the atomic nuclei of the passive material [29, p.31-34]. The majority of the radiated photons are absorbed through Compton scattering and the photoelectric effect. Compton scattering describes the scattering of a photon and an atomic electron after collision. The scattering transfers energy to the electron, which unbinds the electron from the atom. The photoelectric effect describes an effect were an atom in the passive material absorbs a low energy photon, resulting in an excitation of the atom, which emits an electron [29, p.39].

An electromagnetic shower started by a photon, depends on the energy of the incident photons. The dominant process for a photon with an energy above twice the energy of the electron rest mass, is pair production, where an electron and positron pair are created. The electron and positron, created under the pair production, may undergo either the ionization or Bremsstrahlung described earlier. The electron will at low energies get absorbed by an ion, and the positron annihilates with an electron from the passive material. The annihilation of the positron creates two back-to-back photons with an energy of 511 keV [29, p.39]. Other processes can also occur at low energies, such as Reyleigh scattering. Reyleigh scattering describes the process where a low energy photon is deflected by an atomic electron. In this process the photons does not lose it energy, only its initial direction. Thus, Reyleigh scattering contributes to the calorimeters spatial energy distribution [29, p.37].

The development of electromagnetic showers is often described by the radiation length (X_0), which is determined as the mean length in which an electron has lost $\frac{1}{E}$ of its energy, when transversing the passive material of the electromagnetic calorimeter. The radiation length for two different electromagnetic showers is shown in figure 10. The radiation length is given by [29, p.59]:

$$X_0[\text{g}/\text{cm}^{-2}] = \frac{716.4 \cdot A}{Z(Z+1) \cdot \ln\left(\frac{287}{\sqrt{Z}}\right)}$$

where A is the mass number and Z is the atomic number of the material. However, the radiation length can also be calculated in other ways depending on a mixture of different materials, or if a material is composed of several materials (e.g. PbWO_4 crystal).

Another factor, which is often used in the description of electromagnetic calorimeters is the Molière radius. The Molière radius describes the transverse particle shower development. The Molière radius

and the radiation length is related by the approximated relation [29, p.60-61]:

$$\rho_M = E_s \cdot \frac{X_0}{\epsilon_c}$$

where E_s is the scale energy, defined as $m_e c^2 \sqrt{\frac{4\pi}{N}} = 21.2 \text{ MeV}$, and ϵ_c is the critical energy defined as $\frac{610 \text{ MeV}}{z+1.24}$ for solid and liquid phase materials.

4.3 Hadronic calorimeter

The purpose of a hadronic calorimeter is to measure the deposited energy of hadrons that transverse the material of a calorimeter. Due to the structure of a hadron induced particle shower, a hadronic calorimeter is constructed to study both particles that interact electromagnetically and strongly. Depending on the incident particle, e.g charged hadron, neutral hadron, or in case of a jet, the hadronic shower development differs. An example of a shower development induced by a hadron can be seen in figure 11.

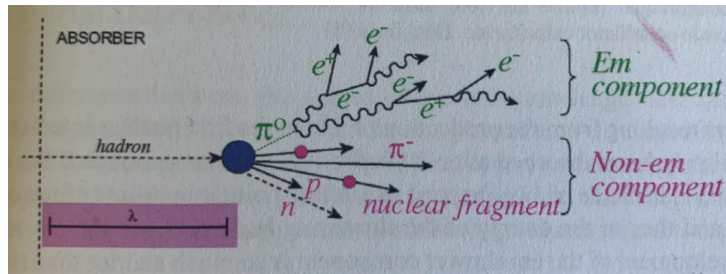


Figure 11: The figure shows a hadron transversing the passive material of a calorimeter. The hadron deposits its energy in the material, inducing a shower consisting of a electromagnetic component (e.g π^0) and a non-electromagnetic component (e.g. charged hadrons and nuclear fragments) [29, p.57].

When a hadron transverse matter different combinations of phenomena can occur depending for instance on the charge of the particle. A hadron induced particle shower consists of two components, an electromagnetic component and a non-electromagnetic component, and it can therefore be complicated to investigate. The particles produced under electromagnetic interactions will shower as described in section 4.2. The non-electromagnetic component of the shower happens through the strong interaction. A charged hadron can ionize atoms the same way as seen in electromagnetic interactions. However, charged hadrons can do this continuously before encountering an atomic nucleus and interacting strongly. The strong interaction comes into play between the shower particles and the nuclei of the passive material of the calorimeter. In this strong interaction, both the shower particle and the atomic nucleus undergo substantial change. The shower particle will in the process break into fragments of new hadrons. Meanwhile, the struck atomic nucleus may in this process get excited and lose some of its neutrons and protons. The nucleus will later decay emitting several photons [29, p.41]. If the hadron is neutral, ionization of the atoms in the passive material does not occur. The only way a neutral hadron can decay is by nuclear interactions, and it is therefore commonly seen that neutrons can exit a hadronic calorimeter without being absorbed.

The development of a hadronic shower is usually described by the interaction length (λ_{int}), which is determined by the average distance a high-energy hadron can travel before undergoing a nuclear inter-

action. The nuclear interaction length is given by:

$$\lambda_{int} = \frac{A}{N_A \cdot \rho \cdot \sigma}$$

where A is the atomic mass, N_A is the Avogadro number, which has the value $N_A = 6.02 \cdot 10^{23} mol^{-1}$, ρ is the atomic density of the target, and σ is the inelastic nuclear cross section.

In the process of nuclear interaction, different reactions in the absorption of the hadron can occur. Some of these are nuclear spallation and nuclear binding energy.

Nuclear spallation is a two step process where a hadron with high energy hits an atomic nucleus. In the first step in this process, the hadron collides with the nucleons (protons and neutrons) inside the nucleus of the atom. This transfers energy to the hit nucleons, which will start moving inside the nucleus and collide with each other. This cascade inside the atomic nucleus can potentially create unstable hadrons, and other particles if the transferred energy is sufficient. The second step in the process is this excitation in the form of particles [29, p.43].

Nuclear binding energy is related to the spallation reaction. During the nucleon cascade inside the atomic nucleus, some of the nucleons may get unbound from the nucleus. The energy needed to release these nucleons from the nucleus, is what is known as the nuclear binding energy. The nuclear binding energy contributes to what is called invisible energy in a hadronic calorimeter, since it does not contribute to the calorimeter signal. Due to the various types of processes which can happen in a hadronic calorimeter, the invisible energy varies from event-to-event. Because of this the fluctuations in the invisible energy mean that it can go from being almost zero to being 60% of the deposited energy. Invisible energy is one of the biggest challenges for reconstructing the energy of the incident particle in the calorimeter, and can lead to difficulties in particle identification [29, p.44/143].

The detectable signal in a hadronic calorimeter is defined as the visible energy, which is the energy deposited in the active material of the calorimeter. This detectable signal is proportional to the total energy deposited by the particle. Other processes that can contribute to the detectable signal, related to the nuclear reactions in absorption of high-energy hadrons could be spallation nucleons, and evaporation neutrons.

The spallation nucleons process is important for the production of α particles. During the spallation reaction when a high-energy hadron is absorbed, multiple nucleons can aggregate. In the aggregation process α particles can get produced by two spallation protons and two neutrons. The production of the α particles generally takes place in the energy range between 3 to 20 MeV [29, p.43-50]. These reactions are not the only ones contributing to a detectable signal in hadronic calorimeters. Additional processes that contribute are interactions of neutrons with matter. These interactions are subject to the processes in which the evaporation neutrons loses their kinetic energy and afterwards get absorbed in the passive material. The absorption of neutrons depends entirely on strong interactions in the material. The possible interactions of the neutrons with matter is: elastic neutron scattering, inelastic neutron scattering, neutron capture, and production of α particles.

For neutrons with an energy of around 2 eV to 1 MeV, the most common process to occur for the neutron energy loss is elastic scattering. In this energy range the cross section between the neutron and the atomic nucleus is large. Depending on the mass of the atom and the centrality of the collision, the fraction of the energy loss can vary from 0 to $\frac{4A}{(A+1)^2}$.

Inelastic neutron scattering, is the process of a scattering between a neutron and the atomic nucleus of the passive material of the calorimeter. In the inelastic scattering, a fraction of the neutrons kinetic energy excites the nucleus and releases the excitation energy in the form of photons.

Neutron capture is one of the important processes when it comes to invisible energy, in the sense that it reduces it. When the neutron is captured by the atomic nucleus, the atom gains the energy back that it lost when releasing it in the nucleon spallation reaction. The atom that captures the neutron may get excited, which leads to an emission of photons, and occasionally α particles. The emission depends on how light the capturing atom is [29, p.43-50].

5 Forward Calorimeter (FoCal)

Forward Calorimeter (FoCal) consists of an electromagnetic calorimeter, called FoCal-E, and a hadronic calorimeter, called FoCal-H. FoCal is as mentioned an upgrade to the ALICE experiment and will be placed in the forward region (See the section 2.2.2) right beside the compensator magnet. FoCal is intended to be installed in ALICE in 2027/2028 and is now in the prototype stage of the project.

This section will go through the conceptual ideas and design behind the FoCal-E and FoCal-H prototypes, with a main focus on the hadronic calorimeter, due to the focus of the this thesis.

5.1 FoCal-E

Forward Electromagnetic Calorimeter (FoCal-E) is the first of the two calorimeters that constitutes FoCal. FoCal-E is constructed to be a longitudinal segmentation calorimeter (sandwich calorimeter) consisting of silicon (active material) and tungsten (passive material) plates (Si+W), summing up to a length of around 20 cm for all layers. The structure of the segmentation is a plate of tungsten (W) layers followed by silicon (Si) layers. The silicon layers are designed using two different technologies, with transverse cells. The two differently designed silicon technologies are called pad and pixel.

The FoCal-E prototype consists of a total number of 20 silicon layers, where 18 are pad layers and 2 are pixel layers, with layers of tungsten in between. The pixel layers are positioned at the 5th and 10th layers. An illustration of the longitudinal segmentation of all layers, and the transverse segmentation of the silicon layers can be seen in figure 12 [1].

The choice of passive and active material for the FoCal-E calorimeter design are not chosen arbitrarily. Tungsten is chosen as the absorber, due to its small Molière radius ($\rho_M = 9mm$) and radiation length ($X_0 = 3.5mm$). Silicon is chosen due to its structure and non-magnetic ability, which is important seen in relation to the final detectors position beside the compensator magnet. The silicon layers is designed using two different technologies. The first technology is the pad layers with a size of $\approx 1 cm^2$ using low gain (LG) cells, similar to the Molière radius. The second is the pixel layers, with a size much smaller than the Molière radius ($\approx 30 \times 30 \mu m^2$), using high gain (HG) cells to obtain a high granularity. Silicon layers are needed to resolve multiple hits, spatial separation of showers and information of the π^0 identification. The structure of the pixel layers provides important information in regards to the π^0 identification, since π^0 -particles decay to two photons. The pixel layers can then distinguish these two photons even though they are close to each other [1].

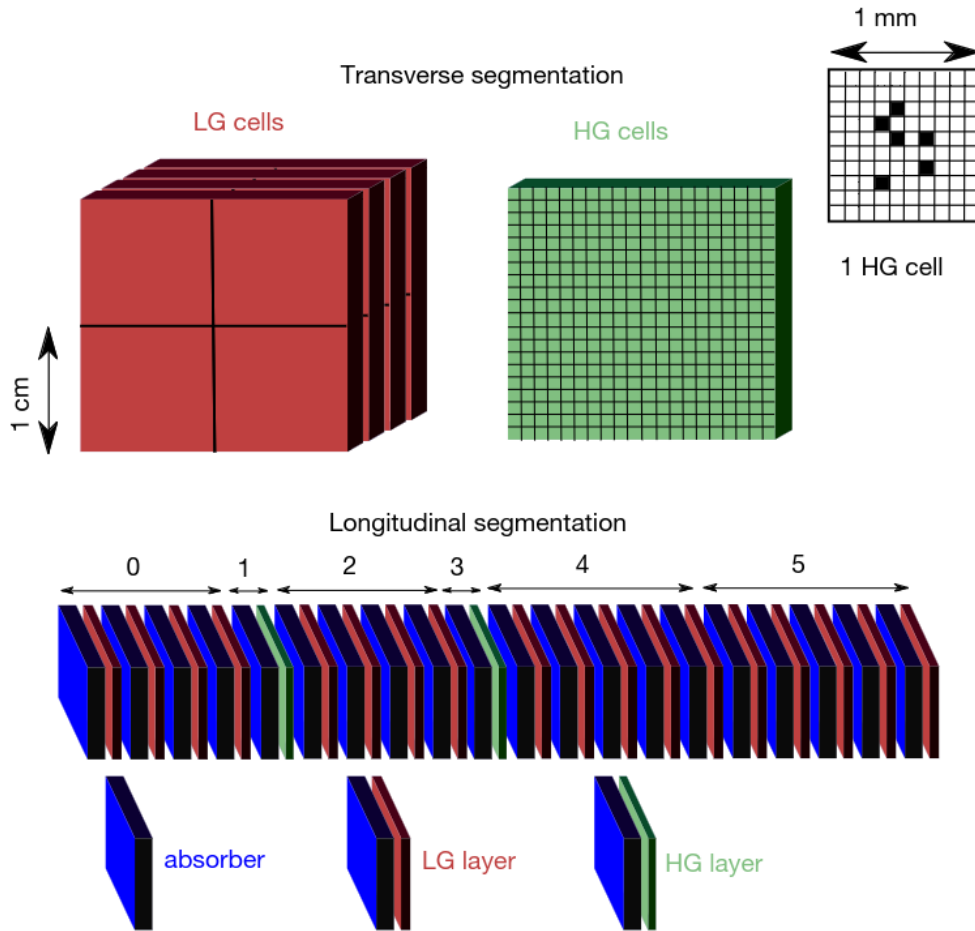


Figure 12: Schematic of the FoCal-E segmentation of the tungsten absorber layers (passive material) and the two types of Silicon layers, Pad and Pixel (active material). The pad layers are designed with low gain (LG) cells and the pixel layers are designed with high gain (HG) cells. [1].

Each cell in the pixel and pad layers is read out individually, but the layers are grouped into 6 segments for the determination of cluster finding. The segmentation, position of the different layers and the 6 segmentation groups can be seen in figure 12.

FoCal-E will have a total depth of $20X_0$ in order to have sufficient linearity at large energies. A longitudinal segmentation of these tungsten and silicon layers ensures particle identification and background rejection [1].

5.2 FoCal-H

Forward Hadronic Calorimeter (FoCal-H) is the second of the two calorimeters that constitute FoCal. FoCal-H is a transverse sampling calorimeter (spaghetti calorimeter). It consists of scintillating fibers, enclosed in copper-tubes. The scintillating fibers have a diameter of 1 mm, and the copper-tubes have an inner diameter of 1.1 mm and an outer diameter of 2.5 mm.

Until now two FoCal-H prototypes have been constructed. The first and second prototype will be described in detail in the following sections 5.2.1-5.2.2.

5.2.1 FoCal-H first prototype

The main focus of the first prototype was to test the conceptual design of the transverse segmentation calorimeter and the readout electronics.

The prototype consisted of 1440 copper-tubes, which were placed in a pattern to get a square calorimeter module. The prototype had a height and width of 95 mm and a length of 550 mm. The length was half of the intended length of the final design of FoCal-H. A scintillating fiber, from the vendor Saint-Gobain, was placed inside each of the copper-tubes. The scintillating fiber used in this prototype was the BCF10. The BCF10 has a blue emission color (432 nm), a decay time of 2.7 ns, and emits ~ 8000 photons per MeV [40].

The scintillating fibers were collected into 48 bundles of 30 fibers, and the bundles were held together in a collector plate. A schematic of the placement of the copper-tubes, as well as the scintillating fiber collector plate can be seen in appendix section 11.1. The collector plate was mounted at the back-end of the calorimeter module, and had the purpose of holding the bundles of scintillating fibers in position, as well as holding the Silicon Photomultiplier (SiPM) readout boards. In front of each bundle of scintillating fibers a SiPM was placed, making sure to measure the photons coming from the fiber bundles. A pictures of the FoCal-H first prototype can be seen in figure 13.

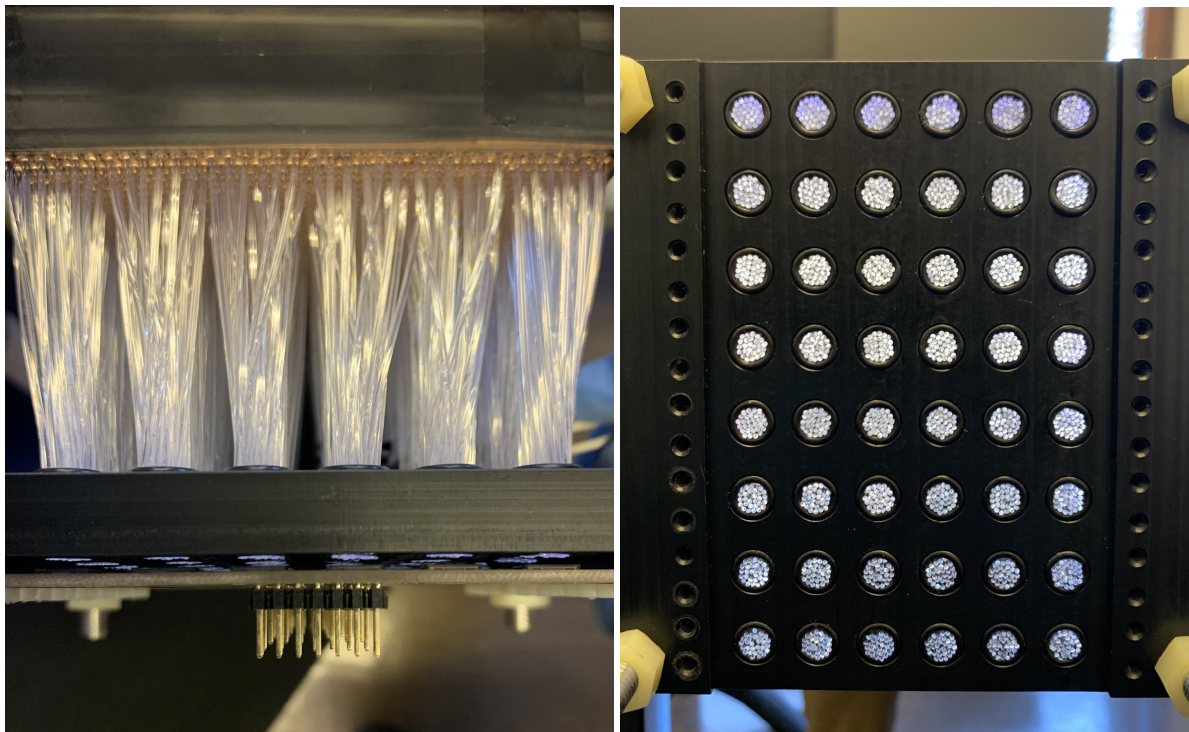


Figure 13: The left-side figure shows the scintillating fibers coming out of the copper-tubes. These fibers are bundled up and collected into a collector plate, which holds them in position. On the other side of the collector plate the SiPM boards are mounted to read out the photons from the scintillating fibers. The right-side figure shows the collector plate without the SiPM boards. This picture shows the ends of the scintillating fibers after they have been bundled up.

A CAEN A1702 readout board was used to read the signal in the SiPMs. The CAEN A1702 board is designed to measure the signal from SiPMs and has 32-channels for the SiPMs to be connected. Two of

these boards were therefore needed to read out the 48 SiPMs [30] used in the FoCal-H first prototype. During the first testbeam of the FoCal-H first prototype, it was discovered that synchronization difficulties occurred between the two CAEN A1702 readout boards. This issue made it difficult to reconstruct particle showers, and for this reason the CAEN A1702 was not used in any further testbeams. The design of the FoCal-H first prototype showed promising results, and the conceptual idea behind the design was therefore optimized to a larger scale⁶.

5.2.2 FoCal-H second prototype

Different shapes of the calorimeter modules were considered for the FoCal-H second prototype. However, to avoid possible construction difficulties and instability of the modules, a square design was chosen for the calorimeter modules of the FoCal-H second prototype.

The FoCal-H second prototype consists of 9 square calorimeter modules placed in a 3x3 stacking. Each of the modules has 668 copper-tubes with a scintillating fiber inside, and 4 rods in the corners to fasten a collector plate for the fibers and SiPM boards. The length of the calorimeter modules is 1100 mm, which is the maximum size possible, due to the placement of FoCal-H in ALICE. This length corresponds to a nuclear interaction length of $6\lambda_{int}$. The height and width of each calorimeter module is 64.75 mm. This size was chosen so that the weight of a calorimeter module would be ($\sim 32kg$), and thereby manageable to carry by two people. However, this is not a requirement for the final design of FoCal-H.

A schematic of the design of the calorimeter modules can be seen in the left-side figure in figure 14, whereas the right-side figure shows the 3x3 stacking of the 9 calorimeter modules which the FoCal-H second prototype consists of. The total height and width of this prototype is 195 mm.

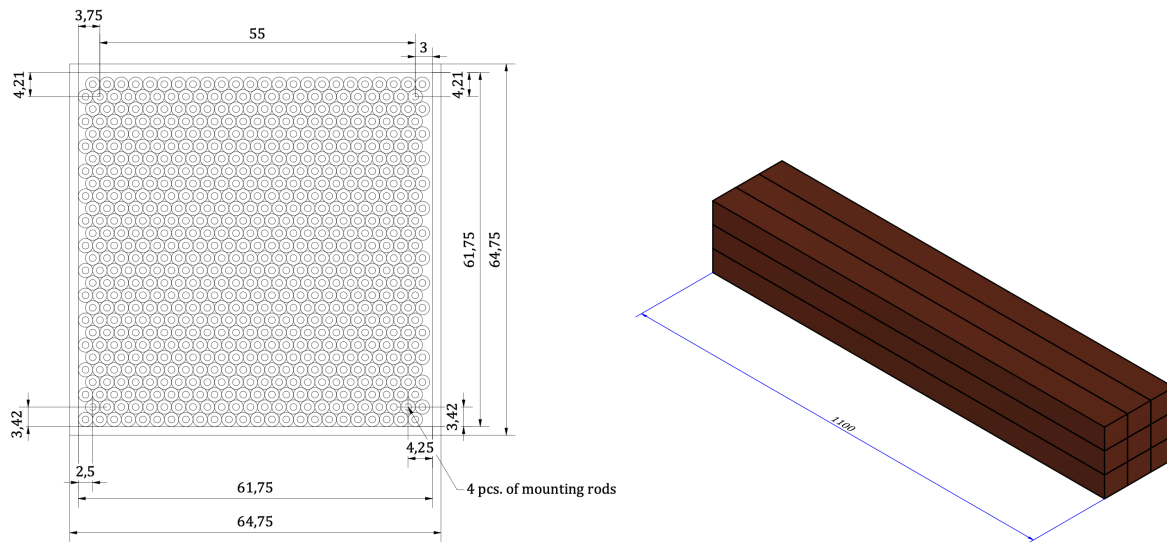


Figure 14: The left-side figure shows a schematic drawing of the design of the calorimeter modules for the FoCal-H second prototype. The right-side figure shows the placement of the 9 square calorimeter modules with respect to each other.

The scintillating fibers chosen for the second prototypes was the BCF12 from the vendor Saint-Gobain. The BCF12 scintillating fiber has a blue emission color (435 nm), a decay time of 3.2 ns, and emits ~ 8000

⁶Optimization of the FoCal-H first prototype to the second prototype was the topic of my thesis preparation project [39].

photons per MeV [40]. One of the reasons why this type of scintillating fiber was chosen, was due to the longer decay time. The intention with the longer decay time was that this would reduce the amount of photons detected by the SiPMs. This was important, since saturation was observed in the FoCal-H first prototype.

As was done for the FoCal-H first prototype, the scintillating fibers were collected into bundles and held in position by a collector plate. Two different collector plates were designed. One for the central calorimeter module, collecting around 14 fibers into each bundle. The central calorimeter module is therefore read out by 48 SiPMs, where each bundle of scintillating fibers is read by one SiPM. The design of this collector plate can be seen in figure 15 below:

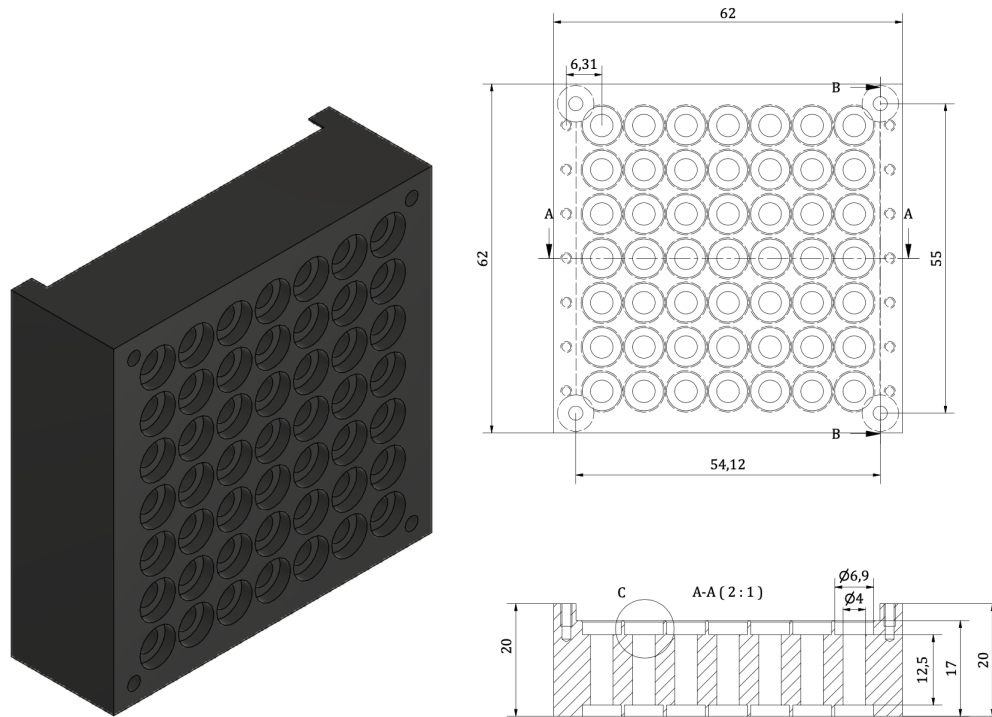


Figure 15: The left-side figure shows a 3D illustration of the 7x7 SiPM collector plate. The right-side figure shows a 2D schematic drawing of the 7x7 SiPM collector plate.

The second collector plate was designed for the outer calorimeter modules, collecting around 27 fibers into each bundle. The outer calorimeter modules are therefore read out by 25 SiPMs, again having one SiPM for each fiber bundle. The design of this collector plate can be seen in figure 16 below:

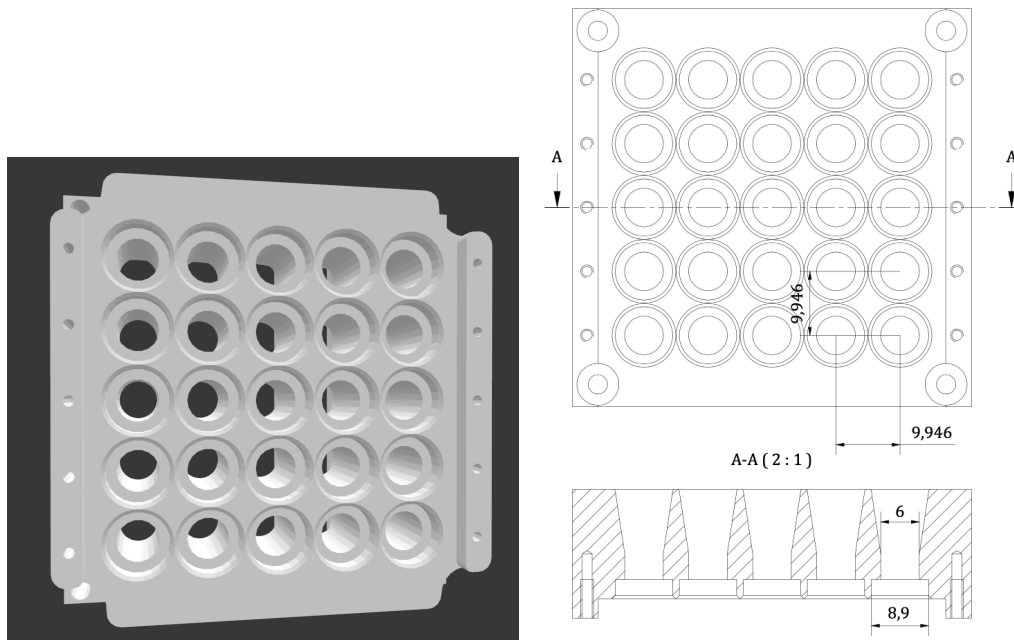


Figure 16: The left-side figure shows a 3D illustration of the 5x5 SiPM collector plate. The right-side figure shows a 2D schematic drawing of the 5x5 SiPM collector plate.

This variation in the bundle size is due to the distribution of particles in the hadronic shower. Hadronic showers tend to be more centered in the middle of the calorimeter, so reducing the number of scintillating fibers for each SiPM will lower the risk of saturating the readout in the center. This will result in higher granularity of the central calorimeter module, and a lower granularity in the outer modules.

5.2.2.1 Silicon photomultipliers (SiPM)

A SiPM is an inexpensive device which can detect low intensity light pulses and convert them into an electronic signal. The SiPMs used in the FoCal-H second prototype was the S13360-6025PE SiPM from the vendor Hamamatsu [32].

A SiPM is constructed of an array of microcells which each consists of a single-photon avalanche photodiode (SPAD) built from a two layered semiconductor junction made of silicon. Depending on the SPAD, the junction can either be a p-on-n junction or a n-on-p junction. The type of junction is dependent on the order of the layers. The two layers are doped differently with two charge carriers, electrons for the n-layer, and holes for the p-layer. The layering of the p and n layers functions as an anode and a cathode and provides that a flow of current, also called photocurrent, can run across the junction, when applying a voltage. The applied voltage is called a reverse bias configuration and sets up an electric field that will cause the charge carriers to be accelerated towards the anode or cathode. The direction of this acceleration depends on the layering. The reverse bias configuration serves an important role to ensure a minimal amount of current to be applied. This minimal current is necessary, since it provides the ability to detect the current produced by the photon absorbed in the active area of the SPAD [34].

The S13360-6025PE SiPM is constructed as a p-on-n junction, which means that the SiPMs used for the FoCal-H second prototype are sensitive to light from the blue to ultraviolet spectrum. The 13360-6025PE SiPM has the largest photon detection efficiency at a wavelength of $\sim 420nm$, which makes it ideal when

having scintillating fibers that emits photons in this range of the spectrum, as is the case with the BCF12 scintillating fibers.

Working with SiPMs, there are some general parameters one would need to know in order to determine their performance. These parameters are: breakdown voltage and overvoltage, gain, and photon detection efficiency (PDE).

The breakdown and overvoltage are two parameters which describe the voltage across the device. The sum of the breakdown voltage and the overvoltage determines the bias voltage, given by:

$$V_{bias} = V_{breakdown} + \Delta V$$

where $V_{breakdown}$ is the breakdown voltage and ΔV is the overvoltage. The breakdown voltage is a description of the minimum voltage which can be applied to the SiPM before it operates in Geiger mode. The overvoltage is a description of the additional applied voltage above the breakdown voltage. The SiPMs used for the FoCal-H second prototype have a breakdown voltage of 53 ± 5 V and a recommended overvoltage of 5 V. Going beyond the recommended value of the overvoltage, leads to an increase of noise parameters, related to the construction of the SiPM. These are optical crosstalk between the microcells, afterpulsing, temperature dependence, and dark count rate. However, not only the noise parameters depend on the overvoltage, the remaining performance parameters also have this dependence.

The SiPM gain is a parameter, which determines the characteristics of the individual microcells in the SiPM. The gain of a SiPM is determined by the ratio between the total charge of the microcells to the initial charge [33].

$$G = \frac{Q}{q} = \frac{C \cdot \Delta V}{q}$$

where C is the capacitance of the microcells, ΔV is the overvoltage and q is the electron charge. Thus, the gain is proportional to the applied overvoltage.

The last of the performance parameters is the photon detection efficiency (PDE). This parameter determines the probability for the SiPM microcells to detect an incoming photon. The photon detection efficiency depends on the wavelength of the incident photon, due to the probability of the incident photon to be absorbed and interact with the material of the SiPM. The PDE also depends on the applied overvoltage, due to the increase in efficiency to detect the incoming photons with increasing overvoltage [33]. For the S13360-6025PE SiPM used in the FoCal-H second prototype the PDE is largest around 420 nm.

These parameters can be useful in the determination of single photon event (SPE) measurements and saturation level.

Multiple factors played a role in the decision of using this SiPM, some due to its performance characteristics and others due to the price and delivery. One of the reasons for choosing the S13360-6025PE SiPM, is due to its cell size and microcell size. The cell size of the S13360-6025PE SiPM is 6x6 mm, which covers the physical size of the largest bundle of scintillating fibers in the outer 5x5 SiPM calorimeter modules. The microcell has a size of $25 \mu m$, which means the SiPM has 57600 microcells ready to detect incoming photons. Microcells in SiPMs vary in size, and the microcell size in the S13360-6025PE SiPM is one of the smaller sizes, which is advantageous in regards to the recovery time of the microcells. SiPMs with large microcells tend to get charged quickly, resulting in a long recovery time. This concept is called the fill factor. A SiPM with a short recovery time is able to detect a larger number of incident photons. This is useful when being in a high rate environment [32]. The environment in which the SiPMs are going

to be placed in also has other consequences for choosing this type of readout device. The back-end of FoCal-H, where the SiPMs are going to be placed, is right next to the compensator magnet. The choice of readout device therefore needs to be one which does not get influenced by the magnetic field from this magnet [34].

5.2.2.2 Readout system - CAEN DT5202

Two different readout systems have been tested with the FoCal-H second prototype. These are the CAEN DT5202 and the VMM+SRS board. This thesis will only describe the CAEN DT5202 readout board, since this board was used in the November SPS H2 testbeam runs. The VMM+SRS board is a readout system which is currently being designed to possibly be used in the final design of the FoCal-H detector. Thus, the VMM+SRS boards are currently still being constructed and tested.

The CAEN DT5202 board is a front-end readout board which is designed for readout of SiPMs. The CAEN DT5202 board consists of two Citiroc-1A chips, which are synchronized with each other. The Citiroc-1A chips in this readout board each have 32 channels, which means that each board has 64 channels available. The synchronization issue from the FoCal-H first prototype is solved for this amount of channels. Multiple of these boards can also be synchronized with each other, by implementation of an external busy trigger system.

The CAEN DT5202 readout board has, in contrast to the CAEN A1702 readout board used for the first prototype, four different ways to trigger on an incoming signal. The first trigger is a Logic OR, which sets the board to initiate a trigger above a certain threshold. The second trigger is majority trigger, which triggers on the majority of the channels. The board reads out all channels when N channels has passed a preset threshold on the number of channels specified. These two trigger systems has the possibility to be externally verified. The third trigger is an external trigger, which triggers on all channels in that readout board collectively. The fourth trigger is a periodic trigger, where the board generated a periodic signal, which initiates the board to trigger on all channels [31]⁷. For the November 2022 SPS H2 testbeam, the external trigger was used to trigger on more than board at the time. In total three CAEN DT5202 readout boards were used, to read out the signal in the testbeam data examined in this thesis.

6 Performance study of calorimeter components

This section will go through different components of the FoCal-H second prototype, which have been studied in order to characterize and optimize them. The components which have been examined in respect to this thesis, are optical crosstalk between SiPMs, scintillating fibers and the way they are cut, and the material of the scintillating fiber collector plate.

6.1 Optical crosstalk

Optical crosstalk was examined in order to determine whether the emitted photons from a given bundle of scintillating fibers are read out by the SiPM corresponding to that bundle. If the photons from a bun-

⁷A detailed description of the optimization of the readout system is given in my thesis preparation project [39].

dle scatter beyond the area that the SiPM covers and are read by the surrounding SiPMs, then optical crosstalk has occurred between the SiPMs. Optical crosstalk between the SiPMs is important to investigate, in regards to particle shower tracking throughout the FoCal-H calorimeter.

The reason why optical crosstalk measurements are prioritized for the FoCal-H second prototype is due to its narrow design compared to the FoCal-H first prototype. The distances between the SiPMs are reduced significantly in the second prototype. Having a 5 mm distance between the SiPMs used for the FoCal-H first prototype, whereas for the second prototype there are a distance of 2.5 mm between the SiPMs used for the outer 5x5 SiPM modules, and no distance between the SiPM used for the central 7x7 SiPM calorimeter module. A picture of all three types of SiPM boards, can be seen in figure 17.

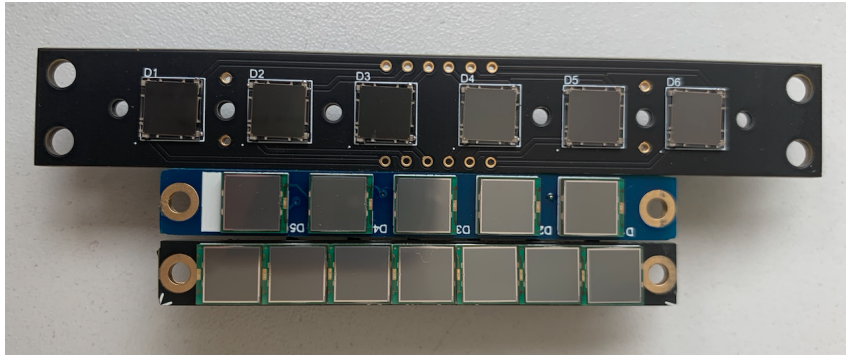


Figure 17: The picture shows the three types of SiPM boards used in the FoCal-H prototypes. The top board shows the SiPM board used in the FoCal-H first prototype. The middle and bottom board show the SiPM boards used for the FoCal-H second prototype. The middle SiPM board shows the board used for the 5x5 SiPM outer modules. The bottom SiPM board shows the SiPM board used in the central 7x7 SiPM module.

Optical crosstalk measurements have been performed for all 9 modules, in order to characterize to what extent it occurs in the FoCal-H second prototype. The results of these measurements are presented in the two following sections, which are split into results for the central 7x7 SiPM calorimeter module and for the outer 5x5 SiPM modules, due to the different amount of scintillating fibers in a bundle. However, the experimental procedure for both types of module layouts is similar.

When testing for optical crosstalk between the SiPMs, one should make sure to test only a few bundles of scintillating fibers at a time. And, for the sake of the measurements, the SiPMs being tested should not be placed close to each other. This can be done by constructing masks for all other channels than for the ones being tested. 3D-printed masks was made for all bundles in both module layouts. In addition to this, the module should be covered in blackout fabric to keep all other surrounding lights out.

To test for optical crosstalk, a blue LED with a pulse of 100 ns was used, together with a diffusing sheet. These two components were carefully chosen to get the best conditions for the measurements. The blue LED was chosen because the SiPMs have their largest photon detection efficiency in the blue spectrum. The diffusing sheet was used because the SiPMs would saturate if not 70-75% of the light is removed since they are very light sensitive. An external trigger was set up between the LED and the CAEN DT5202 readout board, to verify that the photons detected by the SiPM/SiPMs did come from the LED⁸. The LED setup was placed in the front-end of the calorimeter, shining light towards the unmasked scintillating fibers. The light then got transported through the fibers, down to the back-end of

⁸The external trigger used in this experiment was the same as the one when taking the testbeam data.

the FoCal-H calorimeter, and detected by the SiPM(s). The optical crosstalk measurements were taken in the laboratory at CERN, and not in a darkened room as I have done with all previous optical crosstalk measurements [39]. However, the modules tested for optical crosstalk were completely covered, to ensure that no light could penetrate. Additionally, each measurement was taken over the same length of time, to ensure that the SiPMs would be illuminated by the same amount of photons. Whether the SiPMs detects all photons are not certain, due to the fact that they were not gain matched. A bias voltage of 53 V was applied to all SiPMs. This bias voltage was also used for the November 2022 SPS H2 testbeam. A picture of the LED behind the diffusing sheet can be seen in figure 18. The picture shows a setup where three SiPMs in module 9 are tested for optical crosstalk. The picture shows only parts of the components used to test for optical crosstalk.

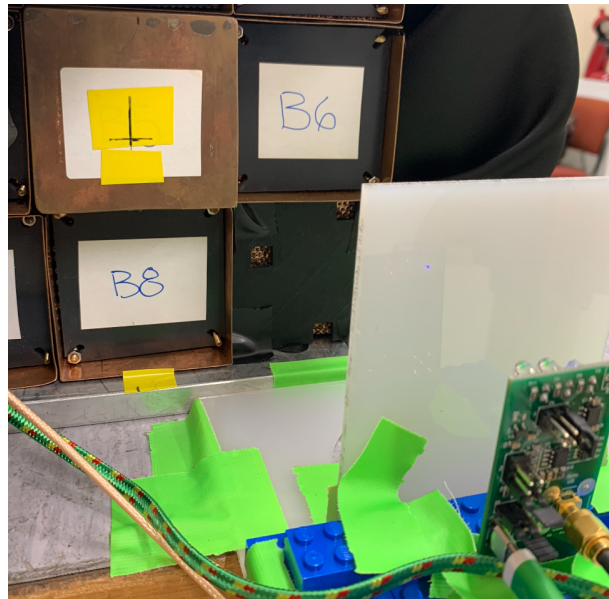


Figure 18: The figure shows part of the experimental setup used to test the 9 calorimeter modules for optical crosstalk. The picture shows the LED placed behind a diffusing sheet, both placed in front of module 9, where 3 of the SiPMs are being tested.

An experimental setup not including this amount of tape would have been preferred to ensure 100% stability of the setup. However, the setup did not move during the measurements for each calorimeter module.

6.1.1 Central 7x7 SiPM module

When testing the FoCal-H second prototype at testbeams, most of the energy will be deposited in the central 7x7 SiPM module, due to the placement of the beam-pipe and how particles spread in a particle shower. Testing for optical crosstalk in the central 7x7 SiPM module is therefore very important in order to reconstruct the tracks from the particles in a shower.

The optical crosstalk measurements for the central 7x7 SiPM calorimeter module were taken by masking up all fibers except those corresponding to the SiPM(s) in question. The SiPMs in the central 7x7 SiPM module should read around 14 fibers from each bundle. During each cycle of measurements, I was able to measure optical crosstalk for up to three SiPMs at a time. Two measurements can be seen in the figure

19, where two (left) and three (right) SiPMs have been tested at once.

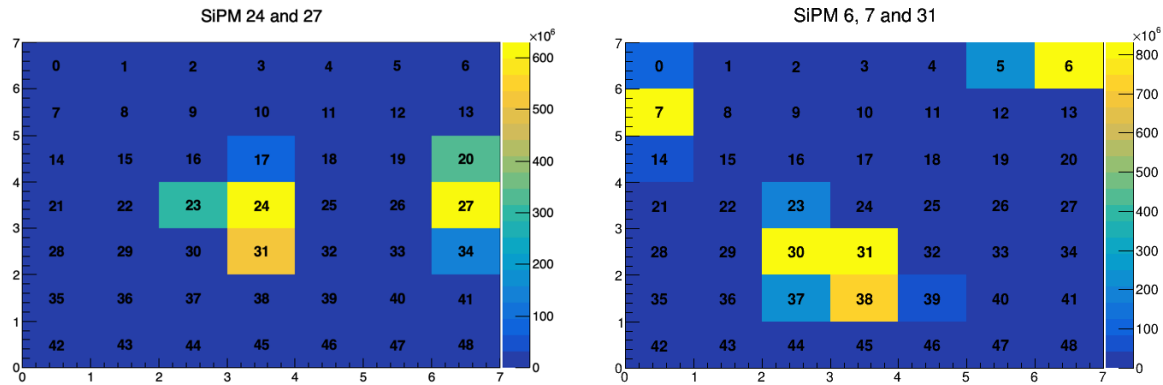


Figure 19: The figure shows two intensity plots of the optical crosstalk measurements made in the central 7x7 SiPM module. The left-side plot shows the intensity plot for SiPM 24 and 27. The right-side plot shows the intensity plot for SiPM 6, 7 and 31. The measurements do show evidence of optical crosstalk between the SiPMs that were tested and the surrounding SiPMs.

The optical crosstalk between the SiPMs is examined by measuring incoming photons in the SiPM that is being tested, as well as in the surrounding SiPMs, as visible in the intensity plots in the figure 19, the extent of optical crosstalk between SiPMs varies across the module. I suspect that the placement of the individual fibers is not necessarily the same across fiber bundles. This can have an effect on the outcome of these measurements. If the LED illuminates scintillating fibers, which are a part of a bundle of fibers for the surround SiPMs, the measurements could indicate a result of optical crosstalk between the SiPMs. To avoid the 3D-printed masks not covering up the correct area, so as to test only a specific SiPM for optical crosstalk, the illumination area in the mask was made smaller than the area of fibers which was to be illuminated. The LED and diffusing sheet were not re-positioned during the measurements on this module. This could therefore not have made an impact on the results.

One thing that can have impacted the results is the 3D-printed masks. Each module has four rods placed in the corners, which are responsible for holding a black PVC plate. The role of the PVC plate is to stop potential light from reaching the ends of the scintillating fibers. By default, each of the 3D-printed masks needed to have room for the rods. During the experiment, I ensured that the rods were covered up so that light from the LED could not get through. This was done by using black electrician tape. However, the possibility of light getting through is not zero.

All the remaining measurements for optical crosstalk between the SiPMs in the central 7x7 SiPM calorimeter module can be seen in appendix section 11.2. Optical crosstalk between the SiPMs seems to be a general issue for the central 7x7 SiPM calorimeter module. Whether it is due to the cut of the scintillating fibers, or the fiber bundles scattering beyond the area of the 6x6 mm SiPM was investigated further⁹. The latter was tested using the same cutting technique used for the scintillating fibers in the FoCal-H second prototype. A bundle of 14 fibers was collected in a 3D-printed holder and illuminated by an LED. The bundle was placed in front of a 8-bit sensor, at the same distance as the distance between the bundles and the SiPMs in the module.

⁹See section 6.2 to read about the cut of the scintillating fibers.

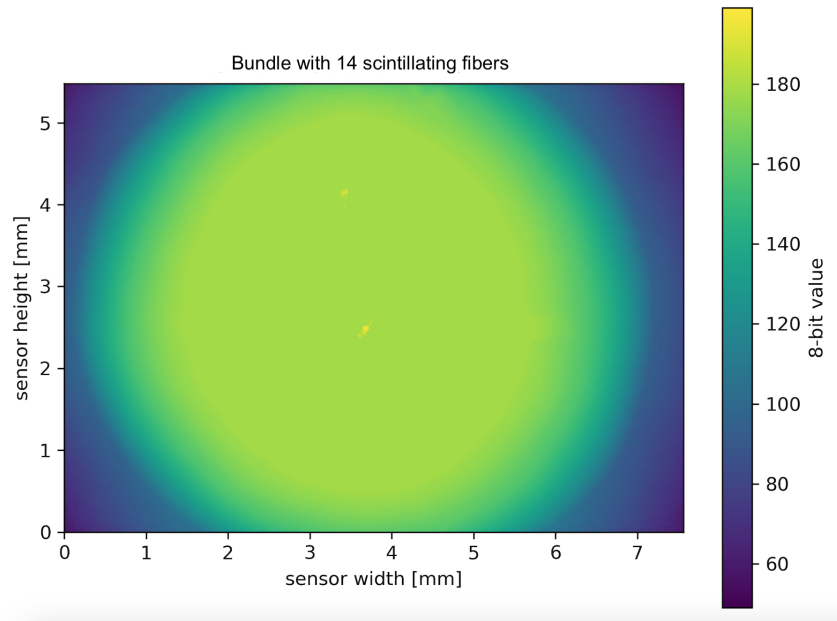


Figure 20: The figure shows an intensity plot of 14 fibers, which has been illuminated by an LED. The light scattering from the fibers, was measured by a 8-bit sensor, which roughly had the dimensions of the 6x6 mm SiPMs.

As can be seen in figure 20, the light from the photons does spread beyond the area of a 6x6 mm SiPM. This is not a lot but it can still have an effect since all the SiPMs in the central 7x7 SiPM module are placed right next to each other. The 8-bit value is a measure of how much the sensor is able to process pr. data block, given by:

$$M = 2^N - 1 = 2^8 - 1 = 255$$

The 8 bit value for this measurement of 14 fibers, has a maximum of around 200.

One solution to this issue could be to change the layout of the plate that keeps the bundles together. The design of this plate could be changed so that surrounding each hole, walls of the height corresponding to the distance from the hole to the SiPMs could be placed. This would ensure that light would not reach the surrounding SiPMs. In addition, this module has previously been tested for electrical crosstalk, due to the small distance between the SiPMs. This test showed that electrical crosstalk did not occur¹⁰

6.1.2 Outer 5x5 SiPM modules

Testing for optical crosstalk in the outer 5x5 SiPM modules was done in the same way as for the central 7x7 SiPM calorimeter module. In the outer 5x5 SiPM modules, the SiPMs are placed at a larger distance from one another. This is due to the higher number of scintillating fibers in each bundle. The hope before testing the modules was that this would reduce the optical crosstalk between the SiPMs. However, throughout the measurements, it quickly became clear that optical crosstalk also did occur in these modules.

¹⁰A description of the test can be found in my thesis preparation project [39].

Optical crosstalk was tested in all 8 outer 5x5 SiPM calorimeter modules, in order to determine the extent of the problem. I suspect that the collection and assembling of all the 668 fibers into bundles placed in front of the SiPMs, was not done in completely the same way for all bundles, due to several people working on this part. Thus, the extent of optical crosstalk might differ between different modules. If the scintillating fibers were not placed in the agreed position, then the 3D-printed masks will not cover the correct area of scintillating fibers to test only a specific SiPM for optical crosstalk. However, as for the 3D-printed masks for the central module, the illumination area in the masks for the outer modules was made smaller than the area of fibers which was to be illuminated.

An example of some of the measurements can be seen in the intensity plots in figure 21 below, where the same two SiPMs, 2 and 18, are tested for optical crosstalk in module 1 and module 2 (see the two top intensity plots.), and SiPM 1 and 24 are tested in module 3 and 4 (see the two bottom intensity plots.)

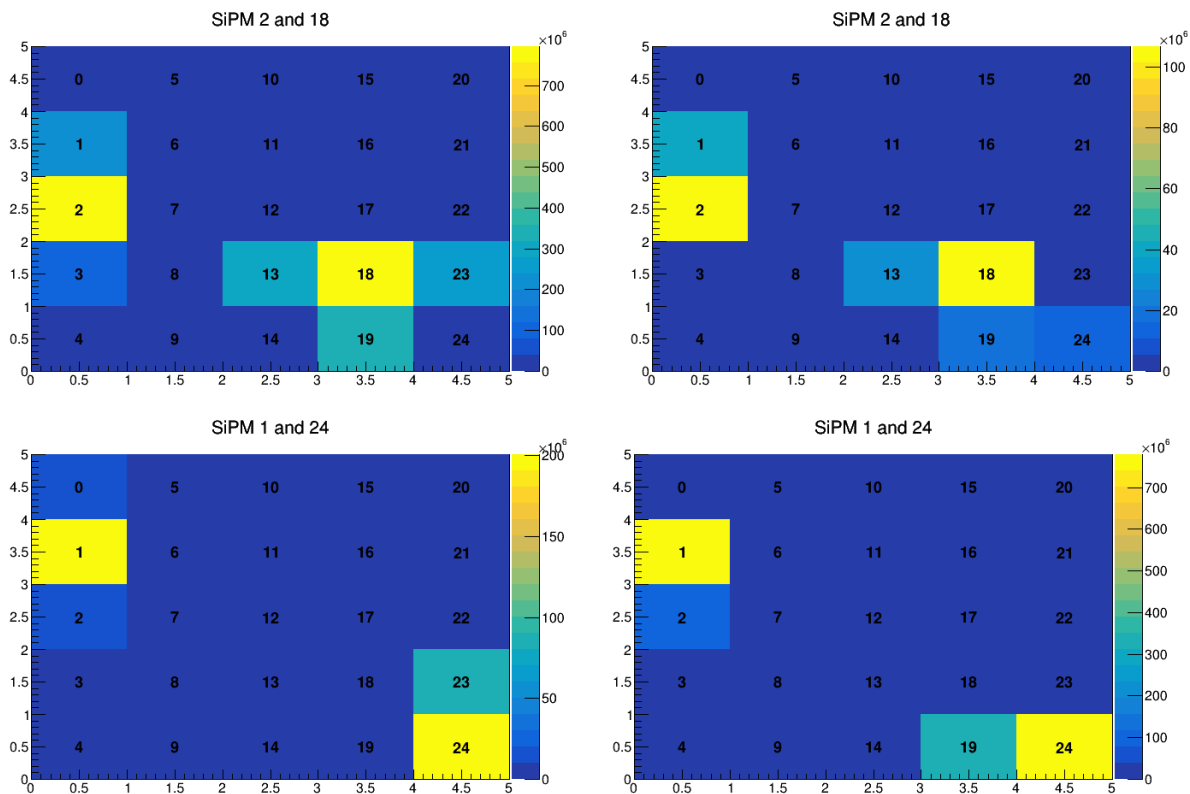


Figure 21: The figure shows four intensity plots of the optical crosstalk measurements made in the 5x5 SiPM modules. The two top plots show SiPM 2 and 18 being tested in modules 1(left) and 2(right). The two bottom plots show SiPM 1 and 24 being tested in modules 3(left) and 4(right). The measurements do show evidence of optical crosstalk between the SiPMs tested and the corresponding surrounding SiPMs.

As shown in figure 21, the optical crosstalk measurements are not consistent across the different calorimeter modules. This can be due to the placement of the scintillating fibers from the copper-tubes into bundles. However, the position of the LED and diffusing sheet, can of course also have an influence on these results, since they are moved when testing different modules. If the LED is not placed in the same position in front of the modules, then the photons from the LED would be reaching the SiPMs differently. The LED and diffusing sheet were not moved during the testing of all the SiPMs in a single module, but they were moved between testing different modules.

A noticeable difference between the measurements is that the number of photons the SiPMs detect is not consistent. This can be due to the SiPMs having different photons detection efficiency (PDE) at different bias voltages. The bias voltage is consistently set to 53 V on all SiPMs, since this is what is used at the testbeams.

To compensate for this variation, one could calibrate the SiPMs. Calibration of the SiPMs can be done by investigating their PDE. The PDE depends on the bias voltage applied to the SiPMs, so by varying the bias voltage and measuring the incoming photons, one could ensure that the SiPMs detect the same amount of photons at different bias voltages.

When testing for optical crosstalk, one need to be very careful covering the module in blackout cloth. However, when performing the tests one also need to make sure to cover up the gap around the 3D-printed mask, to prevent light from reaching the outermost SiPMs. An example of such a measurement performed on module 8, where I did not cover this gap carefully enough is shown in figure 22.

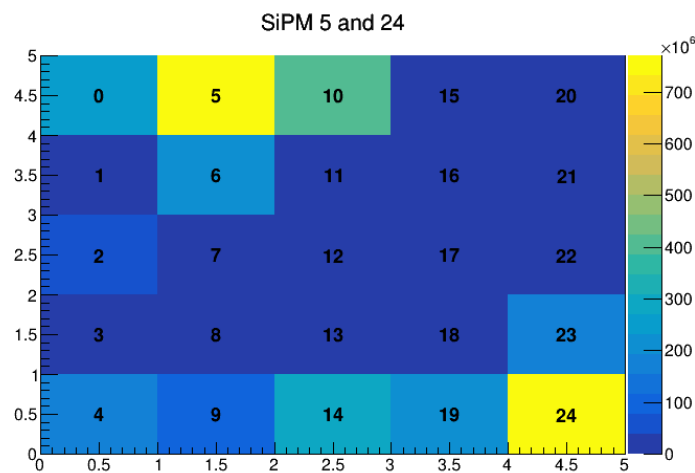


Figure 22: The figure shows an intensity plot of the optical crosstalk measurements made for the 5x5 SiPM module 8. The plot shows evidence of optical crosstalk between the SiPMs tested and the corresponding surrounding SiPMs. However, the plot also shows that the gap around the 3D-printed mask was not covered up well enough.

The intensity plot seen in figure 22, shows evidence of optical crosstalk, as seen for other measurements. The SiPMs around SiPM 5 and 24, which are being tested, also detect some of the photons from the illuminated scintillating fibers. However, what can also be seen in these measurements, is that SiPM 2, 4, 9, and 14 also detect light. These SiPMs having detected light does not make sense in regards to the fibers getting illuminated. However, this was seen when the gap around the 3D-printed mask was not covered up correctly. To characterize the optical crosstalk for these SiPMs one would need to make the measurement again.

All remaining optical crosstalk measurements performed on the outer 5x5 SiPMs calorimeter modules can be found in appendix section 11.2.2.1 to 11.2.2.8.

As was the case for the central 7x7 SiPM calorimeter module, optical crosstalk between the SiPMs seems to be a general issue for the outer 5x5 SiPM calorimeter modules. The extra space between the SiPMs, compared to the central module, was not sufficient to remove optical crosstalk. Again, the cut of the fibers or the possible scattering of the fiber bundles beyond the area of the 6x6 mm SiPM could be the

explanation. To check for the possible scattering of the fibers, I tested a bundle of 27 scintillating fibers (instead of 14 as before), since there are around 27 fibers in each bundle for the outer modules. The result of this test can be seen in figure 23 below.

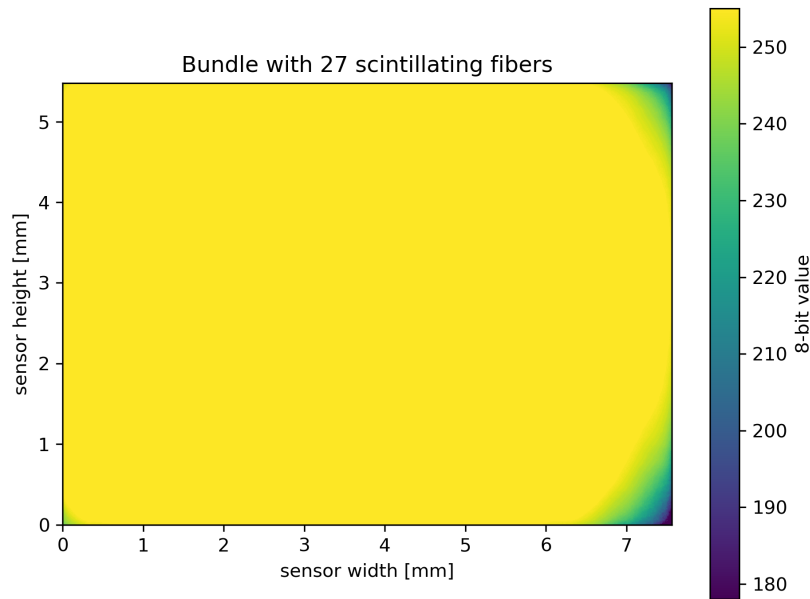


Figure 23: The figure shows a plot of a bundle of 27 scintillating fibers which are illuminated by an LED. As illustrated, the photons transmitted from the fibers spread beyond the area of the 8-bit sensor size, which is approximately the size of the SiPMs.

As can be seen in figure 23, the light from the photons does spread beyond the area of a 6x6 mm SiPM. It seems like the area of light from a bundle of 27 fibers, is around 2-5 mm bigger than the size of the 6x6 mm SiPMs. To determine how large the area of the scattering exactly is, would require a sensor with a bigger area.

The 8-bit value for this measurement of 27 fibers, has a maximum of 255. However, the maximum value for an 8-bit sensor is 255, which means that there is a possibility that the light from the bundle of 27 fibers is more intense than the sensor is able to process. In order to determine if this is the case, a 16-bit sensor could be applied.

A solution to reduce the amount of optical crosstalk between the SiPMs in the outer 5x5 SiPM modules, could be to implement walls around the holes in the collector plate that holds the bundles of fibers in place. An additional solution could be to buy the scintillating fibers with an EMA (Extra Mural Absorber) cladding around the fibers. The EMA cladding is an extra cladding layer which can be added on top of the PMMA (polymethylmethacrylate, $C_5H_8O_2$) cladding that the BCF10 and BCF12 has. The EMA cladding is either white or black, and has a thickness of around 10 to 15 microns. Applying this extra layer of cladding will eliminate crosstalk among closely packed fibers [35].

A third solution could be to use a different technique to cut the scintillating fibers. This solution have been tested in connection to this thesis, and the results will be presented in the next section.

6.2 Scintillating fibers

This section will go through three experimental setups, which were constructed in order to investigate the cut of the scintillating fibers used in the FoCal-H second prototype. The scintillating fibers play a major role in the FoCal-H setup, being the active material in the sampling structure of the FoCal-H calorimeter.

6.2.1 Cutting techniques of scintillating fibers

The technique used to cut the scintillating fibers was one of the components, which was important to investigate in connection to reducing optical crosstalk between the SiPMs. Different techniques of cutting a scintillating fiber causes the intensity and the light scattering from the end of that fiber to be spread differently. Two experiments that support this claim, were done in the Spring of 2022 in a previous project of mine, namely my thesis preparation project. These two results, which can be seen below in figure 24, were part of a larger experiment testing the luminosity of the fibers for different cutting techniques, in order to make a qualified decision of how the scintillating fibers should be cut for the FoCal-H second prototype. [39].

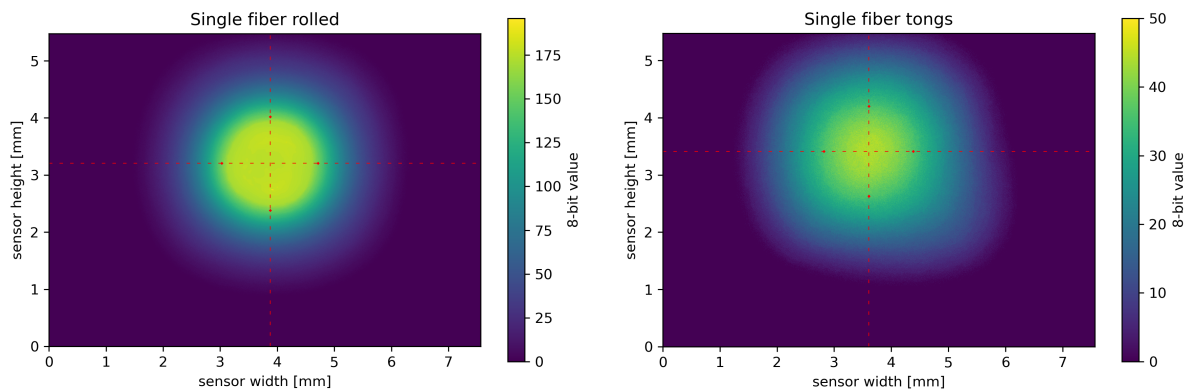


Figure 24: This figure shows a previous measurement from [39]. The figure shows two intensity plots of scintillating fibers cut using two different methods. The left-side plot shows an intensity plot of a single fiber cut using a scalpel, which was rolled over the fiber. The right-side plot shows a single fiber cut using tongs.

The method using a scalpel that is rolled over the scintillating fiber was used when building the FoCal-H second prototype. The reason is the spherical scattering from the fiber, obtained when using this cutting technique.

As a continuation of these measurements, three more techniques were investigated to further optimize the scintillating fiber cutting. The three techniques were examined in regards to this thesis. I built two small versions of the FoCal-H second prototype for the examination of the three techniques. As for the FoCal-H second prototype, the scintillating fibers in the small versions were bundled up and a SiPM was placed in front of each bundle.

The same experimental setup used for the optical crosstalk measurements was used again to test the different cutting techniques of the scintillating fibers. The setup was used, for two reasons, 1) It would

give an indication of whether optical crosstalk could vary depending on different methods for cutting the scintillating fibers, and 2) It would show whether the intensity of the scintillating fibers would differ depending on different cuts.

A LED was placed in the front-end of a module. The LED would illuminate the scintillating fibers and the SiPM would read out the emitted photons from the scintillating fibers. To only test one SiPM at a time, a 3D-printed mask was placed in the front end of the modules, between the LED and the fiber ends. This mask covered up all fibers to the SiPMs, which were not being tested. By repeating this measurement for all the different techniques and SiPMs, one can compare the results from one technique to another. The sections describing the techniques highlights some of the results, and the remaining can be found in appendix section 11.3.

6.2.2 Rolled scalpel cut

The rolled scalpel cutting technique was the first technique that was tested. This technique was important to include in the measurements to have a reference to the scintillating fibers used in the FoCal-H second prototype.

For the rolled scalpel cutting technique, three types of scintillating fibers from the company Saint-Gobain were tested, the BCF10, BCF 12 and BCF60s.

6.2.2.1 BCF10

The BCF10 scintillating fibers were used for the FoCal-H first prototype, but cut using a different method, than the one being tested in this thesis¹¹. An intensity plot, using the rolled scalpel technique, for the BCF10 scintillating fiber can be seen in figure 25.

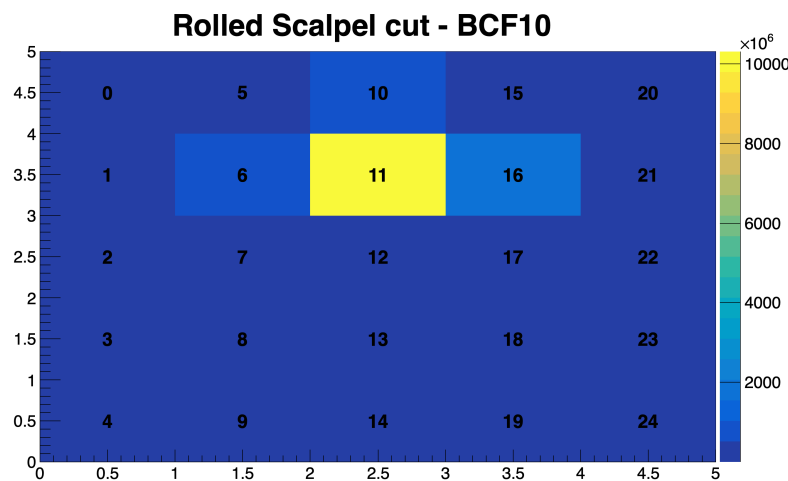


Figure 25: The figure shows an intensity plot of a bundle of scintillating fibers of the type BCF10, where SiPM/Channel 11 is tested. This bundle of fibers was cut using a scalpel, which was rolled over the scintillating fibers.

This plot shows a bundle of the BCF10 scintillating fibers (SiPM/Channel 11), which have been illumi-

¹¹See section 5.2.1 for a description of the BCF10 performance characteristics.

nated by a blue LED. Three surrounding SiPMs to SiPM 11, show also to have detected photons during this measurement. The rolled scalpel cutting technique, does in this measurement of the BCF10 scintillating fibers, not seem to ensure that the light is contained within the SiPM. However, the amount of photons detected by the surrounding SiPMs for this specific measurement seem negligible compared to the results from the optical crosstalk measurements.

6.2.2.2 BCF12

The BCF12 scintillating fiber is the type used for the FoCal-H second prototype, using this specific technique to cut them. An intensity plot, using the rolled scalpel technique, for the BCF12 scintillating fiber can be seen in figure 26, where the fibers to SiPM/Channel 6 has been illuminated.

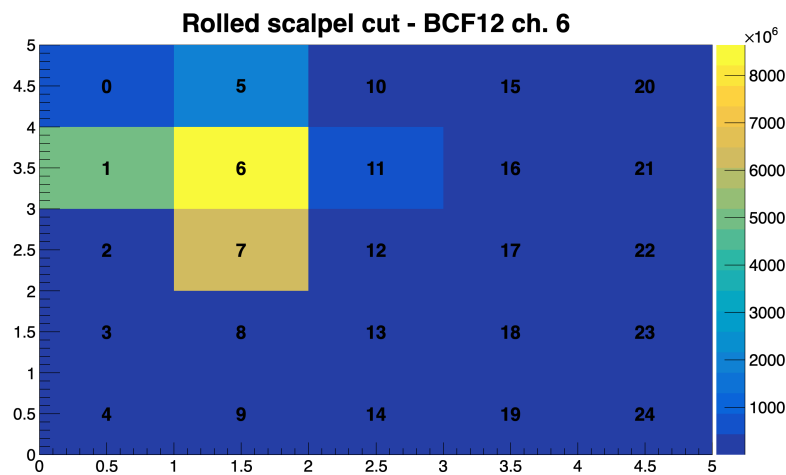


Figure 26: The figure shows an intensity plot of a bundle of scintillating fibers of the type BCF12, where SiPM/Channel 6 is tested. This bundle of fibers was cut using a scalpel, which was rolled over the scintillating fibers.

The plot shows a bundle of BCF12 scintillating fibers, which has been illuminated. The measurement tests a bundle of 27 scintillating fibers to the SiPM/Channel 6, but shows that the surrounding SiPMs also detect photons. The method using the rolled scalpel technique on the BCF12 scintillating fibers shows consistency with the measurements for optical crosstalk. However, compared to the rolled scalpel technique on the BCF10, these fibers seem to scatter the photons to the surrounding SiPMs more. Whether this is due to the scattering from the fiber-ends or the collection of fibers into a bundle leading to the SiPM is unknown. To exclude the possible effect of the collection of fibers, I would suggest to test different cutting techniques in a calorimeter module where the collection of fibers is identical to the one in the BCF10 calorimeter module. However, this was not possible to do, since it would require a new module to be build. A smaller examination of the scattering of photons from a single fiber, could possibly also be done.

6.2.2.3 BCF60s

The BCF60s scintillating fibers have a green emission color (530 nm), a decay time of 7 ns, and emit ~ 7100 photons per MeV [40]. The BCF60s scintillating fibers are radiation hard, and could for this reason be a good alternative to the BCF12 scintillating fibers since the environment in ALICE is radioactive when the experiment is running.

The BCF60s scintillating fibers are tested for two different reasons. The first is the possibility of reducing the amount of light that reaches the SiPMs, by using the fact that fewer photons are emitted per MeV. The second reason also relates to reducing the amount of light but is in regard to the SiPMs. The SiPMs used for the FoCal-H second prototype have the most optimal photon detection efficiency (PDE) in the blue spectrum. By choosing a scintillating fiber, which emits photons in the green spectrum, one automatically reduces the chance of SiPMs detecting the photons. The PDE for each wavelength from 300 to 900 nm for the SiPMs is known, so it is possible to calculate the number of photons that are not detected afterwards. Choosing this fiber could potentially also contribute to solving the saturation issue in the readout¹² if its the SiPM, by reducing the information/number of photons the readout board needs to process for the SiPMs.

An intensity plot, using the rolled scalpel technique, for the BCF60s scintillating fiber can be seen in figure 27, where SiPM/Channel 15 has been illuminated.

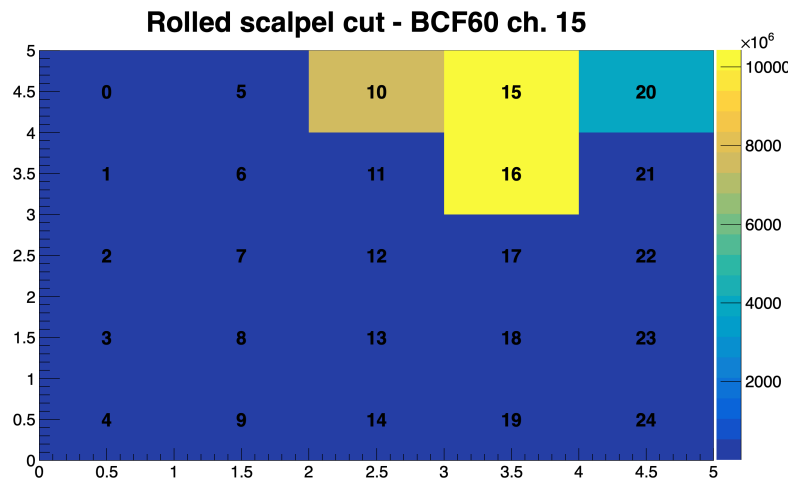


Figure 27: The figure shows an intensity plot of a bundle of scintillating fibers of the type BCF60s, where SiPM/Channel 15 is tested. This bundle of fibers was cut using a scalpel, which was rolled over the scintillating fibers.

This measurement using the rolled scalpel technique and the BCF60s, show a larger extent of photons getting detected from the surrounding SiPMs, compared to the BCF10 and BCF12. To what extent this is due to the placement of the scintillating fibers, or the scattering of photons from the fibers is for now unknown.

¹²The readout for the SiPMs and the CAEN DT5202 will be described in detail in sections 5.2.2.2.

6.2.3 Rolled scalpel and polished cut

The rolled scalpel with polished scintillating fibers is another technique that has been tested. This technique was tested to see if a polished fiber would give a smaller light scattering from the fibers and if there would be a potential difference in the number of emitted photons that could be read by the SiPMs.

The scintillating fibers was cut the same way as in the rolled scalpel cut, and was polished afterwards. To polish the scintillating fibers two different polishing sheets for plastic optical fibers from the firm Industrial Fiber Optics was used.

The scintillating fibers were polished by gently moving the fibers in circles, for about 20 strokes. This was first done on a 2000-grit polishing sheet, which is a flagrant polishing sheet. After the 20 strokes, the end of the fibers were examined. If the end of the fiber was cloudy, uneven, or had any scratches, around 5 stokes of the polishing sheet was performed again. The same procedure was then performed using a 3 μm polishing sheet, which is a fine grit sheet.

The rolled scalpel and polished cut, was only performed on the BCF12 scintillating fiber.

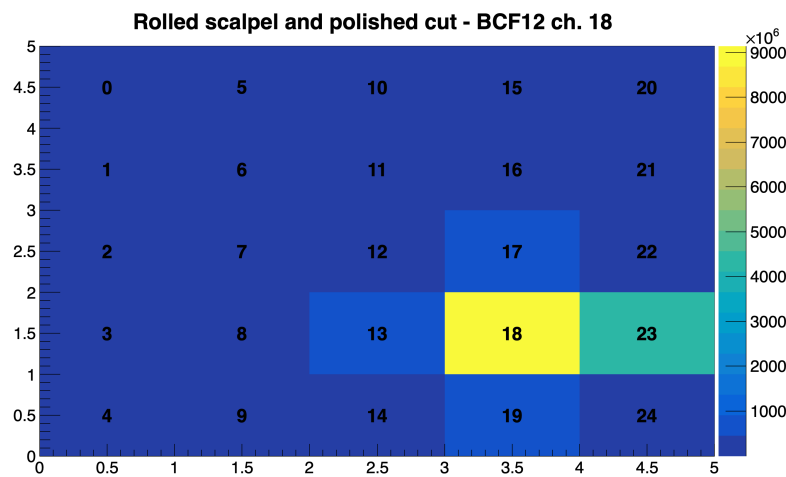


Figure 28: The figure shows an intensity plot of a bundle of scintillating fibers of the type BCF12, where SiPM/Channel 18 is tested. This bundle of fibers was cut using a scalpel, which was rolled over the scintillating fibers which were then polished.

The plot shows a bundle of 27 BCF12 scintillating fibers, which has been illuminated. The measurement tests the fibers corresponding to SiPM/Channel 18. However, the surrounding SiPMs also detect some photons coming from the scintillating fibers corresponding to SiPM/Channel 18. In comparison to the rolled scalpel technique, where the scintillating fibers were not polished, these measurements show a reduced amount of optical crosstalk between the SiPMs. I therefore suspect that polishing the scintillating fibers focuses the photons more forward, making them scatter less to the side and getting detected by the surrounding SiPMs.

6.2.4 Optical glue and diamond blade cut

The last cutting technique which was tested was done by using optical glue and a diamond blade cut. Optical glue is a type of glue used in application where optical components should be collected. The

optical glue used in this thesis is composed of two components of Polytec EP 601-LV.

The technique was tested with the aim of optimizing the cutting technique for the scintillating fibers for future prototypes and/or the final FoCal-H detector. The idea of using this technique came from a conversation I had with a detector physicist from the experiment LHCb, who had a lot of experience with scintillating fibers.

The process of this technique is very different from the previously described ones. The scintillating fibers were for this technique placed in the copper-tubes and bundled up, the same way as done for the FoCal-H first and second prototypes. However, instead of cutting all fibers individually, I mixed the two components that composite the optical glue. Making sure that no air bubbles were present in the optical glue mixture. The optical glue was when carefully poured into a 3D-printed bowl. The smaller version of a FoCal-H second prototype module was secured by three clamps to a cabinet wall to make sure it could be fixed for the time it took the optical glue to harden. The bowl with the glue was then placed so that the bundles of scintillating fibers were dipping into the glue in the collector plate. A pressure causes the optical glue to get sucked up into the collector plate. The module was placed like this for 2-3 days, until the optical glue had hardened.

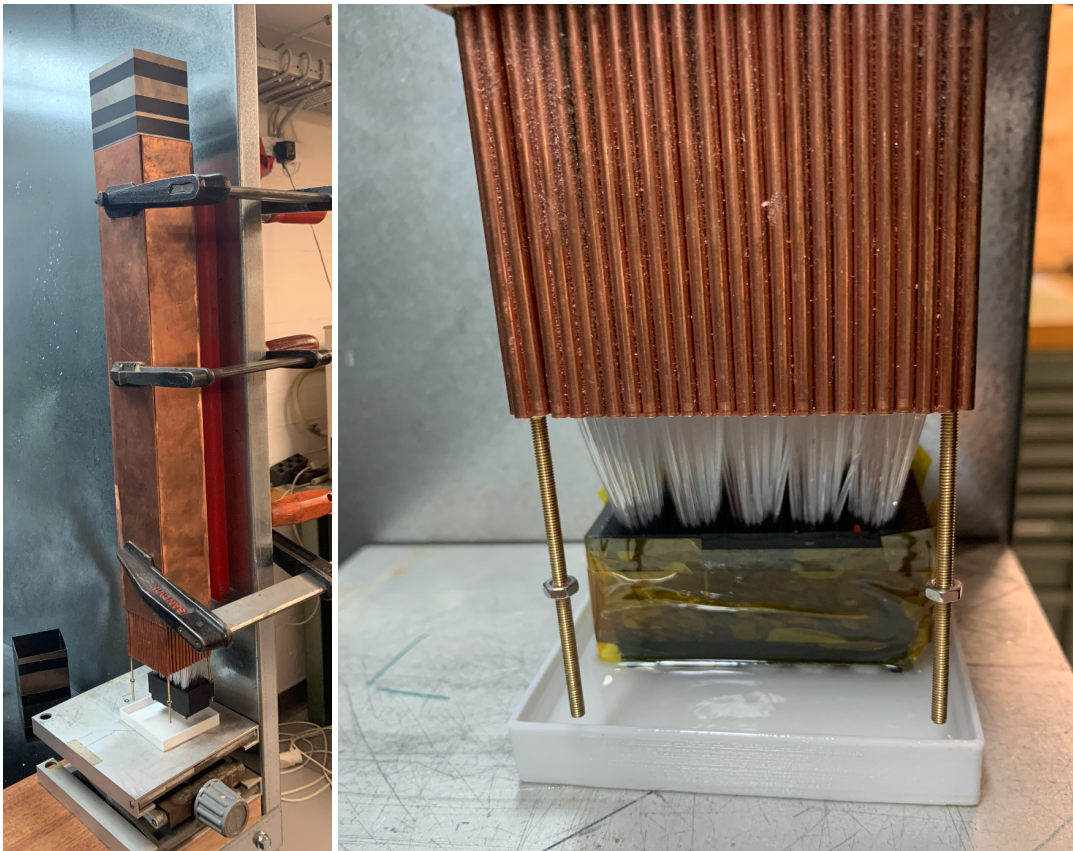


Figure 29: The figure shows two pictures of the process using optical glue to collect the scintillating fibers. The left-side figure shows how the module is secured to a cabinet wall and placed in the optical glue to harden. The right-side figure shows the modules placement in the optical glue.

To cut the bundles of scintillating fibers, I transported the module to CERN where a technician connected to the scintillator lab, helped me cut the fibers using a diamond blade. During the transport to CERN some of the fibers broke, due to the rough treatment in the airplane. The transport of the modules to

CERN is something that should be taken into consideration, if this method is used in the future, and if the modules are assembled in Denmark.

Pictures of how the diamond blade cut looks compared to the rolled scalpel cut can be seen in figure 30.

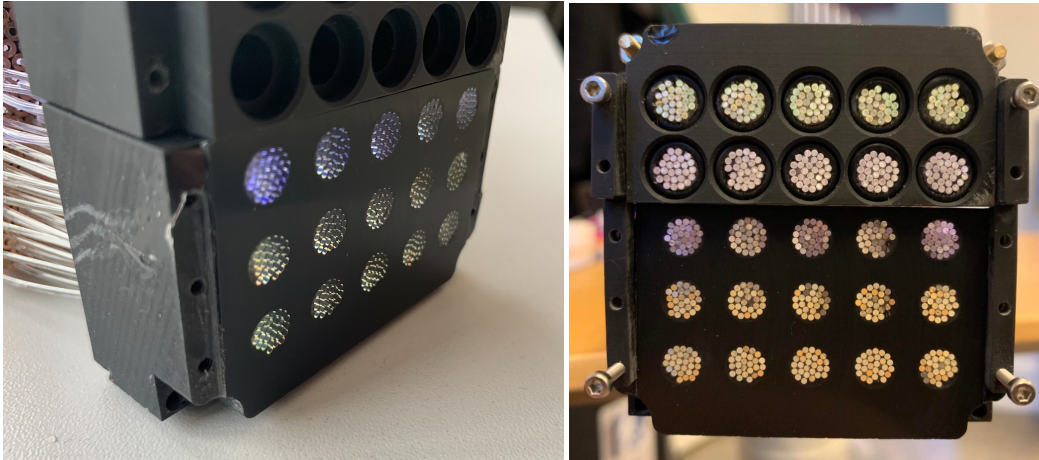


Figure 30: The left-side figure shows a picture of the scintillating fibers where they have been cut by the diamond blade. The right-side figure shows a comparison of the scintillating fibers cut using the rolled scalpel cut (top two rows) and the optical glue with diamond blade cut (bottom three rows).

6.2.4.1 BCF10, BCF12 and BCF60s

This technique using optical glue and the diamond blade cut, shows a significant reduction in the optical crosstalk between the SiPMs, compared to the two other techniques tested in this thesis. As can be seen in figure 31, 32, and 33, using this method reduces the optical crosstalk between the SiPMs for all three types of fibers. I suspect the stable collection of the fibers, together with a cleaner cut, focus the scattering of the photons forward instead of to the sides.

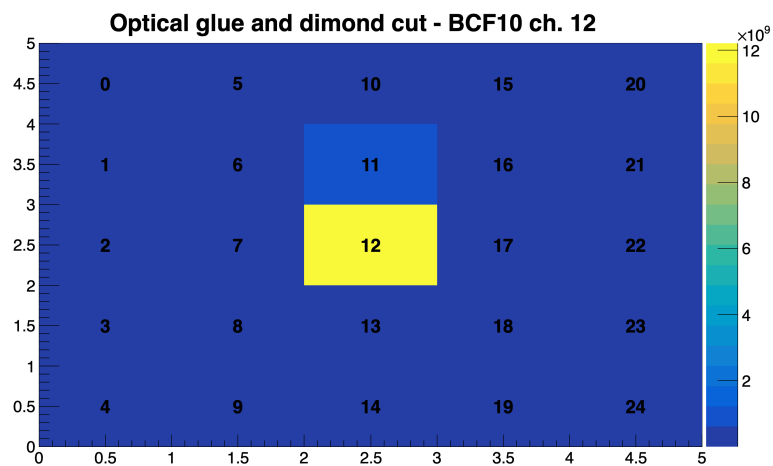


Figure 31: The figure shows an intensity plot of a bundle of scintillating fibers of the type BCF10, where SiPM/Channel 10 is tested. This bundle of fibers was cut using optical glue technique.

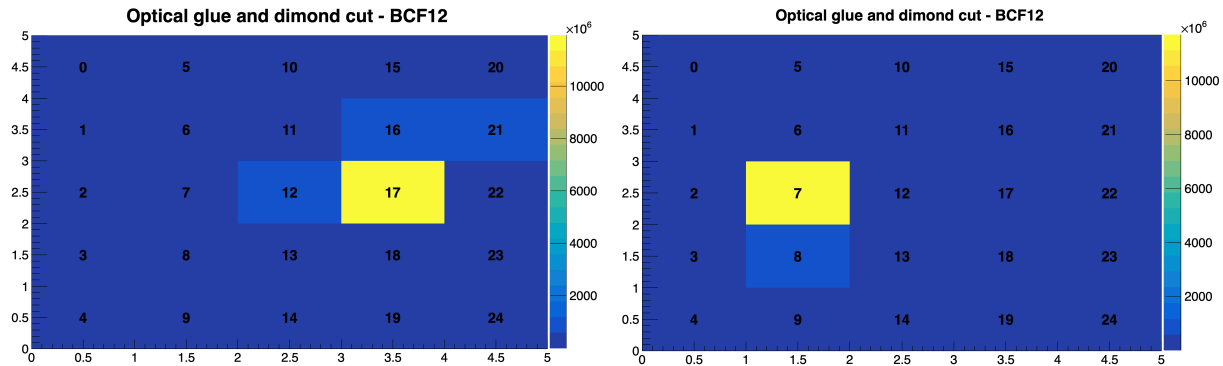


Figure 32: The figure shows intensity plots of two different bundles of scintillating fibers of the type BCF12. These bundles of fibers were cut using optical glue technique. The left-side figure shows the intensity plot of SiPM/Channel 17. The right-side figure shows the intensity plot of SiPM/Channel 7.

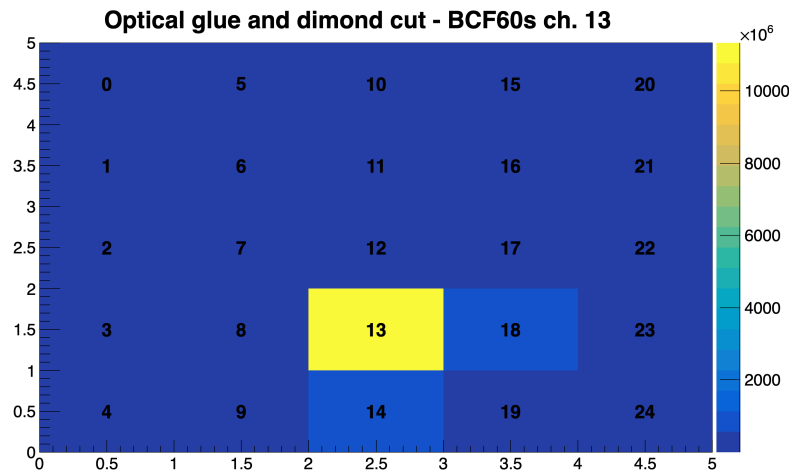


Figure 33: The figure shows an intensity plot of a bundle of scintillating fibers of the type BCF60s. This bundle of fibers was cut using optical glue technique.

The aim of reducing optical crosstalk between the SiPMs by studying the cutting technique of the scintillating fibers is found by applying the optical glue technique. This technique is consistent across the three different scintillating fiber types, which the two remaining cutting techniques were not.

The difference between the amount of optical crosstalk between the SiPMs when using the rolled scalpel cut and the optical glue technique can be seen in figure 34. The intensity plot in figure 34 shows two bundles of BCF60s scintillating fibers, cut using different methods. The fibers to SiPM/Channel 4 are cut using the optical glue technique, while the fibers to SiPM/Channel 15 are cut using the rolled scalpel cut. This intensity plots clearly shows a difference when using the two different techniques.

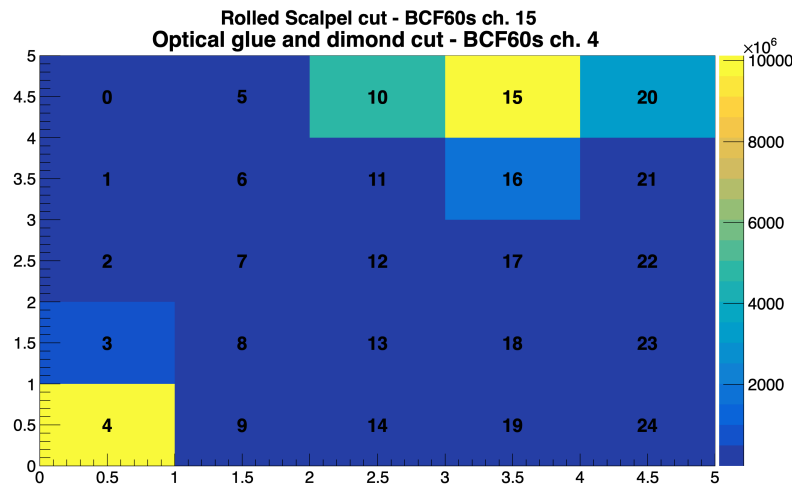


Figure 34: The figure shows a measurements of the BCF60s scintillating fiber, cut using two different techniques. The SiPM/Channel 15 is cut using the rolled scalpel technique, while the SiPM/Channel 4 is cut using the optical glue technique.

Due to the significant reduction of optical crosstalk between the SiPMs, and the stability of the fibers, I would highly recommend this method to be used in any future prototype and/or the final design of FoCal-H.

6.3 Collector plate material

The material of the collector plate is an element, which needs to be considered when using the optical glue technique. This is due to the diamond blade's cut in the material. Thus, the consideration of the collector plate material should not be considered in connection the quality of the cut of the scintillating fibers, but in regards to the quality of the collector plate itself.

I tested three different types of material. The first material was resin, which was also the material used for the 5x5 SiPM collector plates for the outer calorimeter modules. The second and third material was in 3D filament, but with two different degrees of compactness of the filament in the print. The 3D filament was the material used for the 7x7 SiPM collector plate, for the central calorimeter module.

These different materials was tested with regards to either a third prototype or the final design of FoCal-H. The reason why the 3D filament plate was tested with this cut, is because the thread for the screws. The collector plates made in resin, showed sign of breaking when the SiPM boards were screwed on and off multiple times. I therefore do not think this material is good enough to be used in any future build. The same thing has not happened to the print in 3D filament, and the diamond blade cut was therefore tested with this material. However, if resin is chosen, I could recommend to use another material than metal screws for connecting the SiPM boards.

To test the three different materials, the same procedure was used as for when I built the smaller calorimeter module. First I mixed the two components for the optical glue, making sure no air bubbles were left. Then the collector plates were placed in the optical glue, and it was left to harden for 2-3 days, before getting cut. A picture of the collector plates after the optical glue has hardened can be seen in figure 35, where the left-side figure shows the collector plate made of resin and the right-side figure shows the one

made of 3D filament.



Figure 35: The two pictures show two collector plates of two different materials, after the fibers have been glued with optical glue. The left-side figure shows the collector plate made of the material called resin. The right-side figure shows the collector plate made of 3D filament.

The three different collector plates, after the plates and the scintillating fibers have been cut by the diamond blade, can be seen in figure 36.

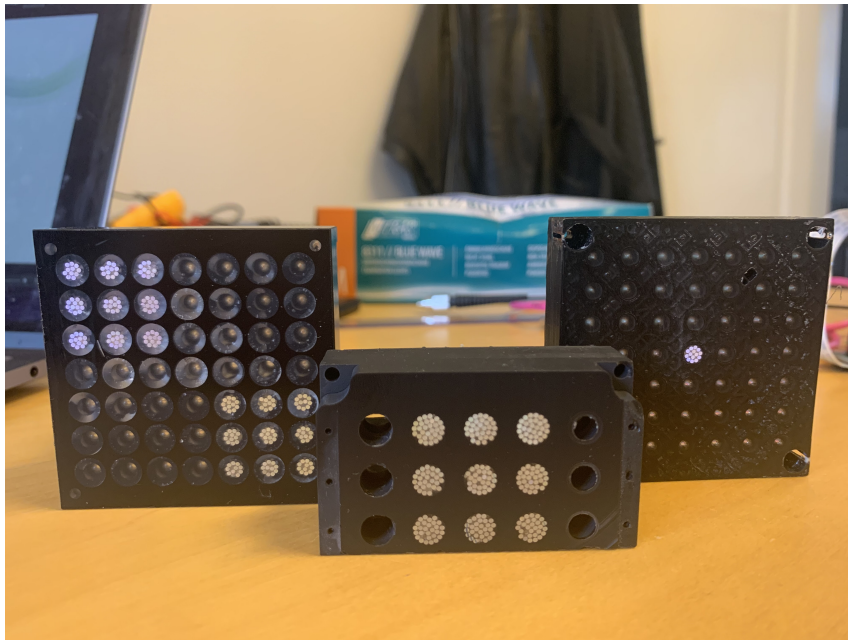


Figure 36: The picture shows the three different materials of collector plates after being glued with optical glue and cut using a diamond blade cut.

All three collector plates showed to be efficient in keeping the scintillating fibers in place after they were cut. However, the 3D filament collector plate with less compactness (see right-side collector plate in figure 36) showed to have some issues between the holes for the fibers, and the holes for mounting it to the calorimeter modules.

Additionally, the left-side collector plate (see figure 36) was tested without an o-ring on the front-side of

the plate, to see if the bundle would be kept in place without it. This showed to be the case, which can potentially lower the prize for the final design of FoCal-H. Two of the three collector plate, namely the plates made of resin and the compact 3D filament plate, showed to promising results in connection to this test of optical glue and a diamond blade cut.

7 November 2022 SPS H2 testbeam setup

This section will go into details with the experimental setup used at the testbeam in November SPS H2 beamline. The section will describe the testbeam facility and how the FoCal prototypes were placed in order to be tested. The section will also give a brief description of the FoCal-H readout system and hardware setup. These details will provides a better understanding of the data analysis, which is presented in section 8.

7.1 Testbeam prototype setup

In order to performance test the FoCal prototypes, in terms of their individual performance as well as their collective performance, the placement of the prototypes with respect to the beam-pipe needs to be considered. Both the FoCal-E and FoCal-H prototype are placed on a DESY table, which can be positioned and adjusted with respect to the beam-pipe. The FoCal-E prototype is placed in front of FoCal-H, which is also the intended setup for the final design, due to FoCal-E's physics purpose of studying particles that interact electromagnetically. However, two detector setup have been tested in this thesis, i.e. setup including and excluding FoCal-E in front of FoCal-H. The runnr. for the datafiles analyzed in this thesis, as well as the corresponding energies are listed in table 1:

Runnr. and corresponding energies including FoCal-E								
$E_{beam}[\text{GeV}]$	60	80	100	150	200	250	300	350
Runnr.	1305	1304	1303	1302	1301	1300	1299	1298
Runnr. and corresponding energies excluding FoCal-E								
$E_{beam}[\text{GeV}]$	60	80	100	150	200	250	300	350
Runnr.	1504	-	1505	-	1503	1502	1501	1500

Table 1: The table lists the runnr. for the datafiles used in the detector setup including and excluding FoCal-E in front of FoCal-H.

FoCal-H is placed as closely behind FoCal-E as possible (15 mm), to avoid blow-up of showers which start in the FoCal-E. This distance was chosen due to the blackout cloth which was placed around FoCal-H to keep all light out. The FoCal detector setup can be seen in figure 37 and figure 38. The FoCal-H readout boards, the CAEN DT5202, are placed in the metal bars at the back-end of FoCal-H. These are placed slightly to the side of the back-end of the FoCal-H calorimeter, due to radiation effects of the readout.

The readout placement can be seen in the left-side schematic in figure 37, where the setup is seen at an angle from above. The right-side schematic in figure 37 shows FoCal-H from the back-end, where

the CAEN DT5202 boards are placed in the metal bars, and the SiPMs are mounted in the 9 calorimeter modules. The SiPM boards are represented as 9 grey squares in this schematic.

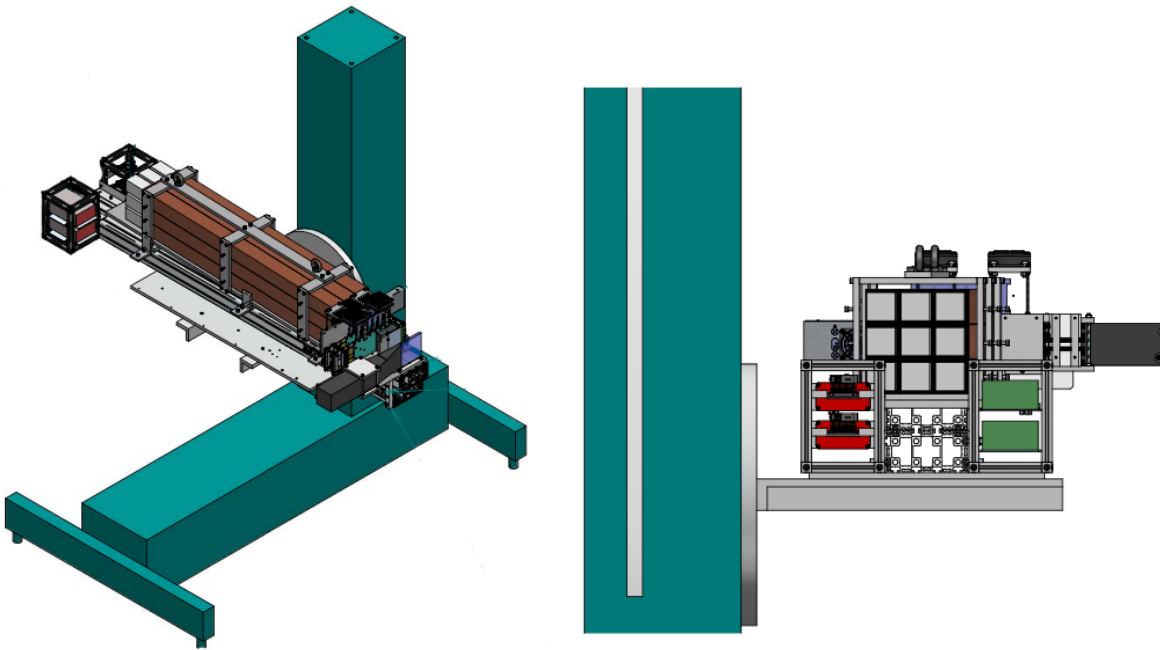


Figure 37: The figure shows two schematics of the FoCal detector placed on a DESY table. The left-side schematic shows the setup with an angle from the top, where it can be seen that FoCal-E is placed in front of FoCal-H, and the corresponding setup for the FoCal-H readout boards. The right-side schematic shows the setup seen from the back-end of FoCal-H.

At the very front, in front of FoCal-E, two scintillator plates are placed, where one of these are visualized in the schematic in figure 37 and figure 38, as the black bar. The scintillator plates are placed with a distance of around 20 cm to each other, and has the purpose of providing a trigger signal to both FoCal-E and FoCal-H. The trigger signal is initiated when a particle passes through the two scintillator plates. This signal is sent to a coincidence module in the trigger logic, called the BUSY logic, where the resulting signal is passed on to the individual readout systems for FoCal-E and FoCal-H.

The FoCal-H prototype is rotated 2.085° with respect to the beam-pipe. This is done to lower the possibility of punch through particles traveling along the scintillating fiber, or copper-tubes, without depositing energy in the calorimeter and starting a particle shower¹³. The rotation of FoCal-H is visualized in the top schematic in figure 38. The bottom schematic shows the FoCal detector setup from the side. The current FoCal-E prototype with its height and width of around 90 mm does not cover the total area of FoCal-H. FoCal-E is therefore placed to have its origo (0,0) at the origo of the FoCal-H central calorimeter module.

The top and bottom schematic in figure 38 also indicates (red lines) a potential start of a particle event. A particle event is the definition for a spill from the beam-pipe, where an incident particle comes out, starting a particle shower in the detector. An event stops when a spill is again activated. The particle shower starts in FoCal-E, and might spread through FoCal-E and into FoCal-H depending on the incident particle.

¹³A further description of punch through particles will be given in section 8

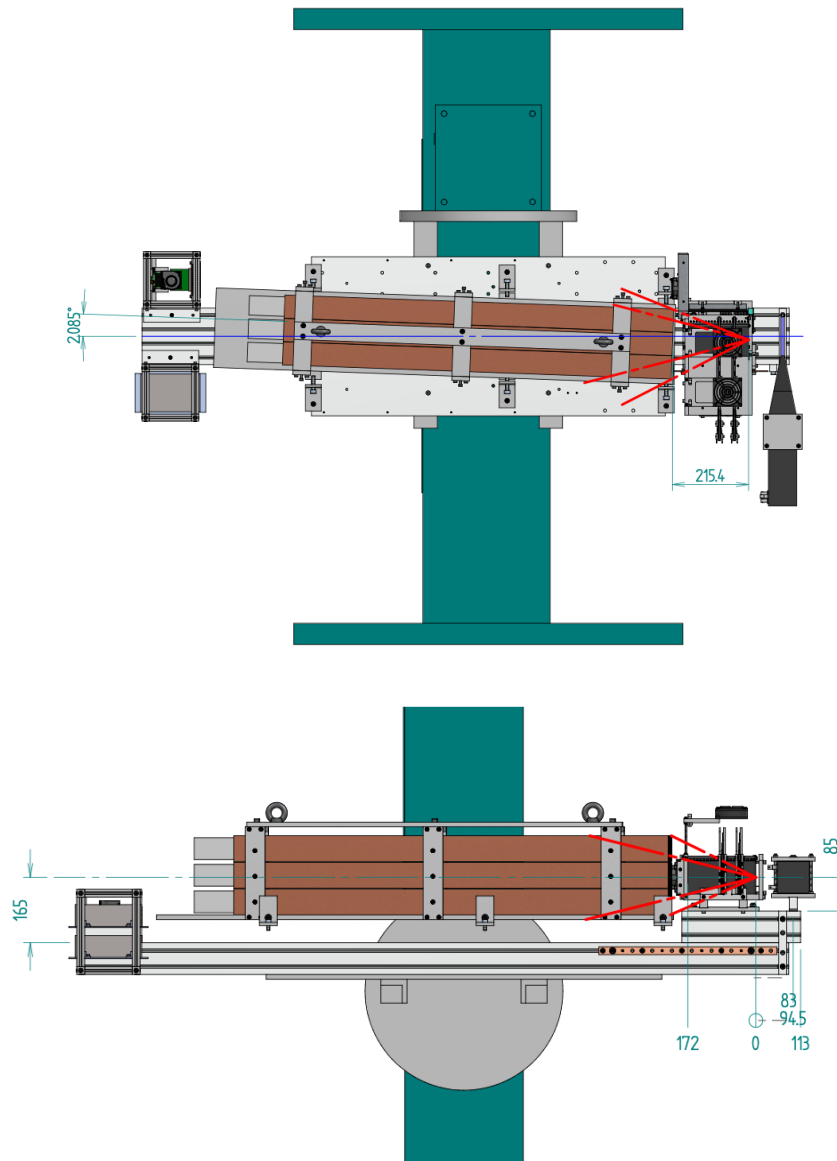


Figure 38: The figure shows two schematics of the FoCal detector placed on a DESY table. The top schematic shows the setup from the top, where the FoCal detector can be seen. The rotation of FoCal-H, with respect to the beam-pipe, is also shown in this schematic. The bottom schematic shows the setup seen from the side, where the placement of FoCal-E with respect to the FoCal-H calorimeter modules is seen.

FoCal-H had for the November SPS H2 testbeam a maximum of 3 CAEN DT5202 readout boards. This means that the FoCal-H calorimeter did not have full coverage to read out all SiPMs. Due to missing readout channels, I constructed a spiral mapping from the SiPMs to the CAEN DT5202 readout channels. This mapping ensured that only the outermost channels were not read out. In terms of the physics program planned to test the FoCal-H second prototype, this mapping made most sense to use in regards to test e.g. shower containment, which will be described in section 8.2.4. In the beginning of the testbeam, only two CAEN DT5202 boards were available, because one was being repaired. The mapping did therefore also serve a practical purpose in that it was easy to add extra boards along the way. The

mapping from the SiPMs to the CAEN DT5202 board’s channels can be seen in figure 39. The intersections between the 9 calorimeter modules are indicated by the red lines. All testbeam data analyzed in this thesis is based in 3 CAEN DT5202 readout boards.

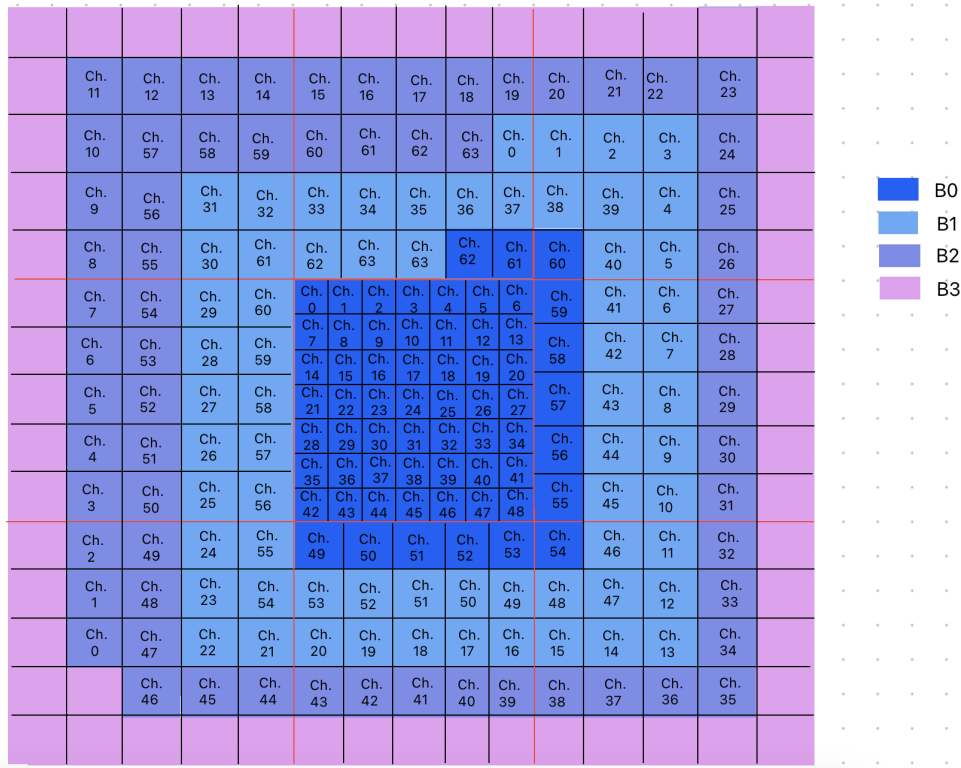


Figure 39: The figure shows the SiPM to CAEN DT5202 channel mapping. The mapping indicates how many SiPMs was covered by the three CAEN DT5202 board, and in terms of coverage of the calorimeter modules.

8 Data analysis of the November 2022 SPS H2 testbeam

This section will analyse and present the testbeam data collected at the November 2022 SPS H2 testbeam, to get a better understanding of the FoCal-H calorimeter. Moreover, the section will go through the performed simulations and the analysis of these. The simulations are generated with the intend to verify observations from the testbeam data.

In addition, the section will compare the testbeam data and the simulated data, in order to verify and/or point out areas which need to be investigated in the future. However, the focus of this thesis has mainly been the FoCal-H simulation data.

8.1 Testbeam data - November 2022 SPS H2

During the testbeam, multiple studies were performed in order to understand the response of FoCal-H. At the SPS H2 testbeam we were able to test the response of FoCal-H at energies from 60 to 350 GeV.

8.1.1 FoCal detector setup

One of the tests at the SPS beamline aimed to examine the total response collected in FoCal-H, in setups where FoCal-E was placed in front, but also where FoCal-E was removed. The reason behind this was that during a FoCal testbeam in September 2022, we saw that the total response in FoCal-H consisted of a larger and a smaller peak. The reason for the smaller peak was discussed, and it was quickly pointed out that a possible reason was a particle shower starting in FoCal-E and continuing into FoCal-H. The tests including and excluding FoCal-E in front of FoCal-H were done at different energies, in order to see if higher energies would have a large influence on the response of the FoCal-H calorimeter. If this would be the case, multiple optimizations, for example in the readout electronics, would be needed before placing the detector in the ALICE experiment.

The response for both the setup including and excluding FoCal-E has been collected summing over the signal collected in all the SiPMs in the FoCal-H calorimeter setup. An improvement, which could be implemented for both setups, would be to remove the saturation signal from the channels. Saturation happens when either SiPMs or the channels in the CAEN DT5202 boards reading out the SiPMs saturate, making it impossible to collect more information. Whether the saturation happens in the SiPMs or the channels in the CAEN DT5202 boards is so far unknown. However, this will be investigated in the May 2023 testbeam, with a newly discovered feature of the CAEN DT5202 board, namely a TOT (Time Over Threshold) and TOA (Time Of Arrival).

An example of this saturation can be seen in the two plots in figure 40. The two plots are presented in a logarithmic scale, making the saturation in the signal visible. Others in the collaboration [42] have shown that most of the saturation signal can be removed by doing a 3D gauss function fit to the signal, rather than summing over the signal.

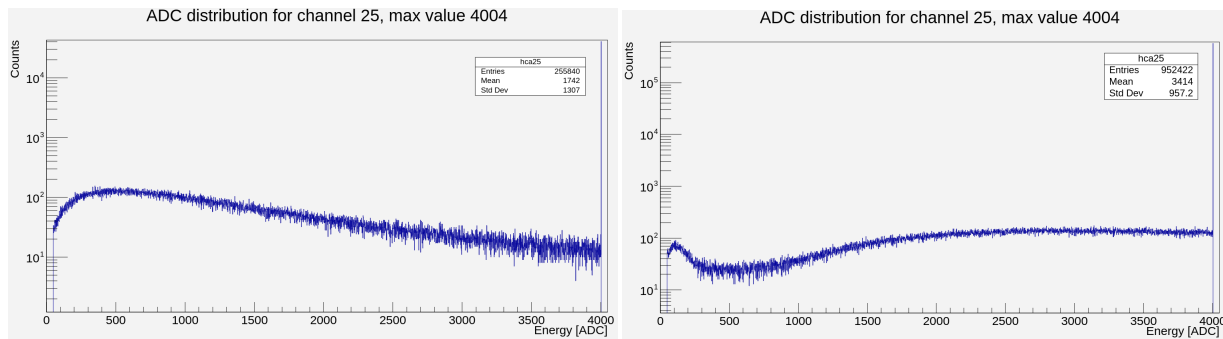


Figure 40: The two plots show an saturation signal in channel 25 for a run at 350 GeV in a setup including and excluding FoCal-E in front of FoCal-H. The left-side figure shows the setup including FoCal-E and the right-side figure shows the setup excluding FoCal-E.

Most noise has been removed by using a pedestal subtraction implemented by the CAEN DT5202 read-out board. This pedestal subtraction was used instead of a lower threshold, due to the fact that the CAEN DT5202 board enables the possibility of using a threshold when having an external trigger. Besides the pedestal subtraction, two other lower thresholds from the trigger setup was also applied, in the form of zero suppression. An example with nearly no noise and saturation can be seen in figure 41.

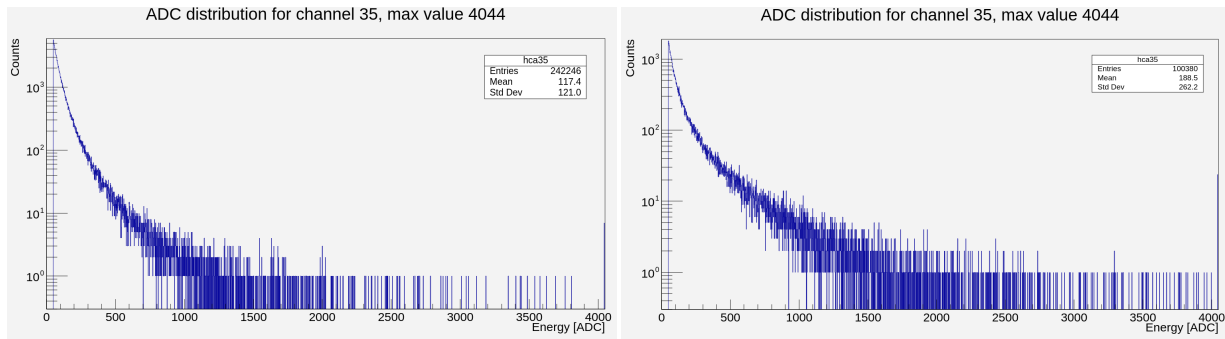


Figure 41: The two plots show a signal with nearly no noise and saturation, in channel 35 for a run at 60 GeV in a setup including and excluding FoCal-E in front of FoCal-H. The left-side figure shows the setup including FoCal-E and the right-side figure shows the setup excluding FoCal-E.

8.1.1.1 FoCal setup including FoCal-E

At the November 2022 SPS H2 testbeam using the setup where FoCal-E was placed in front, the total response in FoCal-H looks different from what was first anticipated. The total response for each of the energies has three characteristic peaks, the reason of which is now known.

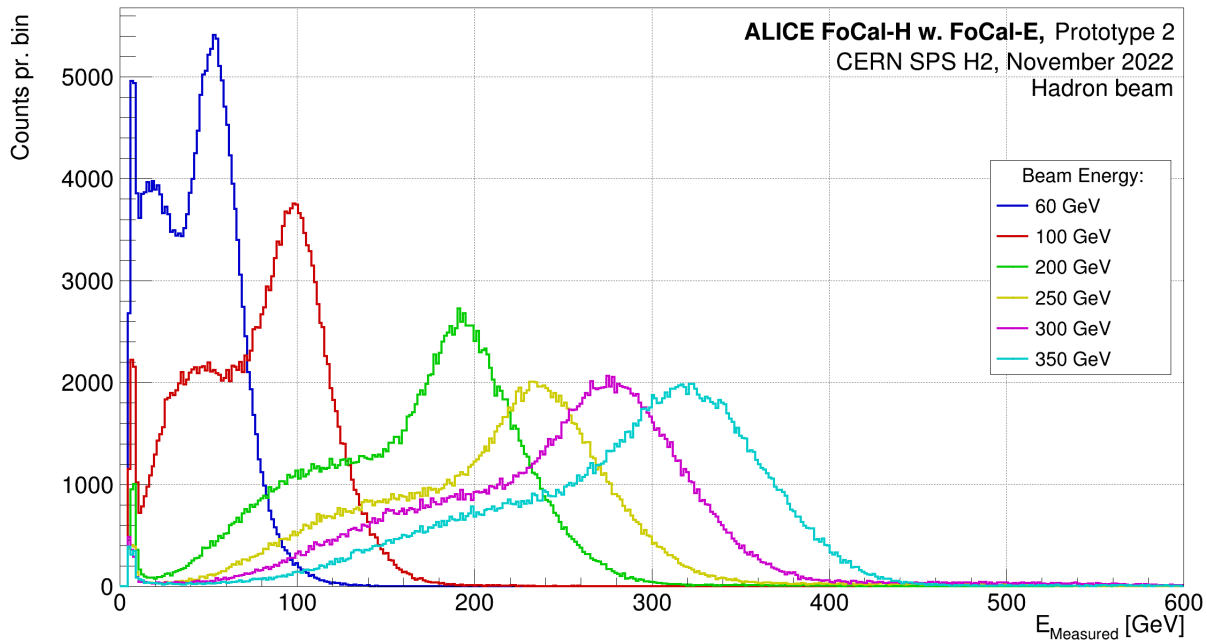


Figure 42: The figure shows a plot of the total charge measured in FoCal-H in testbeam data using the setup including FoCal-E.

The first peak is at around 6 GeV, and is common for each energy. This peak is understood to be a punch through particle, possibly a minimum ionizing particle (MIP), coming from a muon punching through the detectors, not creating a shower in the two detectors.

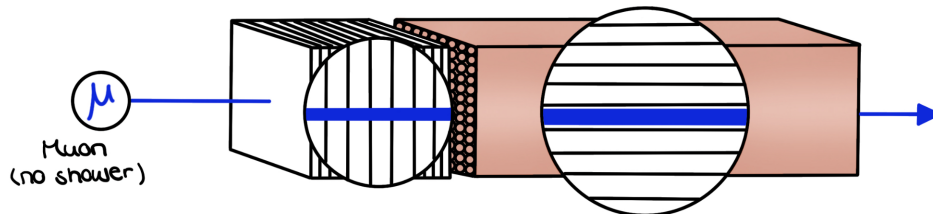


Figure 43: Schematic of the FoCal detector setup where a muon is punching through FoCal-E and FoCal-H. The muon does not create a particle shower in the detector.

The second peak appears in relation to a particle shower starting in FoCal-E (pre-shower) and continuing to shower inside FoCal-H. Such a particle shower can start in one or more of the tungsten plates in FoCal-E, creating particles that have lower energies than the particles that start their first particle shower in FoCal-H. The second peak was not anticipated before the fall testbeams.

The third peak is the opposite case of the second peak. The third peak represents particle showers, which start in FoCal-H and are seen as a punch through peak in FoCal-E (See figure 47 for visualization.).

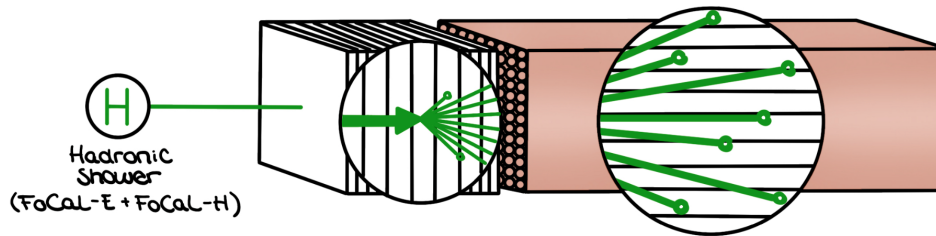


Figure 44: Schematic of the FoCal detector setup where a particle shower starts in one/more of the FoCal-E tungsten plates and continues to shower inside FoCal-H.

Besides these three types of responses in FoCal-H, one can also have particle showers, which are captured in FoCal-E. This type of particle shower will not give a signal in FoCal-H. A schematic of such a signal can be seen in figure 45.

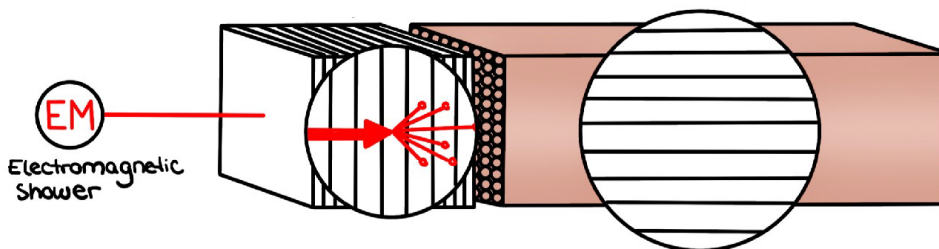


Figure 45: Schematic of the FoCal where a particle shower is fully captured in FoCal-E.

To confirm the interpretation of the second peaks seen in FoCal-H, two things needed to be tested. The first was to remove FoCal-E from the setup, to see if the pre-shower would disappear. These results can be seen in 8.1.1.2. The second thing was to simulate these two setups, including and excluding FoCal-E, to see if the results could be reproduced in simulations. These results can be seen in section 8.2.3.

8.1.1.2 FoCal setup excluding FoCal-E

The November 2022 SPS H2 testbeam using the testbeam setup excluding FoCal-E in front of FoCal-H was run at some of the same beam energies as the setup including FoCal-E. The energies 80 GeV and 150 GeV were excluded in this test due to time limitations. The total response in FoCal-H at this setup has two characteristic peaks, as can be seen in figure 46.

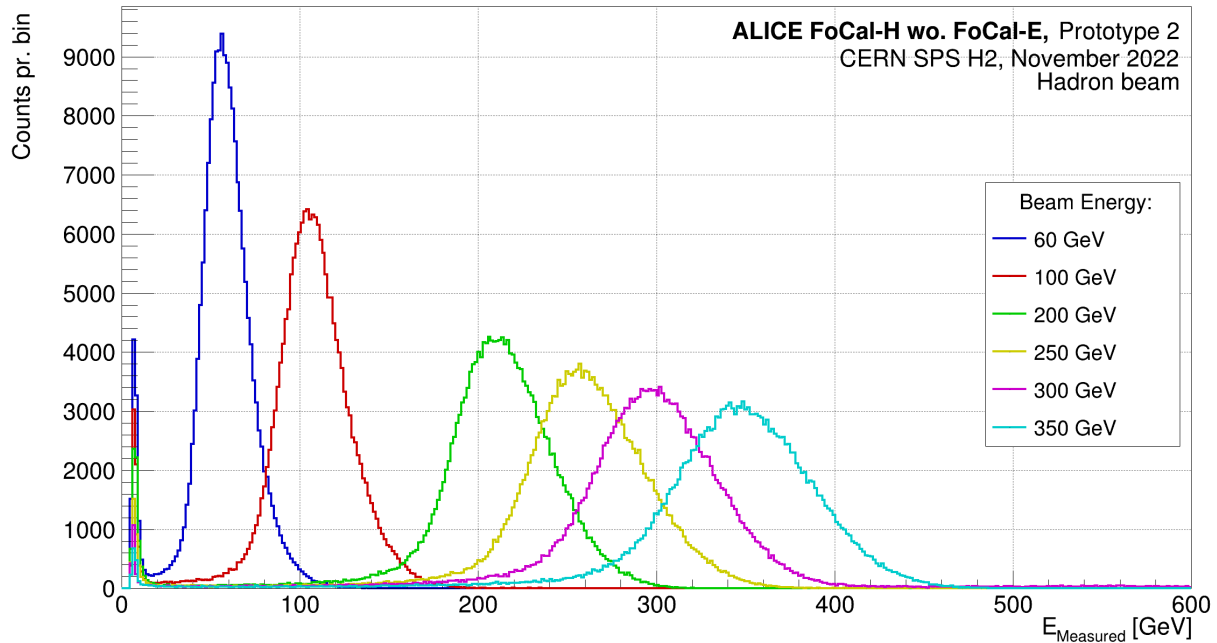


Figure 46: The figure shows a plot of the total charge measured in FoCal-H in testbeam data using the setup excluding FoCal-E.

The first peak is placed around 6 GeV, as was the case for the setup including FoCal-E. This peak is again related to particles punching through the two detectors. The second peak is related to the particle shower starting in FoCal-H and will be referred to as the hadron peak. As can be seen in figure 46, this peak now has a cleaner shape, without the pre-shower peak attached to it.

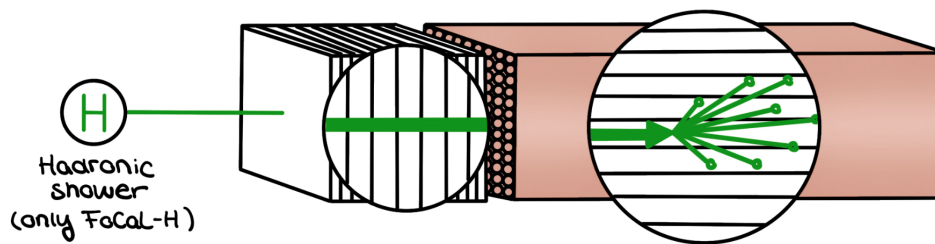


Figure 47: Schematic of the FoCal detector setup where a particle shower starts in FoCal-H.

8.1.1.3 Energy comparison between testbeam setups

In order to estimate how much energy is lost to the pre-shower in FoCal-E, I fitted a gaussian function fit to what corresponds to the hadron peak for both the detector setup including and excluding the FoCal-E in front of FoCal-H. This was done for each of the beam energies for the two detector setups. For each energy the mean of the fit was calculated, which should correspond to the measured energy of the hadron peak in FoCal-H. The mean value as a function of the beam energies can be seen in figure 48.

The percentage difference between the mean values for the same energy in the two detector setups has later been calculated. The calculation of the percentage difference is also given as the difference in energy [GeV] and is illustrated in the figure.

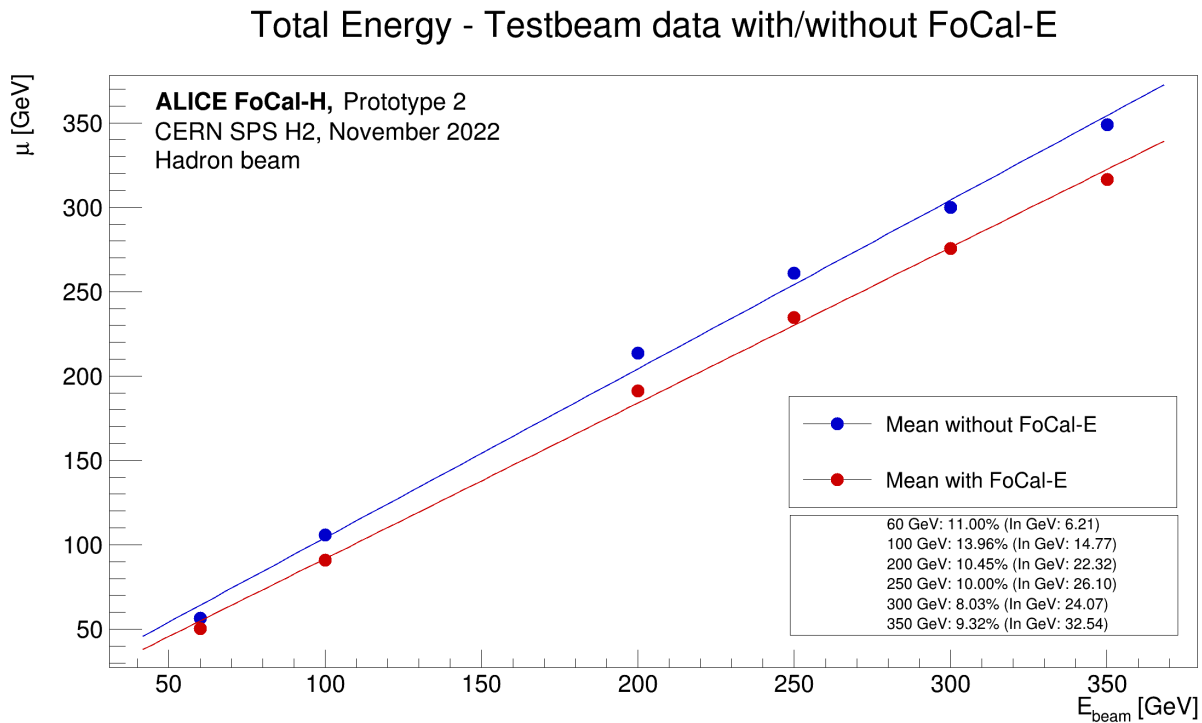


Figure 48: Mean value of the gaussian function fit to the hadron peak, for testbeam setup including and excluding FoCal-H. The mean value corresponds to the measured energy of the hadron peak and is plotted as a function of the beam energies.

As visible from the calculations of the energy difference between the two detector setups, the difference in GeV gets larger as the beam energy gets higher. With one exception, for the 300 GeV measurement. From a theoretical perspective, this tendency makes sense. However, the theoretical predictions of how much energy should be lost in FoCal-E are a great deal lower than what is observed.

To calculate the expected energy loss in FoCal-E, one can use the Bethe-Bloch formula. Specifically the relativistic Bethe-Bloch formula, since we are working with particles that move relativistically. Working with the non-relativistic Bethe-Bloch formula requires $\beta = \frac{v}{c} \ll 1$. For the November SPS H2 testbeam energies using a beam mainly consisting of π^+ , would for the lowest and highest energy give a β -value

of:

$$60\text{GeV} : \beta = \sqrt{1 - \left(\frac{1}{\gamma}\right)^2} = \sqrt{1 - \left(\frac{1}{\frac{E_{tot}}{E_{rest}}}\right)^2} = \sqrt{1 - \left(\frac{1}{\frac{60000[\text{MeV}]}{139.57039[\text{MeV}]}}\right)^2} = 0.9999972944$$

Where E_{tot} is the total energy of the π^+ in the beam, and E_{rest} is the rest energy of the π^+ .

$$350\text{GeV} : \beta = 0.9999999205$$

This means that we, in the energy range we tested the FoCal-H second prototype under, can use the relativistic Bethe-Bloch formula. This is given by [37]:

$$\left\langle \frac{dE}{dx} \right\rangle = K \cdot z^2 \cdot \frac{Z}{A} \cdot \frac{1}{\beta^2} \cdot \left[\frac{1}{2} \cdot \ln \left(\frac{2 \cdot m_e \cdot c^2 \cdot \beta^2 \cdot \gamma^2 \cdot W_{max}}{I^2} \right) - \beta^2 - \frac{\delta(\beta\gamma)}{2} \right]$$

where $K = 4\pi \cdot N_A \cdot r_e^2 \cdot m_e \cdot c^2 = 0.307075 \frac{\text{MeV} \cdot \text{cm}^2}{\text{g}}$, z is the charge number of the incident particle, Z is the atomic number of the absorber, A is the atomic mass number of the absorber, m_e is the mass of the electron, I is the mean excitation energy, $\delta(\beta\gamma)$ is the density effect correction to ionization energy loss, and W_{max} is the maximum energy transfer in a single collision given by:

$$W_{max} = \frac{2 \cdot m_e \cdot c^2 \cdot \beta^2 \cdot \gamma^2}{1 + \frac{2 \cdot \gamma \cdot m_e}{M} + \left(\frac{m_e}{M}\right)^2}$$

which can be approximated to $W_{max} = M \cdot \beta^2 \cdot \gamma$, when $2m_e\gamma \gg M$, as is the case for these measurements.

Energy Loss in FoCal-E		
$E_{beam}[\text{GeV}]$	$\frac{dE}{dx} [\frac{\text{MeV} \cdot \text{cm}^2}{\text{g}}]$	Energy Loss [MeV]
60	2.12	286.40
80	2.16	291.19
100	2.18	294.91
150	2.23	301.66
200	2.27	306.45
250	2.30	310.17
300	2.32	313.21
350	2.34	315.78

Table 2: The table lists the Bethe-Bloch calculated energy loss in FoCal-E. The table provides information about the beam energy (first column), the corresponding Bethe-Bloch value (second column), and the corresponding energy loss of the pion after transversing all FoCal-E tungsten layers (third column).

The reason why the theoretical calculations of the energy loss in FoCal-E is that different from the measured ones, is at this point unknown. An option is that other physics processes than the ones contained in the Bethe-Bloch is needed. However, the calculated method could possibly also be biased to be higher than it should.

Doing the same analysis for runs where the FoCal-E and FoCal-H ran on a common trigger, makes it possible to make a TOT cut (TOT=0) and ADC cut (ADC<65000) in FoCal-E. Demanding a TOT=0 in FoCal-E ensures an examination in a low energy range, by neglecting the TOT readout in FoCal-E. The TOT readout enables FoCal-E to examine high energy signals without saturation the readout, since the

TOT readout takes over from the ADC readout at very high signals. The $ADC < 65000$ is chosen due to an approximate ADC signal from a MIP in FoCal-E.

This removes the pre-shower in the FoCal-H data and one can analyse based on the hadron peak¹⁴. These runs with the applied cuts in the TOT and the ADC, are characterized in FoCal-E as being a MIP. Performing the same analysis, calculating the estimated energy loss in FoCal-E for the testbeam data, with these cuts for the runs with FoCal-E in front can be seen in figure 49.

The synchronization between FoCal-E and FoCal-H, when using the common trigger, had some issues in that the two different readout systems got out of sync after some time. The statistics on the datafiles with FoCal-E in front of FoCal-H using these cuts, are therefore fairly low. However, the statistics are good enough for further analysis. The 100 GeV comparison is not included in this analysis, since there were issues in removal of the pre-shower peak, due to low statistics. A common trigger study among the priorities investigations in the collaboration, since the FoCal-E and FoCal-H detectors should be synchronized in the final detector, to be able to fulfil the physics goals of the detector¹⁵.

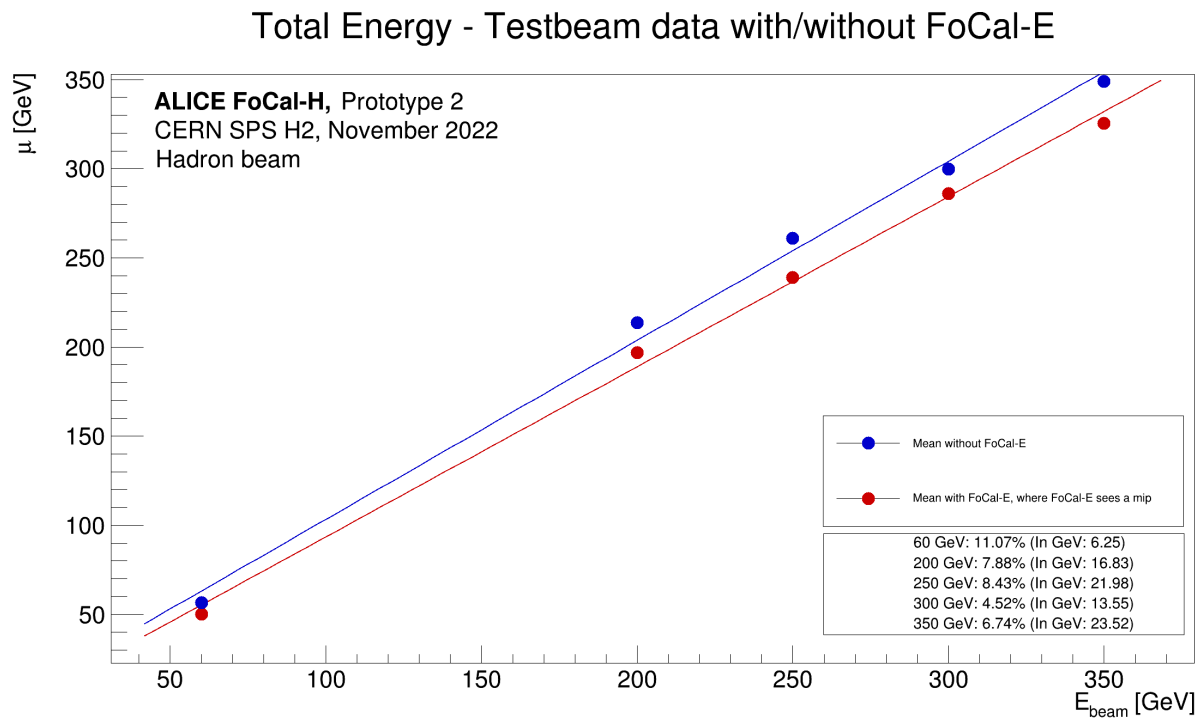


Figure 49: The mean value of the gauss function fit to the hadron peak for each energy, for testbeam setups including and excluding FoCal-H. The mean value corresponds to the measured energy of the hadron peak and is plotted as a function of the beam energies.

The energy difference between setups including and excluding FoCal-E in front of FoCal-H using the ADC and TOT cuts, lowers the calculated values of the energy loss in FoCal-E with several GeV, compared to the calculations without the cuts. This is true for all energies except 60 GeV, which is roughly the same. The energy difference, i.e. the energy loss in FoCal-E, is still far too high compared to the theoretical Bethe-Bloch calculations. Other physics contributions to the theoretical calculations should be found, in order to explain the energy loss we see in the data.

¹⁴The common trigger analysis is conducted by someone else in the collaboration (Max Rauch and Alexander Buhl) [42].

¹⁵See section 3 for a description of the FoCal physics goals.

8.2 Simulation data - November 2022 SPS H2

This section will go through the performed simulations corresponding to the different experiments tested at the November 2022 SPS H2 testbeam. The section will also go through the analysis of various studies aiming to understand the FoCal-H testbeam data.

The simulations done in this thesis have been generated using Geant4 version 10.07 patch 03. All further analysis of the simulations has been made using c++ and ROOT. The majority of the simulations have been run to 100.000 events, due to the time it takes for the simulation to run. However, smaller studies have been run to 10.000 events, but can be run with increased number of events if the need for better statistics is prioritized.

At the November 2022 SPS H2 testbeam, energies from 60 GeV to 350 GeV were measured using the FoCal-H second prototype setup, which where performance tested using various detector configurations. Corresponding simulations for these performance tests, have been performed and will be presented in this section.

8.2.1 Comparison between updates in simulations

During the first simulations of the testbeam FoCal setup, a lot of parameters were changed from week to week in order to optimize the FoCal prototype setup. These changes were both from the FoCal-H team but also from FoCal-E.

One of the changes in FoCal-H was done because I noticed that the first simulations had been run with air gaps between the FoCal-H calorimeter modules. This is not the case in real life and would simulate areas where particles would not get detected in the simulations. A visualization of the detector setup with these air gaps can be seen in figure 50 below.

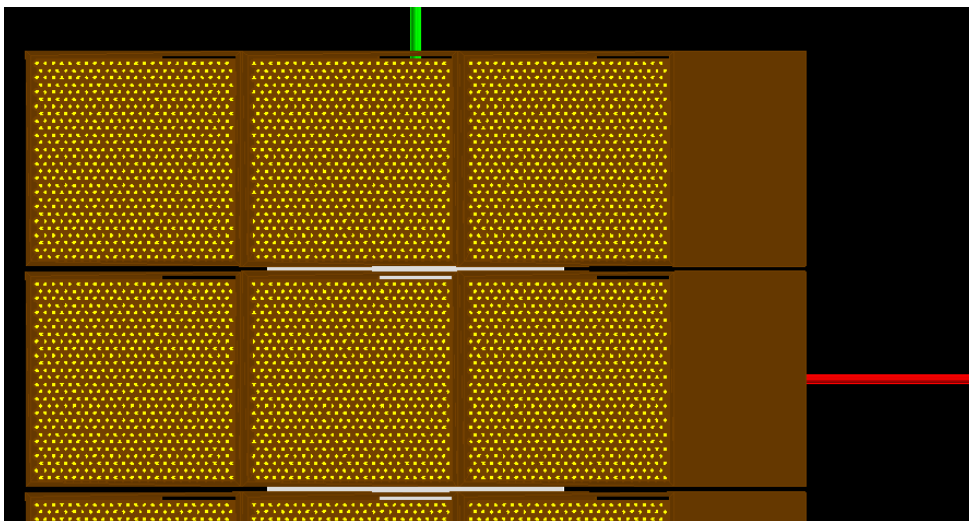


Figure 50: The figure shows a visualization of the Geant4 simulations where the FoCal-H calorimeter setup has air gaps between the calorimeter modules.

In order to examine how big an effect a mistake like this could have on the simulation, I simulated the FoCal setup at 200 GeV, with and without the air gaps. The two different simulations can be seen in

figure 51. The figure in the upper section shows the energy response detected in FoCal-H, whereas the lower section shows the ratio between the two simulations. Taking the ratio between the two different simulations would show areas where the bin content is different. The error pr. bin in this histogram is calculated by default using the *divide()* function in root, where the *Sumw2()* is implemented. *Sumw2()* computes the error pr. bin by computing the square root of the sum of the entries in each bin squared [41]. If the bin content is similar for the two simulations, then the green line should be around the value 1, if it is different then the green line would deviate from 1. As is clear from figure 51, the simulations with and without the implemented air gaps do not show a large effect of air gaps on the response in FoCal-H. This is important knowledge to have when studying ones simulations. However, in all simulations continuing from hereon the air gaps are removed in order to be as close to reality as possible.

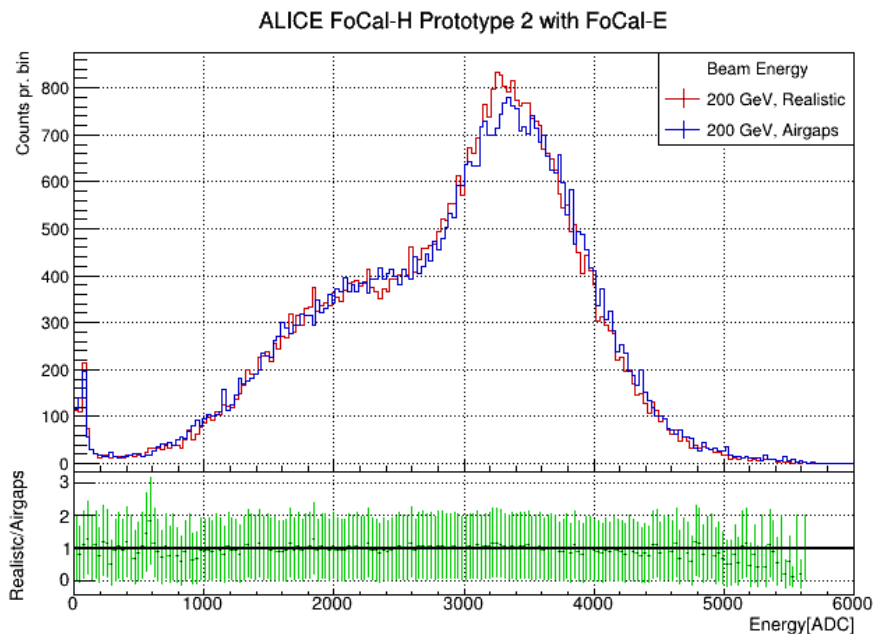


Figure 51: The figure shows a comparison between simulations with and without air gaps between the FoCal-H calorimeter modules.

The FoCal-H team also changed the size of the inner diameter from 1.1 mm to 1.12 mm in order to reduce the spacing between the scintillating fiber and the copper tube. The outer diameter was also changed from 2.5 mm to 2.52 mm in order to reduce the spacing between the copper-tubes and the copper-box around all 668 copper-tubes. A comparison study between these simulations can be seen in the appendix section 11.4.1. The FoCal-E team also implemented some changes in the sizes of the pixel layers, as well as the spacing between the pixel and the pad layers. The result of this comparison study can also be seen in the appendix section 11.4.1. Neither of the last two comparison studies showed to have any large effects on the simulations.

8.2.2 Beam shape and size

Additional important considerations when setting up the simulation are the beam shape and size. These factors give an important contribution in regard to comparing the simulated response in the detector to

the testbeam data. The simulation was initially set to have a square beam shape and a size of 4x4 cm. However, these configurations do not relate to the beam size and shape in the November 2022 SPS H2 testbeam, and were therefore changed.

3D plots showing an implementation of a round 4x4 cm beam size, compared to a round 1x1 cm beam size can be seen in figure 52 and figure 53. The round 1x1 cm beam has been used in the remaining studies, in order to compare with testbeam data. The beam shape and size study was performed for two energies, 60 GeV and 350 GeV.

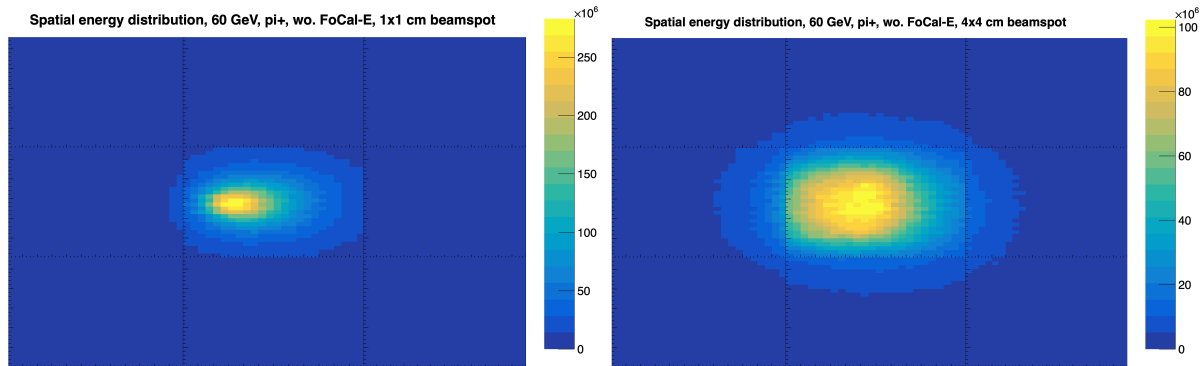


Figure 52: The figure shows the shower profile in FoCal-H at 60 GeV for two different sizes of beamspot. The left-side plot shows a simulation implementing a round 1x1 cm beam. The right-side plot shows a simulation implementing a round 4x4 cm beam.

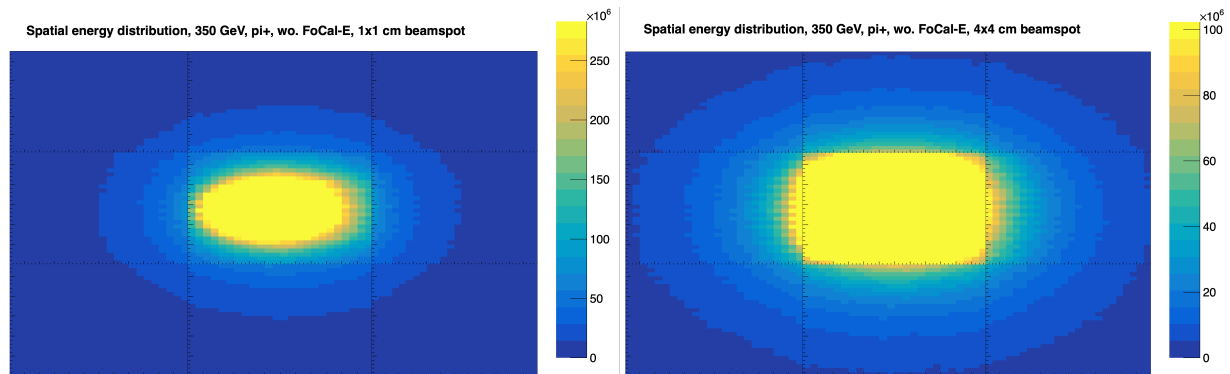


Figure 53: The figure shows the shower profile in FoCal-H at 350 GeV for two different sizes of beamspot. The left-side plot shows a simulation implementing a round 1x1 cm beam. The right-side plot shows a simulation implementing a round 4x4 cm beam.

The difference in the beam size has importance in relation to the response in FoCal-H. Figure 54 shows the total response in FoCal-H for simulations at 60 GeV (top) and 350 GeV (bottom) implementing the round 4x4 beam (red), compared to the round 1x1 cm beam (blue). These simulations do not include FoCal-E in front of FoCal-H in the FoCal detector setup. The plot also shows the ratio between the two beam configurations (green), giving a understanding of the difference between the two beam configurations. The corresponding analysis can be performed with FoCal-E in front of FoCal-H, to estimate the difference for the total FoCal detector setup. I suspect that with a 4x4 cm beamspot, some particles could interact with the edges of FoCal-E, resulting in unexpected response in FoCal-H, but also in FoCal-E.

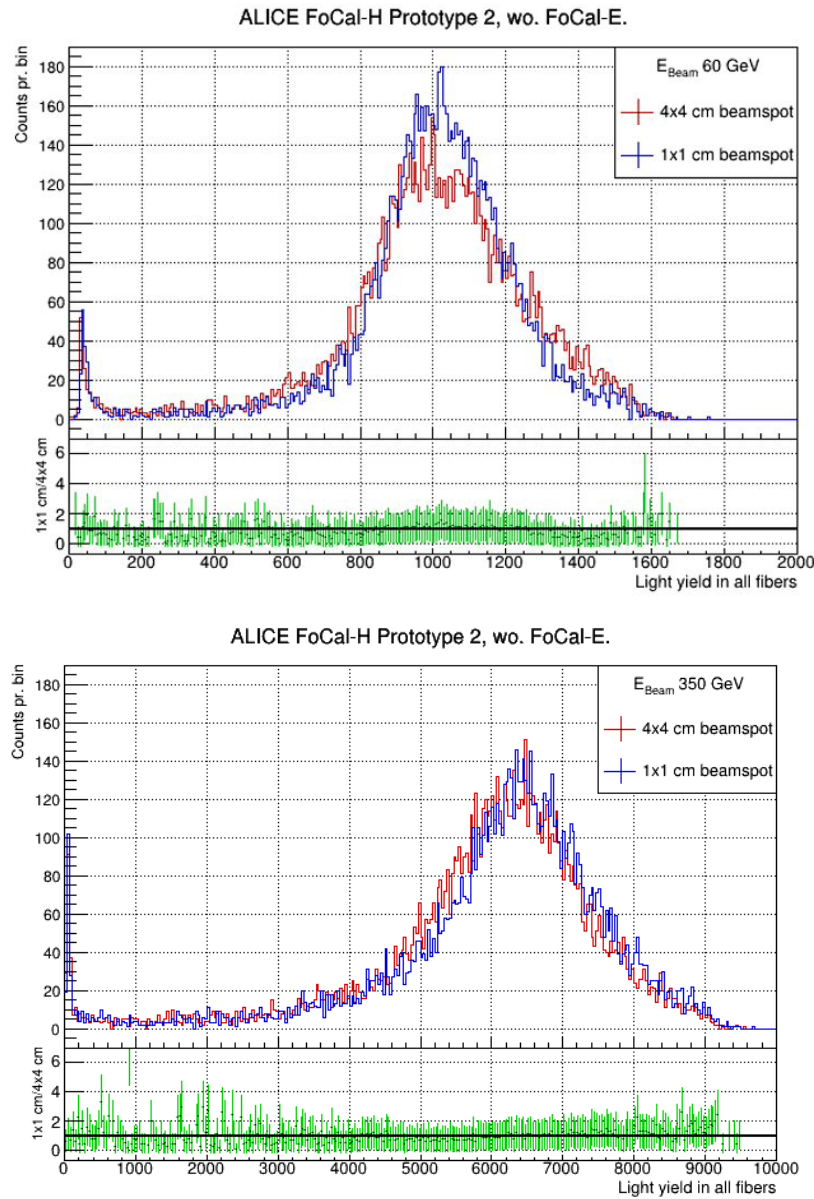


Figure 54: The figure shows the total response in FoCal-H for two different beam configurations. The top figure is for 60 GeV and the bottom figure is for 350 GeV. The red line shows the total response using a round 4x4 cm beam. The blue line shows the total response using a round 1x1 cm beam. The ratio between the total response for the two beam configurations is represented by the green line.

The response for the two different beam configurations is fairly compatible. The largest differences in the two configurations are seen in the low energy and high energy range, for both 60 GeV and 350 GeV. I suspect these differences are related to the significant change in the beam size, leading to a larger particle shower with a larger amount of fluctuations in the response of the FoCal-H calorimeter modules. In addition, the hadron peak in the 60 GeV simulations using the round 4x4 cm beam, seems to be reduced in high compared to the round 1x1 cm beam. Whether this could be due to particles e.g. hitting the edge of FoCal-E resulting in an unexpected response in FoCal-H, or a possible saturation of the scintillating fibers in FoCal-H, is unknown. A study where the beam size is increase and/or decreased could be

performed, in order to eliminate one or the other possible explanation.

When comparing simulations to testbeam data, one should use configurations as close as possible to those used in the November SPS H2 testbeam.

8.2.3 FoCal detector setup

Detector setups including and excluding FoCal-E in front of FoCal-H were one of the configurations tested in simulations. These simulations were prioritized to verify the trend of the pre-shower peak, which was seen in the testbeam data from the September and November 2022 testbeam. The results of these studies will be presented in this section.

8.2.3.1 FoCal setup including FoCal-E

The first step was to simulate the full detector setup, using both FoCal-E and FoCal-H. The response in FoCal-H could then be studied, to see if a pre-shower peak similar to what was seen in the testbeam data would appear. To do so, the following simulated detector setup was used, as can be seen in figure 55.

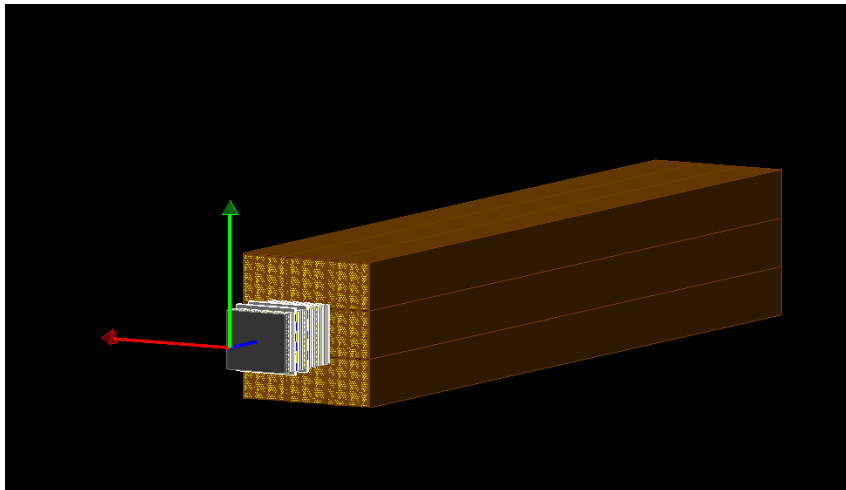


Figure 55: The figure shows a Geant4 illustration of the detector setup of both FoCal-E and FoCal-H. The illustration shows the FoCal-E and FoCal-H prototype setup, and not the final version of the two calorimeters.

The setup has been simulated using two different Geant4 physics lists, the QGSP-BERT and the FTFP-BERT. Both physics lists are recommended for simulations of high-energy calorimeter physics. The difference between the two physics lists will be explained in section 8.2.3.3, where the simulation data is examined in greater detail. Furthermore, the reason for using two different Geant4 physics lists will be discussed in section 8.3.2.

Both physics list have been simulated using a pion (π^+) beam for 100.000 events. Figure 56 shows simulations from 60 GeV to 350 GeV using the QGSP-BERT physics list, for the detector setup including FoCal-E in front of FoCal-H.

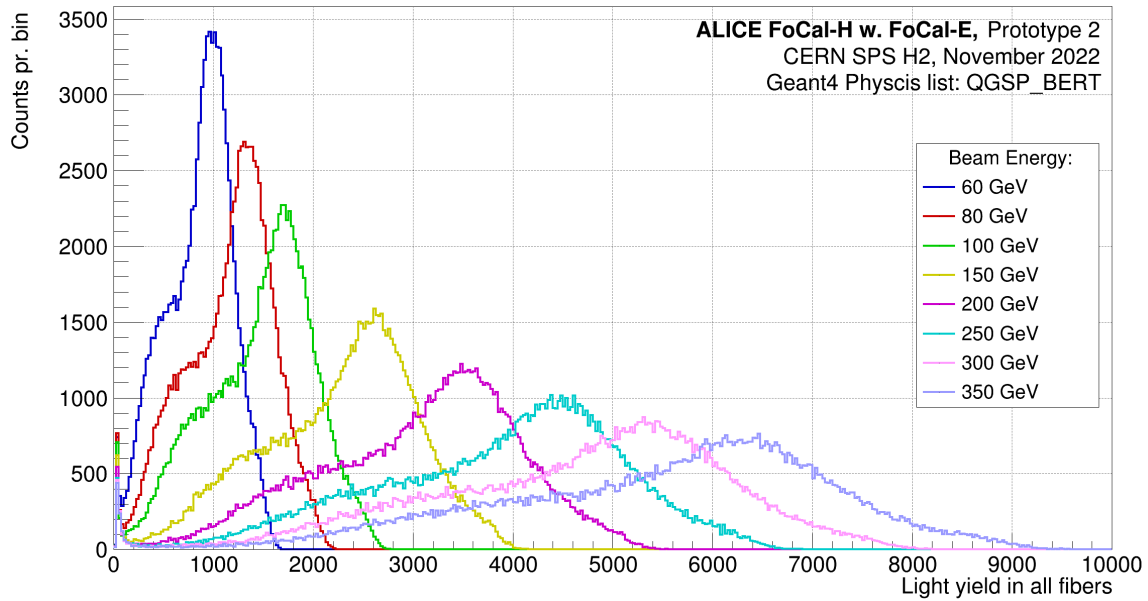


Figure 56: The figure shows a plot of the total response measured in FoCal-H in simulations using the detector setup including FoCal-E, and the QGSP-BERT physics list. The simulated responses are performed for energies from 60 GeV to 350 GeV.

Figure 57 shows the corresponding simulations from 60 GeV to 350 GeV using the FTFP-BERT physics list. The FoCal-H response using the FTFP-BERT physics list has a larger contribution in the pre-shower peak. The possible reason for this will be discussed in section 8.2.3.3. A comparison between the FoCal-H response for the two physics lists at 60 GeV, can be found in appendix section 11.4.2.

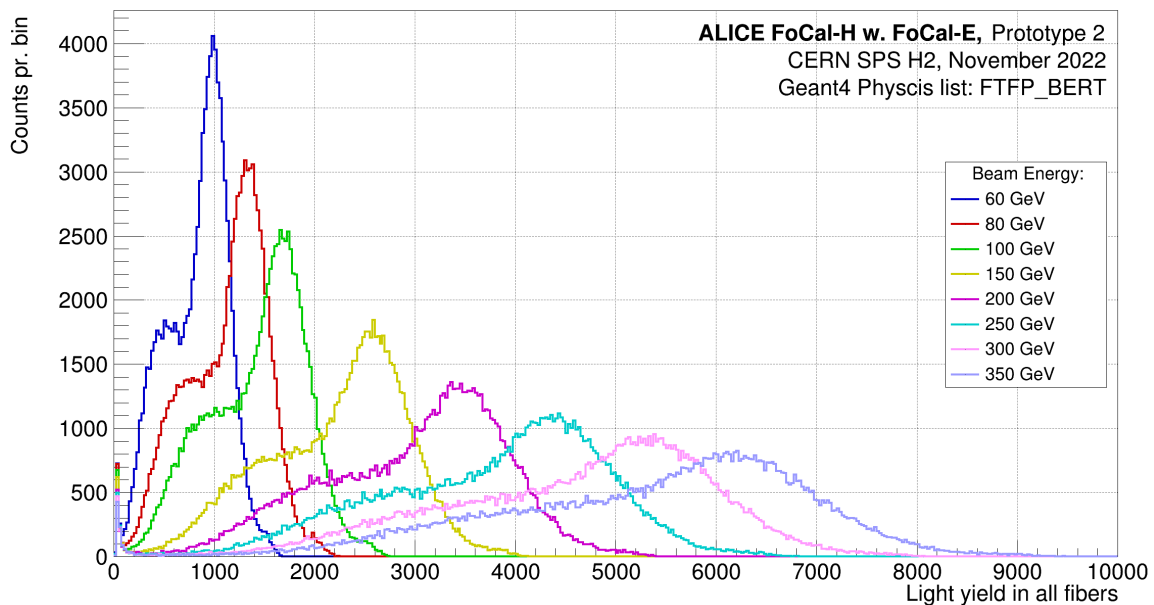


Figure 57: The figure shows a plot of the total response measured in FoCal-H in simulations using the detector setup including FoCal-E, and the FTFP-BERT physics list. The simulated responses are performed for energies from 60 GeV to 350 GeV.

Both Geant4 physics lists show to be consistent with testbeam data for the detector setup including FoCal-E, and this is true for all simulated energies. The hypothesis that the pre-shower peak could be due to the particle shower starting in FoCal-E is therefore confirmed.

To examine the pre-shower peak in further detail, one could possibly study the response in FoCal-E for the simulations. Due to the composition of FoCal-E, the response for a high-energy hadron would most likely be seen as a punch through particle. A detailed punch through study in simulation for FoCal-E has not been performed in connection to this thesis. However, the response of FoCal-E for this setup has been studied elsewhere. The response in both FoCal-H and FoCal-E for both Geant4 physics lists can be seen in figure 58 and figure 59. The plots in the two figures are shown on a logarithmic scale, so that the dissimilarities in the response for FoCal-E and FoCal-H are visible.

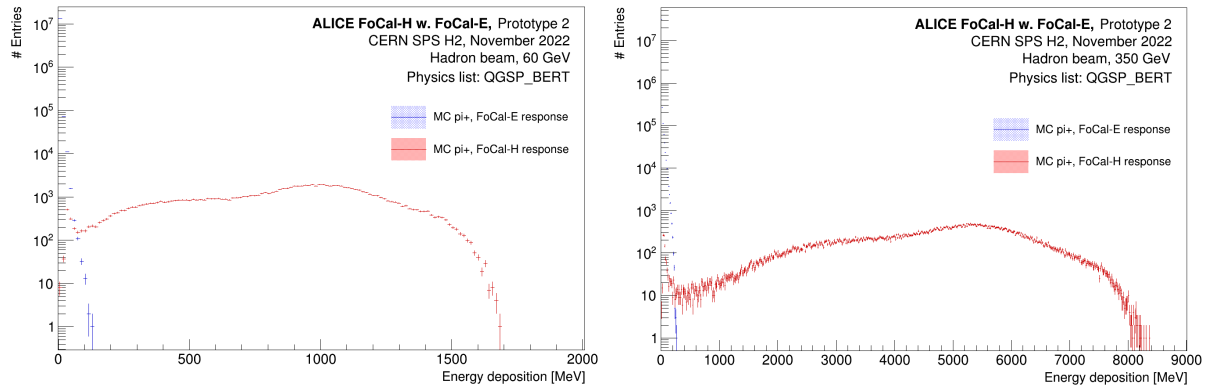


Figure 58: The figure shows a plot of the total response measured in FoCal-H and in FoCal-E, for simulations including FoCal-E in the detector setup, and the physics list QGSP-BERT using a pion beam. The left-side figure shows the responses at 60 GeV. The right-side figure shows the response at 350 GeV.

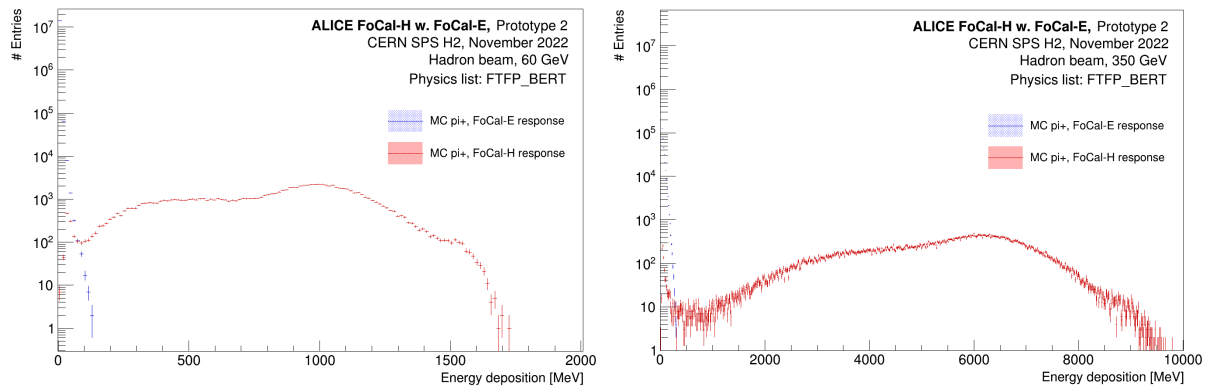


Figure 59: The figure shows a plot of the total response measured in FoCal-H and in FoCal-E, for simulations including FoCal-E in the detector setup and the physics list FTFP-BERT using a pion beam. The left-side figure shows the responses at 60 GeV. The right-side figure shows the response at 350 GeV.

The simulated response in FoCal-E and in FoCal-H both increase as the energy increases. This agrees with the expectation of a shower development of electromagnetic and hadronic calorimeters. The response in FoCal-H is significantly larger than the response in FoCal-E, since the performed simulations are hadronic using a π^+ beam. However, if the simulations were performed with e.g. an electromagnetic

e^- beam, the response would be large in FoCal-E, since an electron would react electromagnetically in FoCal-E.

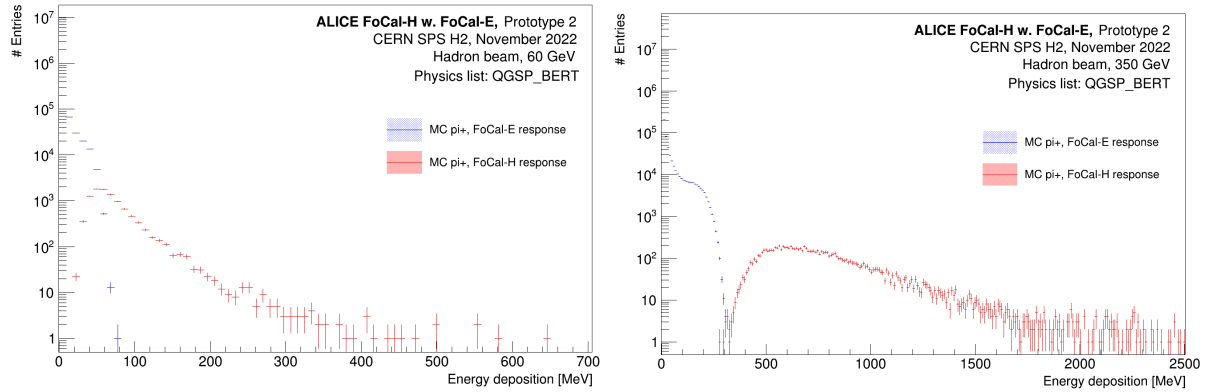


Figure 60: The figure shows a plot of the total response measured in FoCal-H and in FoCal-E, for simulations including FoCal-E in the detector setup and the physics list QGSP-BERT using an electron beam. The left-side figure shows the responses at 60 GeV. The right-side figure shows the response at 350 GeV.

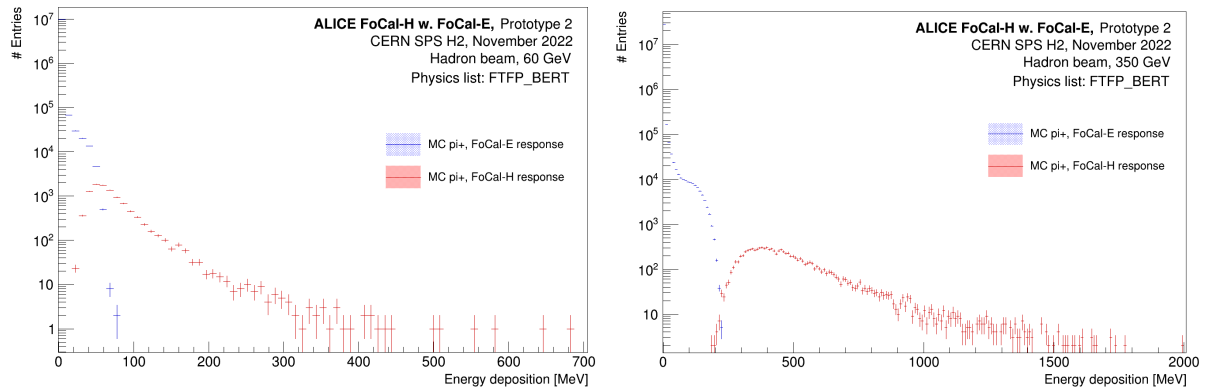


Figure 61: The figure shows a plot of the total response measured in FoCal-H and in FoCal-E, for simulations including FoCal-E in the detector setup and the physics list FTFP-BERT using an electron beam. The left-side figure shows the responses at 60 GeV. The right-side figure shows the response at 350 GeV.

8.2.3.2 FoCal setup excluding FoCal-E

To see if the pre-shower peak would disappear, as we saw in the testbeam data, simulations excluding FoCal-E in the detector setup, also needed to be performed. An illustration of the Geant4 simulated detector setup excluding FoCal-E in front of FoCal-H can be seen in figure 62.

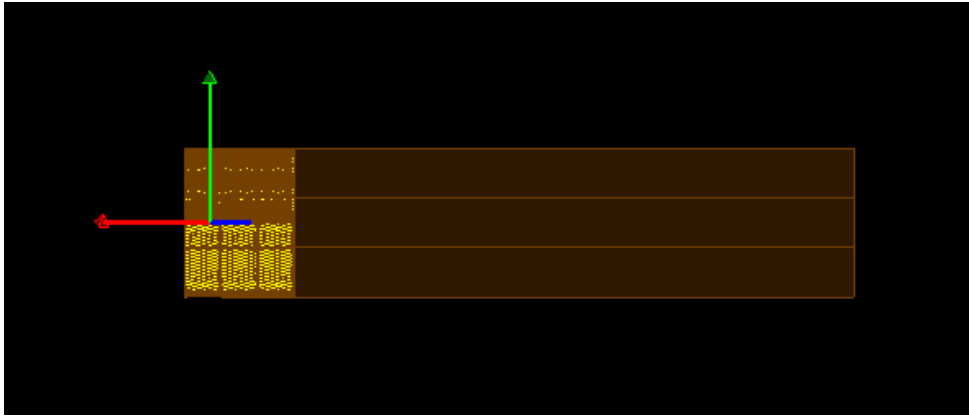


Figure 62: The figure shows a Geant4 illustration of the detector setup of FoCal-H, where FoCal-E has been excluded from the simulation setup. The illustration shows the FoCal-H second prototype setup, and not the final FoCal-H detector.

As for the setup including FoCal-E in front of FoCal-H, these simulations were run at energies from 60 to 350 GeV, using the QGSP-BERT and FTFP-BERT physics lists. Figure 64 and 63 below show the results of these simulations.

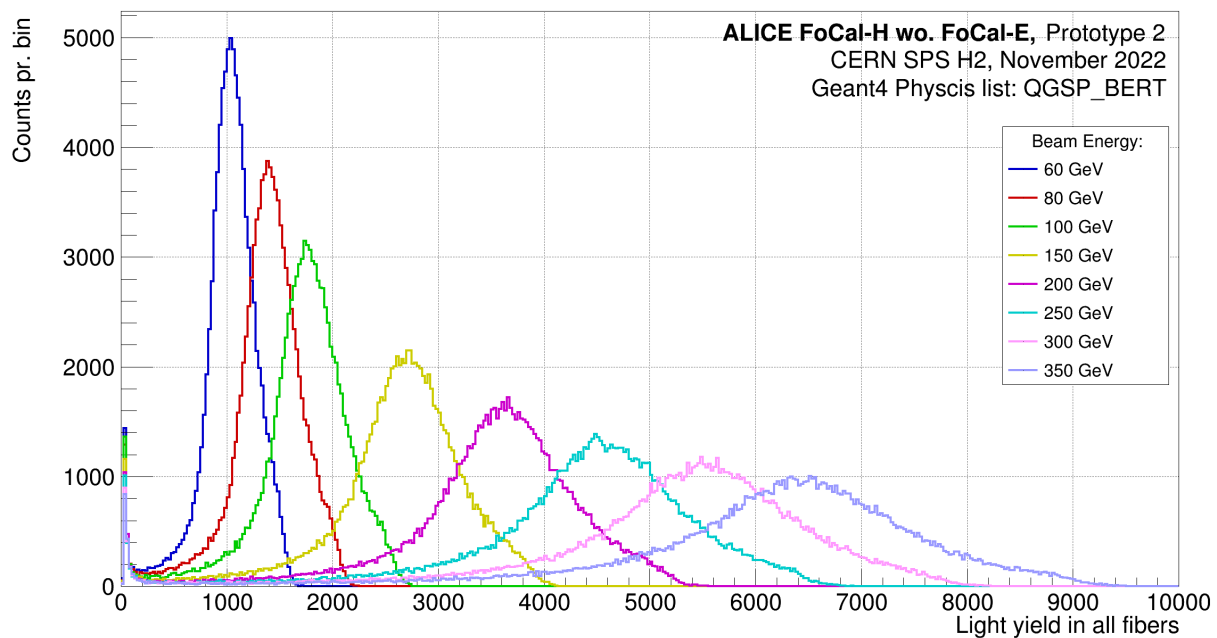


Figure 63: The figure shows a plot of the total response measured in FoCal-H in simulations excluding FoCal-E from the detector setup using the QGSP-BERT physics list. The simulated FoCal-H responses are performed for energies from 60 GeV to 350 GeV.

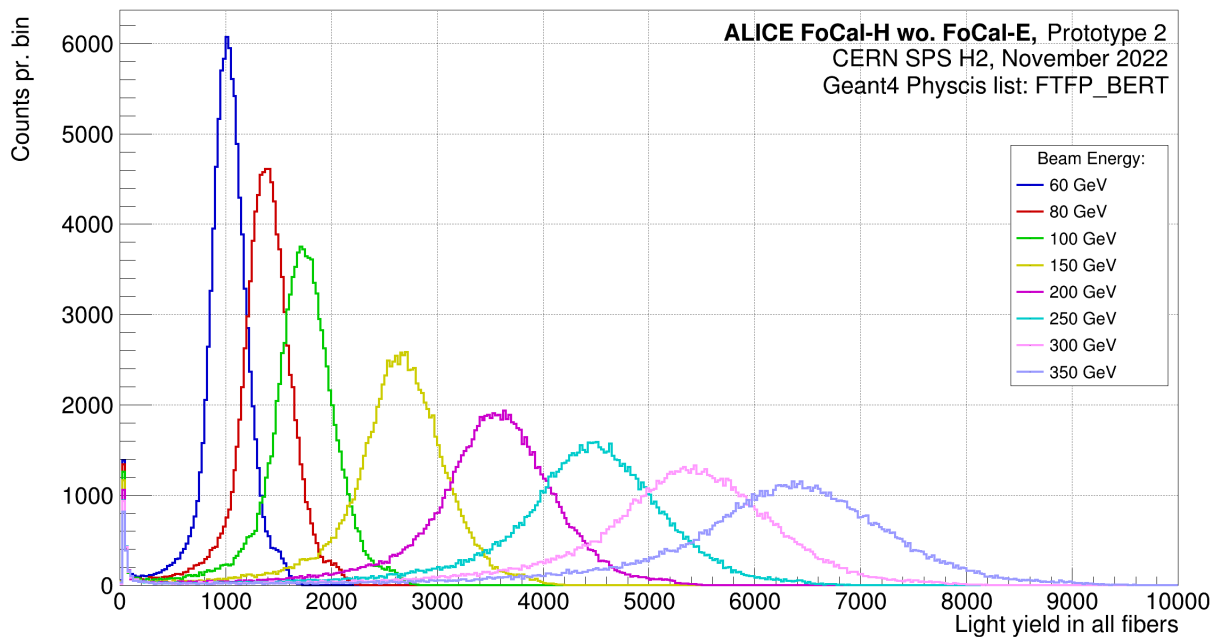


Figure 64: The figure shows a plot of the total response measured in FoCal-H in simulations excluding FoCal-E using the FTFP-BERT physics list. The simulated responses are performed for energies from 60 GeV to 350 GeV.

From the two plots showing all simulated energies using the detector setup excluding FoCal-E in front of FoCal-H, one can see that the pre-shower peak indeed disappears, indicating that the theory of FoCal-E starting a particle shower which continues into FoCal-H, is validated in simulations. This is true for both physics lists, as seen in figure 63 and figure 64.

The simulation using the FTFP-BERT physics list at energies from 60 GeV to 100 GeV shows a small bump in the high-energy end of the hadron peak. A possible reason for this can be found in section 8.2.3.3.

Comparisons between the FoCal-H response including and excluding FoCal-E in front of FoCal-H in simulations using the QGSP-BERT physics list can be found in appendix section 11.4.3.

8.2.3.3 Comparison between simulation physics lists

Simulations using both the QGSP-BERT and FTFP-BERT physics lists were shown to be consistent with the total response in FoCal-H for the testbeam data. However, the two physics lists do not contain the same physics contribution. This section will examine the difference between the two physics lists, in order to determine which one of them contains the most relevant physics information for the FoCal simulations.

Both the Geant4 QGSP-BERT and the FTFP-BERT physics lists are recommended for use in simulations revolving around high-energy calorimeter physics, specifically processes where the primary particle is hadronic. The Geant4 FTFP-BERT physics list was the former default package, but is now replaced by the QGSP-BERT physics list in connection to this thesis. However, this does not necessarily mean that the QGSP-BERT physics list is the correct choice for the FoCal full scale simulations, where the final design

of FoCal is tested.

Both physics lists have implemented packages that handle both hadronic components and electromagnetic components. The hadronic part of both lists consists of inelastic, elastic, capture, and fission processes. These processes are in the Geant4 framework built from cross-sections and interaction models. In the following, I will compare the two lists with respect to how they handle inelastic contributions [38].

Common for both the QGSP-BERT and FTFP-BERT is the BERT sublist. BERT stands for 'Bertini intranuclear cascade' and handles hadronic interactions with energies from 0 to 6 GeV. The sublist handles hadrons with a long lifetime as projectiles, making it possible to have gamma- and lepton-nuclear interactions.

Both the QGSP-BERT and the FTFP-BERT also have the P sublist, which stands for 'Precompound model'. The P sublist handles the de-excitation of the remaining nucleus after a great fraction of the incident particle has interacted. In regards to the FoCal simulation, this sublist could be important e.g. the FoCal-H copper-tubes, when accounting for the last fraction of a particle shower from an incident pion. The differences between the two physics lists are seen in the QGS and FTF part of their names. The QGS part of the QGSP-BERT physics list stands for the 'Quark gluon model'. This hadronic component of the list handles inelastic hadron-nucleus processes above 12 GeV in the simulations. The particles that the QGS takes into account are protons, neutrons, pions and kaons. The FTF part of the FTFP-BERT physics list stands for the 'Fritiof parton model'. This hadronic component of the list handles the same types of particles as QGS, but only in the range of 3 GeV to 26 GeV [38].

The electromagnetic part for both the QGSP-BERT and the FTFP-BERT physics lists is handled by the same standard package called G4EmStandardPhysics constructor. Additional electromagnetic physics lists can be added, but this was not done for the FoCal simulations [38] in this thesis.

None of the two physics lists takes optical photons into account, because it is very CPU-heavy. However, if one has a detector setup including optical photons, as we have for the FoCal setup, then this should be added. For the FoCal simulations performed in this thesis, the optical photons physics list called 'OpticalPhotonPhysics' is used.

In order to understand the different contributions to the total response detected in FoCal-H excluding FoCal-E in front, the two physics lists for a given energy have been plotted. Figure 65 below shows the QGSP-BERT and FTFP-BERT physics lists for 60 GeV and 300 GeV. The calculated ratio between the total responses for the two physics lists is also shown. As described in section 8.2.1, the error in the histogram is calculated by default using the *divide()* function in root, where the *Sumw2()* is implemented. *Sumw2()* computed the error pr. bin by computing the square-root of the sum of the entries in each bin squared [41].

As can be seen from figure 65, the low energy part of the signal indicates a relatively good agreement between the QGSP-BERT and FTFP-BERT physics lists. However, the contribution from the two lists starts to differ around the hadron peak. The peak for the FTFP-BERT physics list is higher for all energies than for QGSP-BERT. I assume that this is due to the gap in energy from 3 GeV to 12 GeV between hadron-nucleus processes, which is taken into account in the FTFP-BERT physics list. However, the difference can also come from the difference in the gap from 6 GeV to 12 GeV, which comes from the hadronic interactions in the BERT sublist in relation to the hadron-nucleus interactions in the QGS sublist.

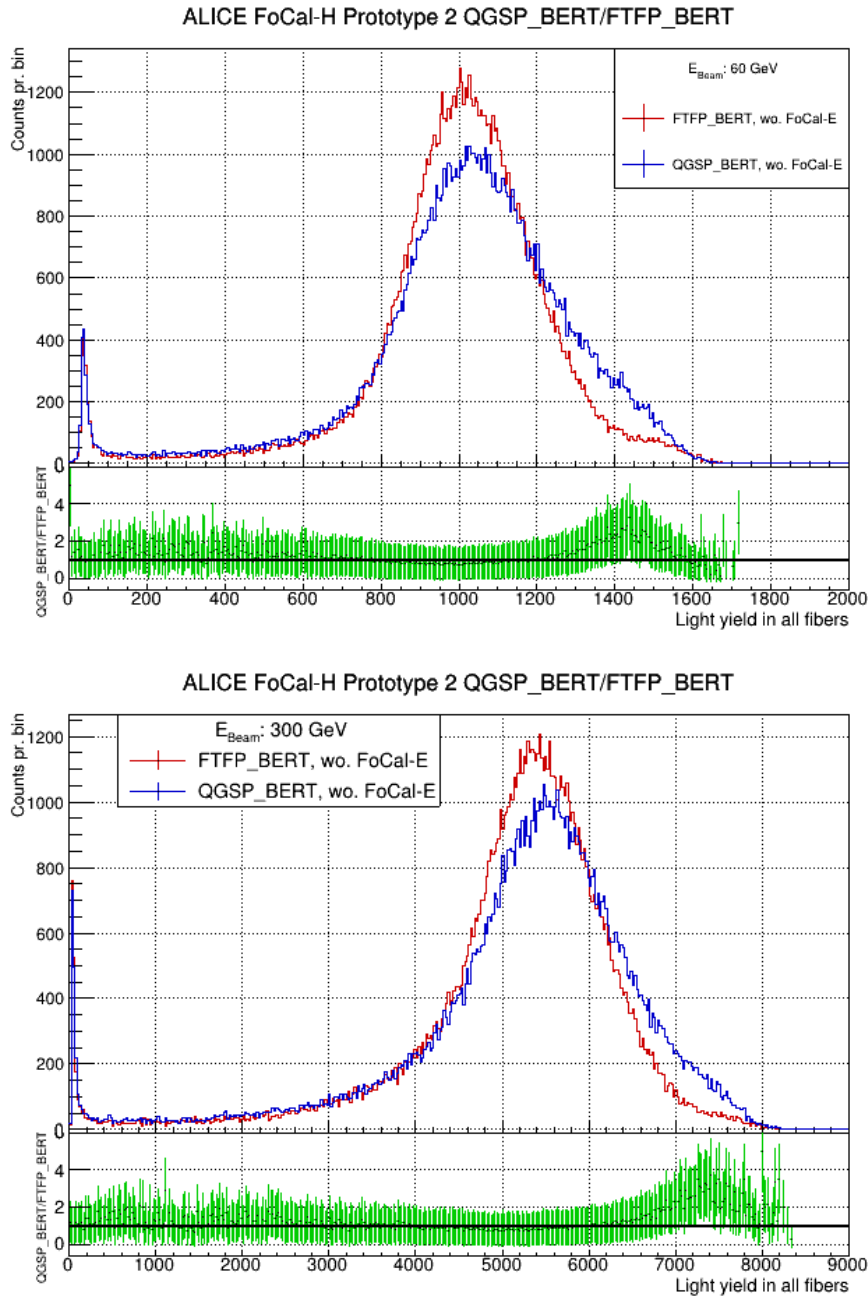


Figure 65: The figure shows a comparison of the two Geant4 physics lists for 60 GeV and 300 GeV. The top plot shows the total response of the QGSP-BERT(blue) and FTFP-BERT(red) physics lists at 60 GeV. The bottom plot shows the total response of the QGSP-BERT(blue) and FTFP-BERT(red) physics lists at 300 GeV. Both plots also show the ratio between the total response for the two Geant4 physics lists plotted below (green).

Another difference between the two physics lists is seen in the higher part of the energy tail. The QGSP-BERT physics list seems to collect a larger contribution of particles with higher energy. I assume that this could stem from the fact that this list does not have a cutoff for hadron-nucleus processes from 26 GeV and up, as had for the FTFP-BERT list. The QGSP-BERT physics list does on the contrary have a lower limit of 12 GeV and collects everything above that. I suspect these cutoffs to have an effect in the

fluctuations contributing in the FoCal-H response.

This physics list comparison has also been performed for energies of 100 GeV, 200 GeV and 250 GeV, and these plots can be seen in the appendix section 11.4.4.

Ideally, the simulations would not have this gap in energies for the hadronic interaction. I have therefore tried to combine the two Geant4 physics lists, in order to cover the hole energy range. However, this study did not lead to any functional solution, since Geant4 either counts the contribution twice or only accounts for the last implemented physics list.

For any further studies in regards to this thesis, it was chosen to continue with the Geant4 physics list QGSP-BERT, since it seems to represent the testbeam data more accurate.

8.2.3.4 Energy comparison between simulation setups

As was done for the testbeam data, the simulations including and excluding FoCal-E in the detector setup needed to be compared. This is done to examine the energy difference between the two setups, but also the energy difference compared to the testbeam data.

In order to estimate the amount of energy lost to the pre-shower in FoCal-E in the simulations, a gaussian function fit was fitted to the hadron peak for both detector setups. For each energy the mean of the fit was calculated, corresponding to the measured energy of the hadron peak in FoCal-H. The mean values for each energy are plotted as a function of the beam energies and can be seen in figure 66. The percentage difference between the mean values for the same energy, and the conversion into GeV, are given in the plot.

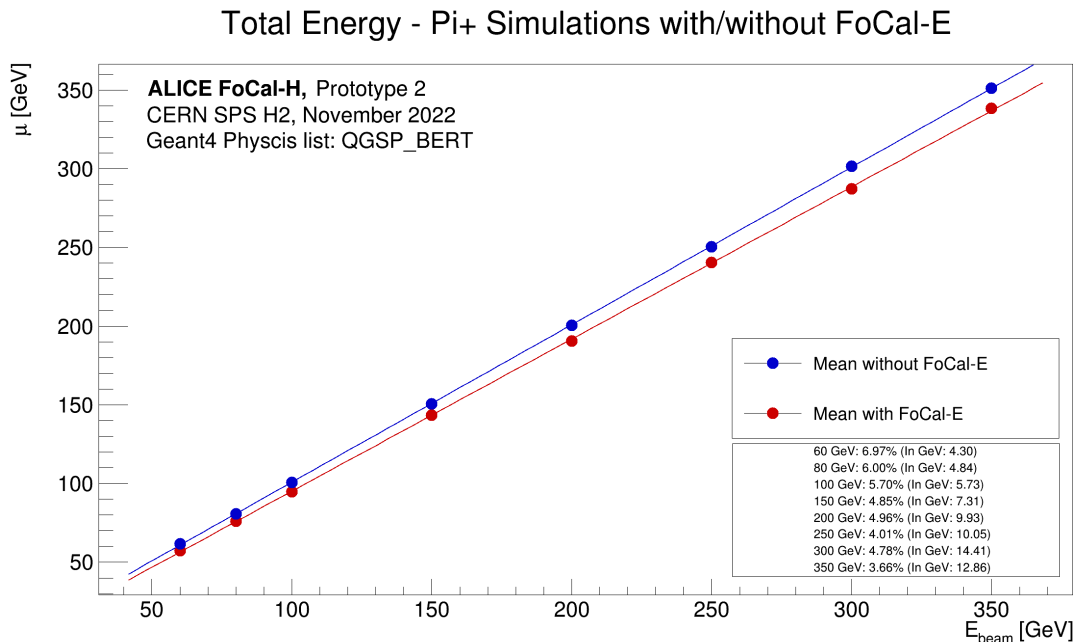


Figure 66: Mean value of the gaussian function fit to the hadron peak, for simulation setups including and excluding FoCal-H, using the QGSP-BERT physics list. The mean value corresponds to the measured energy of the hadron peak and is plotted as a function of the beam energies.

As visible in the calculated energy difference between the two detector setups, the energy difference gets

larger for higher beam energies, with one exception at 300 GeV. This was also the case for the testbeam data. The energy difference, i.e. the energy loss in FoCal-E, is significantly smaller than for the testbeam data, almost by a factor two for all the energies. I suspect this difference can be influenced by the lack of implementation of noise, air gaps, and electronic fluctuations, which is present in the testbeam data. However, since the simulated energy loss calculations are nowhere near the measured values on the testbeam data, this could still indicate that other physics processes should be included in the theoretical calculations, or a biasing of the calculations to be too large.

8.2.4 Shower containment

The spatial energy distribution is important to study, to shed light on shower containment in the calorimeter. The purpose of a calorimeter is to measure the energy of particles. When a particle enters the calorimeter, it starts a particle shower, which is then read out by the electronics. If the particle shower is not contained within the size of the calorimeter, it will result in what is called leakage, and the energy of the entering particle can not be reconstructed. This can result in experimental measurements of that particle's energy being orders of magnitude smaller than the real energy of that particle. Lack of shower containment can have an effect on the energy resolution of a calorimeter in two different ways, namely longitudinal leakage and lateral leakage. These two types of leakage have a great importance in regard to hadronic calorimeters.

Longitudinal leakage describes cases where the particle shower is not contained within the longitudinal direction of the calorimeter. Therefore, high-energy particles from particles showers in the calorimeter can exit the active volume of the calorimeter, without depositing all their energy. The risk of longitudinal leakage fluctuates from event-to-event due to the differences in particle showers.

Lateral leakage describes cases where the particle shower is not contained within the sides (height and width) of the calorimeter. At high-energy particle shower the shower-size, i.e. the area of the spread of the shower where particles have deposited energy, has a tendency to increase at higher energies. This means that a calorimeter, which is to be placed in a high-energy environment, needs to cover a large area to contain the development of different types of particles showers. As for the longitudinal leakage, lateral leakage fluctuates from event-to-event due to the differences in particle showers.

The most commonly known constraints leading to longitudinal and lateral leakage, is the physical space where the calorimeter should be placed, and the cost of the materials. Both longitudinal and lateral leakage, contributes to a worse calculated spacial and energy resolution of the calorimeters, since the energy of the particles cannot be reconstructed [29].

This thesis has studied the lateral shower containment in FoCal-H, for the setups including and excluding FoCal-E in front of FoCal-H. The 60 GeV and 350 GeV results of the shower containment study for the two detector setup can be found in the following sections 8.2.4.1 and 8.2.4.2, while the remaining can be found in appendix section 11.4.5.

The shower containment can be studied by looking into the total response for each of the FoCal-H calorimeter modules. First, a global maximum and minimum between the 9 modules is found. The maximum and minimum value is then set to be the same, for all 9 modules in order to compare the deposited energy for an event for each energy. A 3D figure is produced for each of the 9 modules, and put together as one figure in order to represent the FoCal-H second prototype layout. In order to be able to compare the showers for each of the different energies from 60 to 350 GeV, the plots are normalized with

respect to the 60 GeV simulation, in order to get the same scale. If the normalization is not implemented, the shower development cannot be compared across different energies.

The simulations have not yet been digitized. The digitization should be implemented by grouping the scintillating fibers into SiPM readout channels, and implementing such parameters as the estimated photon detection efficiency (PDE) for the SiPM. In order to compare the shower containment in simulations to the testbeam data, the digitization should be implemented, and this is currently being worked on. The lateral shower containment is therefore so far calculated from the energy (light yield) in the individual scintillating fiber.

8.2.4.1 FoCal setup including FoCal-E

The lateral shower containment, or spatial energy distribution, in the 9 FoCal-H calorimeter modules, has been studied for energies from 60 GeV to 350 GeV, using the setup including FoCal-E. As mentioned, the shower size increases at higher energies, meaning that the area where the shower spreads and deposits the energy increases at higher energies. This is clearly visible in figure 67. At the 60 GeV simulation most of the shower is contained within the size of the central calorimeter module. The shower profile seems to be flat in the top and bottom part. I suspect this to be purely analyse related, from the way the figures overlap, to create the FoCal-H second prototype layout. At 350 GeV the shower size has spread to cover half the size of the outer calorimeter modules. This indicates that for the setup including FoCal-E in front of FoCal-H the lateral shower is contained within the lateral size of FoCal-H second prototype.

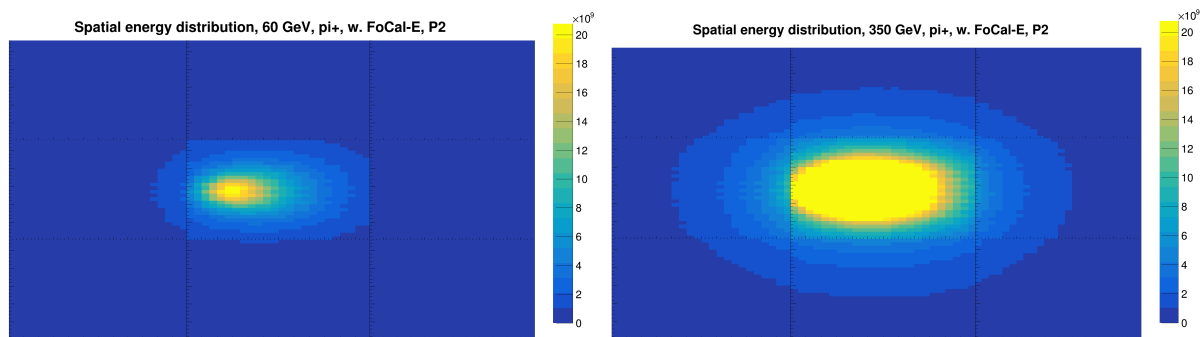


Figure 67: The figure shows the lateral shower size, also called the spatial energy distribution, in the detector setup including FoCal-E in front of FoCal-H. The left-side plot shows the shower size at 60 GeV, and the right-side plot shows it at 350 GeV.

I would suggest to perform a study for the highest energy possible to contain within the lateral direction of FoCal-H including FoCal-E in front of FoCal-H. This study has not been performed due to lack of time.

8.2.4.2 FoCal setup excluding FoCal-E

The lateral shower containment, in the 9 FoCal-H calorimeter modules, has also been studied in regards to a detector setup excluding FoCal-E in front of FoCal-H. This study covers energies from 60 GeV to 350 GeV. Comparing the two spatial energy distribution plots in figure 68 to those in figure 67 with a setup including FoCal-E, one can see that the lateral shower size is smaller for the detector setup excluding

FoCal-E. I assume that the size difference comes from the lack of pre-showers in FoCal-E, which continues into FoCal-H. The pre-shower particles would naturally contribute to a larger shower size since these already have been started showering in FoCal-E. The lack of pre-shower particles, therefore results in a smaller shower size.

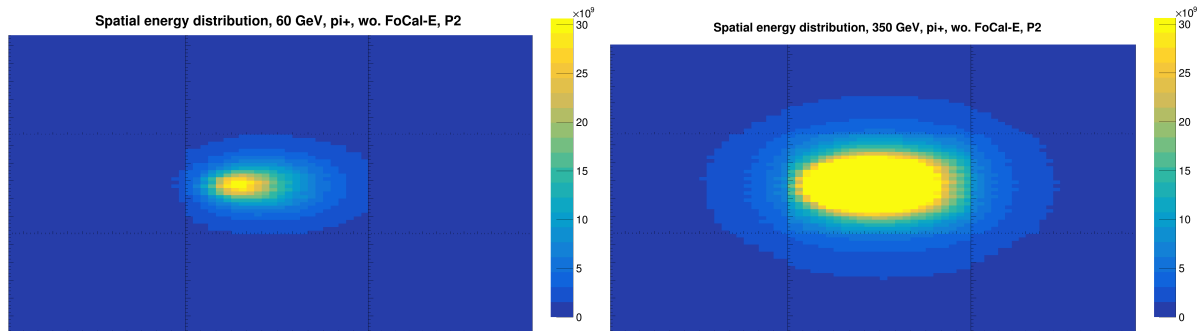


Figure 68: The figure shows the lateral shower size, also called the spatial energy distribution, in the detector setup excluding FoCal-E in front of FoCal-H. The left-side plot shows the shower size at 60 GeV, and the right-side plot shows it at 350 GeV.

I would again suggest to perform a study for the highest energy possible to contain within the lateral direction of FoCal-H excluding FoCal-E in front of FoCal-H. This study has not been performed due to the lack of time. I suspect the detector setup excluding FoCal-E could go a smaller amount of energy above the detector setup including FoCal-E, due to the lack of pre-shower particles. Hence, the shower would be a bit more forward focused.

8.2.5 Position scan

The position scan is performed in order to examine the response of FoCal-H if a particle hits the intersections between the modules. In these intersections, two sides of a 1.5 mm copper-box surrounding the copper-tubes are facing each other, providing a fairly large amount of passive material. This examination is performed using the detector setup including FoCal-E in front of FoCal-H. This setup has been chosen in order to be compared to the position scan taken at the November 2022 SPS H2 testbeam.

This study has been performed in light of a group of first year students' project, where an analysis of the testbeam data position scan was studied. In their study, they found that in the position 2 and 3 shown in figure 69, the energy of the response was significantly smaller, and without the pre-shower peak on one of these positions [43]. These results can be found in section 11.4.6.1.

The particle(s) from the beam used at the testbeam for the position scan can potentially have hit the intersection between the copper-plates. Hence, this simulation study focus on examining the FoCal-H response in these intersections. The particle(s) would in this scenario hit a larger amount of passive material than if it hit the copper-tubes, leading to the particle(s) depositing their energy. Due to the lack of active material in this area of the FoCal-H calorimeter, the response would be lower than usual, and the pre-shower particles would not necessarily be as visible.

The simulation study of the position scan has been performed at 23 different positions, all around the intersections between copper-plates. Two corners have been examined particularly closely since it was not certain whether the simulated and real FoCal-H are rotated in the same direction around the y-axis.

By comparing my simulations with the testbeam data it seems like the simulations are rotated the other way with respect to the beam-pipe.

In addition, the positions from the testbeam position scan was written down in terms of the position of the DESY table, on which the FoCal prototypes was placed. The positions used in the simulations are therefore recreated to the best of my ability.

Figure 69 indicates where on the FoCal-H second prototype the beam-pipe hits the calorimeter for the 23 different positions. The red box in the figure shows the area that FoCal-E covers in front of FoCal-H. As represented in the figure, some of the positions in the study, lie on the edge of the area that FoCal-E covers. I suspect that these areas can lead to unexpected results, or blowups in the FoCal-H response.

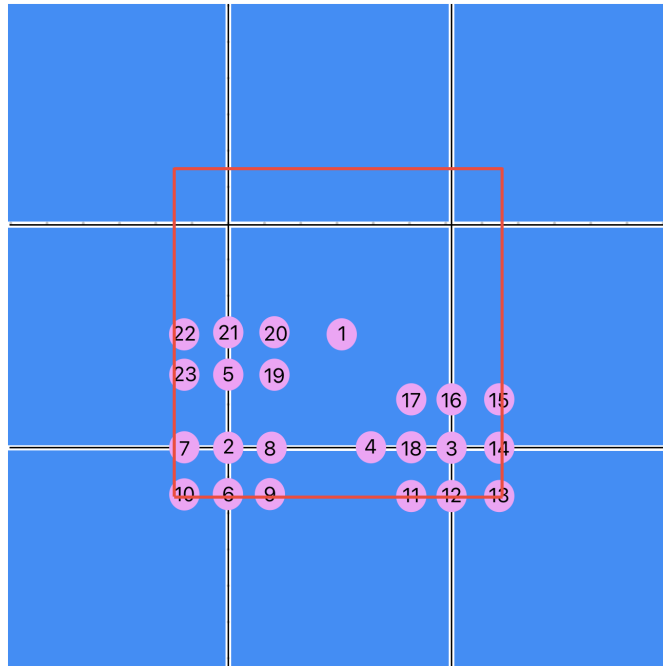


Figure 69: The figure shows a schematic of the FoCal-H 9 calorimeter modules, and where on these modules the beam-pipe has been placed to examine the intersections between the modules. The figure also shows the area (red line) that FoCal-E covers in front of FoCal-H.

The specific offsets of the beam-pipe with respect to origo of the FoCal detector layout can be found in table 3 in appendix section 11.4.6.2. The positions in the intersections have been determined by calculating half the length of one of the calorimeter modules¹⁶. Using an offset in either the x or y direction, positions the simulated beam-pipe in the area of the intersections between the copper-plates. Offset1 does in the simulations correspond to the x-coordinate and offset2 corresponds to the y-coordinate.

Firstly, I examined the same two positions as the first year students did in their project, to see whether the simulations yielded the same results. The spatial energy distributions of the two positions are shown in figure 70. The spatial energy distributions for the two figures indicates the position of the beam-pipe, and thus the beam-spot, on the FoCal-H second prototype. The intensity of the two particle showers is almost similar, with a lower value for the position 3. This can be due to the rotation of the FoCal-H and the hitpoint of the beam particles.

¹⁶The layout of a calorimeter module can be seen in figure 14

The total response in FoCal-H for the position 2 and 3 can be seen in figure 71, where the smaller energy deposit in position 3 is also visible. However, this difference is almost negligible.

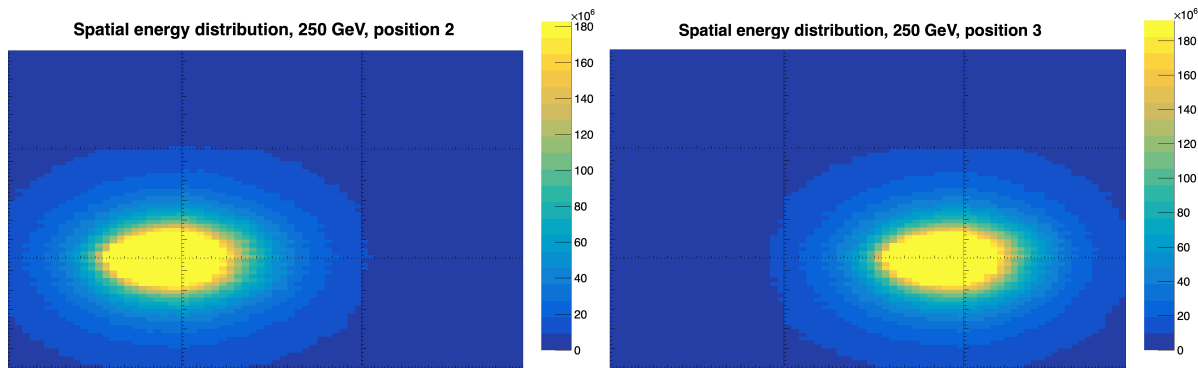


Figure 70: The figure shows the spatial energy distribution of the particle shower for two positions in the position scan. The left-side figure shows the spatial energy distribution for position 2. The right-side figure shows the spatial energy distribution for position 3

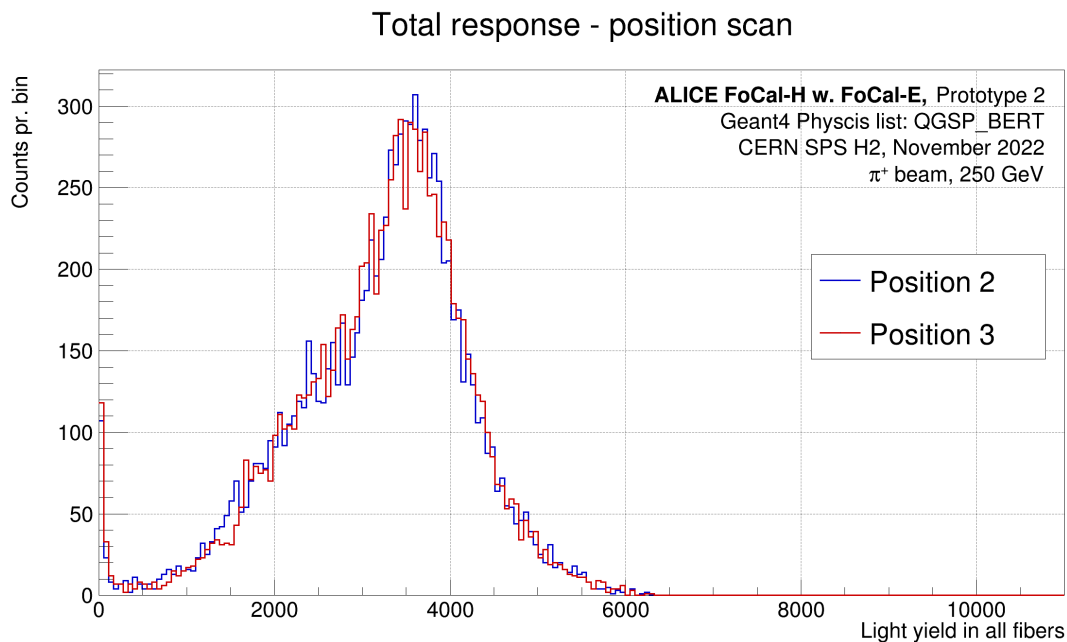


Figure 71: The figure shows two response curves in FoCal-H for two positions examined in the intersections between the FoCal-H calorimeter modules. The blue line shows the response for position 2, and the red line shows the response for position 3.

Both positions were tested in case the rotation of the simulated and real FoCal-H second prototype was not implemented in the same direction. However, none of the two positions show indication of the pre-shower peak being removed. Nevertheless, the pre-shower peak does seem to have decreased a bit at position 3, and have for this reason been studied further. The study is performed for the positions surrounding position 3, in case the simulated beam-pipe and the testbeam beam-pipe have not been position at the exact same position, as I think it seems like. The two vertical positions lying in the intersection on either side of position 3 can be seen in figure 72. Position 14 lies on the edge of the area

covered by FoCal-E.

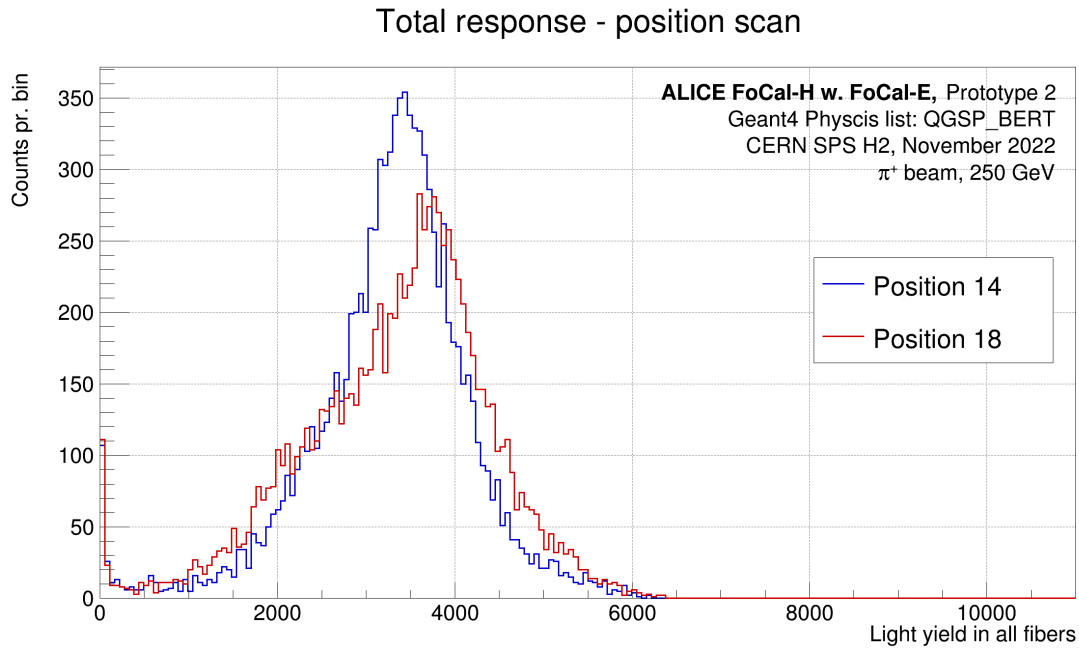


Figure 72: The figure shows two response curves for the vertical position lying in the intersection on either side of position 3. The blue line shows the response for position 14, and the red line shows the response for position 18.

The two horizontal positions lying in the intersection in relation to position 3 can be seen in figure 73. In this case, position 12 lies on the edge of the area covered by FoCal-E.

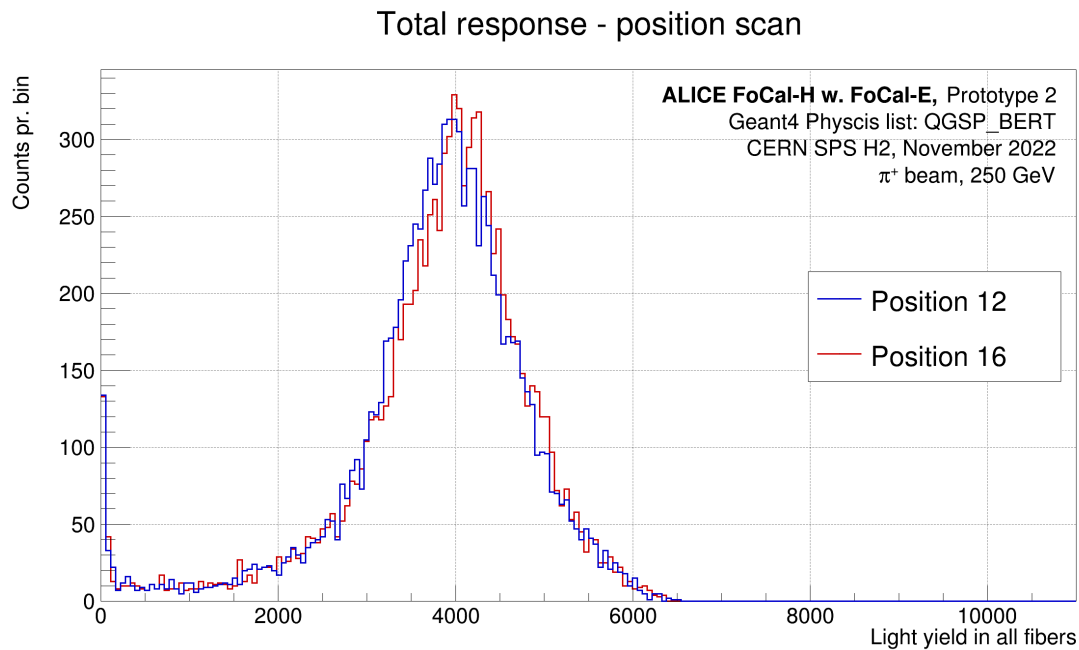


Figure 73: The figure shows two response curves for the horizontal position lying in the intersection on either side of position 3. The blue line shows the response for position 12, and the red line shows the response for position 16.

The positions 16 and 18 lie inside the coverage of FoCal-E, and should for this reason contain the pre-shower peak as shown in previous studies using the detector setup including FoCal-E. However, for position 16 the pre-shower peak is not clearly visible in the response, and could indicate that the response in the intersection is changed. For the case of position 12 and 14, these positions lies right on the edge of the FoCal-E coverage, and I would therefore assume that the response of these positions could have been different, regarding the pre-shower peaks. This seem to be the case, since these position do not include the pre-shower peak either.

These preliminary results of the position scan indicate that the pre-shower peak indeed gets reduced in the intersections of the FoCal-H calorimeter modules. I assume that the beam-pipe position in the simulations is not positioned in the complete same spot as in the testbeam position scan. This assumption is built upon the compatibility of the results produced in the surrounding positions to position 3.

In addition, the mean energy of the peak has decreased with respect to position 1 at origo (0,0) for the FoCal detectors, as can be seen in figure 74. The assumption that the particles deposits a larger fraction of their energy in these intersection seems plausible. An comparison between position 1 and 3 can be seen in figure 74.

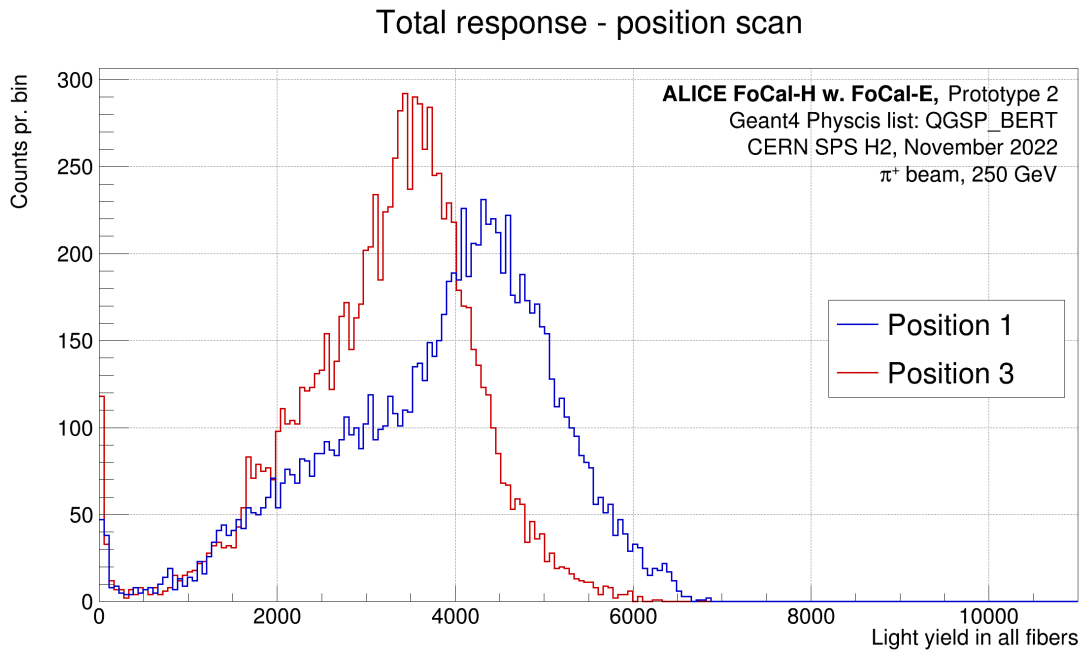


Figure 74: The figure shows two response curves for the position scan. The blue line shows the response for position 1, which is the normal position at the center of FoCal-H. The red line shows the response for position 3.

The simulated position scan produces results compatible with the ones from the position scan of the testbeam. Thus, I would say that the hypothesis regarding the particle(s) hitting large amount of passive material in these intersection areas, leading to the particle(s) depositing their energy, without it being transferred to the active material, is likely to be true and to have a significant influence on the response in FoCal-H.

I would for a future design of the FoCal-H detector recommend to increase the size of the calorimeter modules. Larger modules would result in fewer intersections of copper-plates that the particles could

interact with. One could possibly also choose another material than copper, with a smaller interaction length for the box around the copper-tubes. However, when choosing this material one would need to bare in mind that the metal needs to be non-magnetic due to the placement of FoCal-H right beside the compensator magnet.

The remaining spatial energy distributions and response curves for the positions studied in this scan, can be found in appendix section 11.4.6 .

8.3 Comparison between testbeam data and simulation data

This section will go through various studies performed to compare the testbeam data and the simulation data, using the November 2022 SPS H2 testbeam setup. The comparison studies are performed with the intention to verify and/or point out areas which need to be investigated in the future.

8.3.1 Energy calibration

The first step in comparing the testbeam data to the simulation data is to make sure the data gets a common axis. The testbeam data has an x-axis given in "Energy [ADC]", which stands for Analogue to digital converter and is a translation value the CAEN DT5202 readout board uses to give a value for a signal based on its energy. However, the simulation data has an x-axis given in "Light yield in all fiber", which is the arbitrary energy value based on the signal which comes from all the scintillating fibers in the FoCal-H prototype simulations in Geant4. The FoCal-H simulations have not yet been grouped into bundles corresponding to the fiber bundles for each SiPM. This digitization would give a better comparison to the testbeam results.

In order to find the common axis one needs to find a common factor between the testbeam data and the simulation data. In this case, we know the beam energy for both the testbeam data and the pion simulated data is the same.

The first step was to find an appropriate fit for the hadron peak. Due to the structure of the hadron peak with the tail, a crystal ball function fit was chosen. The crystal ball function fit is a combination of a gaussian core and a power-law tail and is commonly used in high-energy physics calculation. However, a gaussian function fit was also tested but showed to be worse¹⁷. All lower and upper boundaries of the crystal ball function fits have been set manually, and can for this reason have some bias. This was done due to the punch through peak at around 6 GeV, which should not contribute to the calibration of the total response measurements.

¹⁷See appendix figure 107 for a comparison between gaussian function fit and crystal ball function fit.

Total Charge - Beam Data without FoCal-E

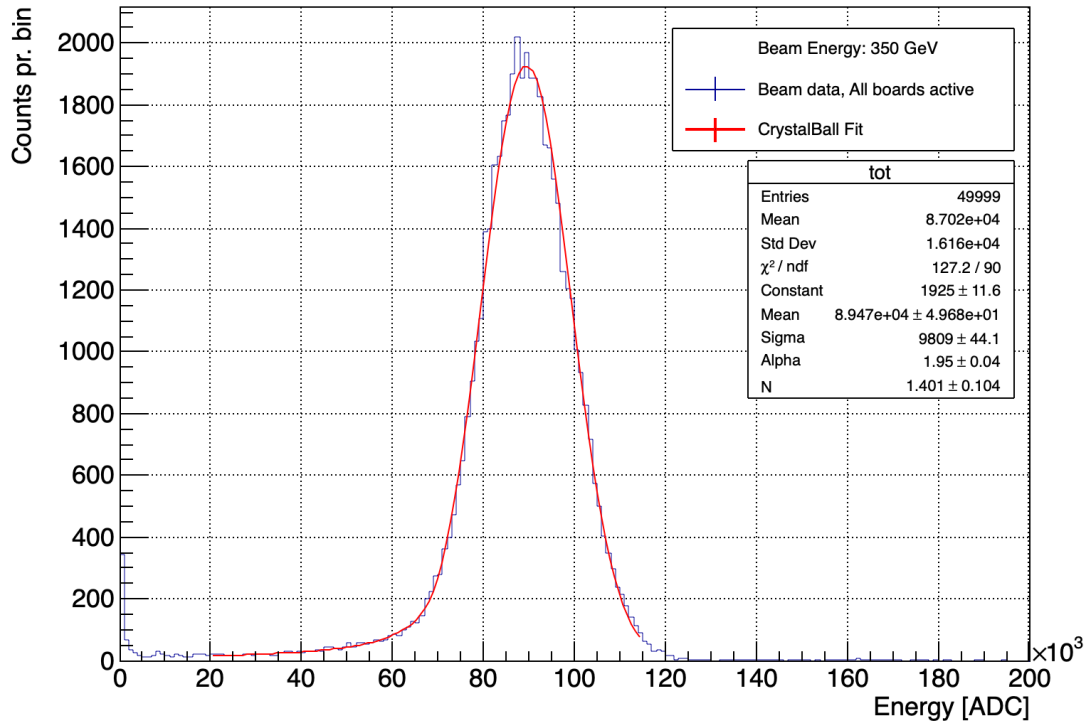


Figure 75: The plot shows the total response for the testbeam data at 350 GeV, where all readout boards were active. The total response is plotted as counts pr. bin as a function of Energy[ADC]. The plot also shows the fitted crystal ball function fit.

The blue curve describes the total response of a 350 GeV hadron beam without FoCal-E in front, and the red line is the crystal ball function fit, in a specific range. After fitting a crystal ball function fit to all the energies, one can determine the mean of the fit. The value of the mean of the fit can then be plotted as a function of the beam energy. The mean of the crystal ball function fit is calculated from the respective energy output for the simulation("Light yield in all fibers") and the testbeam data (Energy[ADC]). A straight line is then fitted to the points, in order to calculate the measured energy with respect to the beam energy.

$$E_{\text{response}} = a \cdot E_{\text{beam}} + b \rightarrow E_{\text{beam}} = \frac{E_{\text{response}} + b}{a}$$

E_{response} is in this case "Energy[ADC]" for the data and "Light yield in all fibers" for the simulations.

The mean of the crystal ball function fit, for both the beam data and the pion simulation data, could then be plotted as a function of the beam energy. The two calibration curves can be seen below in figure 76.

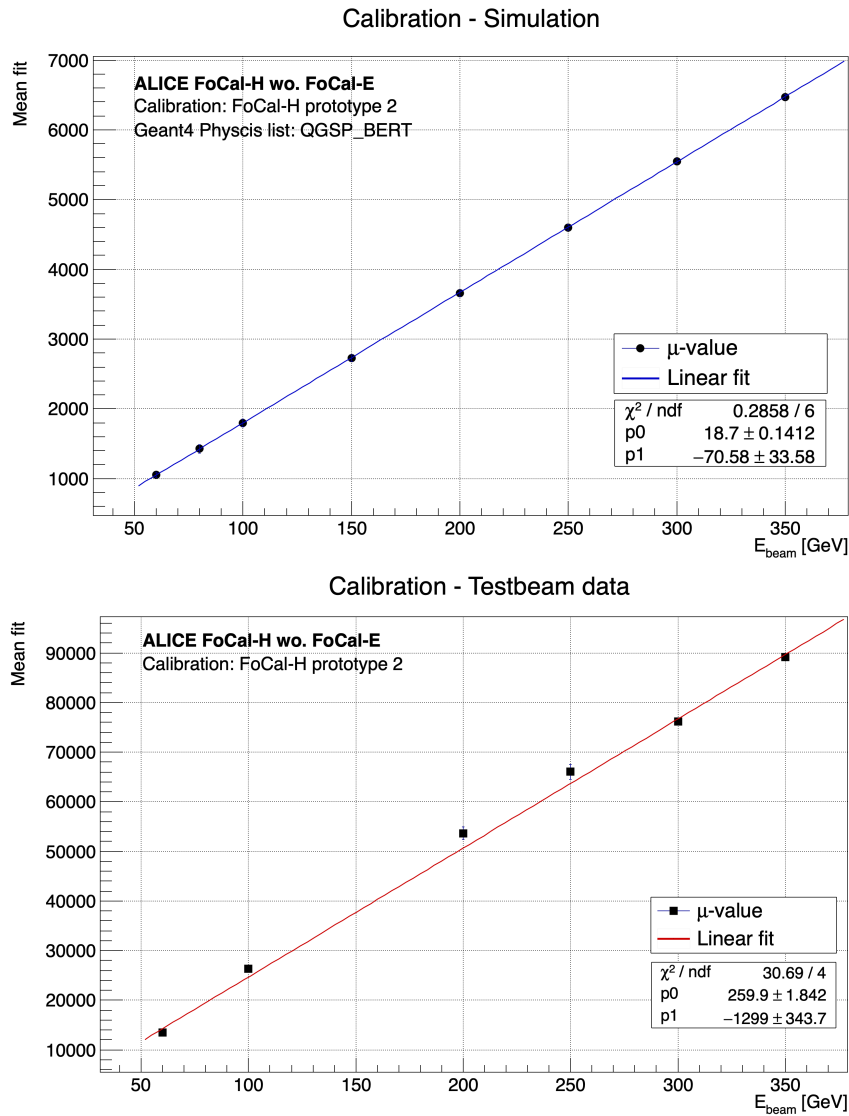


Figure 76: The figure shows the calibration fit for the testbeam data and the simulations. The top plot shows the calculated mean values of the crystal ball function fit for all pion simulated energies as a function of the beam energy. The plot also shows a linear fit through the points. The bottom plots shows the corresponding calculations and linear fit for all testbeam data energies. The plots have beam energy on the x-axis and the mean of the crystal ball function fit on the y-axis

The linear fit to the simulated pion data has a χ^2 -value of 0.2, indicating that the linear fit is too good. A χ^2 -value should in general be 1, for the linear to be a good representation of the data. However, a good χ^2 -value is expected for the simulated pion data, since simulations should be theoretically better than the testbeam data since it is tuned on theoretical models. In contrast to the pion simulation, the testbeam data does not have a good χ^2 -value. The χ^2 -value of 30.69 for the testbeam data indicates that the linear fit is not a good representation of the data points.

Examining the total response of the testbeam data and the simulated pion data, one could get an idea of why this difference occurs between the testbeam data and the simulations. As is clear from the two plots in figure 77, showing the total response for the pion simulations and testbeam data for the energies of 200 GeV and 350 GeV, the hadron peak for the testbeam data is higher than for the simulations. The

reason for this could for instance be beam-related noise, which is detected and therefore contributes to the total response in the testbeam data. However, the physics contribution in the Geant4 QGSP-BERT physics list can also be the reason for this difference.

The testbeam data has in this case been cut down to 100.000 events to match the statistic of the simulations. The two curves for the total response have also been plotted using the same binning. This can therefore not have an effect on the curves for the responses. The remaining comparison of the testbeam data and QGSP-BERT simulation data at different energies can be seen in appendix section 11.5.2.1.

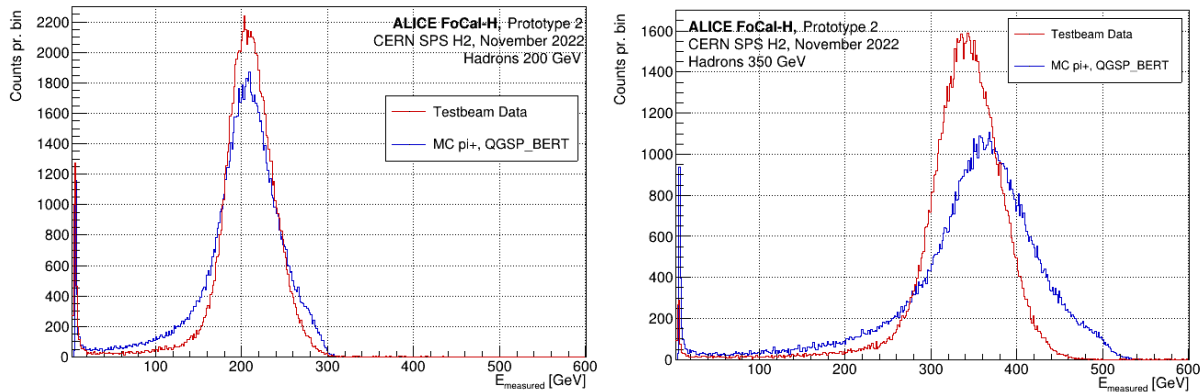


Figure 77: The left-side plot shows the total response in FoCal-H at 200 GeV for the testbeam data (red) and the QGSP-BERT simulations (blue). The right-side plot shows the total charge in FoCal-H at 350 GeV for the testbeam data (red) and the QGSP-BERT simulations (blue).

As already mentioned, the testbeam data has a significantly higher hadron peak for both the 200 GeV and 350 GeV. Besides this difference, the peak also differs in relation to how broad the hadron peak is compared to the testbeam data. This difference could be related to beam noise in the detector setup, or other noise contributions in the testbeam hall. However, this can also be related to the physics contributions in the Geant4 QGSP-BERT physics list.¹⁸

The peak differences between the simulations and the testbeam data can also be influenced by the physics processes produced in the particle showers. Processes as e.g. π^0 production is one of the processes which fluctuates from event-to-event in pion induced showers. These fluctuations contributes to a broader peak and an asymmetric peak [29, p.150].

Although it was decided to use the Geant4 QGSP-BERT physics list, I have compared the total response in FoCal-H for the testbeam data with the Geant4 FTFP-BERT physics list, to see this relation. The hadron peak for the FTFP-BERT physics list does to some extent show a better agreement to the hadron peak for the testbeam data. This could indicate that the answer to why the hadron peaks look different lies within the physics processes. A comparison of the remaining testbeam data responses to the simulations using the FTFP-BERT physics list can be found in appendix section 11.5.2.2.

¹⁸See section 8.2.3.3 to get a detailed description of the physics contribution in the QGSP-BERT physics list.

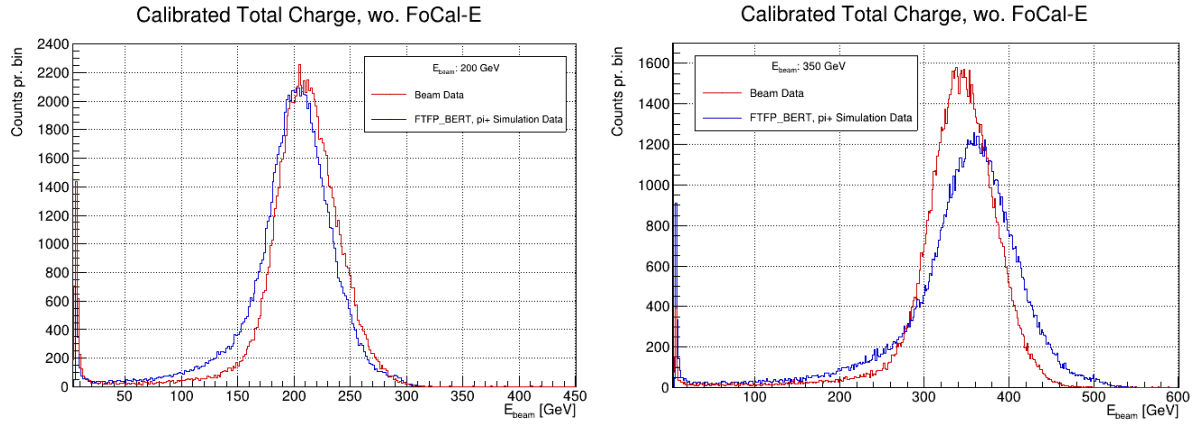


Figure 78: The left-side plot shows the total response in FoCal-H at 200 GeV for the testbeam data (red) and the FTFP-BERT simulations (blue). The right-side plot shows the total response in FoCal-H at 350 GeV for the testbeam data (red) and the FTFP-BERT simulations (blue).

8.3.2 Energy resolution

The energy resolution of a sampling calorimeter determines how precisely the calorimeter can measure the energy of the particle. As mentioned, a calorimeter is a detector that measures the deposited energy of particles that interact with the detector-E setup. Thus, the energy resolution is an important tool to estimate the efficiency of the calorimeter.

The energy resolution is determined by the following equation:

$$\frac{\sigma}{E} = \sqrt{\left(\frac{a}{\sqrt{E}}\right)^2 + \left(\frac{b}{E}\right)^2 + c^2} \quad (2)$$

The right-hand side of the equation has three contributing terms, where two depends on the energy of the incident particle in the calorimeter. The first term is called the stochastic term, and is related to the particle processes, i.e. the particle shower development. This term needs to be included to account for fluctuations in the development of the showers from event-to-event. However, these fluctuations can also have a contribution in regards to the shower development through the active and passive materials in the calorimeter. The stochastic term, and the fluctuations which it depends on, contributes to limitations in the energy resolution for sampling calorimeters. The second term is called the noise term, and is related to electronic noise in the calorimeter setup. The noise term increases the energy resolution as the energy of the incident particle decreases. The noise term is almost negligible for scintillating sampling calorimeters, due to the small levels of noise when using a photosensitive device, e.g. a SiPM, as the first step in the electronic system. The contribution of the noise term, is easy to decrease in sampling calorimeters. To decrease the noise term, the sampling fraction should be increased by having a larger amount of active material (see equation 1). Increasing the sampling fraction leads to a larger signal from the active medium and thereby a higher signal-to-noise ratio. The third term is called the constant term, and is related to non-uniformities in the response of the calorimeter. Some of these non-uniformities can be related to construction of the passive and active materials (e.g. air gaps or deformities of the materials), temperature fluctuations, radiation damage, and damage of the readout system. The constant term is not related to the energy of the incident particle, and can if noticed be fixed by changing the e.g. damaged components [28].

To calculate the energy resolution of the FoCal-H second prototype setup excluding FoCal-E in front of FoCal-H, the calibrated total response of the testbeam data and pion simulation data was used. Using the earlier calculations, as seen in figure 75, a crystal ball function fit was used to extract the mean, mean error, standard deviation, and standard deviation error. The lower and upper boundaries of the crystal ball function fit are again defined manually. Extracting these values makes it possible to calculate the energy resolution of the calorimeter by using $\frac{\sigma}{E} \approx \frac{\sigma}{\mu}$. It is assumed that the energy of the incident particle is roughly the mean value of the response.

The energy resolution has been calculated using the testbeam data, and both the QGSP-BERT and FTFP-BERT physics lists. These calculations can be seen in figure 79.

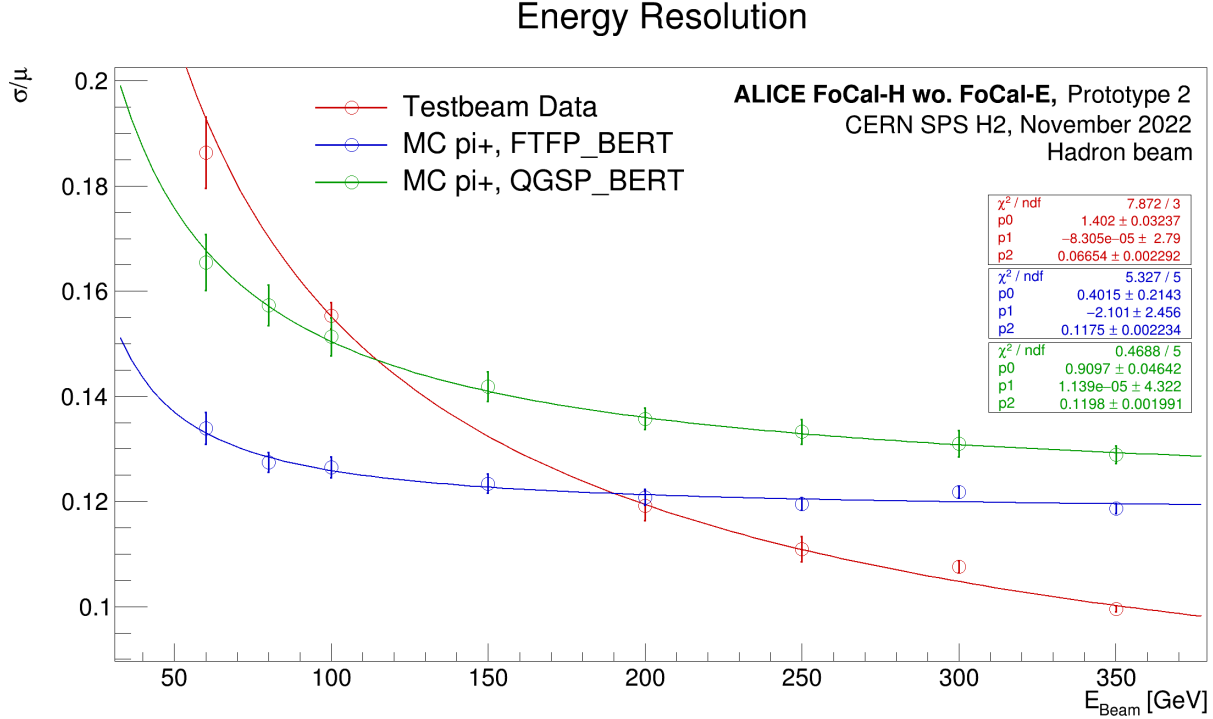


Figure 79: The figure shows the calculated energy resolutions for the testbeam data (red), simulations using the QGSP-BERT physics list (green), and the simulations using the FTFP-BERT physics list (blue).

The error propagation calculated for these resolution curves consist of a contribution for the statistical error and the estimated error of the mean value.

$$Error = \sqrt{\left(\frac{1}{\mu}\right) \cdot \sigma_{error}^2 + \left(\frac{\sigma}{\mu^2}\right)^2 \cdot \left(\frac{\mu_{error}^{estimated} \cdot \mu_{error}}{100}\right)^2} \quad (3)$$

The values μ , σ , μ_{error} , and σ_{error} are drawn from the crystal ball function fits, for each energy. The estimated errors were needed, since the errors derived from the statistical errors were underestimated, making it impossible to determine if the fit of the energy resolution was suitable. The estimated error is determined by extracting the mean from the crystal ball function fit, from the fit-range used to get the statistical error. From an interval of 0.5σ , on either side of this mean, from a range of 0.5σ to 5σ a crystal ball function fit was applied. From the fit for each interval the mean was again extracted. It was determined that the estimated mean should be the mean from 5σ with the mean from 0.5σ subtracted. The examination of the estimated error of the mean value is performed by someone else in the collaboration [42].

The calculations of the energy resolutions for the testbeam data and the simulations using different physics lists are not compatible with each other, as would have been expected. The calculations of the energy resolution lead to many questions, and in that connection multiple studies, to figure out why they look like they do.

The first question is regarding the flat slope at higher energies of the energy resolution for the simulations using the FTFP-BERT physics list. The energy resolution of the simulations using the FTFP-BERT physics list deviates from the theoretical expectations of a hadronic calorimeter, where the incident particle is a hadron. This deviation was the first reason for the test of other physics lists recommended for high-energy calorimeter physics (QGSP-BERT). The simulations using the QGSP-BERT physics list look as theoretically expected. However, the simulated energy resolution is worse than the one calculated for the testbeam data. Having a good energy resolution is preferable, but an energy resolution which is better than the simulated energy resolution brings the results into question. The present theory regarding the result of the energy resolution for the testbeam data, is that it is artificially better due to saturation. This theory will be described in further detail in section 8.3.2.1.

Other elements which were tested to figure out why the energy resolutions look like they do were: binning of the response curves, physics sub-lists, fit function, fit range, and correct calibration. However, non of these had any meaningful effect on the calculations for the energy calibration, regarding both the testbeam data and the simulations.

The results of the energy resolution have only been calculated using the detector setup excluding FoCal-E in front of FoCal-H. The first reason for this is the inability to remove the pre-shower peak from the simulations, so a compatible energy calibration between the testbeam data and the simulations can be performed. To calculate the energy calibration, a MIP study in FoCal-E would be needed. The second reason is the low statistics of the testbeam data (50.000 event out of 1 mio. events) after removing a fraction of the pre-shower. However, a preliminary energy resolution of the testbeam data could be calculated, using the common trigger runs, where some fraction of the pre-shower can be removed. Thus, one should still find a solution to why the energy resolution of the testbeam data is better than in the simulations.

8.3.2.1 Saturation

Saturation is an effect of the intrinsic limitations, e.g. small dynamic range, of the readout that generates the signal. Saturation is an issue which has been noticed in the testbeam data. It is so far unknown whether it is the SiPMs that saturate or the CAEN DT5202. However, this is one of the elements, which is going to be examined in the upcoming testbeam in May 2023, by using the newly discovered TOT readout in the CAEN DT5202.

Examining the total response for the simulations and the testbeam data, show indications of saturation in multiple ways. Examining the 60 GeV total charge for the simulations and the testbeam data (see top plot in figure 80), one can see that the testbeam data has a tail in the response. At an energy of 60 GeV, this tail could either be a part of the particle shower, or it could be an effect of saturated channels. At the 60 GeV run excluding FoCal-E in front of FoCal-H, around 1-3 channels in the central module saturated. The simulation at 60 GeV also indicates that a saturation limit is reached. This is indicated by the steep curve in the high-energy part of the peak. The same indication of saturation can be seen in the simulation at 300 GeV (see bottom plot in figure 80). Why the simulations show indications of saturation,

without being digitized is currently unknown. I suspect the saturation stems from the implementation of the scintillating fibers, and the implementation of number of photons pr. MeV. Saturation in the simulations is currently being examined, by grouping the scintillating fibers into bundles representing the channels in the FoCal-H second prototype. Summing up the energy (light yield) for the scintillating fibers in each bundle, one gets the threshold for each channel, which can be adjusted whereby saturation can be lowered, or removed. The testbeam data at 300 GeV show clear indication of saturation at the high energy side of the peak. At 300 GeV excluding FoCal-E in front of FoCal-H, around 1-10 channels saturate in the central calorimeter module.

Another noticeable difference between the simulations and the testbeam data, is that the simulations seem to overestimate the energy loss in the low-energy part of the peak. I assume this difference could come from the physics processes in the physics list.

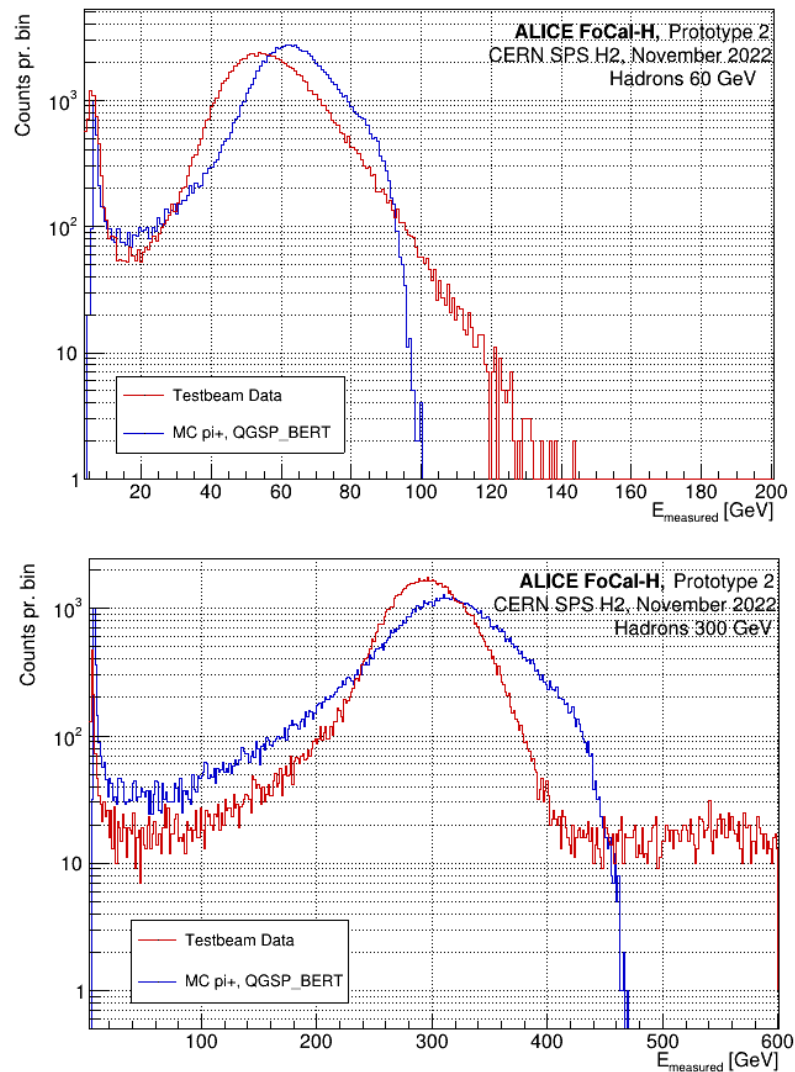


Figure 80: The figure shows the saturation of the response curves for testbeam data and simulations. The top plot shows the response curve at 60 GeV for the testbeam data (red) and simulations (blue) in a logarithmic scale. The bottom plot shows the response curve at 300 GeV for the testbeam data (red) and simulations (blue) in a logarithmic scale.

From the point where the readout reaches the saturation limit, it would produce the same signal for any other events, until the readout can reset. Saturation can have an effect on e.g. the energy resolution of the calorimeter. Saturated channels in the testbeam data would result in an improvement of the energy resolution. The improvement of the energy resolution is a consequence of the saturated channels not being able to detect a signal lower than the saturated level. For such cases the energy resolution would be determined by event-to-event fluctuations, thus suppressing certain sources of fluctuations. Saturation also leads to non-linearity of the calorimeter response, and would lead to the response not being proportional to the energy of the incident particle [29, p.80-81]. This exact consequence is to some extent visible on the calibration of the testbeam data seen in the bottom plot in figure 76.

The effect of the saturation on the energy resolution for the testbeam data, has been examined by someone else in the collaboration [42]. The examination of the saturation has been studied by gradually lowering the maximum value (saturation limit in ADC) for each channel. Changing this value, one can examine the effect of the energy resolution for each beam energy. This preliminary investigation has so far showed that lowering the maximum value, the energy resolution for the testbeam data gets remarkable close to the one for the simulations using the QGSP-BERT physics list. For some energies it even gets worse than the simulated energy resolution. This study is still being examined in great detail.

8.3.3 Punch through peak

The punch through peak is one of the peaks present in both testbeam data and in simulated data. This section revolves around the study of the punch through peak, and the investigation of what it might be caused by.

I suspect that the punch through peak can be caused by two different scenarios. The first scenario is particles from the beam-pipe that travels along a copper-tube or scintillating fiber, without depositing their energy and starting a particle shower. The other scenario could be that the punch through peak is muons. High-energy muons need a relatively large stopping power in order to decay. This is e.g. why an entire side of ALICE is dedicated to the study of muons¹⁹. For the November SPS H2 testbeam a hadronic beam was chosen, which consisted of pions. However, the beam had some minor fraction of other particles, i.e. the beam did not have a 100% beam-purity.

The comparison of the punch through peak between testbeam data and simulations, has been performed on both the QGSP-BERT and FTFP-BERT physics list. The comparison between testbeam data and the FTFP-BERT simulations can be found in appendix section 11.5.4.2. To investigate the punch through peak, one needs to look in the range of importance. For this reason, I have focused my attention to the region of 0 GeV to 25 GeV. The comparison of the punch through peak of the testbeam data and the simulation is remarkable on different aspects. The first noticeable point is the mean energy of the two peaks. The testbeam data peak has a mean energy at around 7 GeV, whereas the simulations have a mean energy around 6 GeV.

The second noticeable point is the overlap in the peaks. From the simulations we know that the beam is a 100% pure π^+ beam. However, this is not the case for the testbeam beam. This overlap could e.g. indicate that some fraction of pions in the testbeam beam punch through peak had decayed into muon in the calorimeter. The question is then, what the other fraction of punch through particles could be. In relation to this, why does the response of the punch through peak change at different energies.

¹⁹See section 2.2.3 for a description of the muon spectrometer

Firstly, I will consider the changing response of the punch through peak for the testbeam data. The response of the peak decreases with higher energies. My assumption regarding this trend is that it is related to a constant flux of particles coming down the beam-pipe. Due to the changing rate of particles at each energy, we experienced that at the lowest energy (60 GeV) the runs took longer time to collect the desired amount of data, compared to at the highest energy. The changing rate together with a constant flux of particles would explain the difference in the response at each energy. A smaller change in the simulation punch through peak is also seen, but the difference from energy to energy is not that profound. The fact that the simulation peak is changing in size, can be due to the QGSP-BERT physics list only accounting for hadron-nucleus interaction from 12 GeV and up. The FTFP-BERT simulations punch through peak, is more or less constant in position and size. I suspect that this can be due to the hadron-nucleus interaction having a cutoff from 3 GeV to 26 GeV, which cuts off any higher energy fluctuations processes.

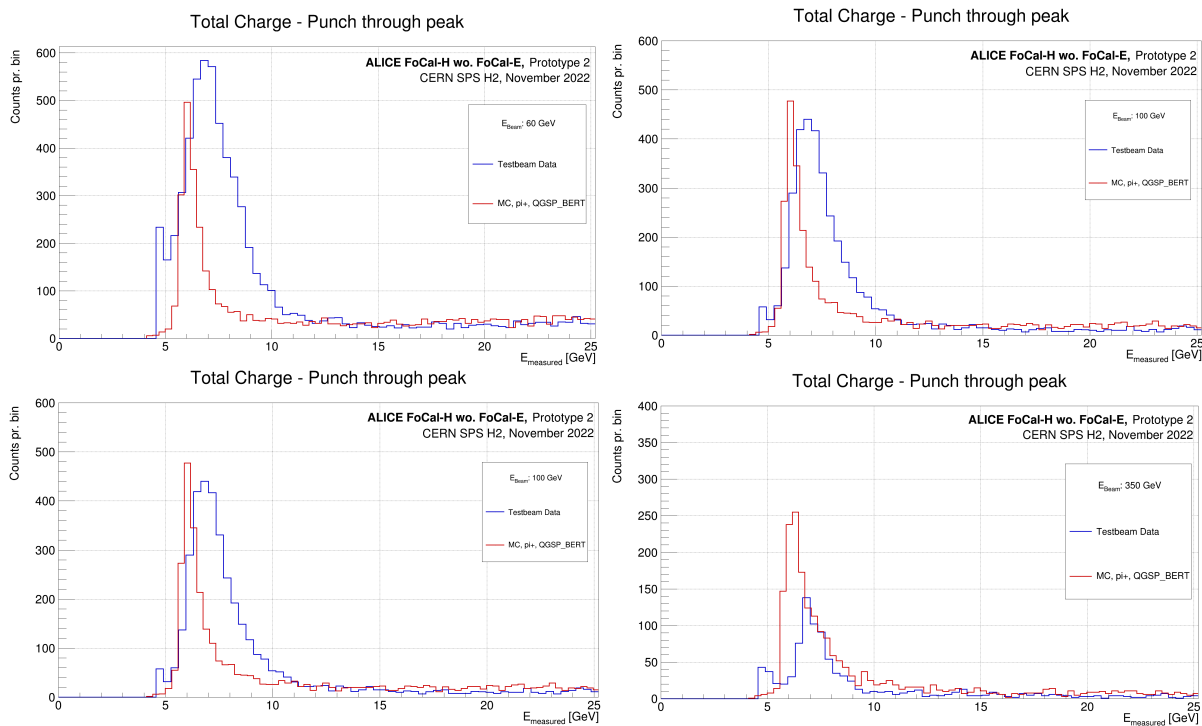


Figure 81: The figure shows a punch through peak comparison between the testbeam data and the π^+ simulations at four different energies. The top left-side plot shows the comparison at 60 GeV, and the top right-side plot shows the comparison at 100 GeV. The bottom left-side plot shows the comparison at 200 GeV, and the bottom right-side plot shows the comparison at 350 GeV.

Then I will consider the mentioned overlap between the punch through peak in the testbeam data and the simulations. The overlap indicates that some fraction of the punch through peak potentially could be pions decaying into muons. However, the remaining fraction needs to be examined. Could it e.g. be related to a constant flux of muons in the beam-pipe. To examine whether a fraction of the punch through peak could be related to muons going through the FoCal-H calorimeter modules, muon simulations were done in order to compare that contribution to the testbeam data and the simulations. These comparisons have been done by normalizing with respect to the hadron peaks and plotting the contribution of the muon simulations at various energies corresponding to the ones of the testbeam data and

the pion simulations. This needed to be done, since the muon simulations only contains 10.000 events. The muon comparison at different energies can be seen in figure 82.

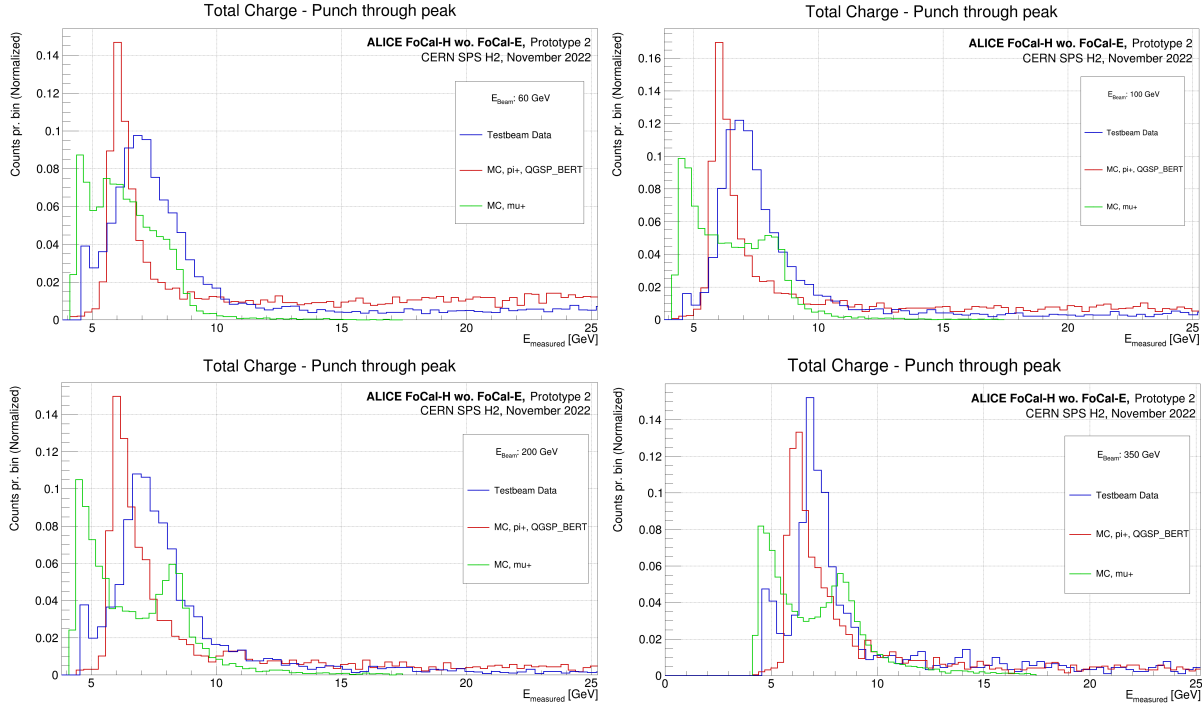


Figure 82: The figure shows a punch through peak comparison between the testbeam data and the π^+ simulations and μ simulations at four different energies. The top left-side plot shows the comparison at 60 GeV, and the top right-side plot shows the comparison at 100 GeV. The bottom left-side plot shows the comparison at 200 GeV, and the bottom right-side plot shows the comparison at 350 GeV.

This examination of whether muons could be part of the response indicates that this is indeed the case. There is a clear overlap in the response of punch through peak for the testbeam data and the muon simulations. The assumption that there is a constant flux of muons in the beam-pipe, which are punching through the FoCal-H second prototype, seems plausible.

8.3.3.1 Rotation of FoCal-H

At the September 2022 SPS H6 testbeam it was chosen to rotate the FoCal-H by 2.085 degrees with respect to the beam-pipe. This rotation was chosen to avoid too large a fraction of punch though particles in FoCal-H. To indicate how much of a difference the rotation makes, a simulation with and without the implementation of the rotation of FoCal-H was performed. This was done for 250 GeV π^+ beam as seen in 83:

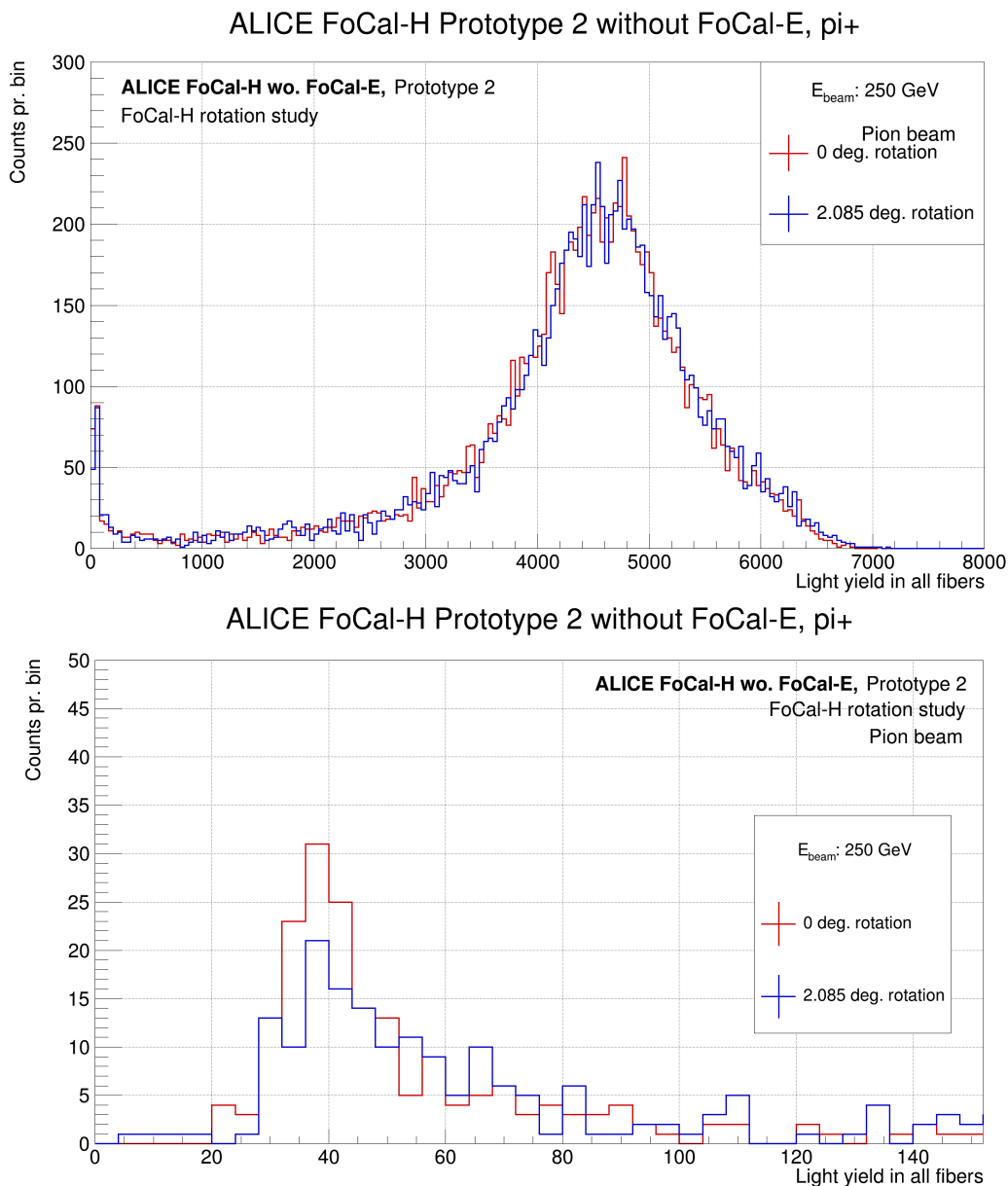


Figure 83: The figure shows a simulation using a 250 GeV pion beam with two different rotations of FoCal-H. The red line represents a rotation of 0 degrees, and the blue line represents a rotation of 2.085 degrees. The top figure shows the full range where both the punch through peak and the hadron peak is visible. The bottom plot shows only the range of the punch through peak. The bottom plot is in the range of the punch through peak.

The rotation of the FoCal-H second prototype does not have a large effect on the hadron peak, or the punch through peak in the pion simulations. The small change in the punch through peak could indicate that some fraction of punch through particles are avoided by implementing the rotation of FoCal-H. I would suggest to perform this study with more than 10.000 events to increase the statistic, to give a final indication of the result. The investigation of the effect of the rotation has also been performed for simulations of 250 GeV muons, as seen in figure 84. This study shows that the rotation of FoCal-H has a significance in terms of the muon fraction of the punch through peak for the testbeam data.

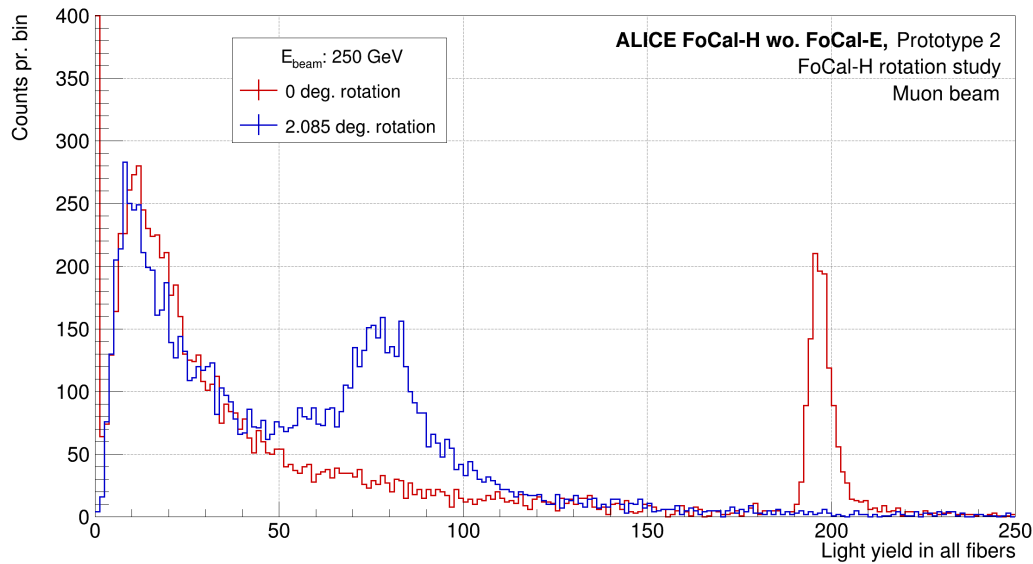


Figure 84: The figure shows a simulation using a 250 GeV muon beam with two different rotations of FoCal-H. The red line represents a rotation of 0 degrees, and the blue line represents a rotation of 2.085 degrees.

The muon simulations with and without the rotation look fairly different. As seen from the simulations with the rotation implemented, the muon response in the calorimeter has two peaks. I suspect the first of these peaks to be muons that interact slightly with the copper-tubes and the scintillating fibers, whereas the second peak represents interactions with a larger fraction of copper-tubes and fibers. However, when considering the muon simulations without the rotation, three peaks are present. I suspect the first (~ 0 light yield in all fibers) of these peaks to be caused by a muon only depositing its energy in the copper-tubes. The simulations would count the muon to be produced but not to contribute to the signal, thus placing the contribution in the zero bin. The second peak (~ 20 light yields in all fibers) is, as for the rotated case, caused by an interaction with a small fraction of the copper-tubes and scintillating fibers. Whereas the third peak (~ 200 light yield in all fibers) is due to the muon traveling along a scintillating fiber.

A visualization of the particle shower with and without the rotation of FoCal-H can be seen in figure 85.

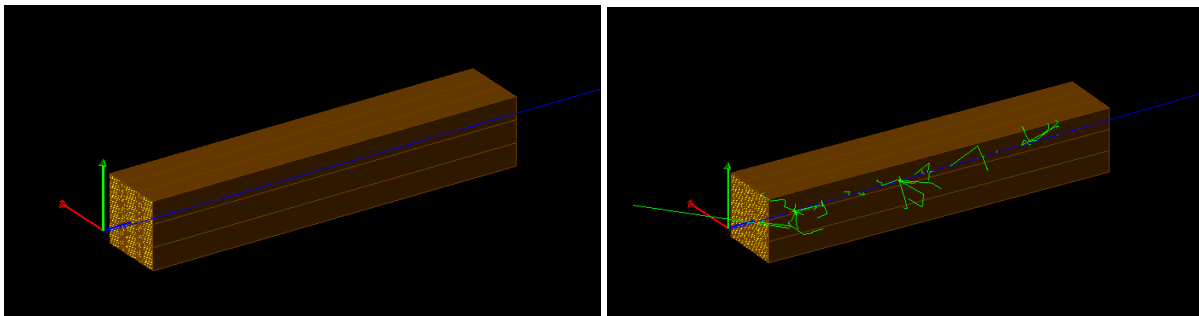


Figure 85: The figure shows a simulation using a 60 GeV muon beam with two different rotations of FoCal-H. The left-side figure shows that there are no shower tracks without the rotation (0 degrees). The right-side figure shows the shower tracks with the rotation (2.085 degrees). The green line indicates places where showers have started.

I would recommend to perform an examination of the muon peaks with a rotation of FoCal-H from e.g. 0 degrees to 5 degrees, to investigate the effect of the rotation on the punch through peak in further detail. This study has not been performed in regards to this thesis due to time limitations. A study of the effect of the hadron peak for rotation from 0 degrees to 5 degrees can be found in appendix section 11.5.5. This study shows that the energy of the hadron peak decreases with larger rotations of FoCal-H with respect to the beam-pipe.

A further examination of the FoCal-H response in simulations with and without a rotation of FoCal-H has been studied for energies from 60 GeV to 350 GeV using a muon beam. This study have been performed to determined whether the punch through mouns have an energy dependence. The result of the study without the rotation can be seen in the left-side figure in figure 86. Whereas the right-side figure shows the corresponding results with the 2.085 degrees rotation.

The response in FoCal-H without the rotation implementation (left-side plot in figure 86) seems more or less consistent across different energies. However, it seems like there is a small decrease in the second peak, representing the interaction with a small fraction of the copper-tubes and scintillating fibers, with increasing energy. Whereas the opposite is the case for third peak, representing the interaction with only scintillating fibers. A possible explanation to this result, could be that it is due to the difference in the time it takes to run the simulations.

The response in FoCal-H with the rotation implementation (right-side plot in figure 86) seems to follow the same trend of having a decreasing response with increasing energy for the peak representing the small fraction of interaction with the copper-tubes and scintillating fibers. A larger difference across the energies are present in the second peak, describing the larger fraction of interaction with the copper-tubes and scintillating fibers. The lower energy simulations, especially 60 GeV and 80 GeV, have a larger contribution to the response representing the the interaction with the copper-tubes and scintillating fibers. I suspect this to be shower related, but a further study could be performed in order to investigate these areas at low energy. However, this was not prioritized in regards to this thesis.

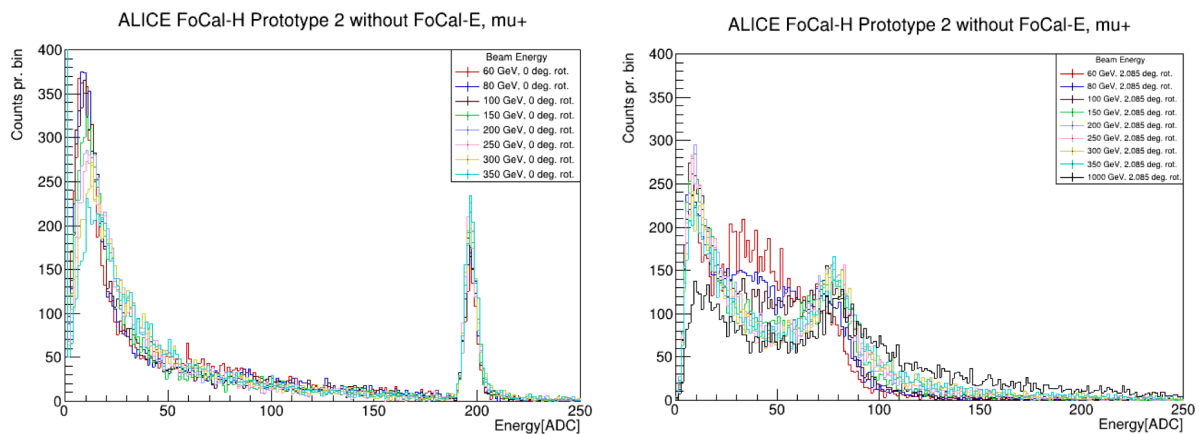


Figure 86: The left-side figure shows a plot for simulations using muon beam without the rotation of FoCal-H, in the energy range from 60 GeV to 350 GeV. The right-side figure shows the corresponding study with the rotation of FoCal-H, for energies from 60 GeV to 350 GeV.

9 FoCal-H third prototype

The FoCal-H third prototype has not been constructed, but is studied in regards to this thesis. In order to test whether it will be useful to change the layout of the FoCal-H second prototype, one can use simulations. This section will describe the potential layout of the FoCal-H third prototype, where the inner diameter of the copper-tubes has been decreased from 1.12 mm to 0.8 mm, leading to the diameter of the scintillating fibers going from 1.0 mm to 0.7 mm. This changes the ratio between the active and passive material in FoCal-H.

This section will go through some of the studies performed on simulations of the FoCal-H third prototype, to test the technical performance up against the second prototype.

9.1 FoCal detector setup

The first thing to study is the FoCal detector setup including and excluding FoCal-E in front of FoCal-H. This should be examined in order to see if the same tendency with the response contributions would be present. The same energies were simulated with a π^+ hadron beam and the QGSP-BERT physics list, as was done for the second prototype in order for them to be compared.

The simulations including and excluding FoCal-E in front of FoCal-H can be seen in 87 and 88 respectively.

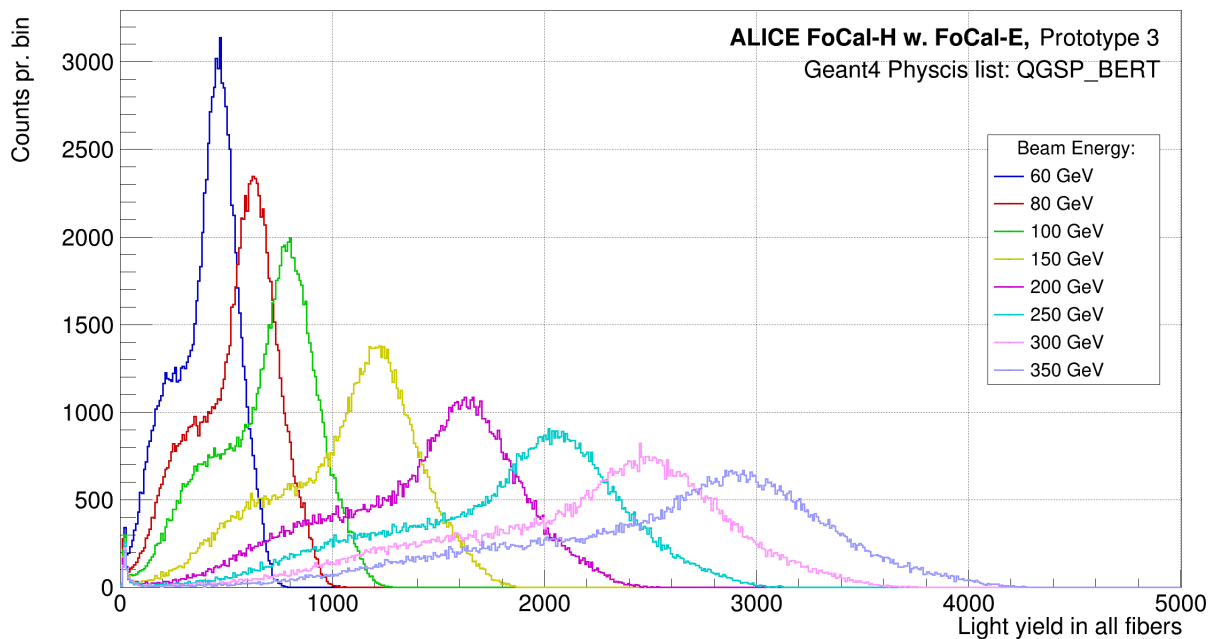


Figure 87: The figure shows a plot of the total response measured in FoCal-H third prototype in simulations including FoCal-E using the QGSP-BERT physics list. The simulations are made for energies from 60 GeV to 350 GeV.

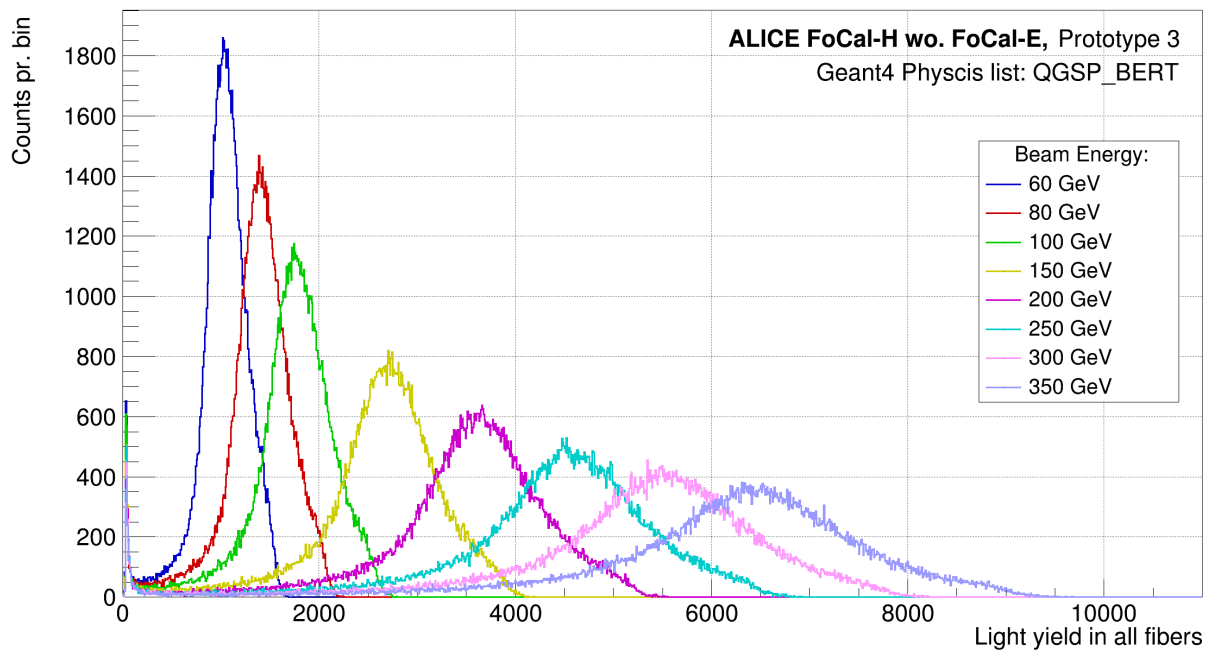


Figure 88: The figure shows a plot of the total response measured in FoCal-H third prototype in simulations excluding FoCal-E using the QGSP-BERT physics list. The simulations are made for energies from 60 GeV to 350 GeV.

Both simulations of the detector setup show the same tendencies as for the second prototype. The detector setup including FoCal-E in front of FoCal-H has three distinguished peaks contributing to the response. The first peak is the punch through peak, the second is the pre-shower peak, and the third peak is the hadron peak. These three peaks can be seen in figure 87. The detector setup excluding FoCal-E has two distinguished peaks contribution to the response. The first is the punch through peak, the second is the hadron peak. These two peaks can be seen in figure 88

Even though the response in the FoCal-H third prototype follows the same tendencies as the second prototype, some differences are still present. The response for all energies is almost half the energy compared to the second prototype. However, this is expected since the ratio between the active and passive material has been changed drastically. Changing this ratio means that there are less active material, i.e. scintillating fibers, to contribute to the response. This could potentially be a solution to reducing the response in the FoCal-H second prototype, seen in regards to saturation.

A comparison of the total response in FoCal-H, between the second and third prototype at a beam energy of 250 GeV has been made for the detector setup excluding and including FoCal-E in front of FoCal-H. These comparisons can be seen in figure 89.

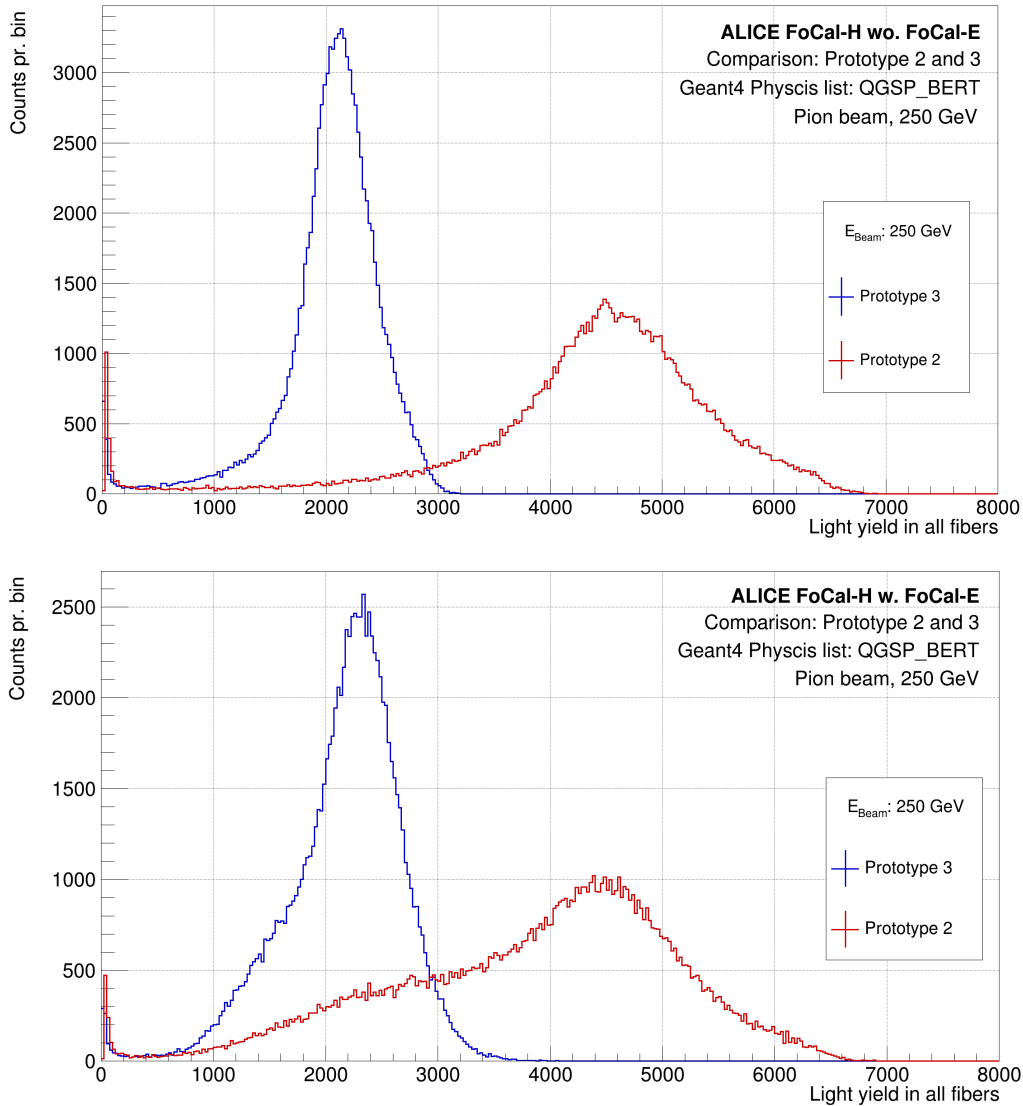


Figure 89: The top figure shows the comparison of the total response between the second and third prototype at 250 GeV, excluding FoCal-E in front of FoCal-H. The bottom figure shows the comparison of the total response between the second and third prototype at 250 GeV, including FoCal-E in front of FoCal-H.

9.2 Energy resolution

Energy resolution is one of the things that needs to be studied in order to examine how substantial the effect of the change in ratio between active and passive material is. The study have been performed for the detector setup excluding FoCal-E in front of FoCal-H. As was the case for the FoCal-H second prototype, a calculation of the energy resolution including FoCal-E in front of FoCal-H would require a dedicated MIP study in the FoCal-E response, in order to remove the pre-shower peak. This study has not been performed in regards to this thesis, but is currently investigated by someone else in the collaboration.

To compute the energy resolution of the FoCal-H third prototype, the same procedure is followed as

when performing the computations for the FoCal-H second prototype. First computing the energy calibration, in order for it to be compared to the energy resolution of the testbeam data, and the second prototype. Then computing the energy resolution, to estimate how precisely the FoCal-H third prototype can measure the energy of the particles. A detail description of the calculations of the energy resolution for the FoCal-H second prototype can be found in section 8.3.1.

The calculations of the energy calibration was performed by applying a crystal ball function fit to each of the response curves. The mean value (μ), mean error, standard deviation (σ), and error of the standard deviation was extracted, and a straight line fitted through the points. A comparison of the energy calibration between the simulations for the FoCal-H second and third prototype can be seen in figure 90.

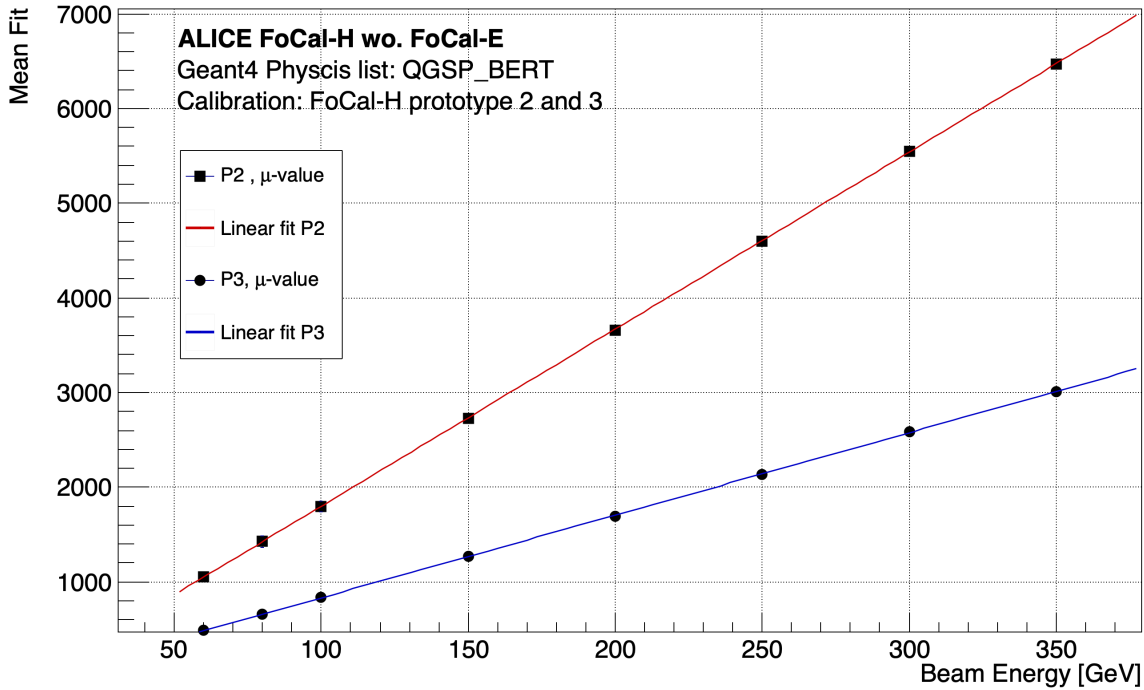


Figure 90: The figure shows the calibration curves for the FoCal-H second and third prototype. The calibration curves are determined by the μ -values of the crystal ball function fit for all pion simulated energies as a function of beam energy, where a linear fit is fitted through the points. The calibration for the FoCal-H second prototype is represented by the square data-points and red linear fit. Whereas the calibration for the third prototype is represented by the round data-points and the blue linear fit.

To calculate the energy resolution a crystal ball function is again fitted to the response for each energy, where the mean of the fit and standard deviation can be extracted to calculate the energy resolution. As for the FoCal-H second prototype, it is assumed that the energy of the incident particle is roughly the mean value of the response, $\frac{\sigma}{E} \approx \frac{\sigma}{\mu}$. To perform the calculations, equation 2 is again applied, together with equation 3 for the error propagation. The result of the energy resolution for the FoCal-H third prototype, together with the corresponding calculations for the testbeam data and the second prototype, can be seen in figure 91.

Energy Resolution

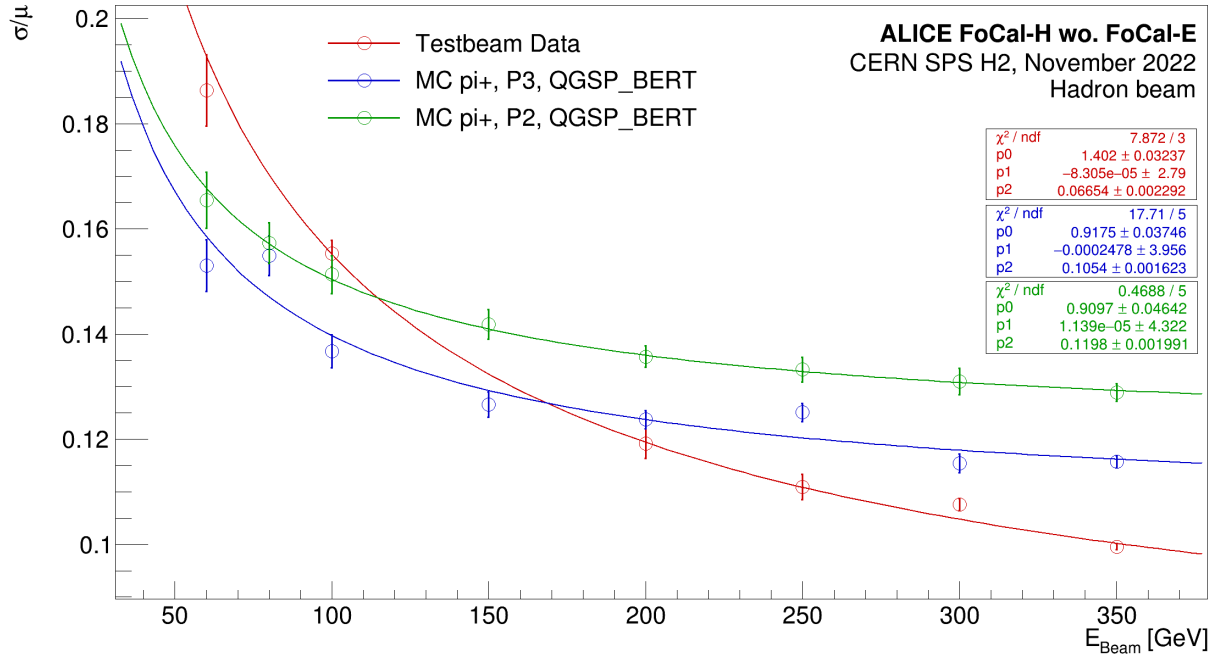


Figure 91: The figure shows the calculated energy resolutions for the testbeam data (red), simulations using the QGSP-BERT physics list (green) for the second prototype, and the simulations using the QGSP-BERT physics list (blue) for the third prototype.

As can be seen in figure 91, the calculated energy resolution is a few percentage better for the FoCal-H third prototype than for the second prototype. The energy resolution for the FoCal-H third prototype was initially computed with the expectation that it would be worse, than for the second prototype. This unexpected result initiated further questions in relation to the energy resolution. One of them being whether the ratio between active and passive material for the second prototype is optimal. To investigate this question one can e.g. look into compensation, which will be described in the next section.

9.2.1 Compensation

As mentioned in section 4.3, the particle showers in a hadronic calorimeter consist of a electromagnetic part and a non-electromagnetic part. Therefore, hadronic calorimeters need to be able to measure both contributing responses equally. The ability to measure these responses equally is called compensation. The response of the electromagnetic and non-electromagnetic contributions are usually not equally measured due to the effect of invisible energy. The response of the two contribution signals can therefore be studied individually. The distribution of the response pr. unit deposited energy around the mean value, called the response function, for the electromagnetic response is defined as e , whereas the non-electromagnetic part is defined as h .

Theoretically in hadronic calorimeters, e would have a larger response than h , but h should have a broader response due to event-to-event fluctuations in the response's fraction of invisible energy. Hadronic calorimeters that archive compensation of the loss of the invisible energy is defined as compensated calorimeters. The efficiency of a hadronic calorimeter in terms of compensating for this loss is character-

ized from the ratio $\frac{e}{h}$. In a well compensated calorimeter the ratio should be $\frac{e}{h} = 1$, in order to have an optimal determination of the energy of the incident particles. In non-compensated calorimeter the ratio would be $\frac{e}{h} \neq 1$ [29, p.143-146]. The biggest consequence of not having a compensated calorimeter, is the effect on the energy resolution of the hadronic calorimeter. For this exact reason, I started to question the compensation of the FoCal-H second and third prototype, since it turns out that the $\frac{e}{h}$ ratio can be modified by changing the ratio between the active and passive material [28, p. 33-36].

The compensation of the FoCal-H second and third prototype has been computed by simulating an electron beam and a pion beam onto the prototype setups for 10.000 events. The ratio between e and h is determined by taking the response function, i.e. the mean of the signal, and differentiating these values. The $\frac{e}{h}$ ratio was firstly computed for the FoCal-H third prototype at energies from 100 GeV to 750 GeV, to stay within the same energy range as for previous studies, but also to investigate the response at even higher energies. The computed ratio for 100 GeV and 350 GeV can be found in figure 92, whereas his remaining calculations can be seen in appendix section 11.6.1.2.

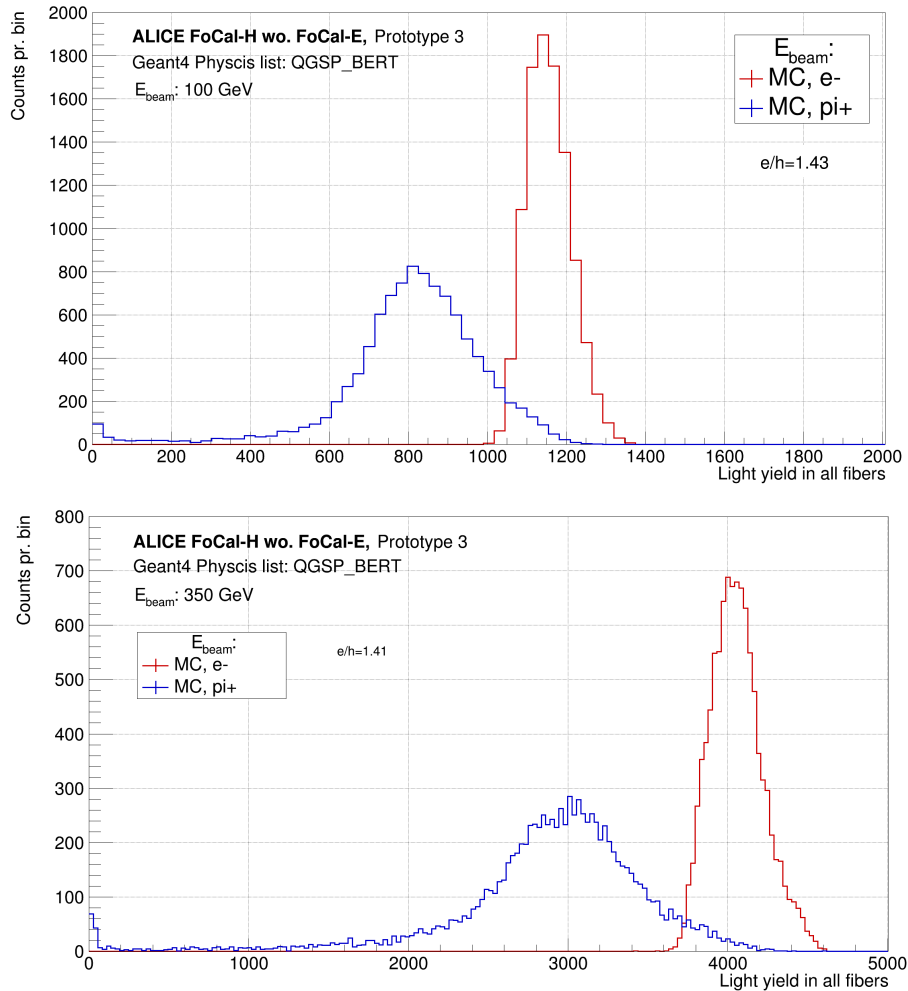


Figure 92: The figure shows the FoCal-H third prototype response for an electron (red) and pion (blue) simulation. The left-side plot shows these simulations at 100 GeV, while the right-side plot show them for 350 GeV. The calculated $\frac{e}{h}$ ratio is shown on each plot.

The FoCal-H third prototype computations of the $\frac{e}{h}$ ratio at 100 GeV and 350 GeV reveal that $\frac{e}{h} = 1.4$,

which means that the ratio is $\frac{e}{h} \neq 1$. Due to the improved calculations of the energy resolution for the third prototype, I would have assumed that the $\frac{e}{h}$ ratio would be closer to 1. This computed value for the $\frac{e}{h}$ ratio show to be consistent up to 750 GeV for the FoCal-H third prototype.

The same calculations was then performed on the FoCal-H second prototype setup, in order to examine if the $\frac{e}{h}$ ratio could be worse than for the third prototype. If so, this could be a possible explanation. The computed ratio for 100 GeV and 350 GeV can be found in figure 93, whereas the remaining calculations can be seen in appendix section 11.6.1.1.

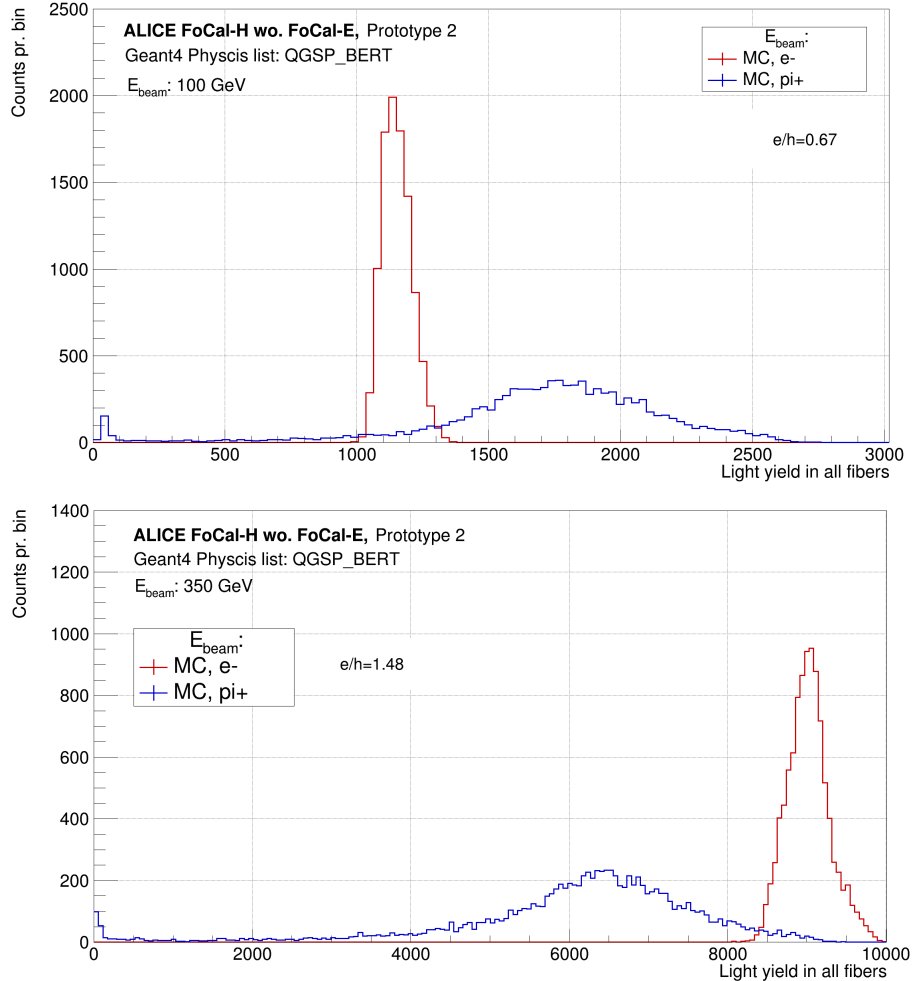


Figure 93: The figure shows the FoCal-H second prototype response for a electron (red) and pion (blue) simulation. The left-side plot shows these simulations at 100 GeV, while the right-side plot shows them for 350 GeV. The calculated $\frac{e}{h}$ ratio is shown on each plot.

The FoCal-H second prototype computations of the $\frac{e}{h}$ ratio at 100 GeV has a value at $\frac{e}{h} = 0.6$, while the ratio at 350 GeV has a a value at $\frac{e}{h} = 1.4$. Both ratios have a $\frac{e}{h} \neq 1$, with around the same factor on either side of $\frac{e}{h} = 1$. This rather prominent shift of the electron peak therefore raised the question about whether the $\frac{e}{h}$ is energy dependent. The answer to this, is that the electromagnetic part has an energy dependence, and this has important consequences for the hadronic energy resolution. The average fraction

of the total shower energy in the electromagnetic part is defined as [29, p. 144]:

$$\langle f_{em} \rangle = 1 - \left[\left(\frac{E}{E_0} \right)^{k-1} \right] \quad (4)$$

where E_0 is a material dependent constant related to the average multiplicity in hadronic interactions, around 0.7 GeV for copper, E is the energy of the initial particle, and $k \sim 0.82$ [29, p. 144].

This exact energy dependence of $\langle f_{em} \rangle$, in the case where $\frac{e}{h} \neq 1$ leads to the response function of the hadronic calorimeter to be non-linear, since the response of hadrons is determined by [29, p. 145]:

$$\langle f_{em} \rangle + [1 - \langle f_{em} \rangle] \cdot \frac{h}{e} \quad (5)$$

Leading to a hadronic energy response, which is also energy dependent. A noticeable similarity is present at 100 GeV for both the FoCal-H second and third prototype. The response peak for the electron simulation looks remarkable similar, and has been examined for potential mistakes when setting up the simulation. However, this is not the case. I would recommend a further study of the compensation for the two prototype setups, at low energies around 60 GeV to 150 GeV, potentially simulating more than 10.000 event to gather more statistics.

The results of the compensation calculations were what lead to several electron and pion simulations at energies from 100 GeV to 750 GeV to be simulated, for both the FoCal-H second and third prototype. This was done to determine the linearity of the response function, since a compensating calorimeter should have a linear response function. The calculations performed for the FoCal-H third prototype can be found in figure 94.

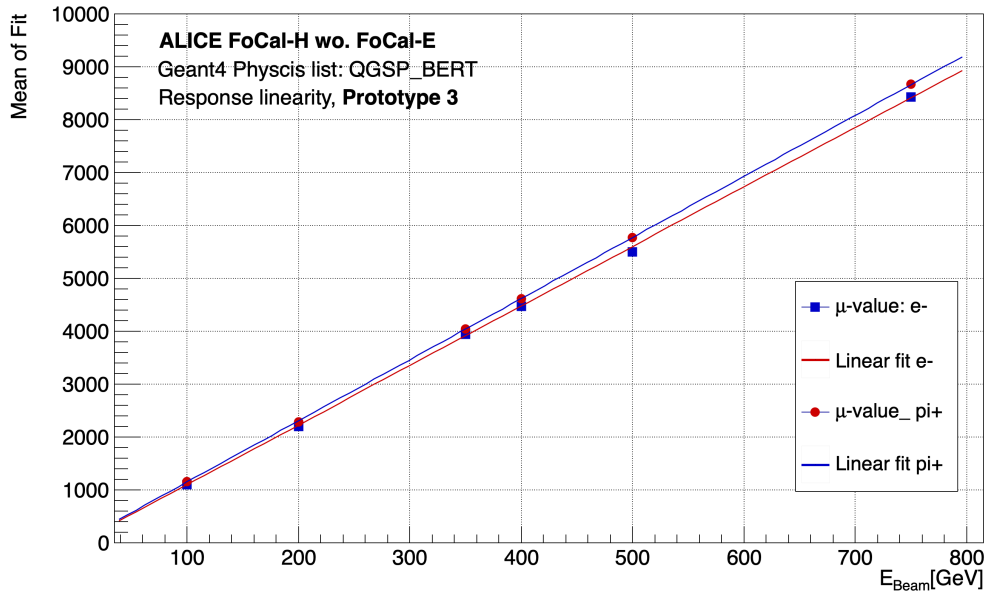


Figure 94: The figure shows the linearity of the response function of the FoCal-H third prototype. The linearity of the response function are measured for an electron induced shower (red) and a pion induced shower (blue).

The computed linearity of the response function for both the electron and pion induced particle shower, for the FoCal-H third prototype, indicates that the setup is compensated across all energies. This compensation of the detector setup is stable for the examined energy range, even though the $\frac{e}{h} = 1.4$. I

suspect this to be due to the consistent value of the $\frac{e}{h}$ ratio across all energies. The linearity has been tested up to an energy of 750 GeV, but it can possibly get non-linear for higher energies.

The linearity of the response function has also been calculated for the FoCal-H second prototype, and can be found in figure 95.

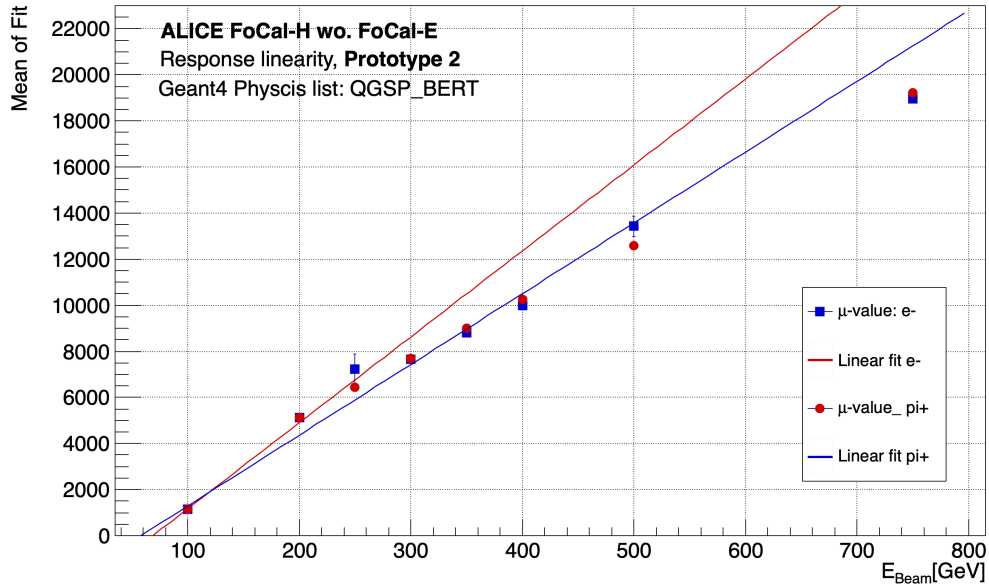


Figure 95: The figure shows the linearity of the response function of the FoCal-H second prototype. The linearity of the response function are measured for an electron induced shower (red) and a pion induced shower (blue)

The linearity of the response function for the FoCal-H second prototype, show tendencies of non-linearity. The non-linearity of the response function indicates that the FoCal-H second prototype is not compensating efficiently across all energies. I suspect this inefficiency to be due to a combination of the ratio between the active to passive material, and the energy dependence of the hadronic and electromagnetic responses, leading to the changing $\frac{e}{h}$ ratio across different energies. The results of the response linearity for the FoCal-H third prototype indicate that this non-linearity seen for the second prototype to some extent is suppressed in the energy range examined in this thesis.

I would for any future prototype or the final design of FoCal-H recommend to modify the ratio between the active and passive material, i.e. also the $\frac{e}{h}$ ratio, to fit into the expected energy range in ALICE, so that the compensations in FoCal-H is optimal.

9.2.2 Shower containment

Lateral shower containment is one of the properties, which has been examined for the FoCal-H third prototype. This is examined by examining the total response for each of the FoCal-H calorimeter modules. A global maximum and minimum between the 9 modules are first found. The maximum and minimum value is set to be the same, for all 9 modules in order to compare the deposited energy for an event for each energy. In order to be able to compare the showers for each of the different energies from 60 to 350 GeV, the plots are normalized with respect to the 60 GeV simulation, in order to get the same scale, as done for the FoCal-H second prototype.

The shower containment study has been performed for the detector setup including and excluding FoCal-E in front of FoCal-H, from energies at 60 GeV to 350 GeV. The 60 GeV and 350 GeV results can be seen in figure 96 for the setup including FoCal-E, while remaining energies for this study can be found in appendix section 11.6.2.1.

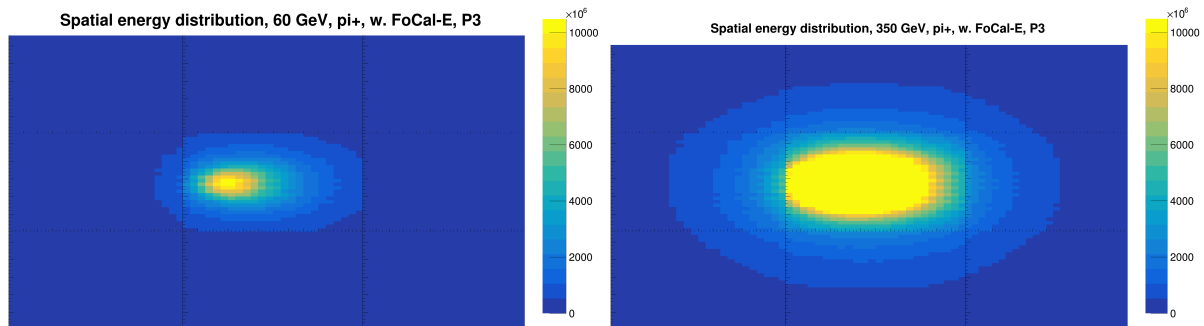


Figure 96: The figure shows the lateral shower size, also called the spatial energy distribution, of the detector setup including FoCal-E in front of FoCal-H third prototype. The left-side plot shows the shower size at 60 GeV, and the right-side plot shows it at 350 GeV.

By examining the lateral shower containment of the FoCal-H third prototype, in the detector setup including FoCal-E, the same tendencies as seen for the FoCal-H second prototype appear. The shower size increases at higher energies, meaning that the area in which the shower spreads and deposits the energy increases at higher energies. At the 60 GeV simulation most of the shower is contained within the size of the central calorimeter module. The shower profile seems to be flat in the top and bottom part. As for the second prototype, I suspect this to be purely analyse related, from the way the figures overlap, to create the layout of the FoCal-H third prototype. At 350 GeV the shower size has spread to cover half the size of the outer calorimeter modules. This indicates that for the setup including FoCal-E in front of FoCal-H the lateral shower is contained within the lateral size of FoCal-H third prototype, not resulting in lateral leakage.

A similar result is seen when examining the lateral shower containment of the FoCal-H third prototype, in the detector setup excluding FoCal-E. The results of the shower containment at 60 GeV and 350 GeV can be seen in figure 97, while the remaining energies can be found in appendix section 11.6.2.2.

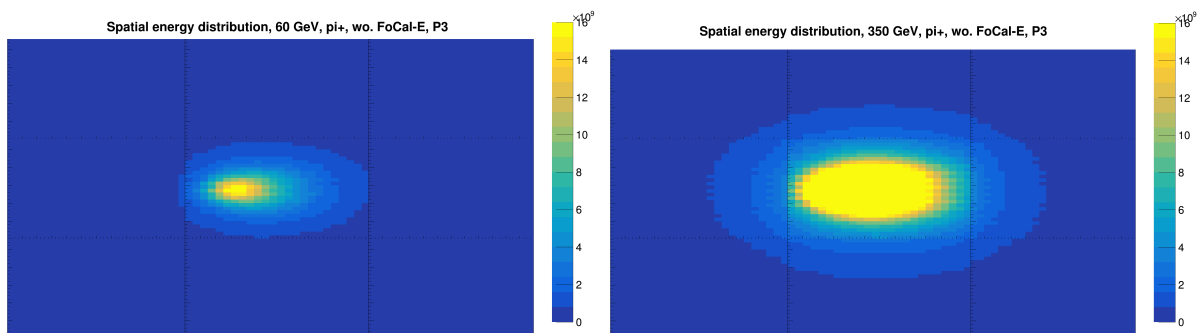


Figure 97: The figure shows the lateral shower size, also called the spatial energy distribution, of the detector setup excluding FoCal-E in front of FoCal-H third prototype. The left-side plot shows the shower size at 60 GeV, and the right-side plot shows it at 350 GeV..

A comparison between the spatial energy distribution seen in figure 97, and the ones seen in figure 96, yields the result that the lateral shower size smaller for the detector setup excluding FoCal-E in front of FoCal-H. I assume, as I did for the FoCal-H second prototype, that the size difference stems from the lack of pre-showers in FoCal-E, which continues into FoCal-H.

In the case of the FoCal-H third prototype, the lateral shower is contained within the size of the calorimeter, resulting in no lateral leakage. The shower profile for the third prototype resembles the one of the second prototype. The main noticeable difference in the showers is the intensity of the signal, which could be a result of the changed ration between the active and passive material.

As for the case of shower containment in the FoCal-H second prototype, I would suggest to perform a study of the highest energy possible to be contained within the lateral direction of FoCal-H, including and excluding FoCal-E in front of FoCal-H. This study has not been performed due to the lack of time. An additional study that could be investigated in regards to the change in the ratio between the passive and active material, is longitudinal shower containment. I assume that in any case where particles come out of the back-end of the FoCal-H second prototype, would be reduced in the third prototype, due to the increase in passive material.

10 Conclusion

This thesis focused on characterizing the performance of the FoCal-H calorimeter components as well as analyzing the November 2022 SPS H2 testbeam data. Simulations corresponding to the testbeam detector setup was performed in order to compare and estimate the FoCal-H second prototype's technical performance.

The performance characteristics of the FoCal-H calorimeter components were studied in order to optimize the design for a future prototype or the final design of FoCal-H. These studies revolved around optical crosstalk measurements between the SiPMs, the cutting technique used when cutting the scintillating fibers, and the ratio between the passive and active material.

The study of optical crosstalk was performed on the central 7x7 SiPM calorimeter module, and the outer 5x5 SiPM calorimeter modules individually, due to differences in the design of the modules. Optical crosstalk between the SiPMs was found to be an issue in both the central 7x7 SiPM calorimeter module and the outer 5x5 SiPM calorimeter modules, due to the compact design leading to a small distance between the SiPMs, as well as the wide scattering of photons from the scintillating fibers.

In relation to the optical crosstalk study, the cutting technique used on the scintillating fibers was examined. The cutting technique was studied with the aim of reducing the wide scattering of the photons from the scintillating fibers. The different techniques studied in this thesis were a rolled scalpel cut, a rolled scalpel cut where the scintillating fibers were polished afterwards, and a technique where the scintillating fibers were glued together with optical glue and then cut with a diamond blade. This study showed that optical crosstalk between the SiPMs could be reduced significantly by cutting the scintillating fibers using the optical glue and diamond blade technique. In addition to the study of the cutting technique, three different types of scintillating fibers were examined with these cutting techniques, to exclude the possibility of achieving different results due to the construction of the scintillating fibers. This did not show to have any effect.

Moreover, the ratio between the passive and active material of the FoCal-H calorimeter was studied.

This study was conducted with the aim of optimizing the technical performance of the FoCal-H second prototype. It was found that by reducing the inner diameter of the copper-tubes, thus reducing the size of the scintillating fibers, the energy resolution and the response linearity across a large range of beam energies could be improved.

The analysis of the November 2022 SPS H2 testbeam data, as well as the analysis of the corresponding simulations, was performed in order to estimate the FoCal-H second prototype's technical performance. The prototype was at the November 2022 SPS H2 testbeam examined for energies between 60 GeV to 350 GeV, with a detector setup including and excluding FoCal-E in front of FoCal-H. Various studies have, in regards to both the testbeam data and the simulations, been examined using these two detector setups. The studies revolved around determining the sources of the response peaks, energy resolution, lateral shower containment, and examination of the effects of the intersections between calorimeter modules by performing a position scan.

The response peaks were found to be caused by different reasons. In the detector setup including FoCal-E in front of FoCal-H three distinguishable peaks were present. The first one, the punch through peak, was caused by particles punching through the detectors without producing a particle shower. The second, the pre-shower peak, was caused by a particle shower starting in the latter layers in FoCal-E. The third, the hadron peak, was caused by particles punching through FoCal-E, and starting a particle shower in FoCal-H. The pre-shower peak, could be removed by excluding FoCal-E from the detector setup, leaving only the response of the punch through peak and the hadron peak.

Energy resolution was examined to determine how precisely the FoCal-H second prototype can measure the energy of particles. This study unexpectedly found that the energy resolution of the testbeam data was better than the one of the simulation. In light of this result, multiple studies were performed in order to point out any potential reason. These studies included the use of physics lists in the simulations, and saturation in simulations and/or in the testbeam data. A reason for this unexpected result of the energy resolution was not found, but potential other studies was suggested.

Lateral shower containment was studied in the simulations of the FoCal-H second prototype. It was found that the FoCal-H second prototype contains the shower in the lateral direction, both for detector setups including and excluding FoCal-E in front of FoCal-H. This study was done before any implementation of digitization in the simulation. Hence, the result of the spread of the particle shower can potentially differ after this implementation.

The examination of the intersections between calorimeter modules was performed by changing the position of the beam-pipe in the simulations. This study found that the FoCal-H response changed significantly when positioning the beam-pipe in front of these intersections. The FoCal-H response was seen to yield a reduced pre-shower peak, as well as a response with lower energy compared to results where the beam-pipe was placed in the center of FoCal-H. A further study on this subject is recommended in light of these results, since this could have a profound effect on the final design of FoCal-H.

11 Appendix

11.1 FoCal-H first prototype

The section includes schematics of the FoCal-H first prototype. A schematic of the sizes, copper-box, and copper-tube design can be seen in figure 98.

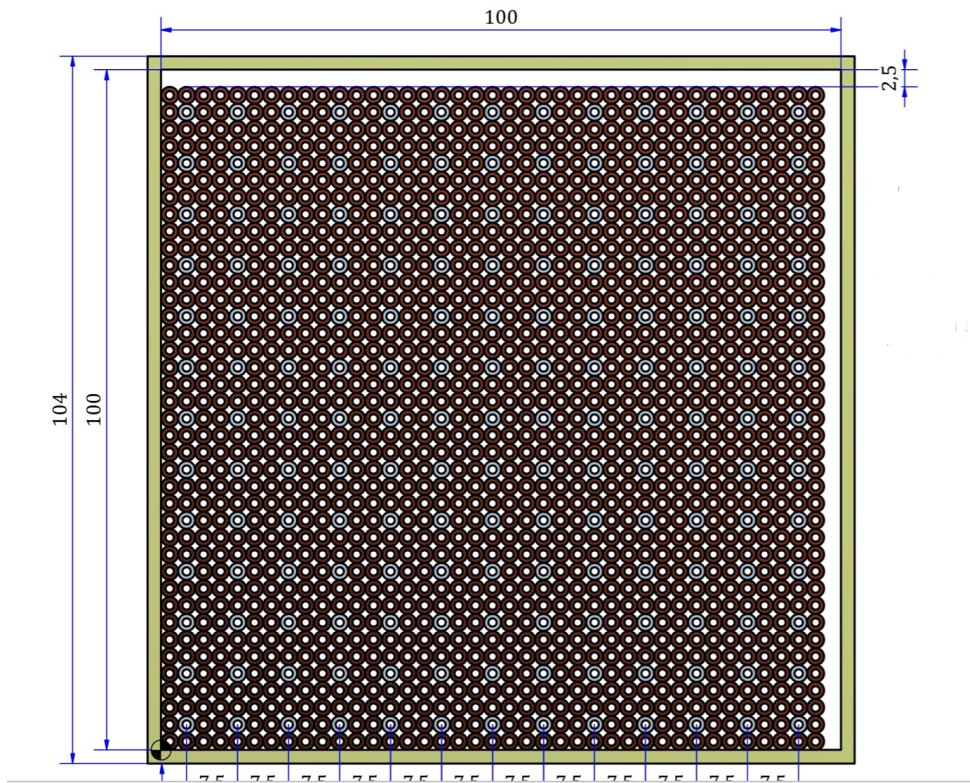


Figure 98: The figure shows the design of the FoCal-H first prototype.

Two schematics of the collector plate, used to bundle up the scintillating fibers, and mounting the SiPM boards, can be seen in figure 99. The collector plate used in the FoCal-H first prototype was mounted around the copper-box, seen in figure 98. Thus the size of the plate, as stated in the left-side schematic in figure 99.

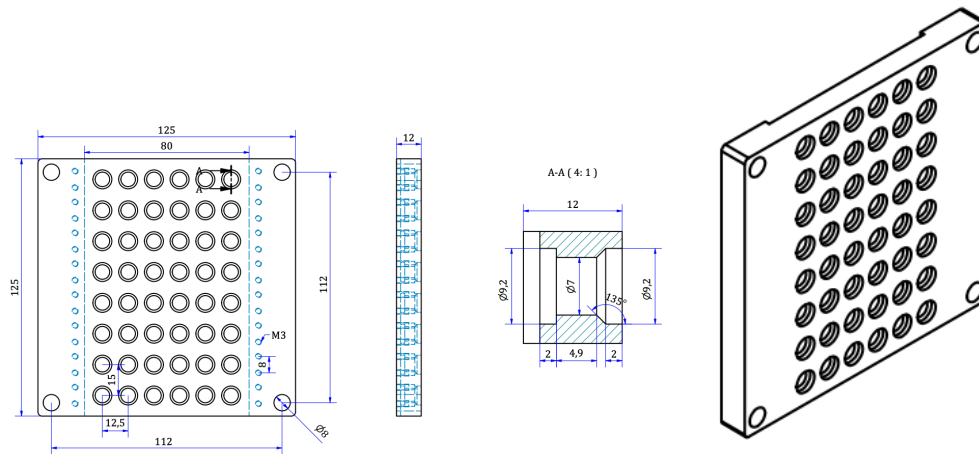


Figure 99: The figure shows two schematics of the collector plate for the FoCal-H first prototype. The left-side schematic shows the different designs and sizes of the components in the plate. The right-side figure shows the 3D schematic of the collector plate.

11.2 Optical crosstalk

This section includes all remaining intensity plots not shown in the optical crosstalk section 6.1. The optical crosstalk measurements between the SiPM for the 49 SiPMs in the central 7x7 SiPM calorimeter module and the 25 SiPMs for the outer 5x5 SiPM modules can be seen in the sections below.

The module position relative to each other, seen from the back-end of the FoCal-H second prototype (The SiPM end), can be seen in figure 100.

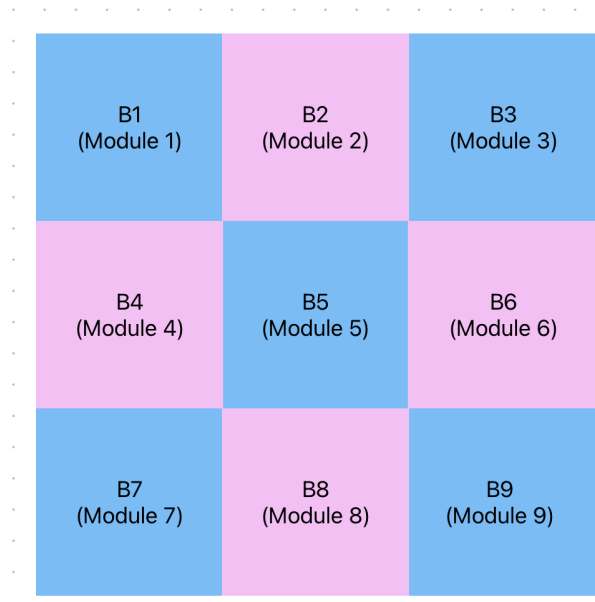
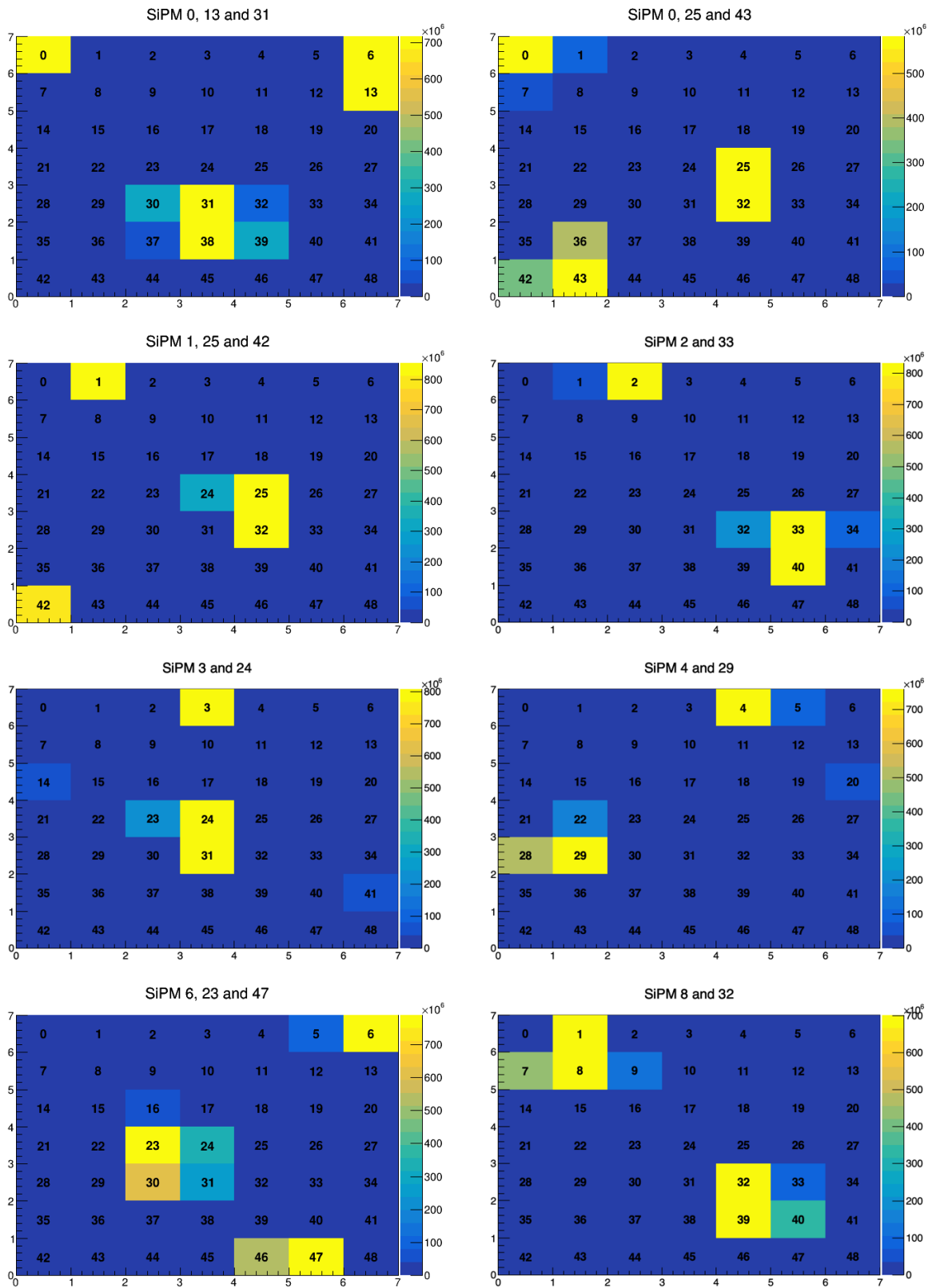
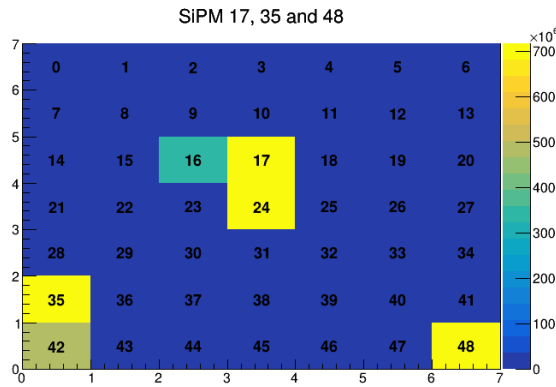
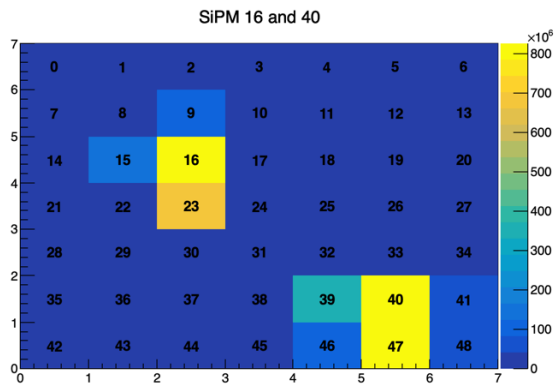
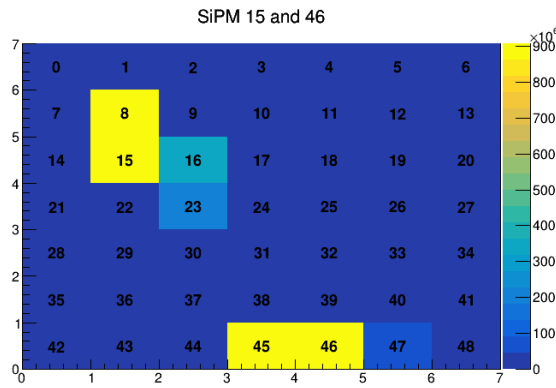
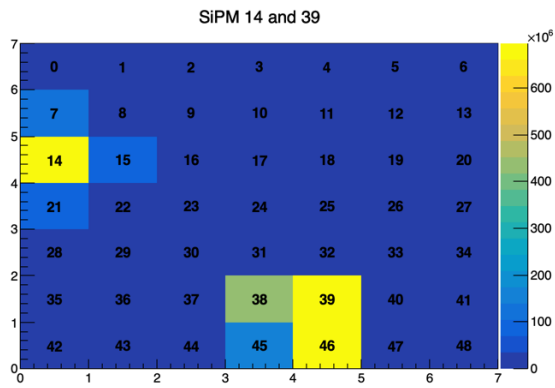
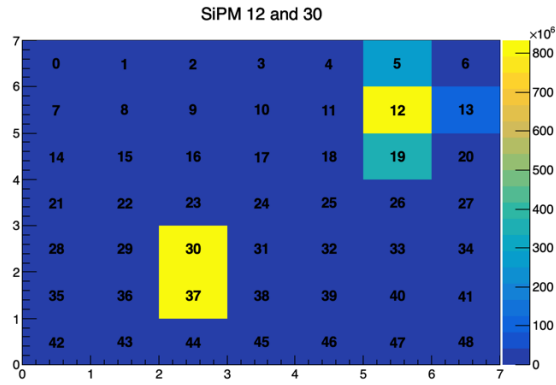
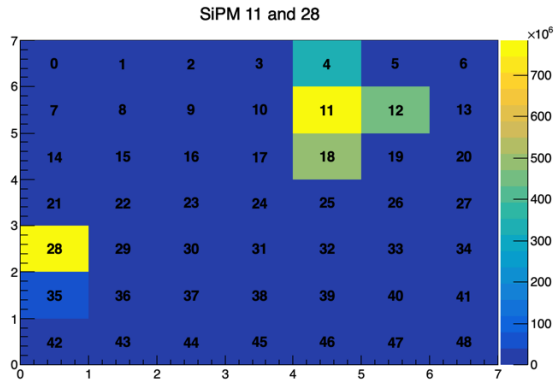
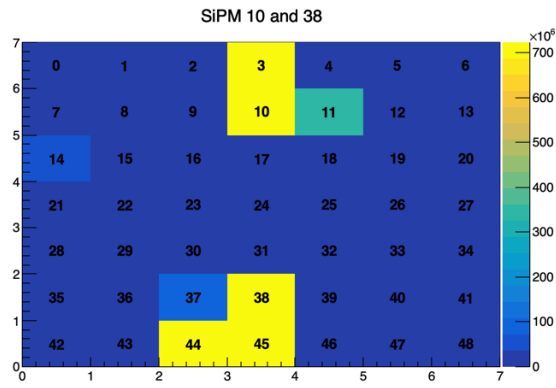
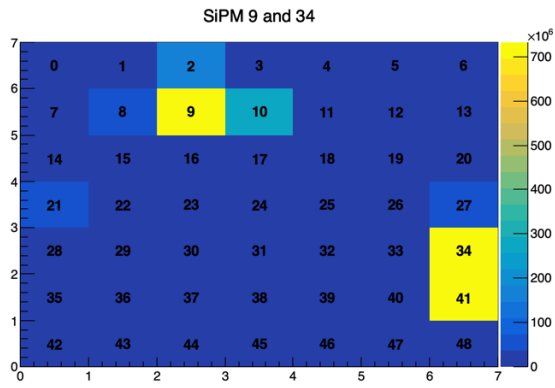
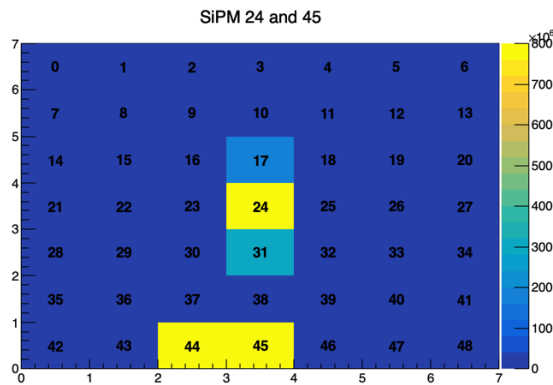
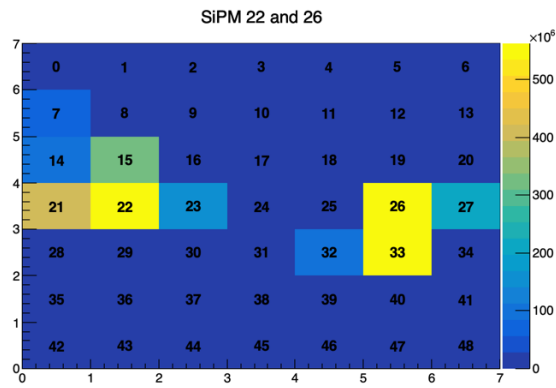
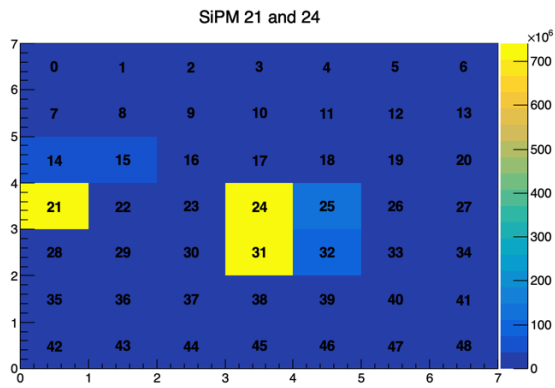
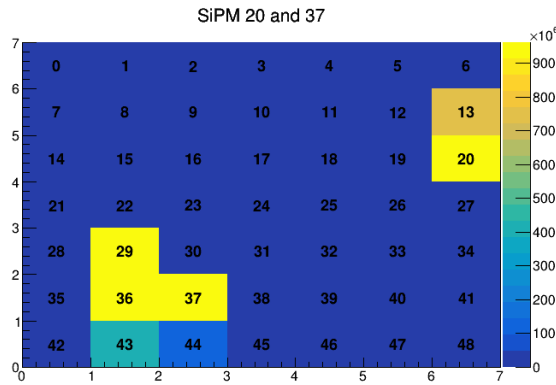
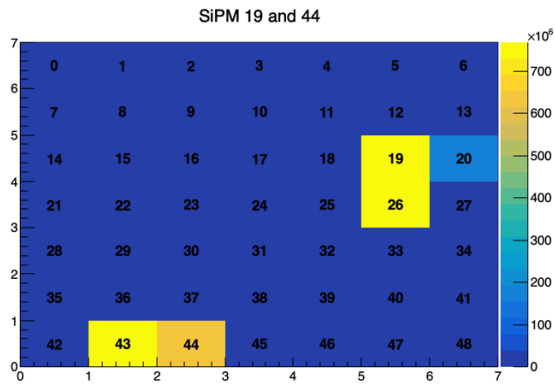
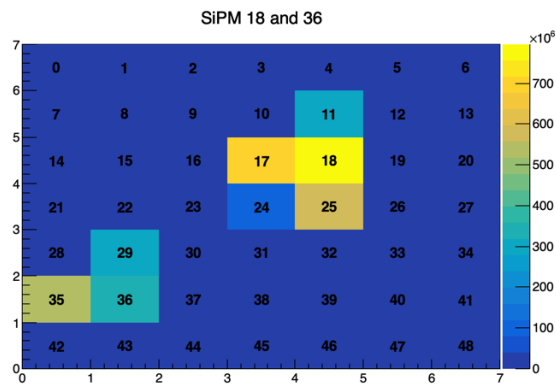
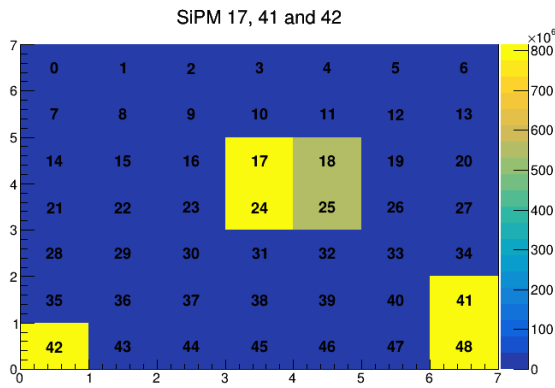


Figure 100: The figure shows the module position with respect to the remaining modules, seen from the back-end of the FoCal-H second prototype.

11.2.1 Central 7x7 SiPM module (Module 5)

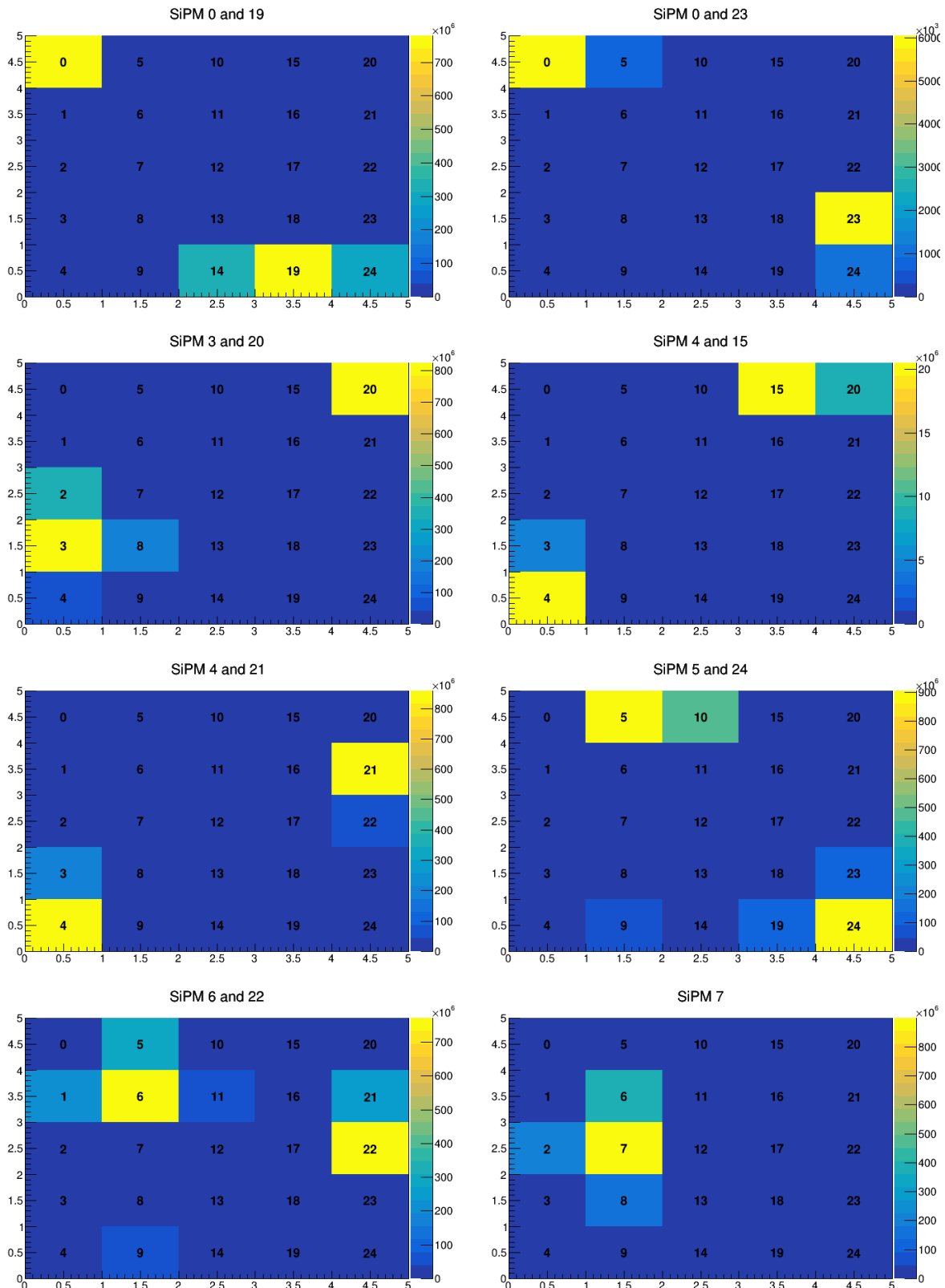


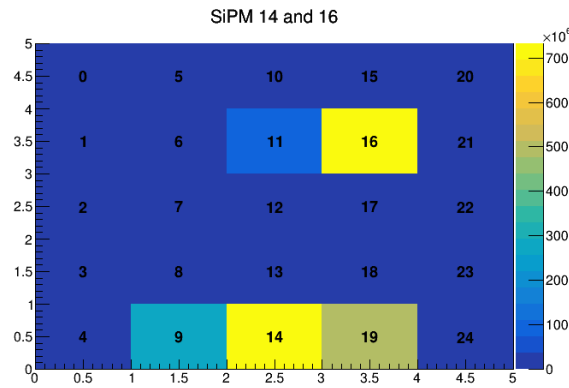
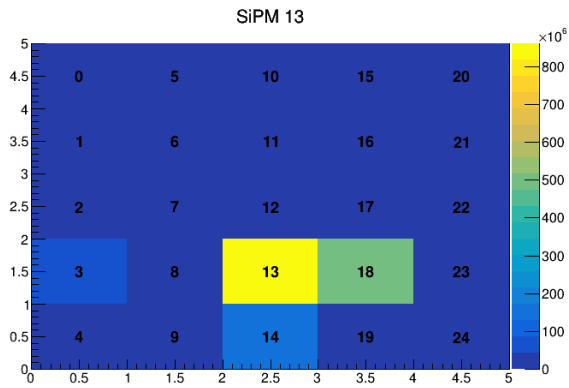
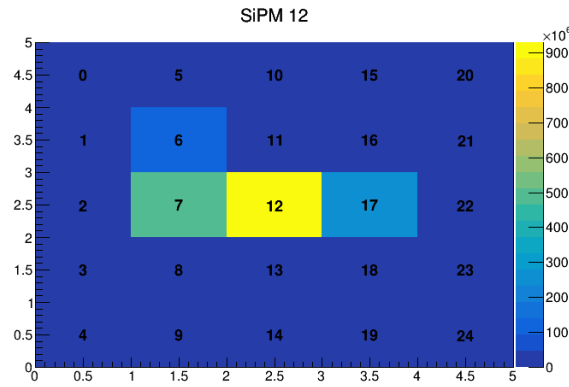
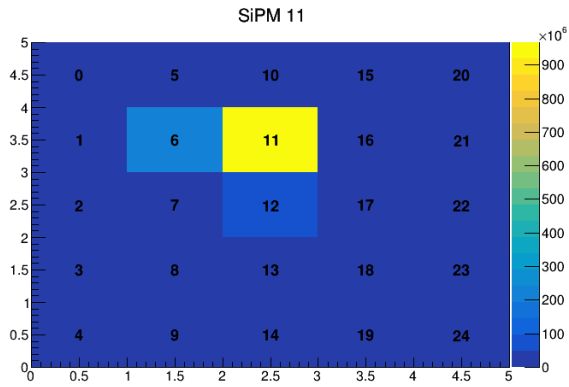
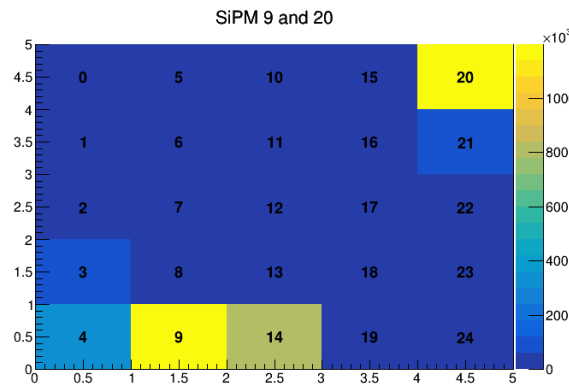
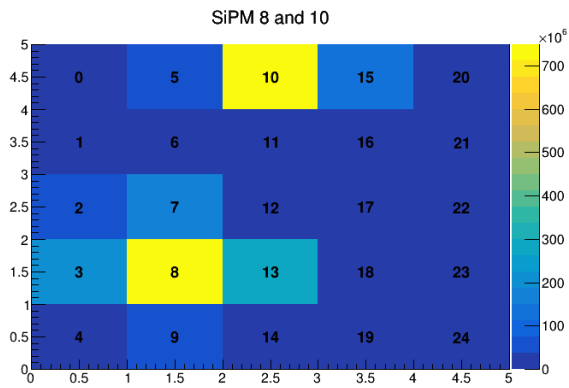




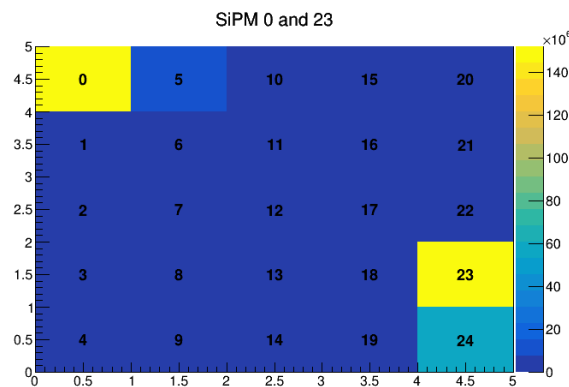
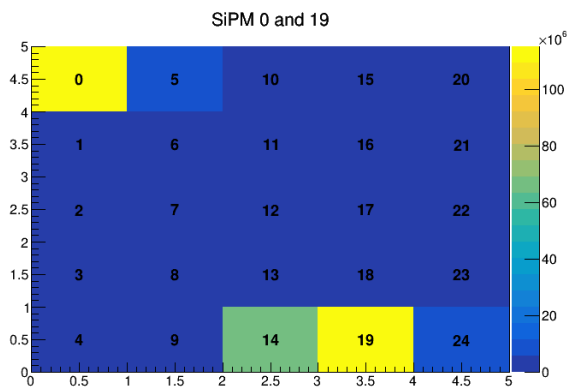
11.2.2 Outer 5x5 SiPM modules

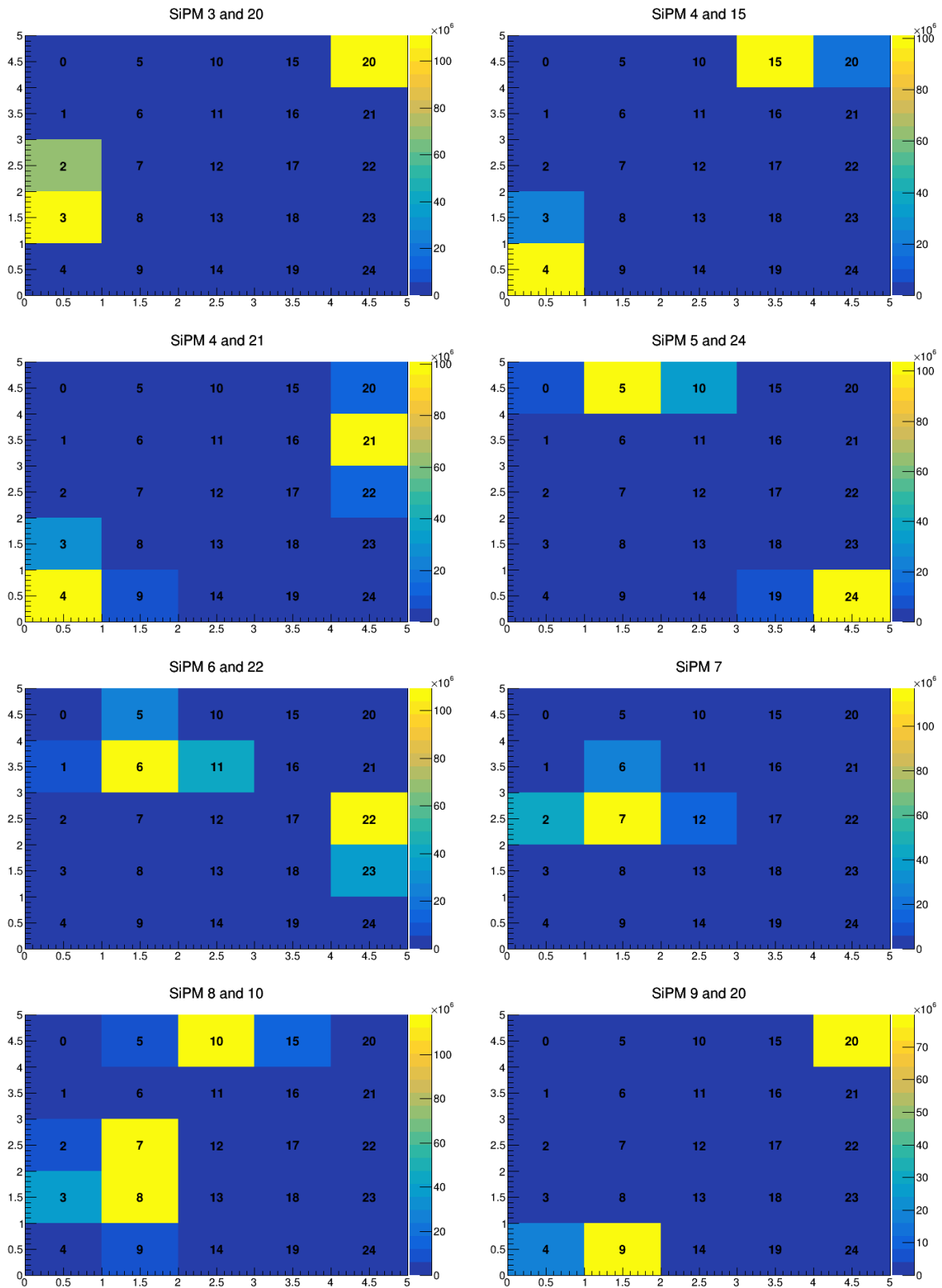
11.2.2.1 Module 1

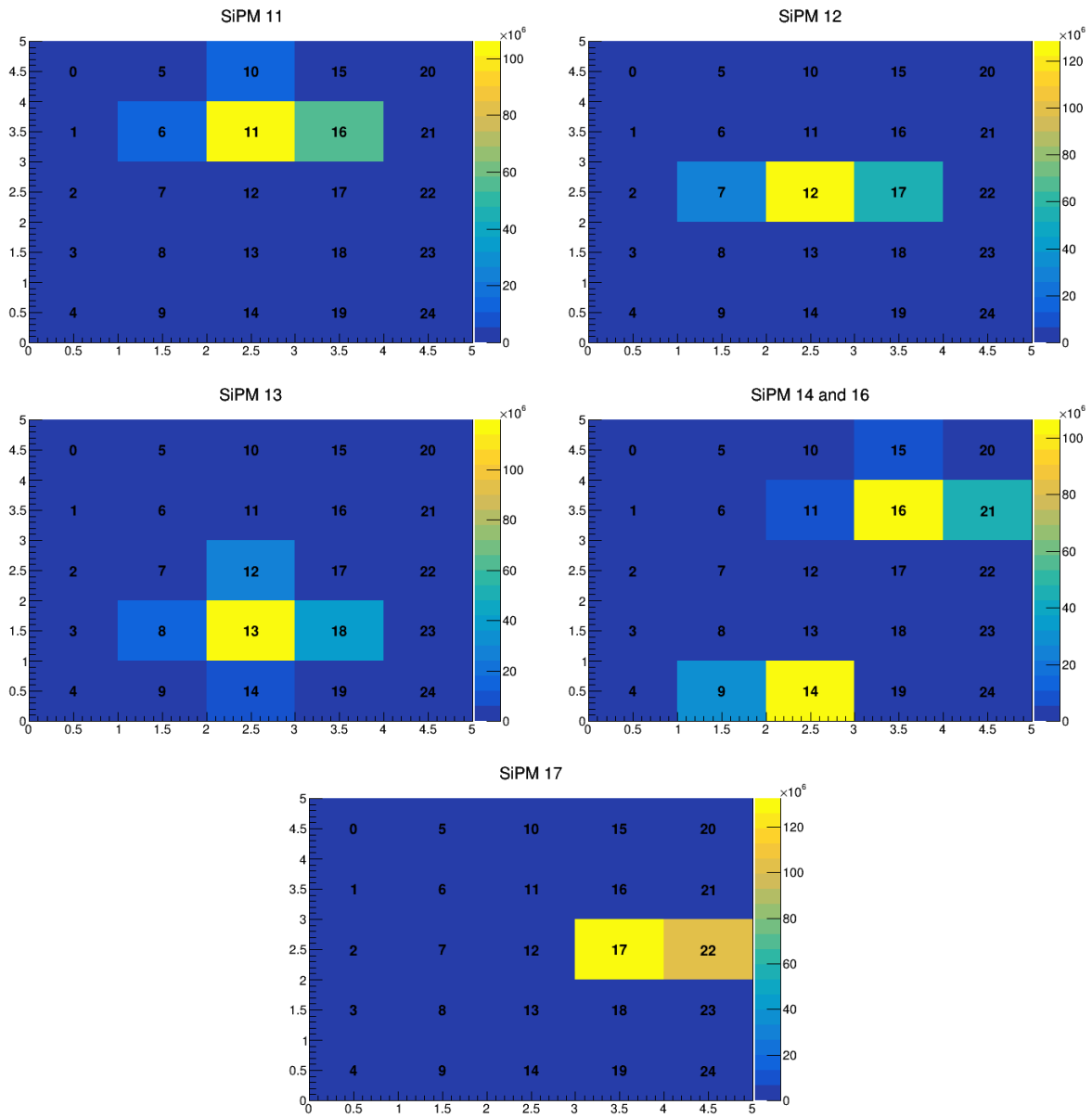




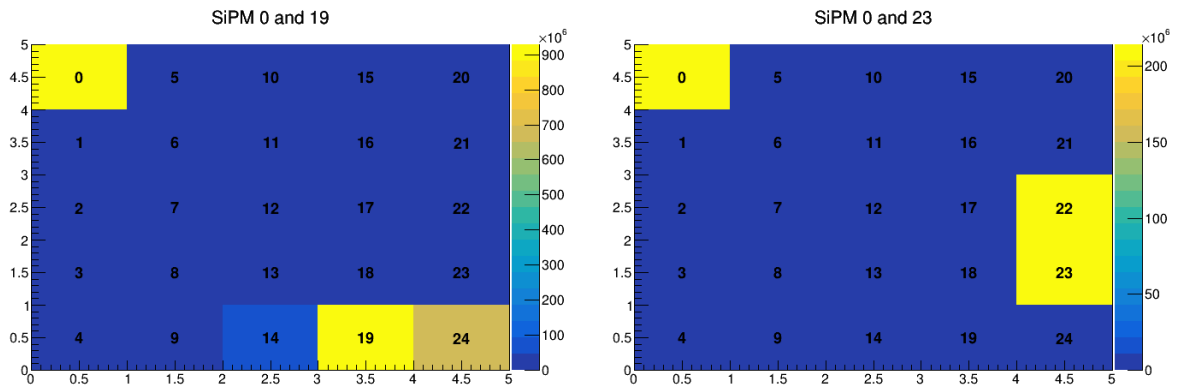
11.2.2.2 Module 2

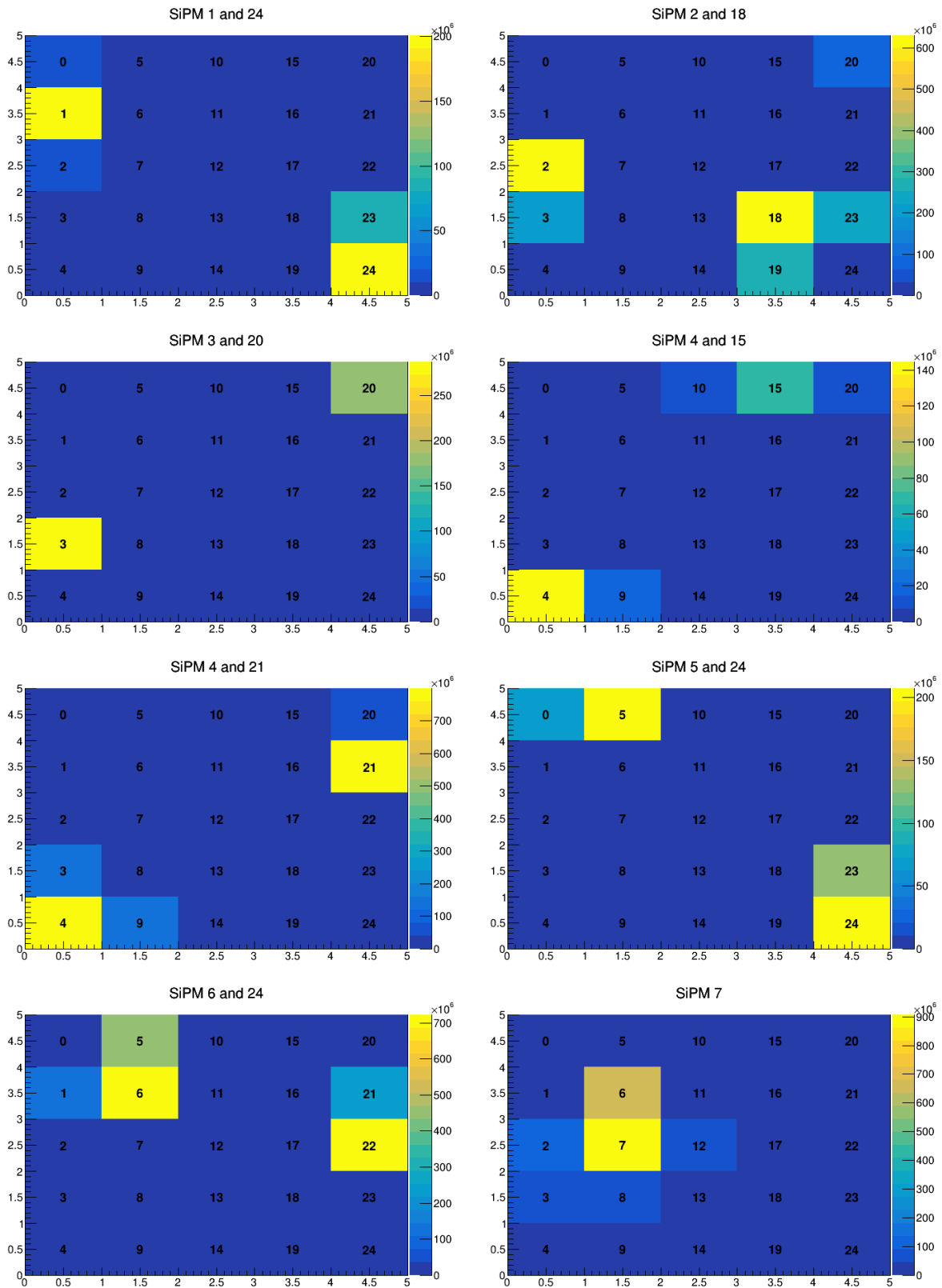


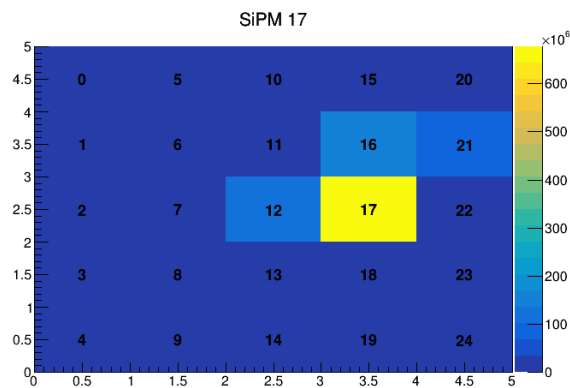
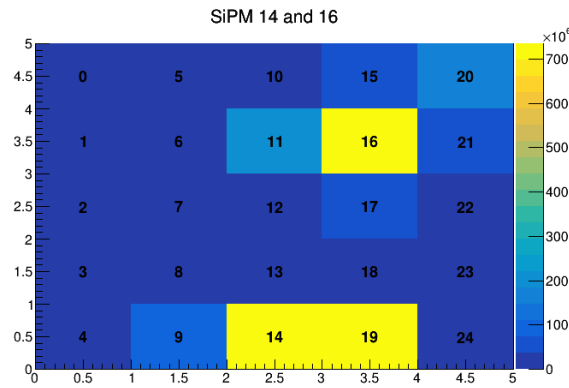
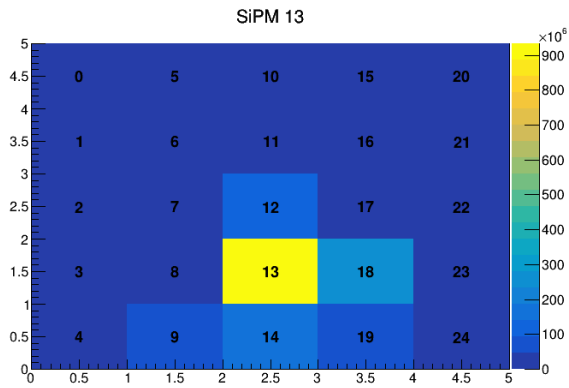
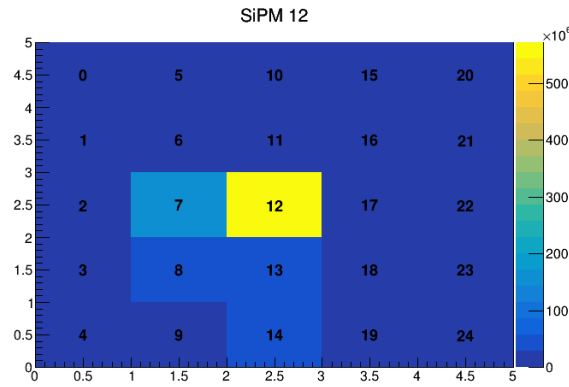
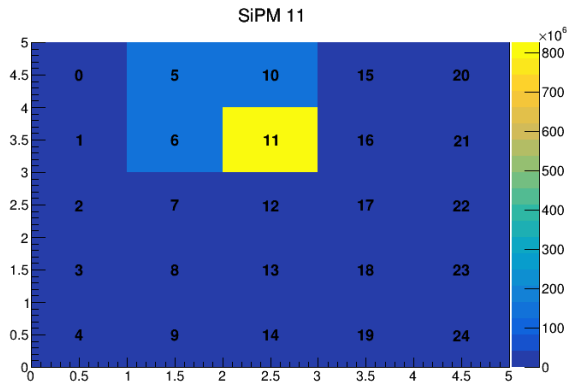
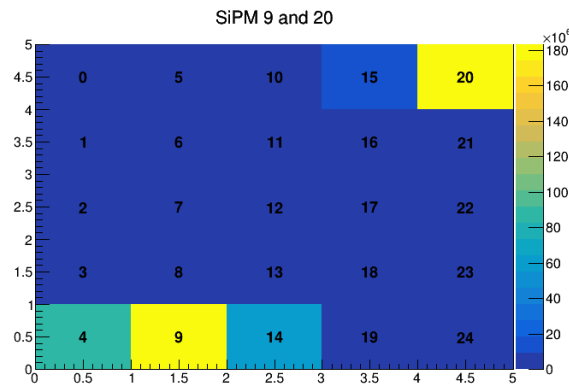
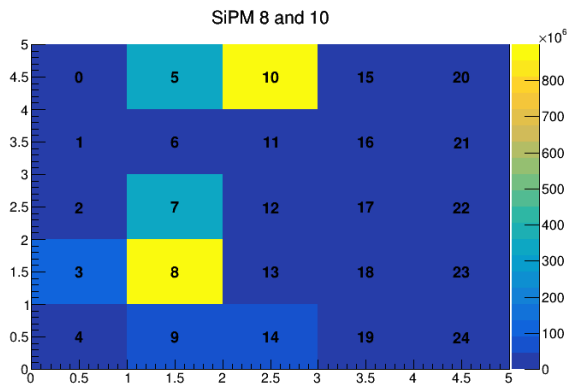




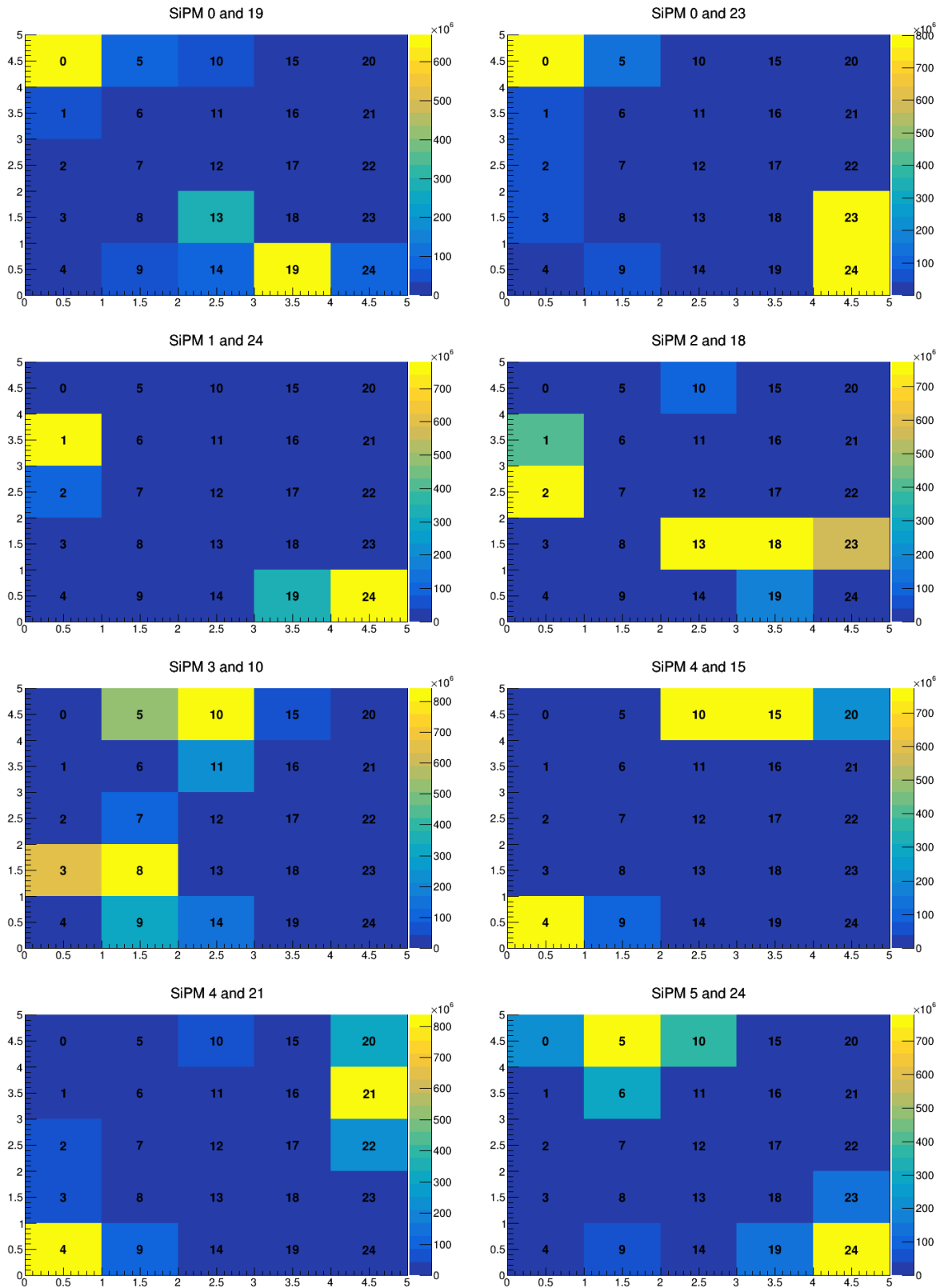
11.2.2.3 Module 3

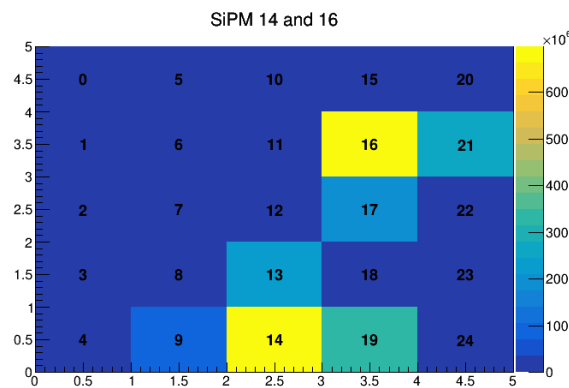
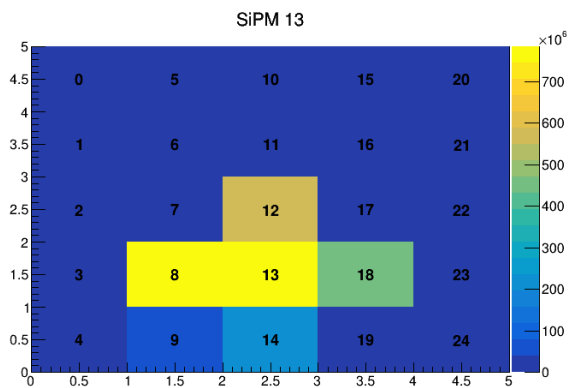
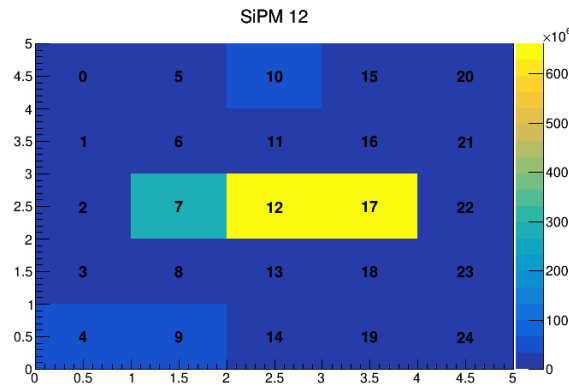
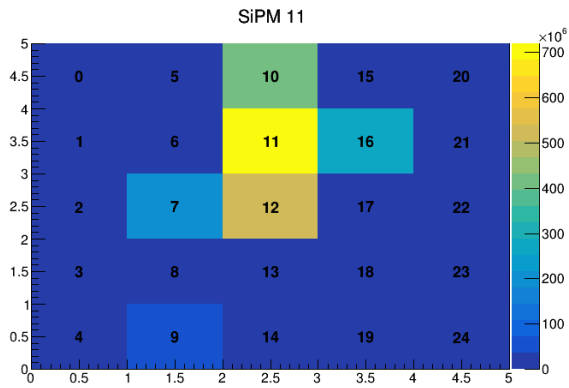
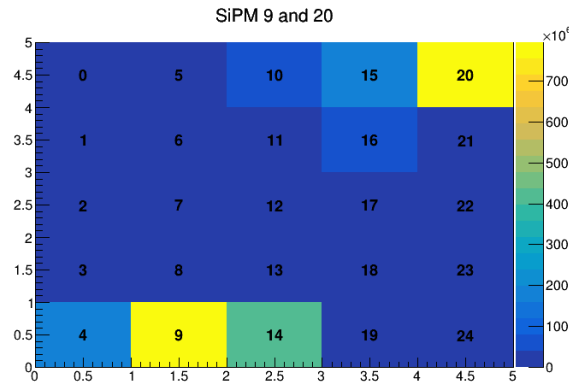
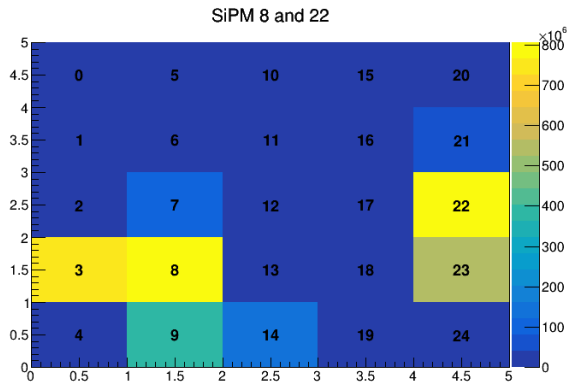
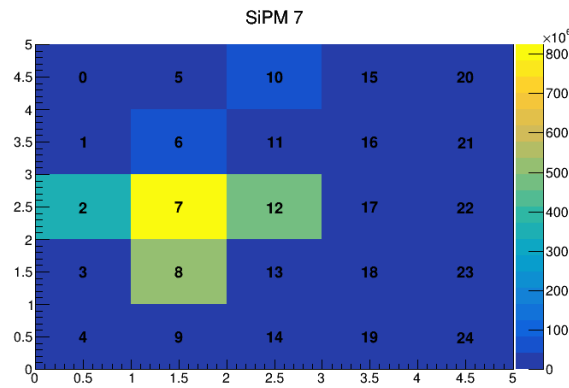
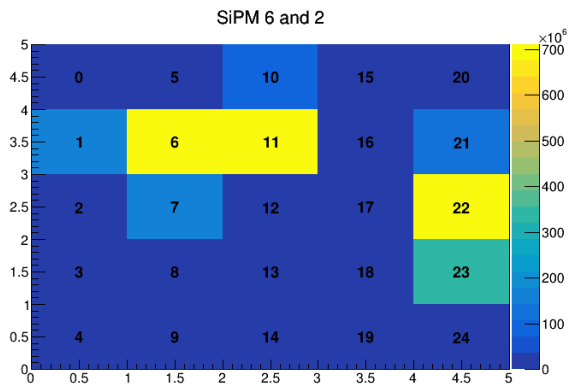


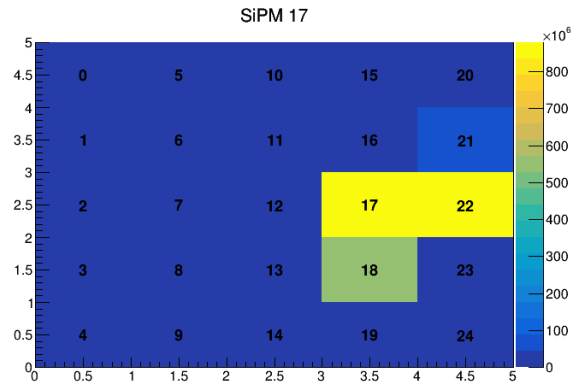




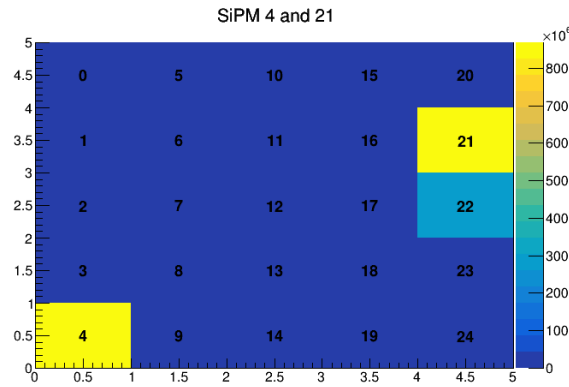
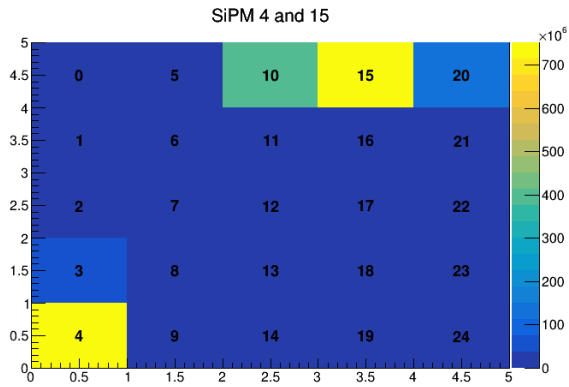
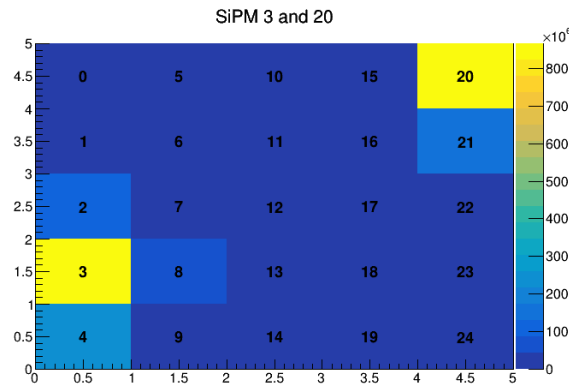
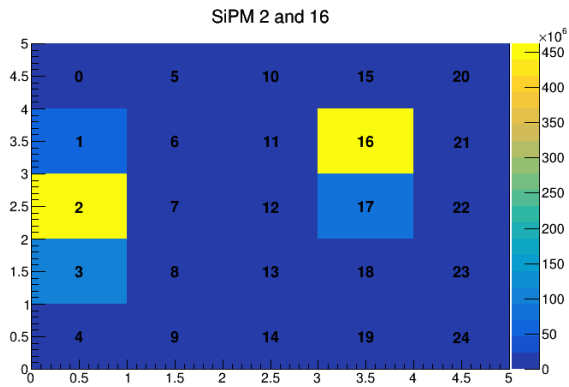
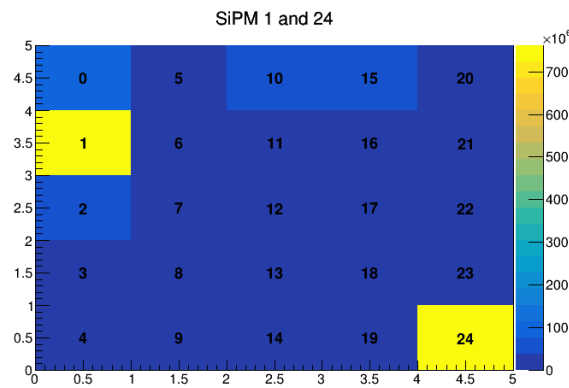
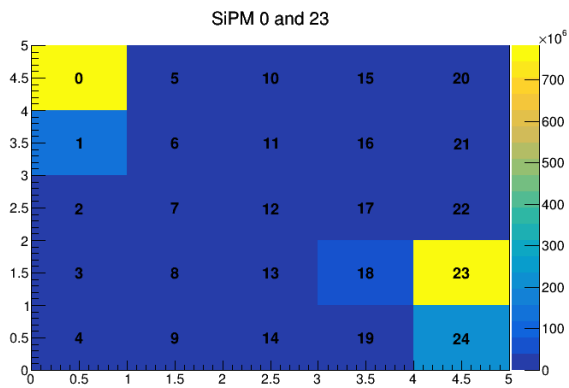
11.2.2.4 Module 4

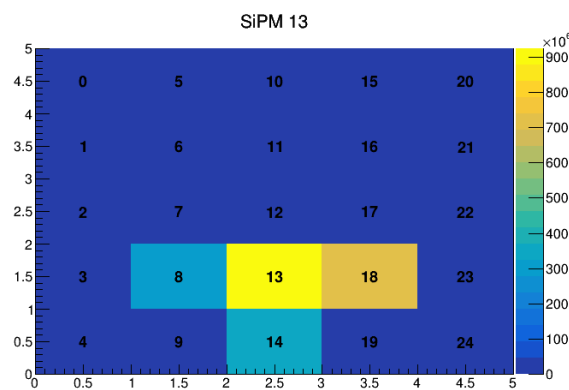
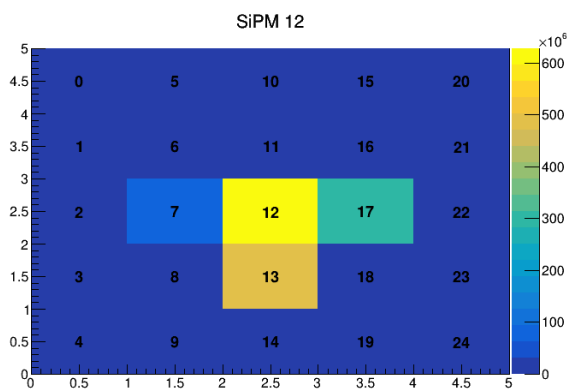
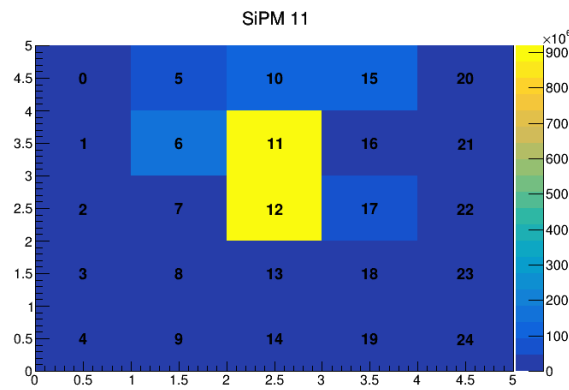
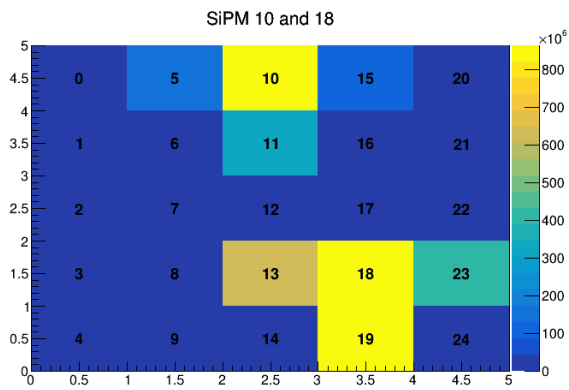
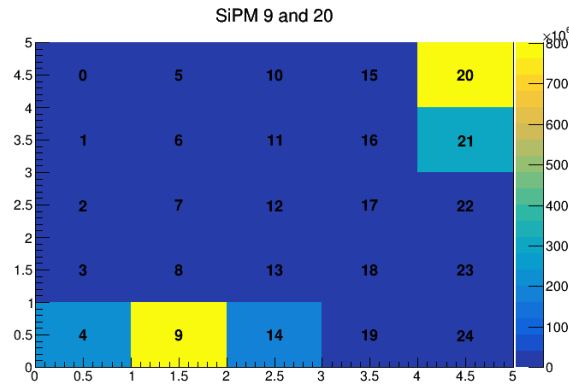
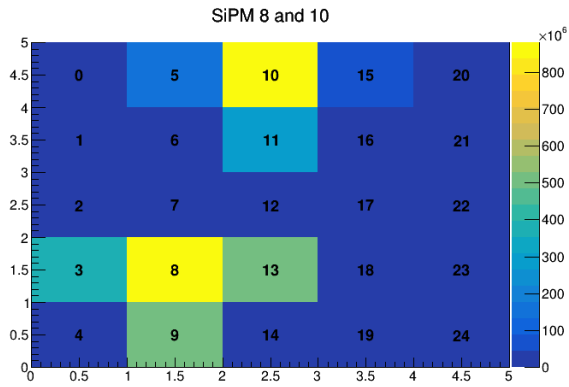
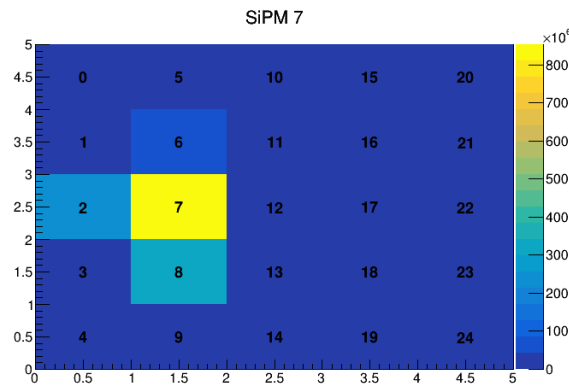
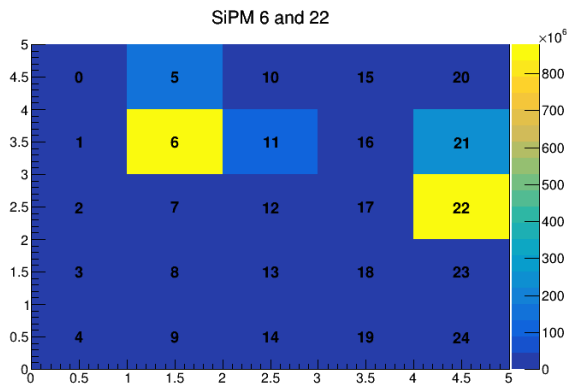


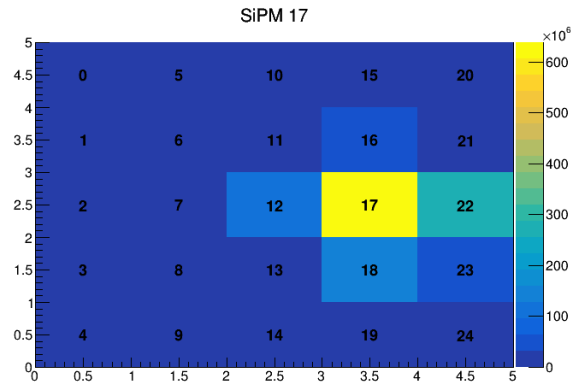




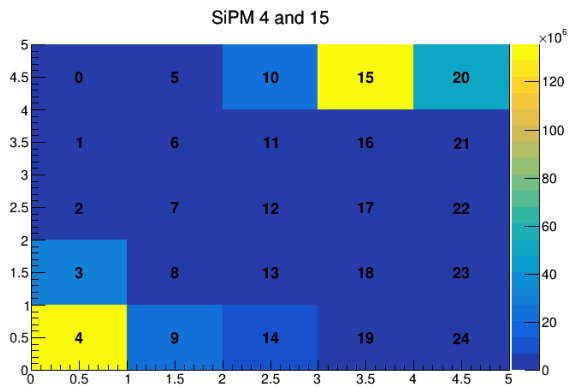
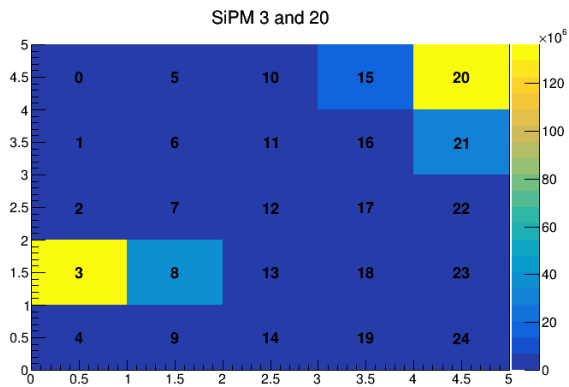
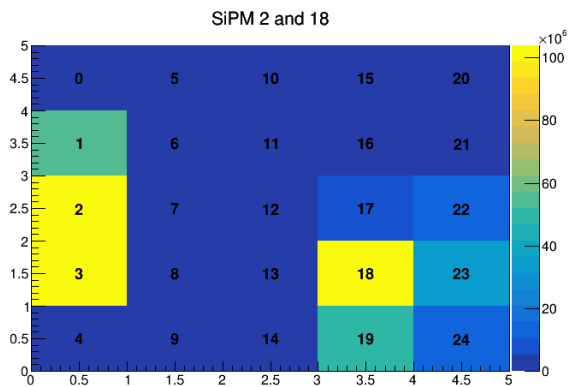
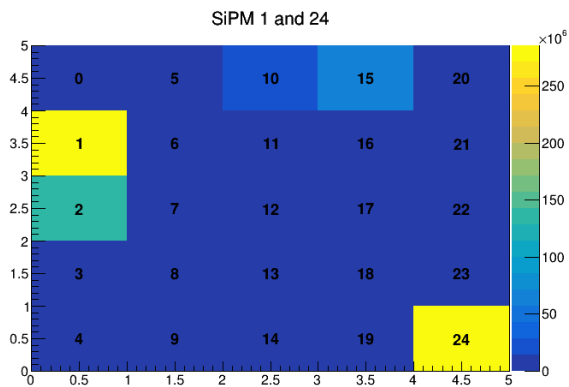
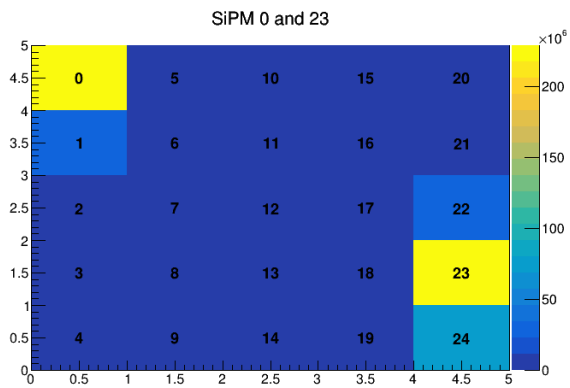
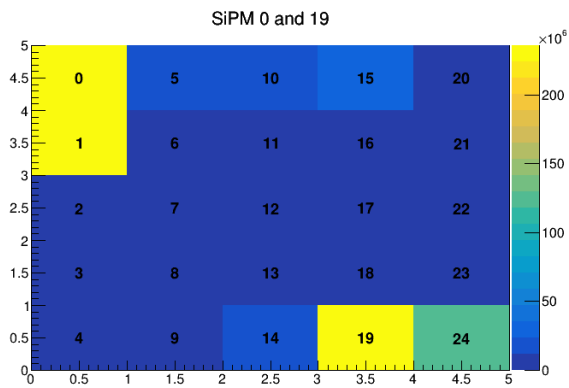
11.2.2.5 Module 6

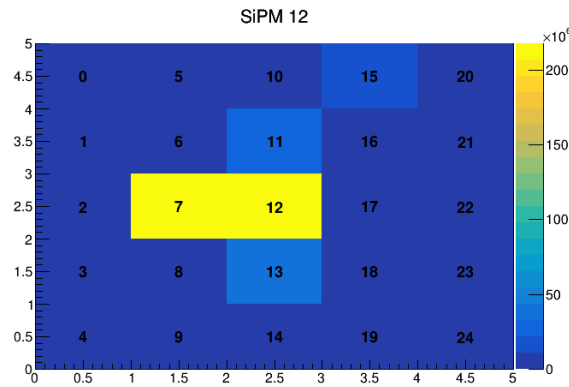
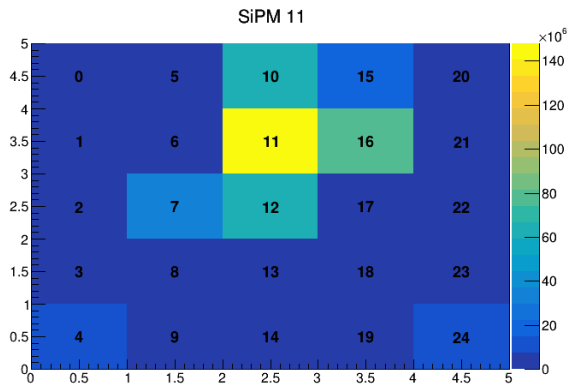
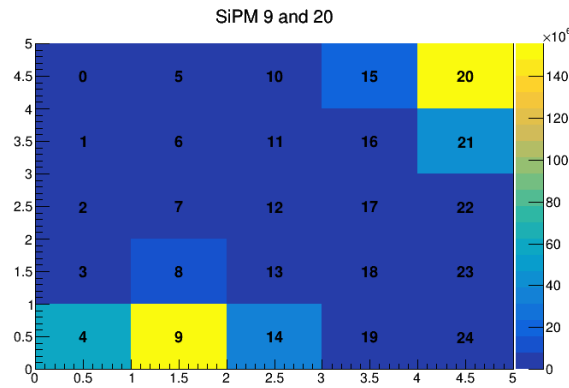
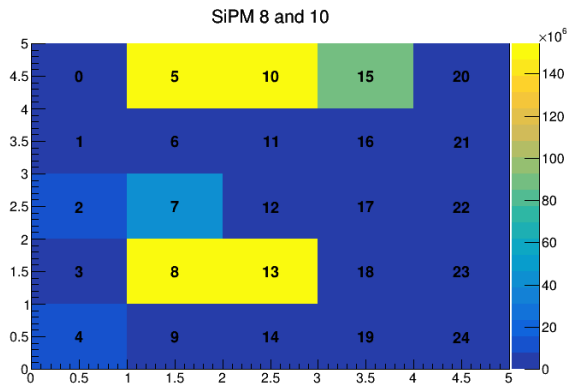
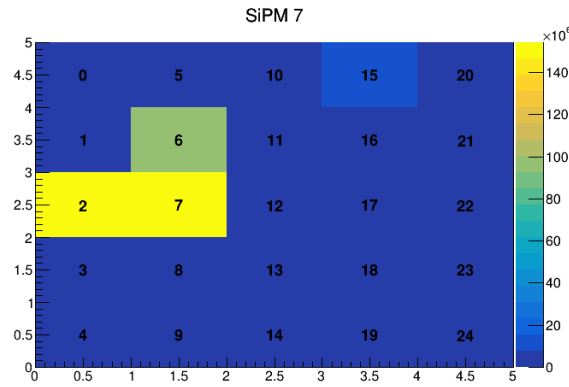
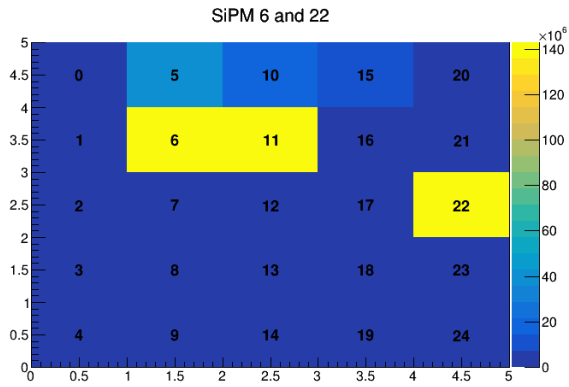
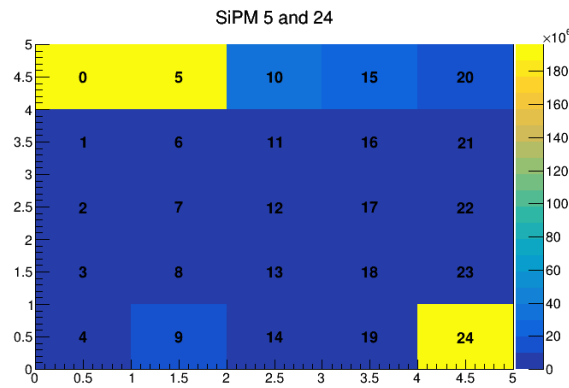
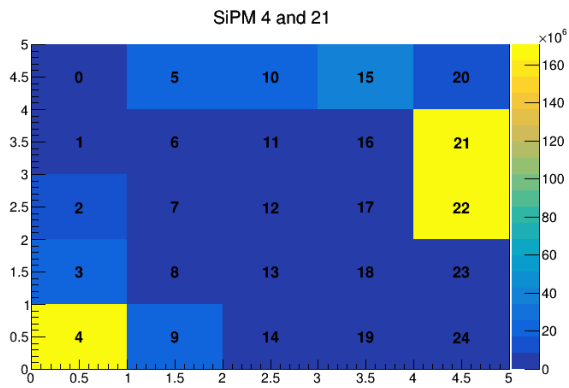


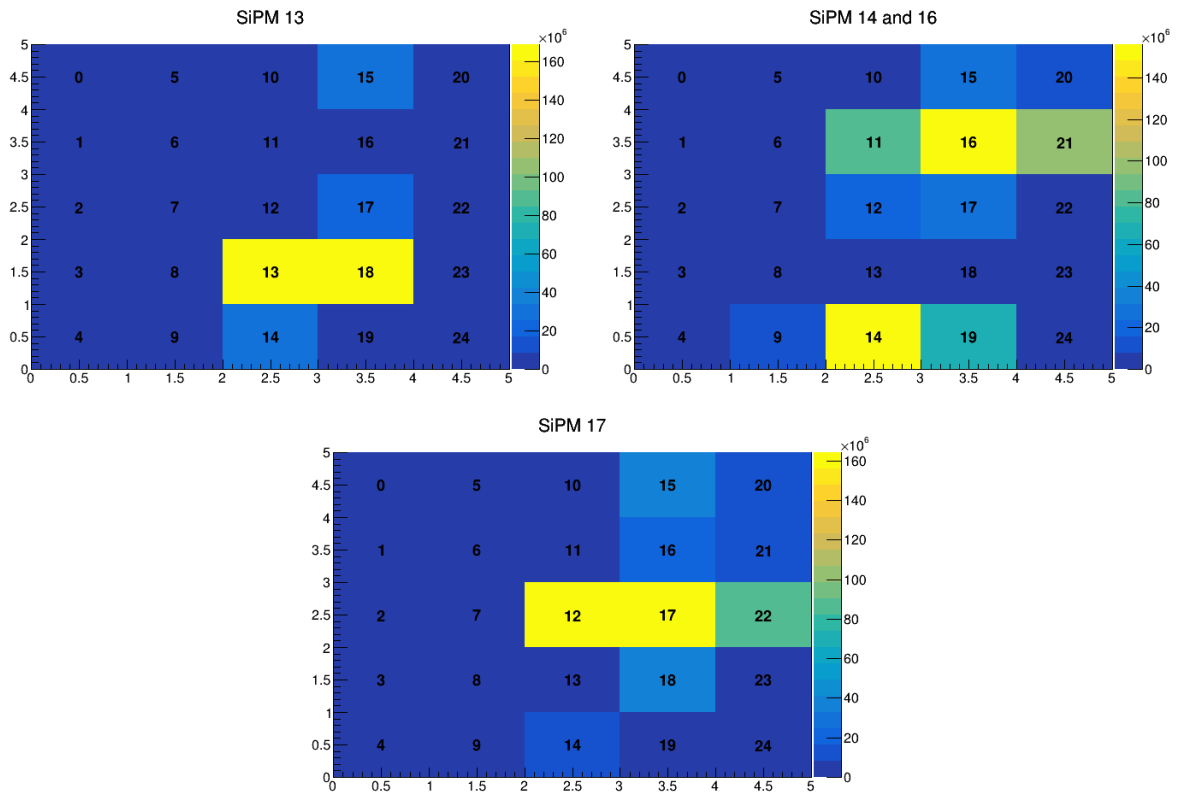




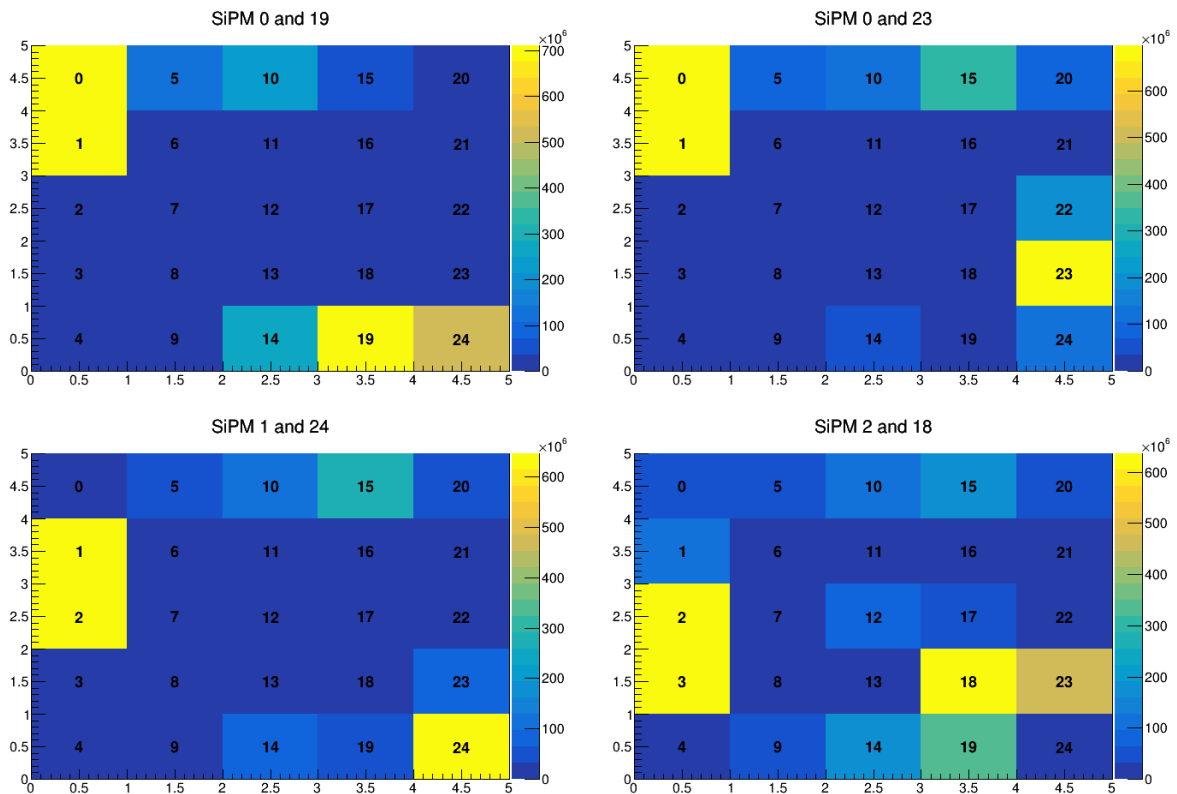
11.2.2.6 Module 7

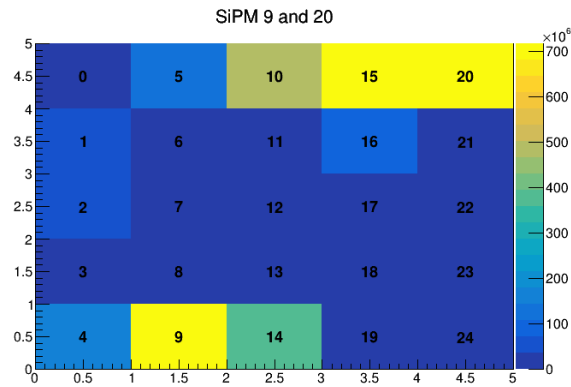
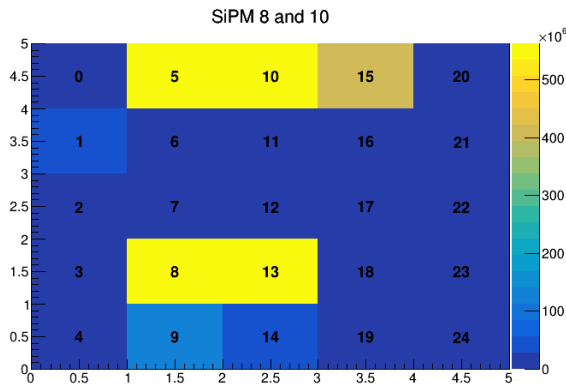
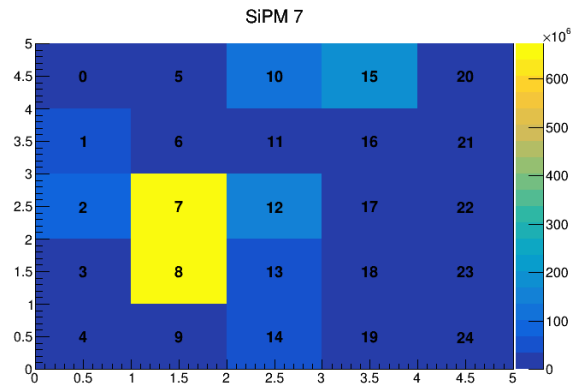
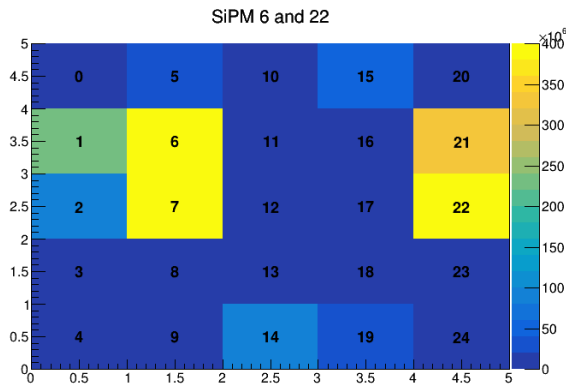
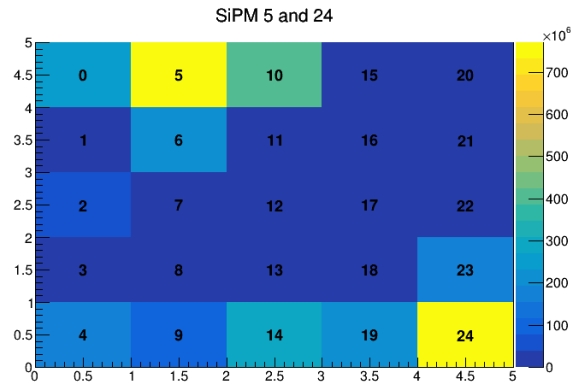
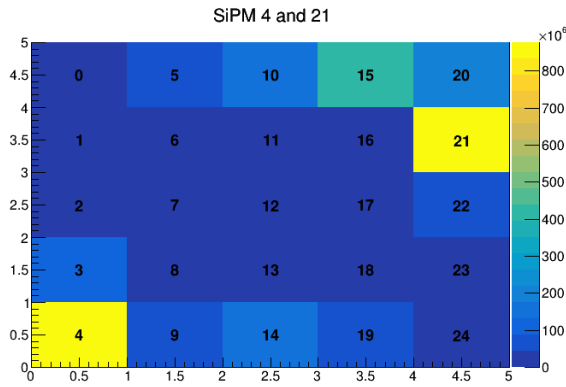
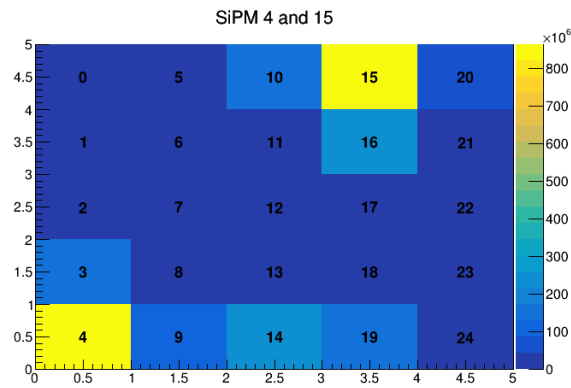
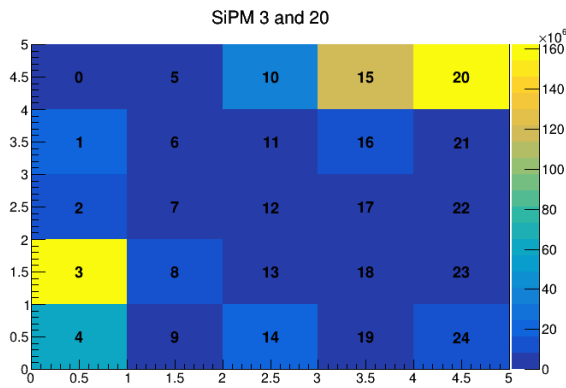


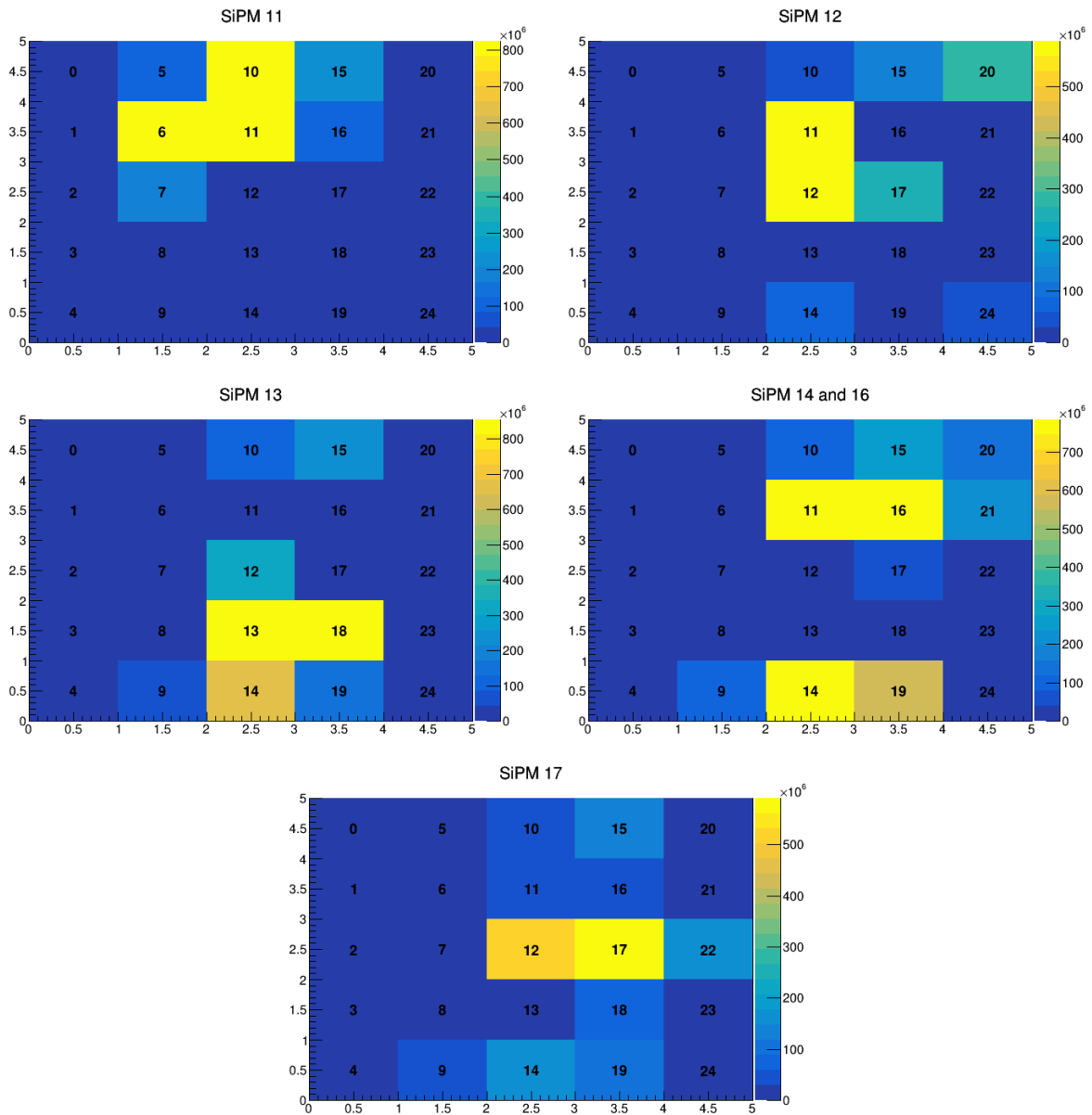




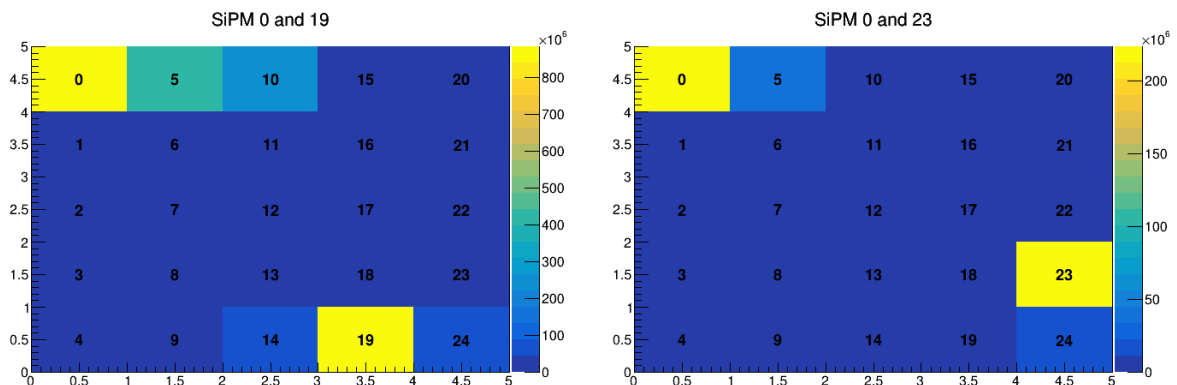
11.2.2.7 Module 8

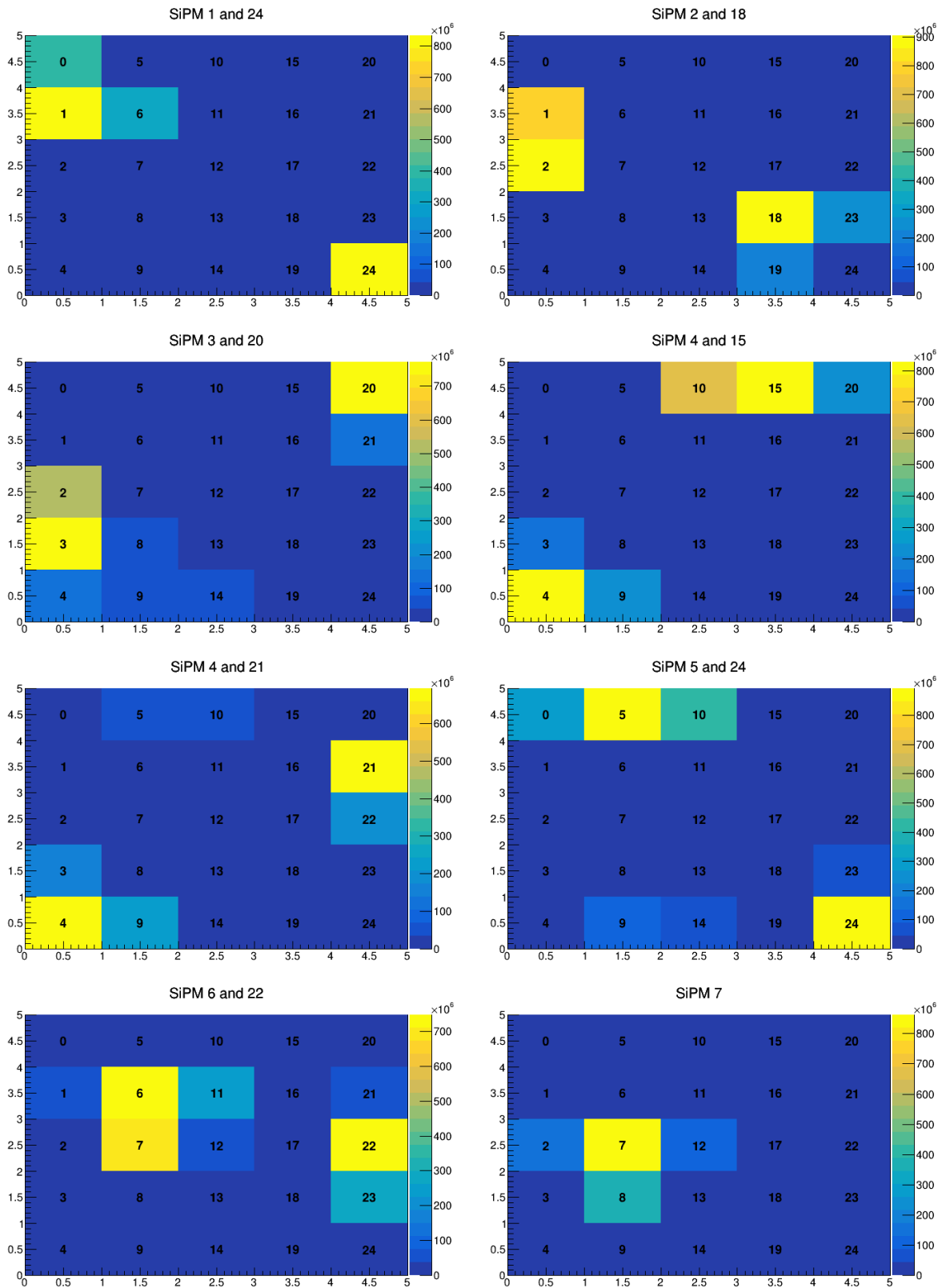


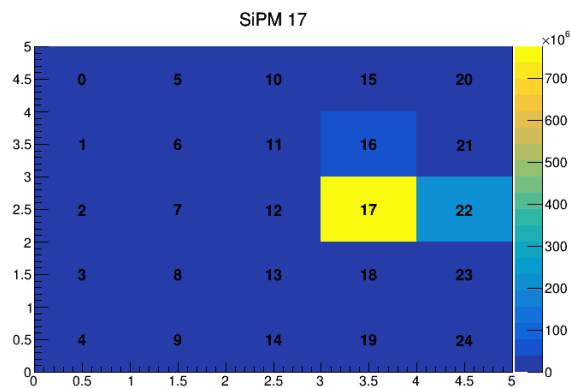
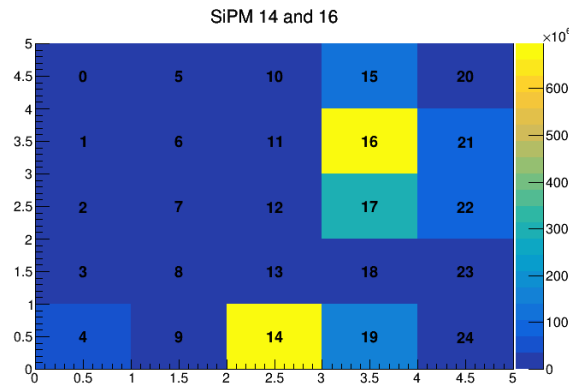
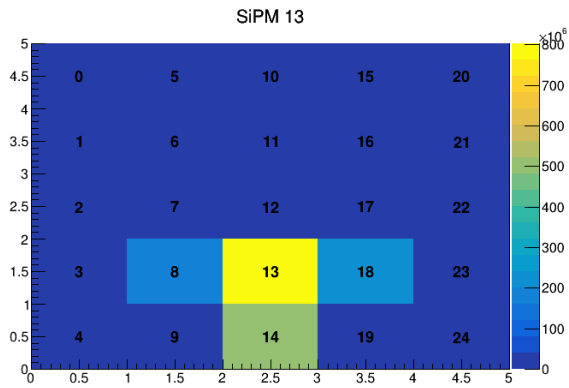
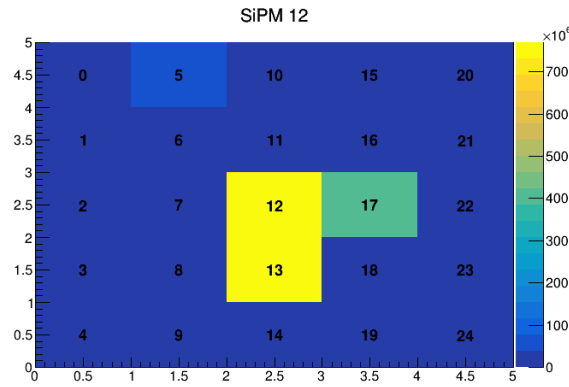
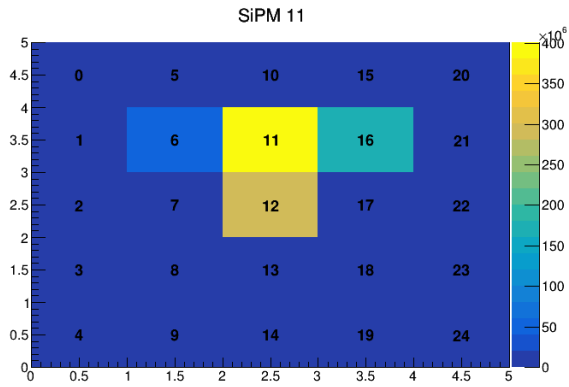
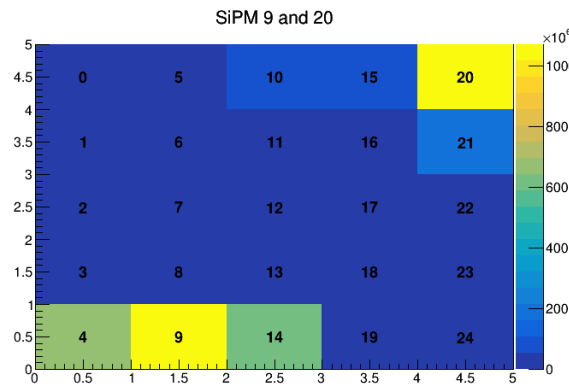
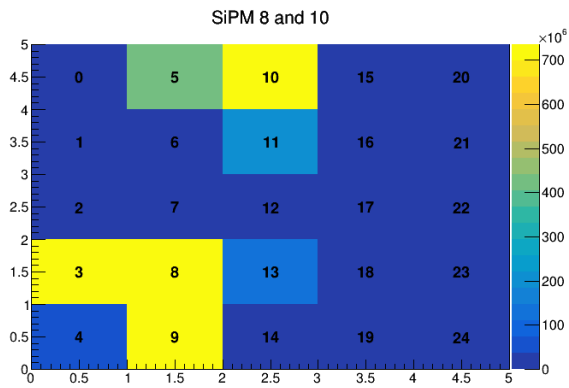




11.2.2.8 Module 9

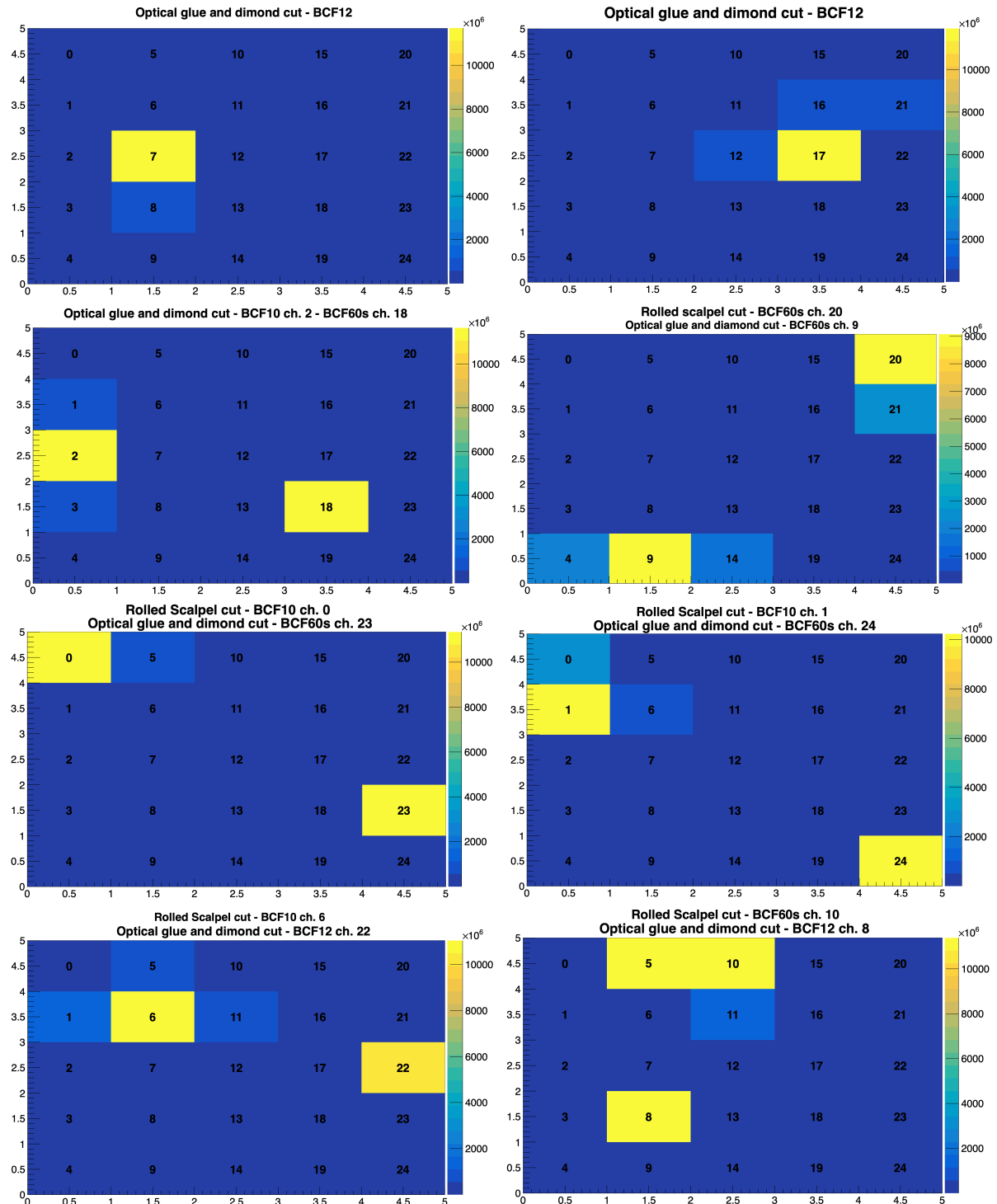


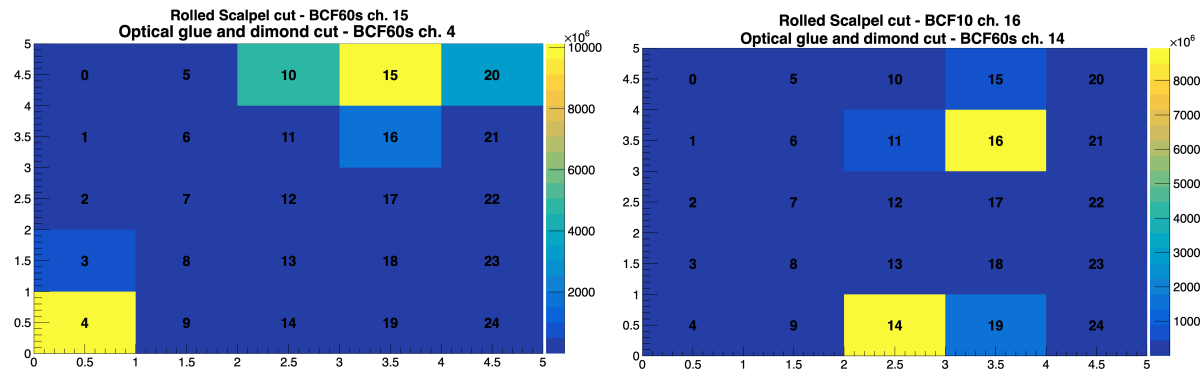




11.3 Cutting techniques of scintillating fibers

This section contains the remaining measurements of the three different techniques used to cut scintillating fibers. The three techniques is a rolled scalpel cut, rolled scalpel and polished cut, and optical glue with a diamond blade cut. In addition, three types of scintillating fibers were tested in this process. The type of cutting technique, as well as the type of scintillating fiber, is indicated in the figures.





11.4 Simulation - November 2022 SPS H2

This section shows results from simulation studies not included in section 8.2 revolving the simulation of the FoCal-H second prototype using the setup from the November 2022 SPS H2 testbeam.

11.4.1 Comparison between updates in simulations

This section shows results from the comparison between the simulations updates, which was not included in section 8.2.1.

Figure 101 below shows two FoCal-H simulations at 200 GeV including FoCal-E in front of FoCal-H, with and without the implementation of increasing the inner and outer diameter of the copper-tubes used in the FoCal-H second prototype setup. The inner diameter has been changed from 1.1 mm to 1.12 mm. The outer diameter has been changed from 2.5 mm to 2.52 mm. This implementation was added, to remove the air gaps between copper-tubes, and between the copper-tube and the copper-box surround the tubes. The two simulations has the names ideal and realistic. Ideal, since the smaller sized of the copper-tubes are the ideal sizes, and realistic because the larger sizes removed the mentioned air gaps, and represents the design of the real FoCal-H more accurately.

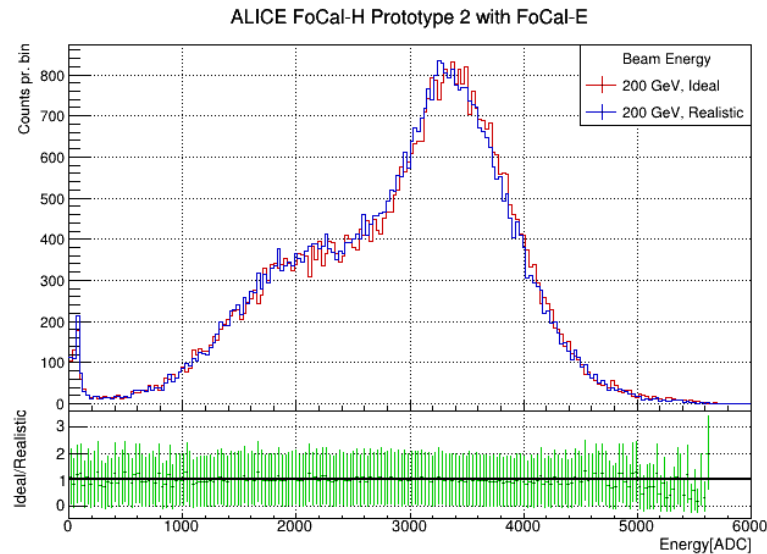


Figure 101: Comparison between simulations with (blue) and without (red) the implementing of larger inner and outer diameter of the copper-tubes used in the FoCal-H second prototype. The green line represents the calculated difference between the two simulations.

Figure 102 below shows two FoCal simulations at 200 GeV including FoCal-E in front of FoCal-H, with and without implementation of the FoCal-E update. In this update both the size of the pixel layers was changed, as well as the spacing between the pixel and pad layers.

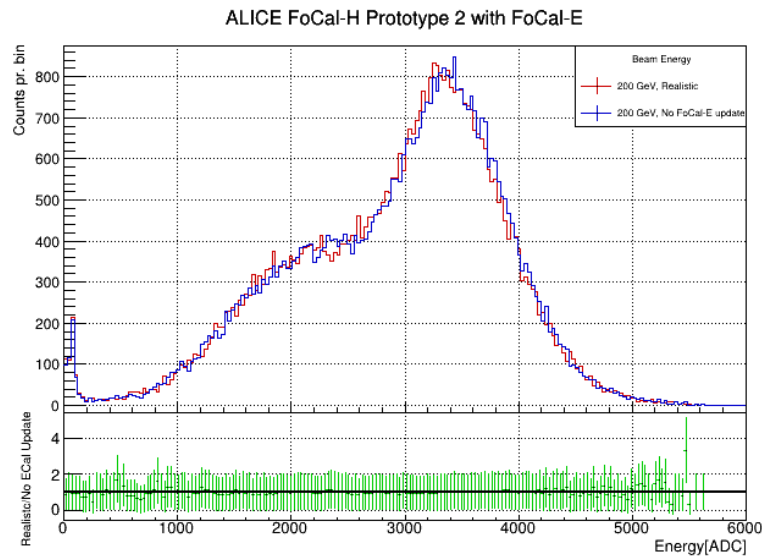
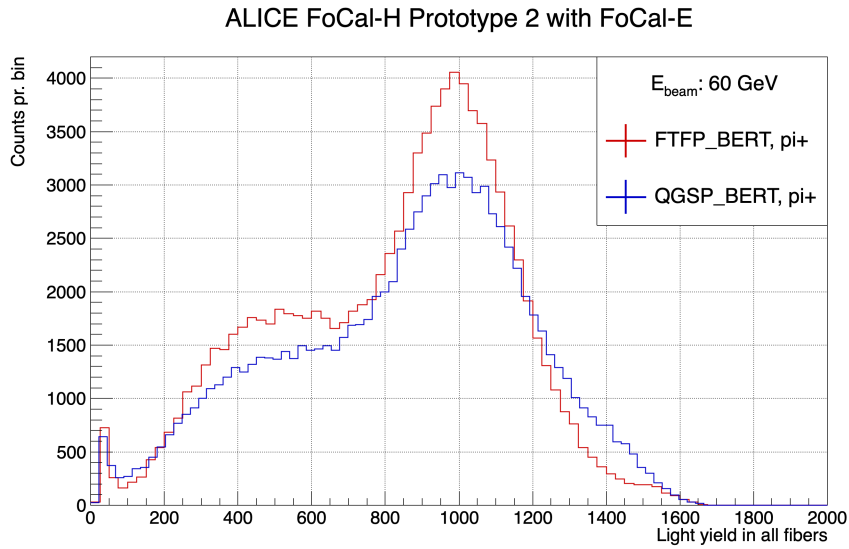


Figure 102: Comparison between simulation with (blue) and without (red) implementing a larger size of the pixel layers and smaller spacing between the pixel and pads layers in the FoCal-E prototype. The green line represents the calculated difference between the two simulations.

11.4.2 Simulations including FoCal-E physics list comparison

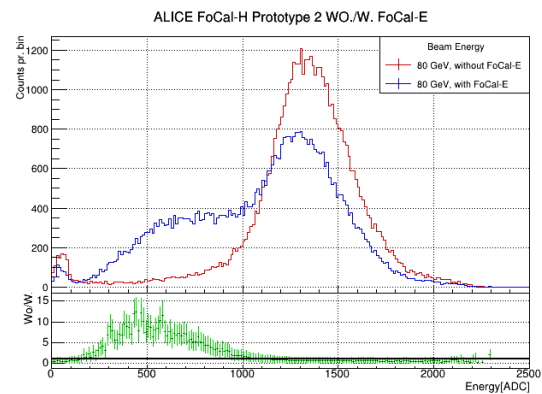
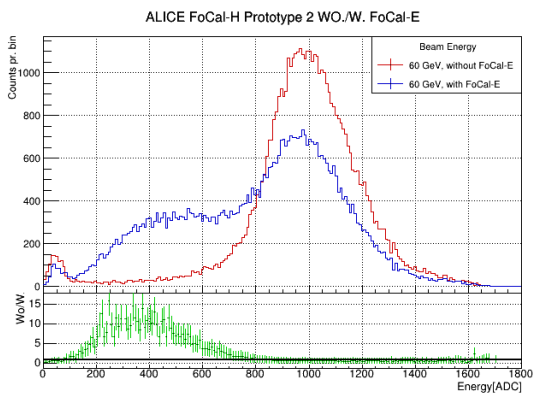
This section shows a comparison of the FoCal-H response for the detector including FoCal-E in front of FoCal-H, using the FTFP-BERT and QGSP-BERT physics list.

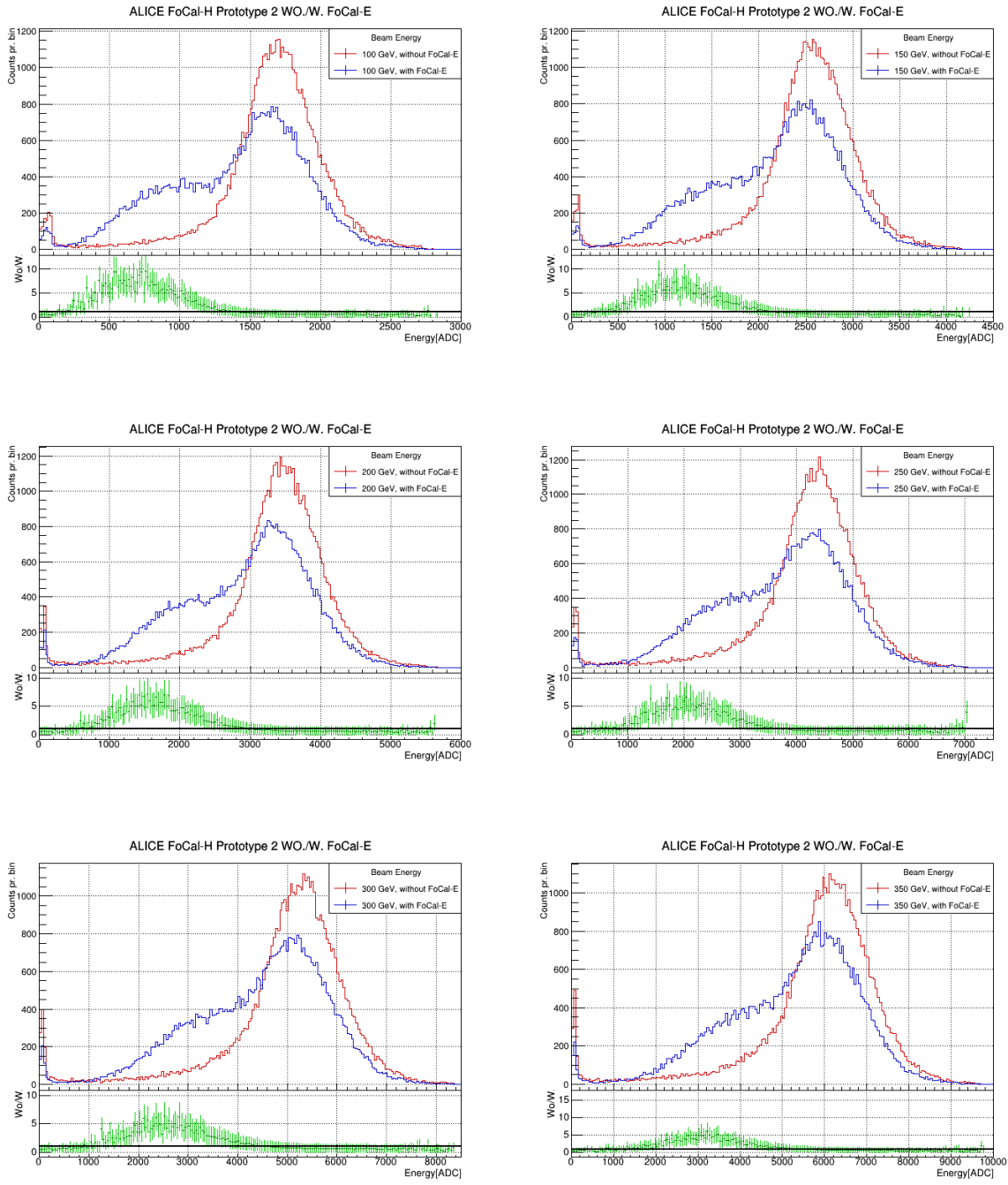


11.4.3 Simulations including and excluding FoCal-E

This section shows results from simulation studies not included in the simulation section 8.2.3. The figures in this section shows comparisons between the detector setups including and excluding FoCal-E in front of FoCal-H, for the simulations using the FTFP-BERT physics list.

11.4.3.1 FoCal-H second prototype





11.4.4 Comparison between simulation physics lists

This section shows results from simulation studies not included in the simulation section 8.2.3.3. The figures in this section shows comparisons between the two Geant4 physics lists, QGSP-BERT and FTFP-BERT. The simulations has been performed using the detector setups excluding FoCal-E in front of FoCal-H.

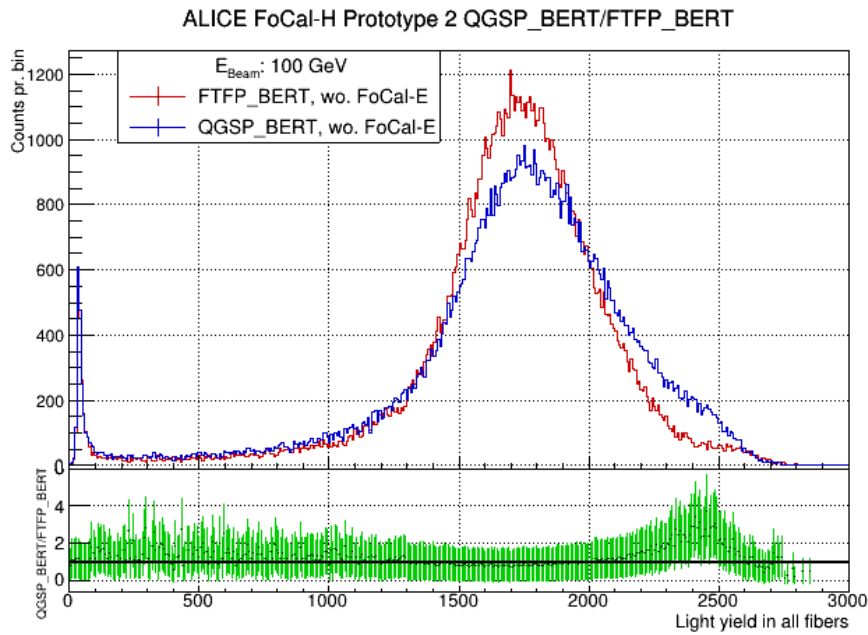


Figure 103: The figure shows a comparison between the physics list QGSP-BERT (blue) and FTFP-BERT (red) at 100 GeV, using the detector setup excluding FoCal-E in front of FoCal-H. The difference between the two simulations are indicates by the green line.

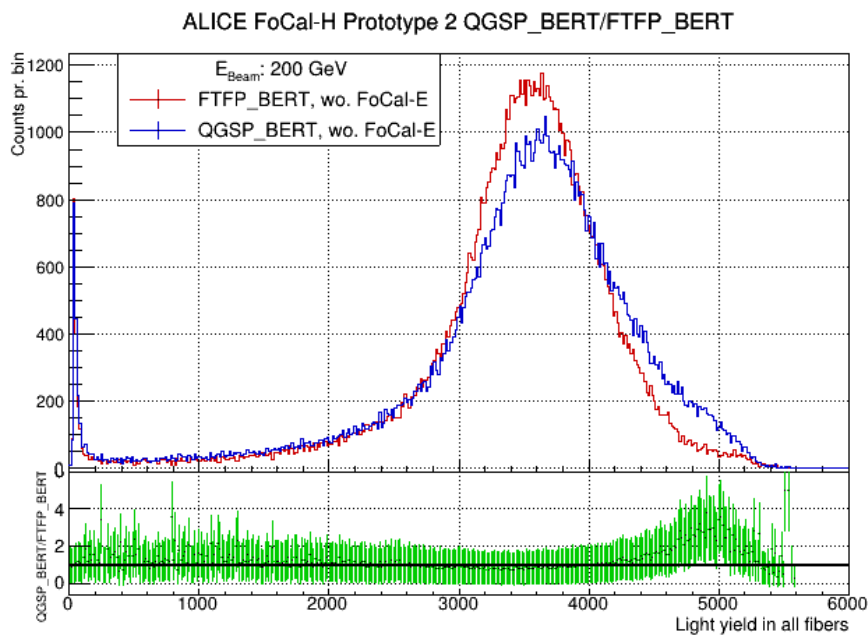


Figure 104: The figure shows a comparison between the physics list QGSP-BERT (blue) and FTFP-BERT (red) at 200 GeV, using the detector setup excluding FoCal-E in front of FoCal-H. The difference between the two simulations are indicates by the green line.

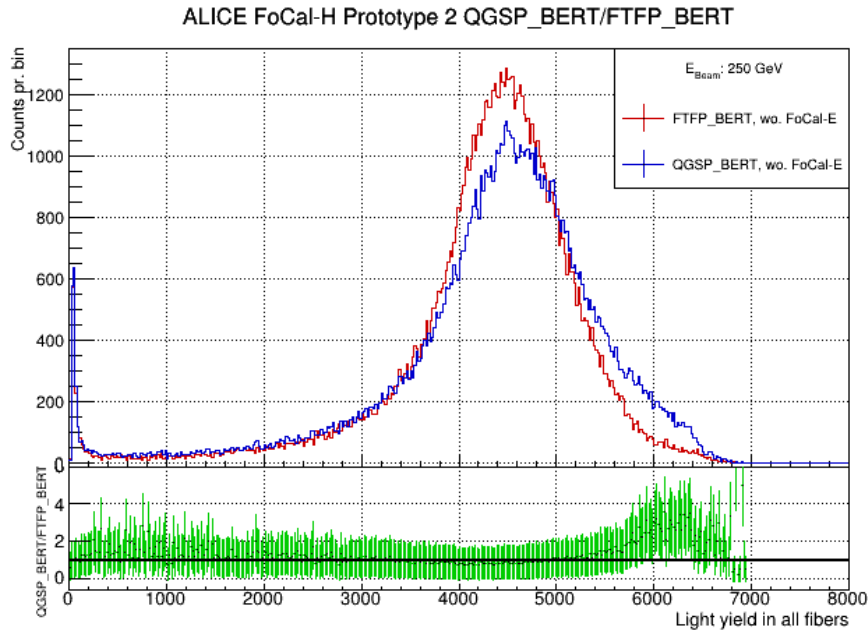
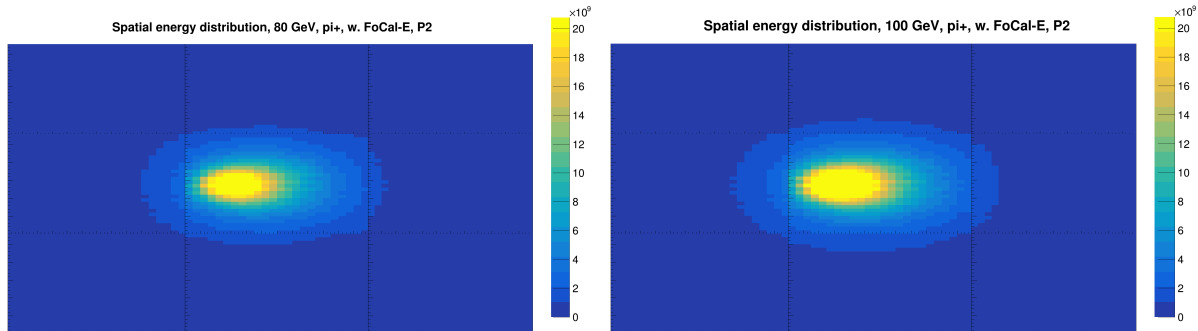


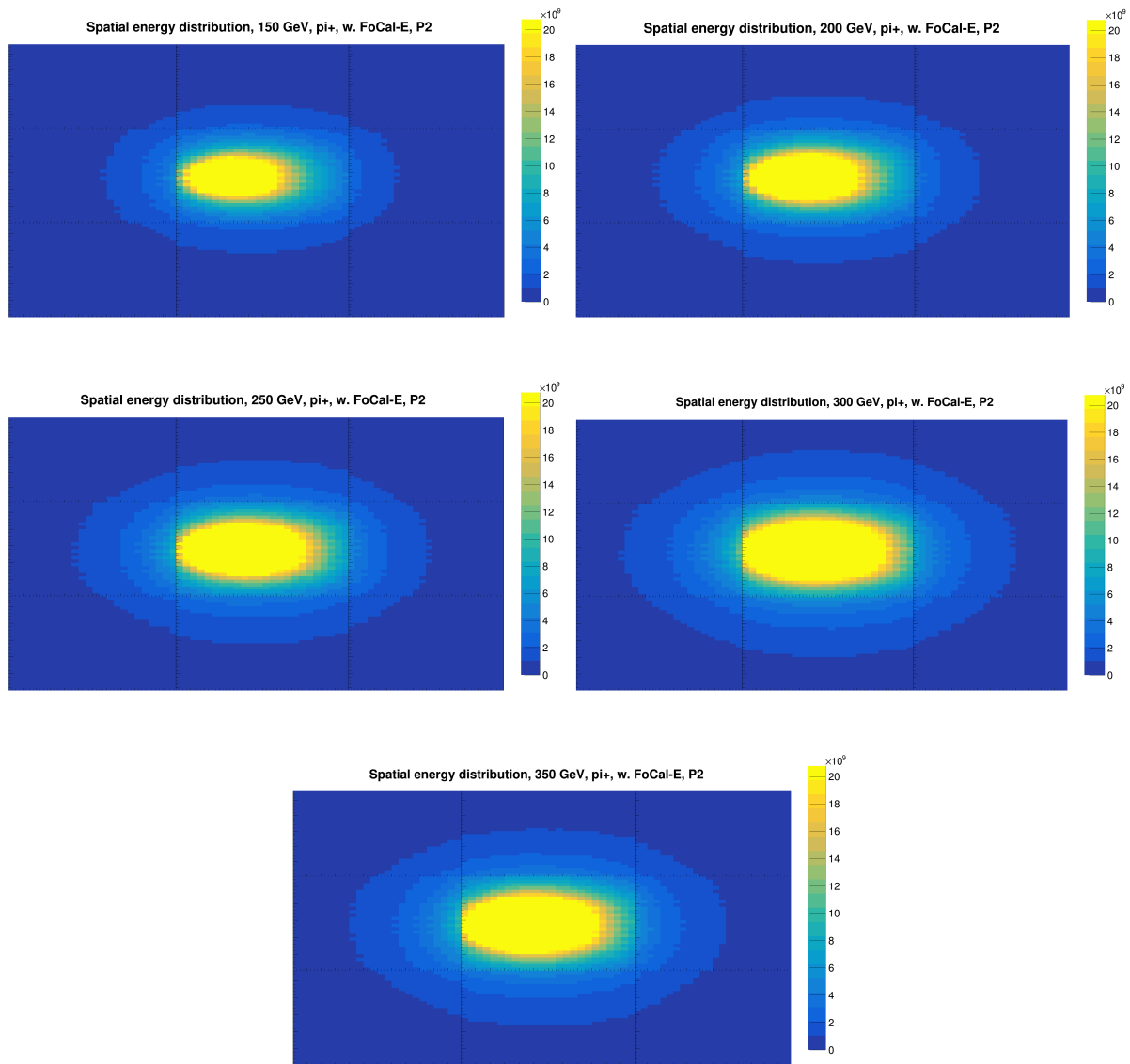
Figure 105: The figure shows a comparison between the physics list QGSP-BERT (blue) and FTFP-BERT (red) at 250 GeV, using the detector setup excluding FoCal-E in front of FoCal-H. The difference between the two simulations are indicates by the green line.

11.4.5 Shower containment

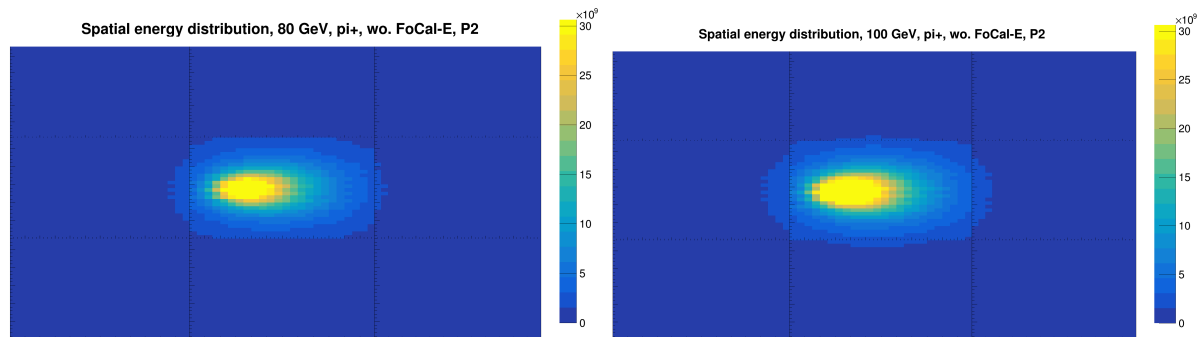
This section shows results of the simulations studies not included in the section 8.2.4 regarding the examination of lateral shower containment, of the FoCal-H second prototype. This section shows the spatial energy distribution, i.e. the particle shower size of an event, in the energy range from 80 GeV to 300 GeV, for the detector setup including and excluding FoCal-E in front of FoCal-H.

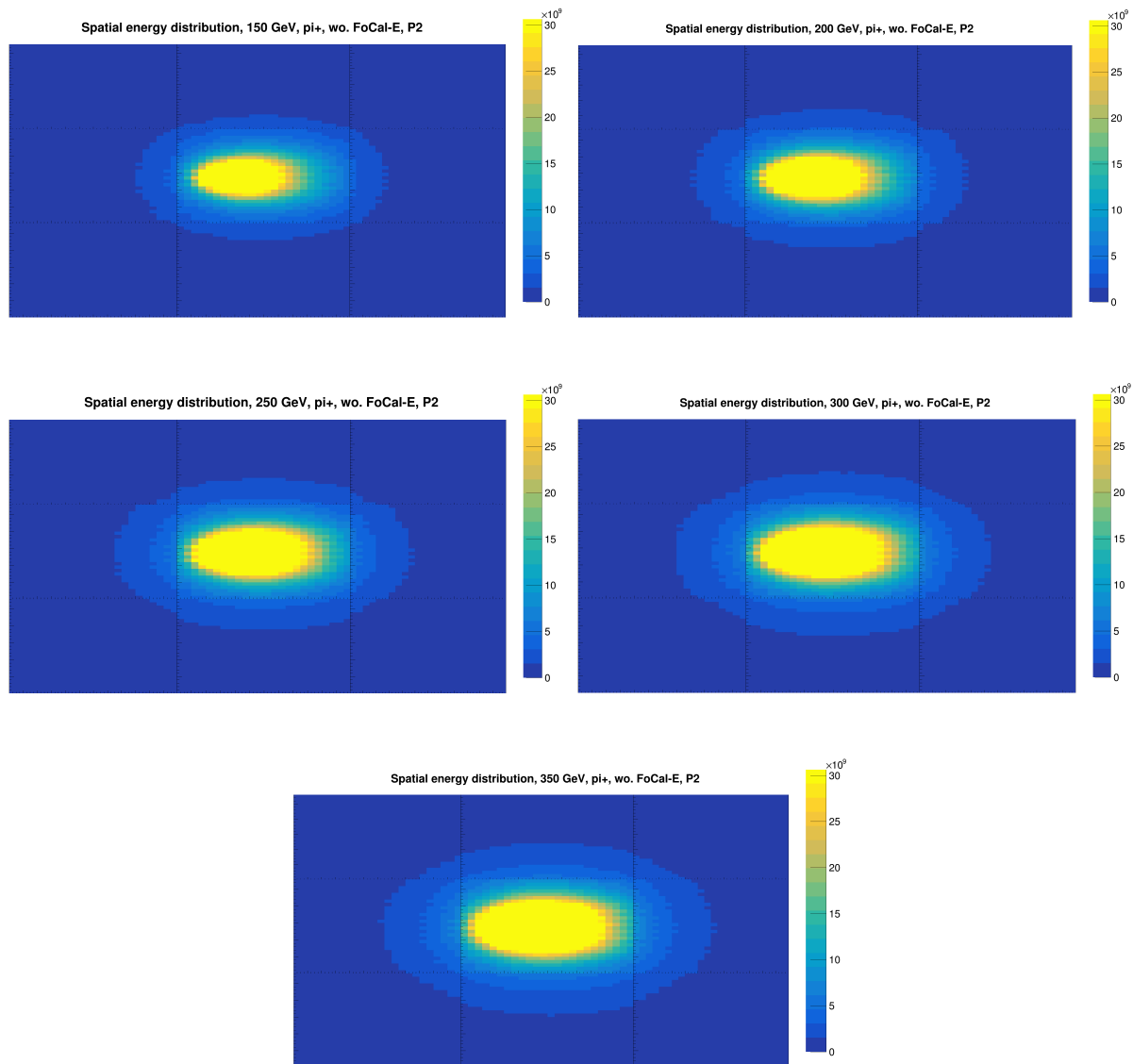
11.4.5.1 FoCal setup including FoCal-E





11.4.5.2 FoCal setup excluding FoCal-E





11.4.6 Position scan

This section includes information about the simulated position scan, e.g. two results from the position scan for testbeam data made in a first year project, the exact position of all the simulated beam-pipe positions, as well as the response curves and spatial energy distribution of the position scans not included in the position scan section 8.2.5.

11.4.6.1 First Year Project discovery

The following two response curves are from the position scan from the November 2022 SPS H2 testbeam. A couple of First Year students made a project involving the positions scan, and found a response curve, which seems to exclude the pre-shower peak. A gaussian function fit has been to the hadron peak [43]. Their position 5 and 7 corresponds to my position 2 and 3 respectively. I suspect that the rotation of FoCal-H in the simulations is rotated the other way in respect to the testbeam data.

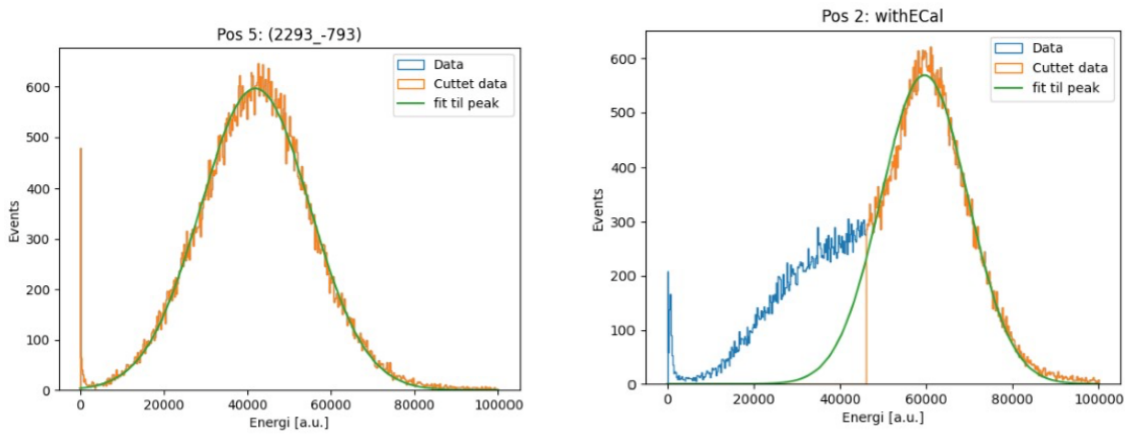


Figure 106: The figure shows two response curves from the position scan performed at the November 2022 SPS H2 testbeam, with FoCal-E in front of FoCal-H. The position scan from the testbeam data has been performed by a group of first year students. The left-side figure shows position 5, where the energy of the response curve is lower than usual and missing the pre-shower peak. The right-side figure shows the position 2, where the energy of the response curve is as usual and the pre-shower peak is present. Both positions has a gaussian function fitted to the peak [43].

11.4.6.2 Position of beam-pipe

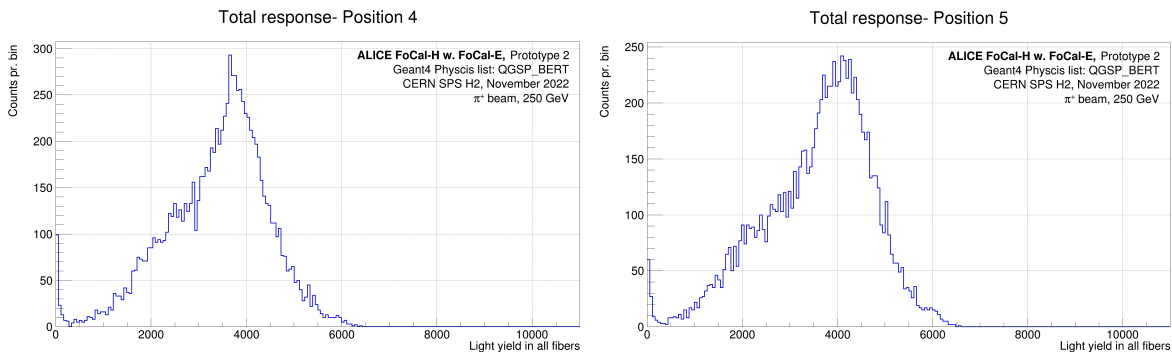
This section includes the table of all simulated beam-pipe position used in the position scan study.

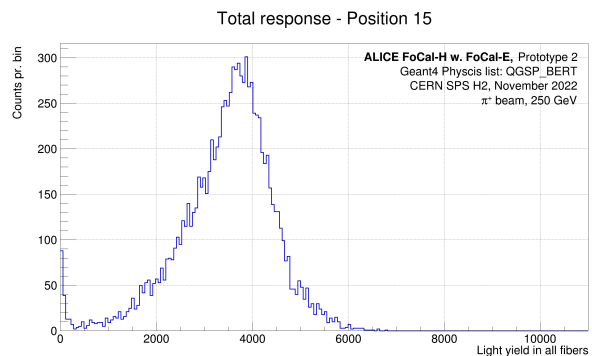
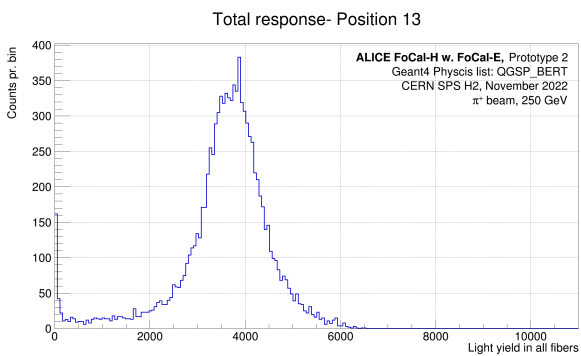
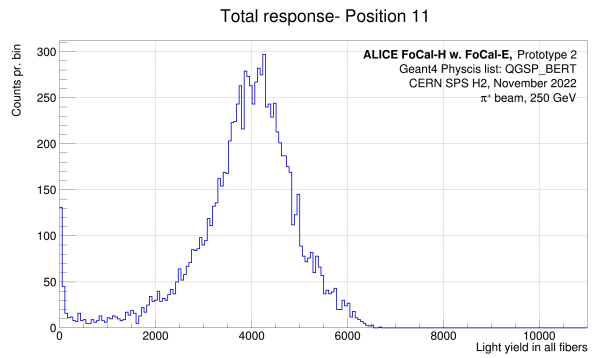
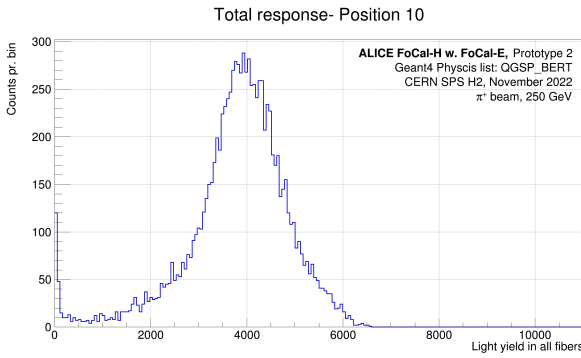
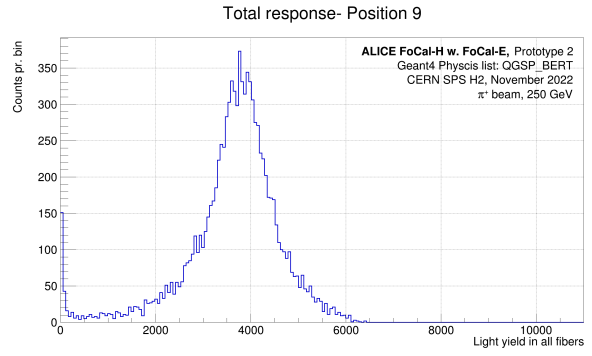
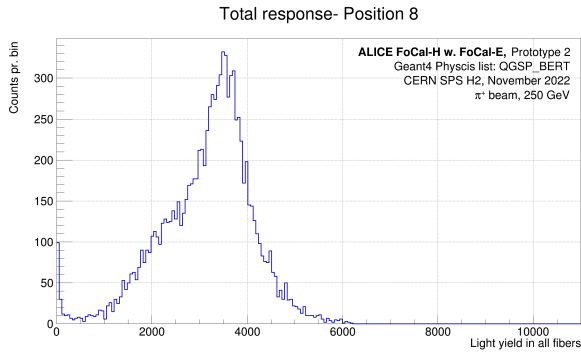
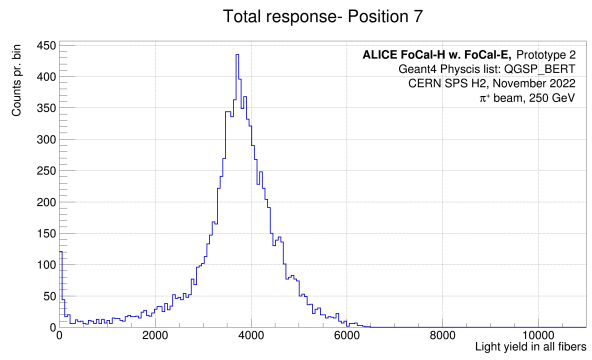
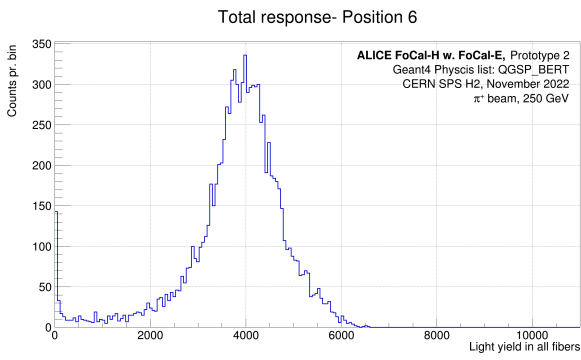
Positions of beam-pipe		
Position number	x- coor. offset [mm]	y-coor. offset [mm]
1	0	0
2	-32.375	+32.375
3	+32.375	+32.375
4	+10.791	+32.375
5	-32.375	+10.791
6	-32.375	+43.166
7	-43.166	+32.375
8	-21.584	+32.375
9	-21.584	+43.166
10	-43.166	+43.166
11	+21.584	+43.166
12	+32.375	+43.166
13	+43.166	+43.166
14	+43.166	+32.375
15	+43.166	+21.584
16	+32.375	+21.584
17	+21.584	+21.584
18	+21.584	+32.375
19	-21.584	+10.791
20	-21.584	0
21	-32.375	0
22	-43.166	0
23	-43.166	+10.791

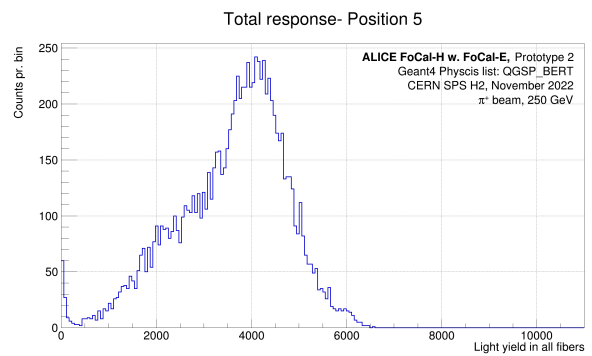
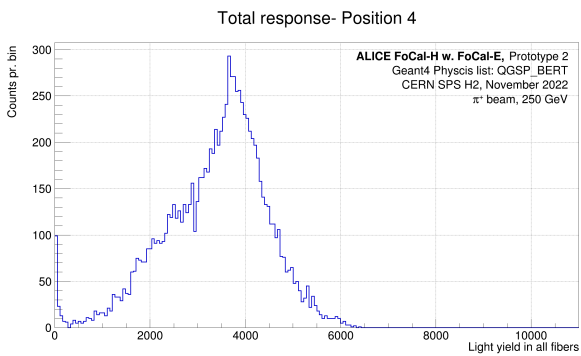
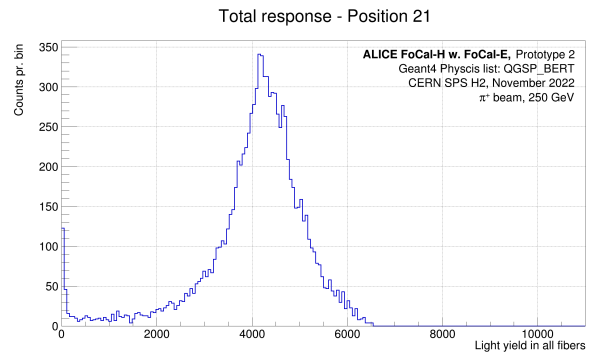
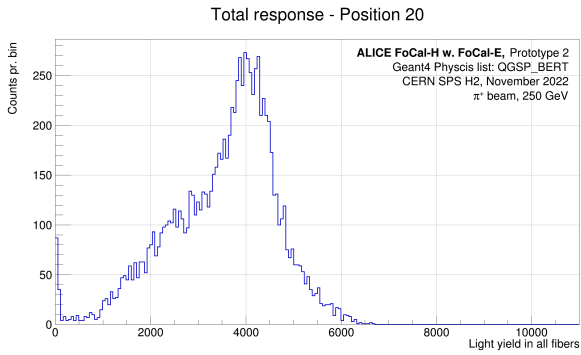
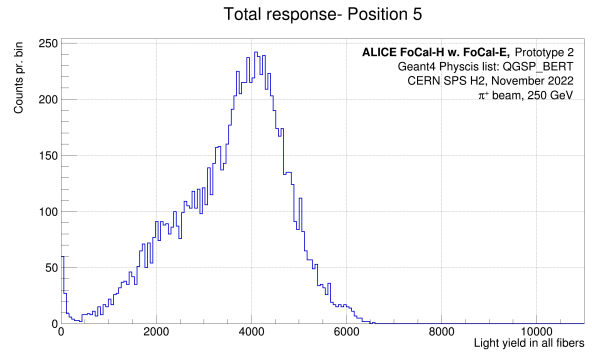
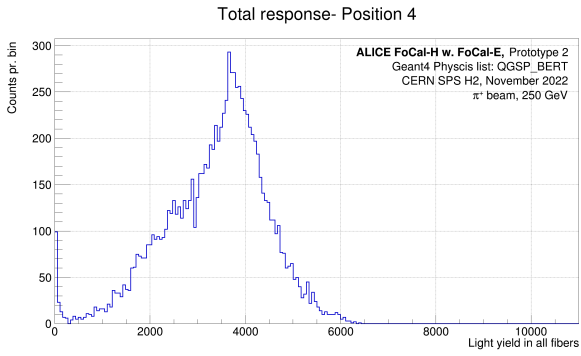
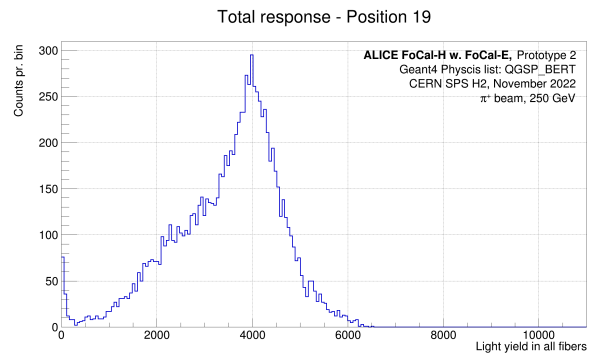
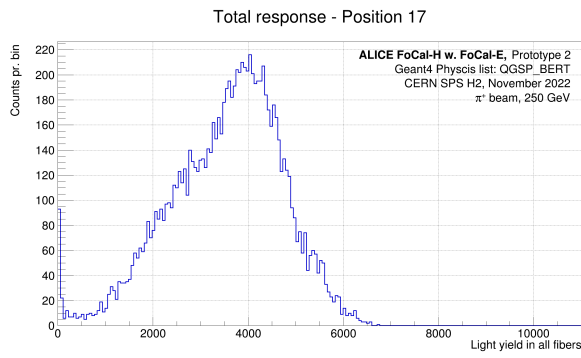
Table 3: That table lists the offset [mm] the beam-pipe has been moved in order to examine the intersection between the calorimeter modules, and the areas around.

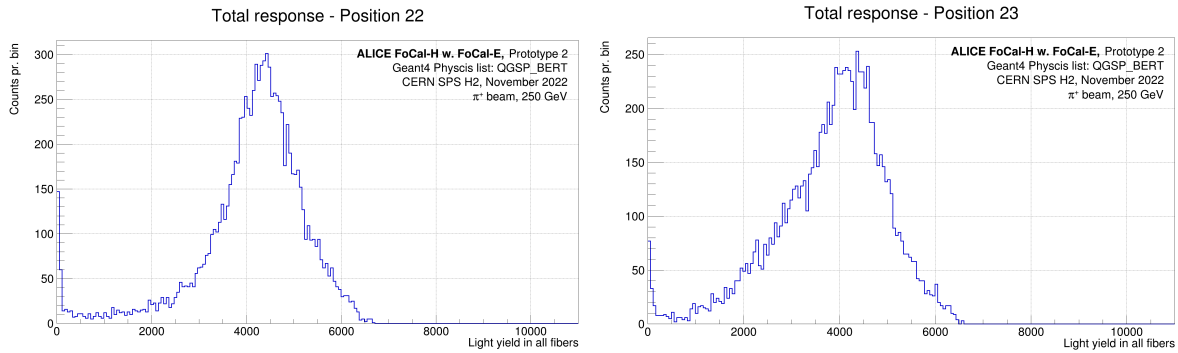
11.4.6.3 Response curves

This section shows results from the response curves not included in section 8.2.5. All figures of the simulated response curves are performed at 250 GeV, using the detector setup including FoCal-E in front of FoCal-H.



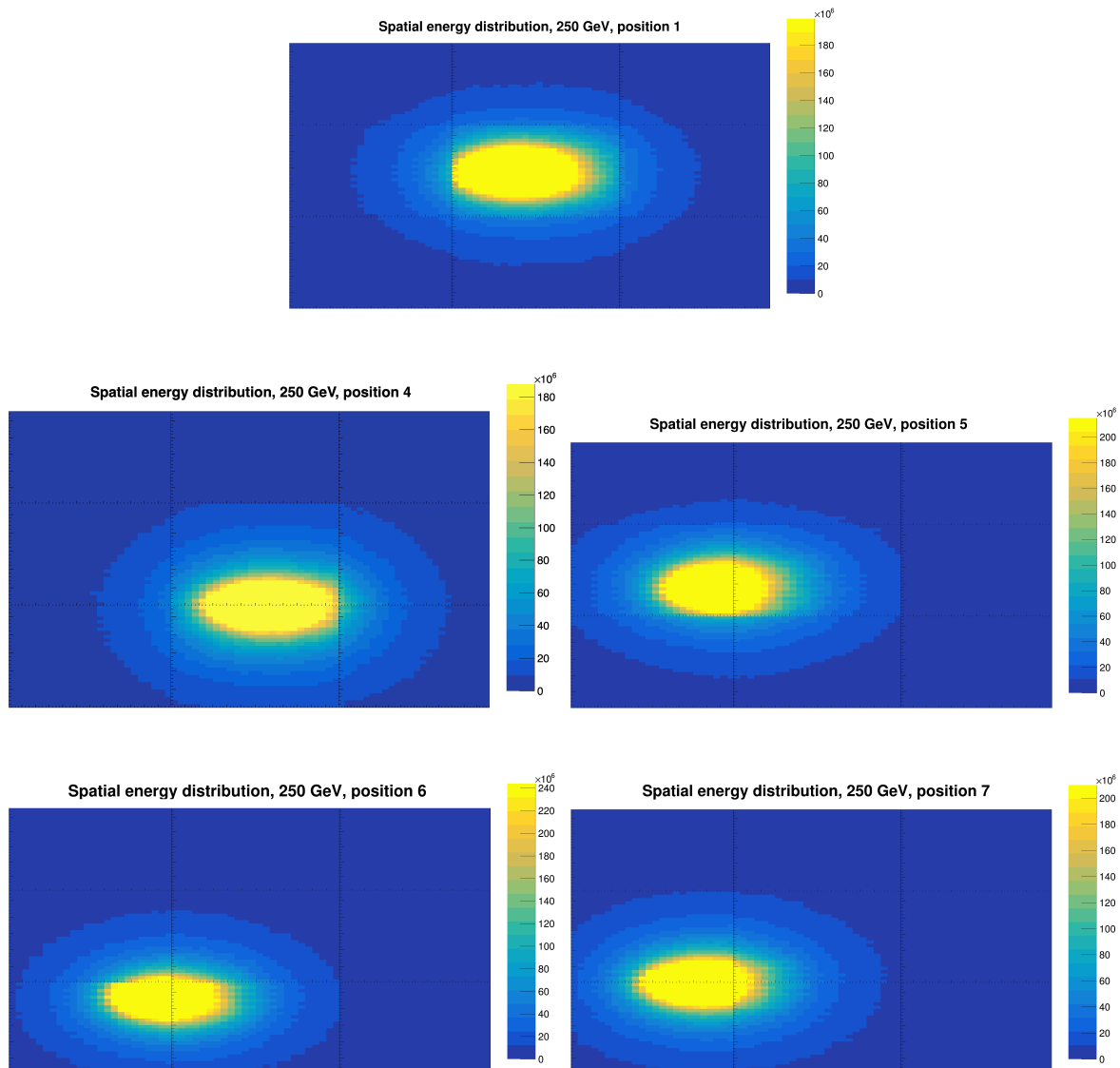


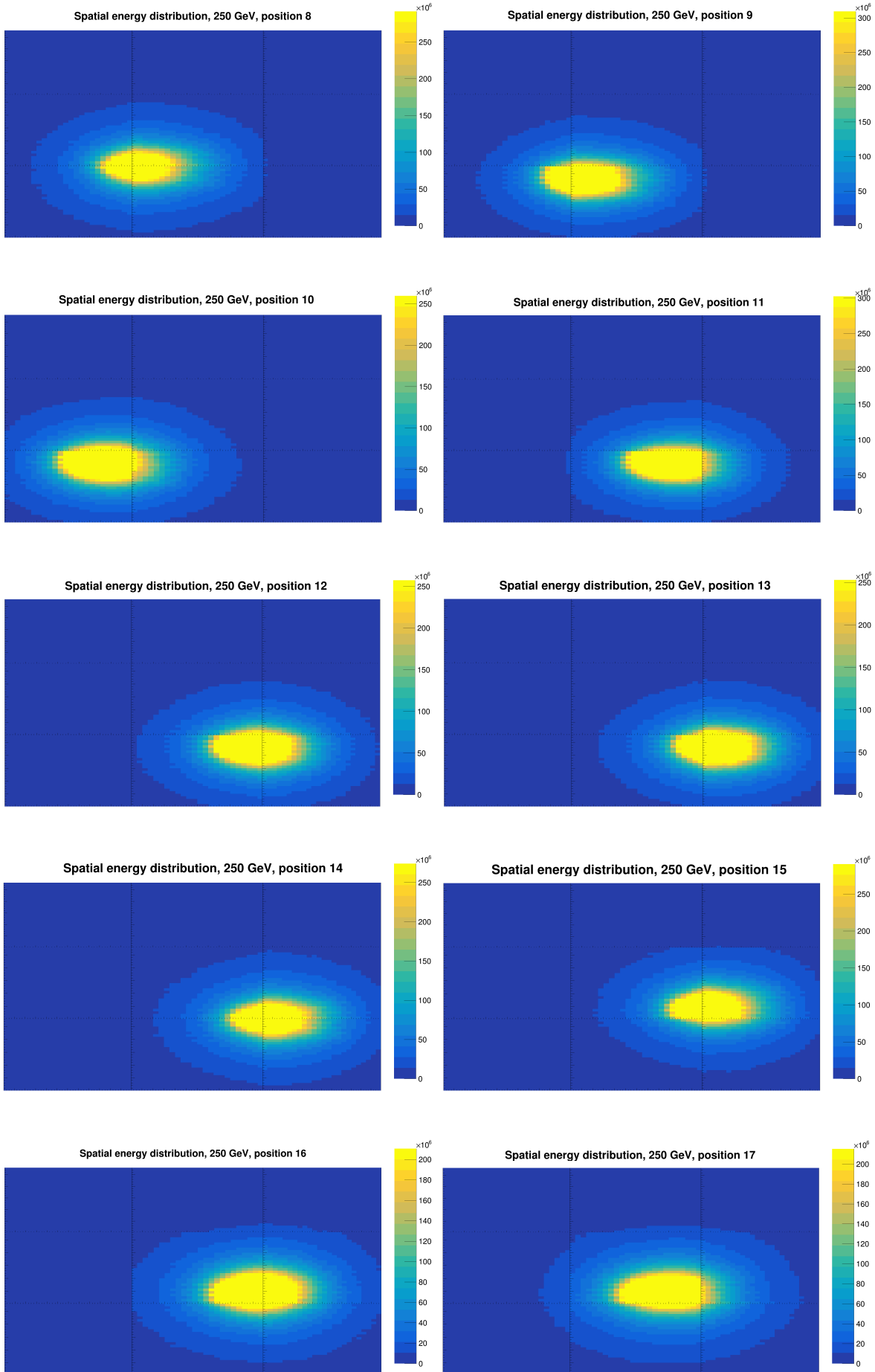


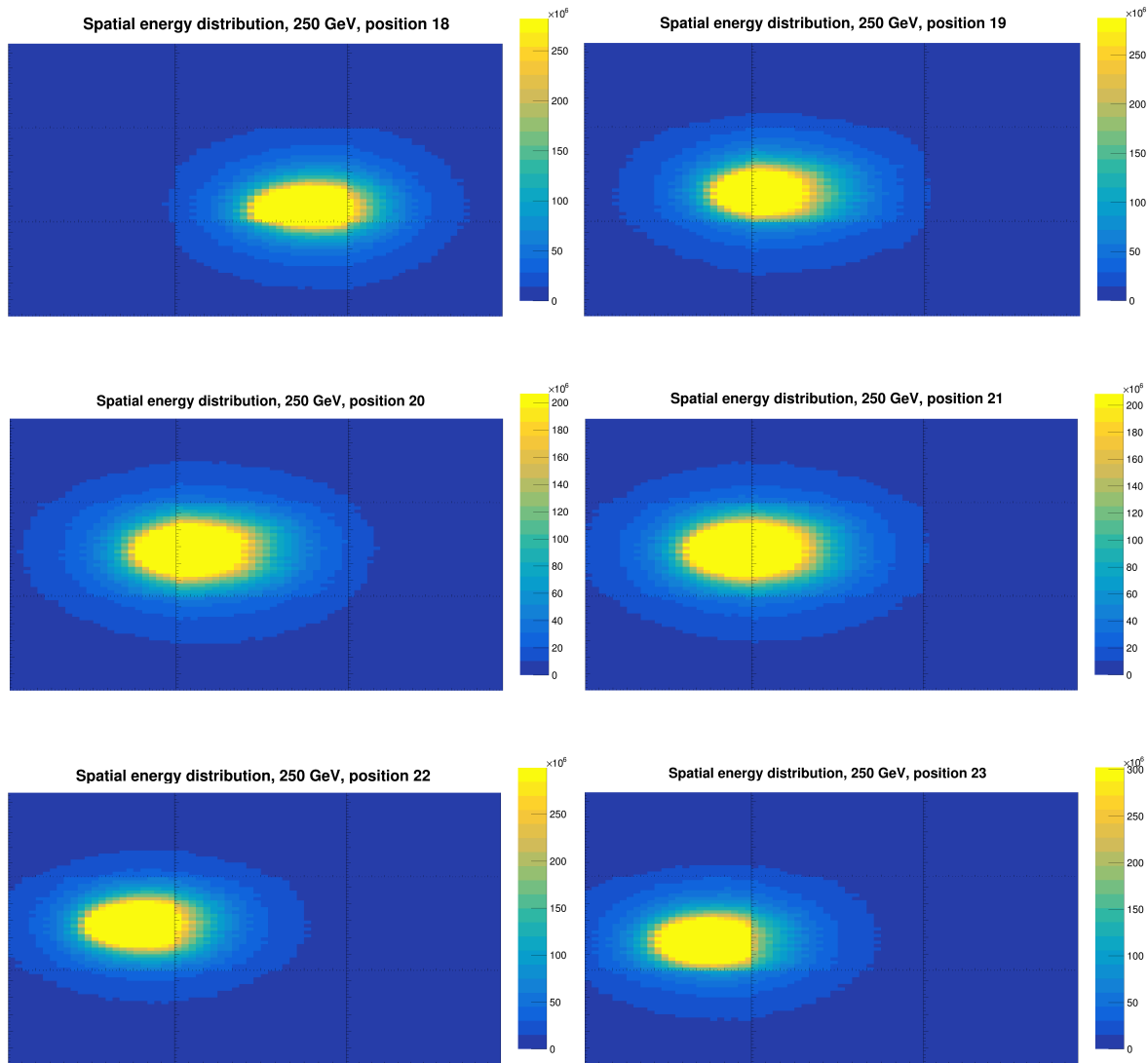


11.4.7 Spatial energy distribution

This section shows results from the spatial energy distributions not included in section 8.2.5. All figures of the simulated spatial energy distributions are performed at 250 GeV, using the detector setup including FoCal-E in front of FoCal-H.







11.5 Comparison between testbeam data and simulation data

This section shows results of various studies performed to compare the testbeam data and the simulation data, using the November 2022 SPS H2 testbeam setup. The results shown in this section was not included in section 8.3.

11.5.1 Difference between Gaussian and Crystal Ball function fit

Figure 107, shown in this section visualises the difference between a crystal ball function fit and a gaussian function fit to the hadron peak seen in the response of FoCal-H.

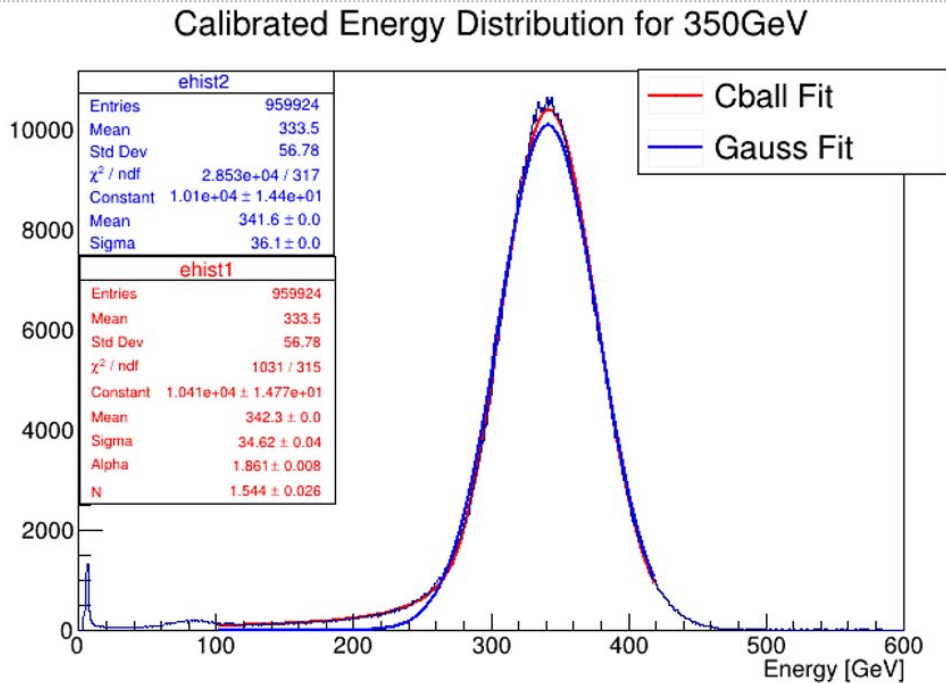
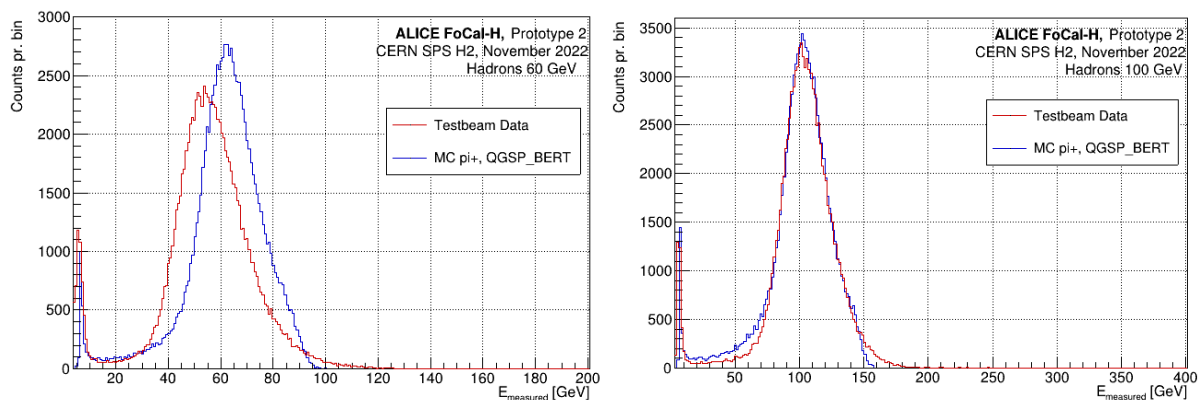


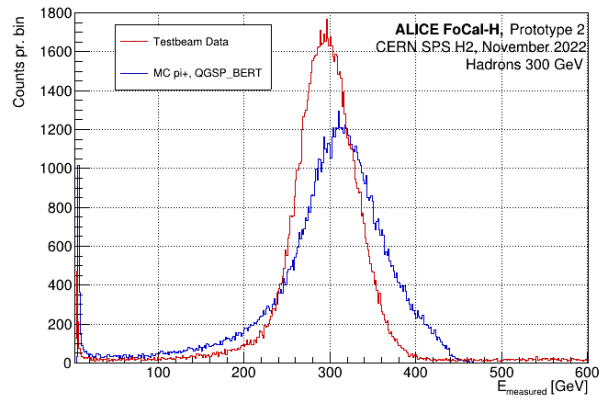
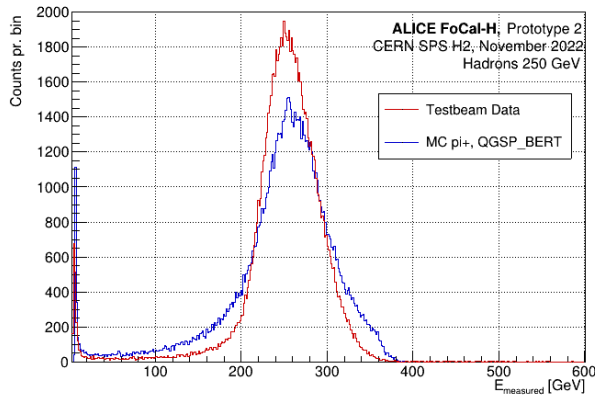
Figure 107: The figure shows the total charge of a measurement at 350 GeV hadrons without FoCal-E in front of FoCal-H for the testbeam data. To the total charge to different fit are plotted to the curve, namely a gaussian function fit and a crystal ball function fit. The crystal ball fit takes the lower energy tail into account, whereas the gaussian function fit does not take this into account [42].

11.5.2 Calibrated total charge

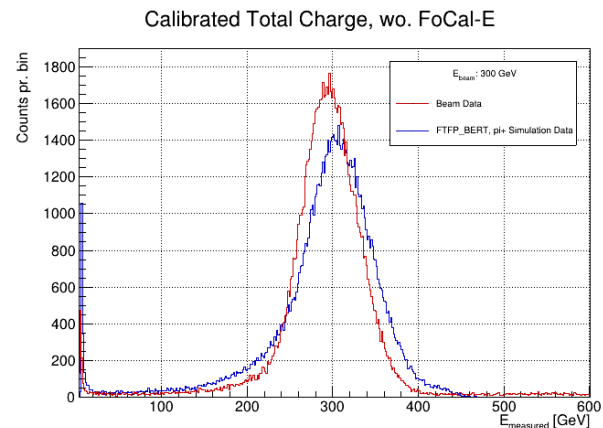
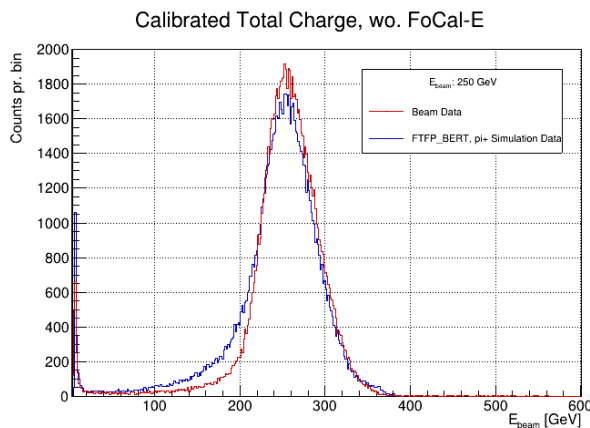
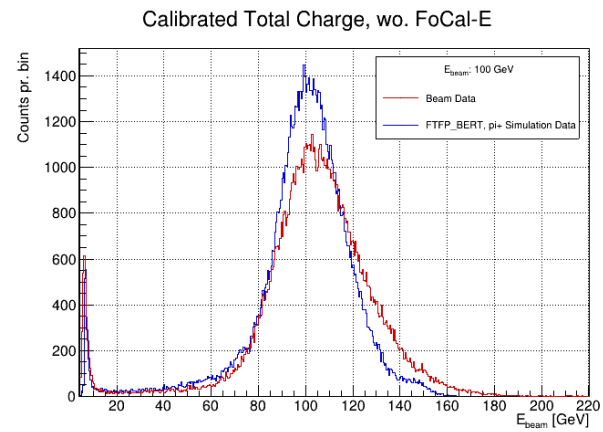
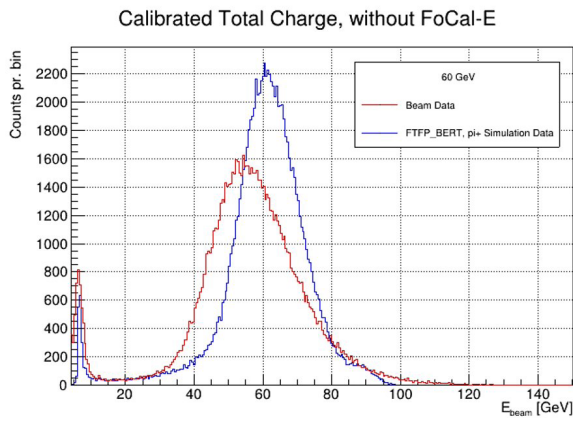
The figures in section 11.5.2.1-11.5.2.2 show the calibrated total charge for testbeam data and pion simulation data at different energies. The Testbeam data is compared to the simulations with the two Geant4 Physics lists QGSP-BERT and FTFP-BERT.

11.5.2.1 QGSP-BERT and Testbeam data



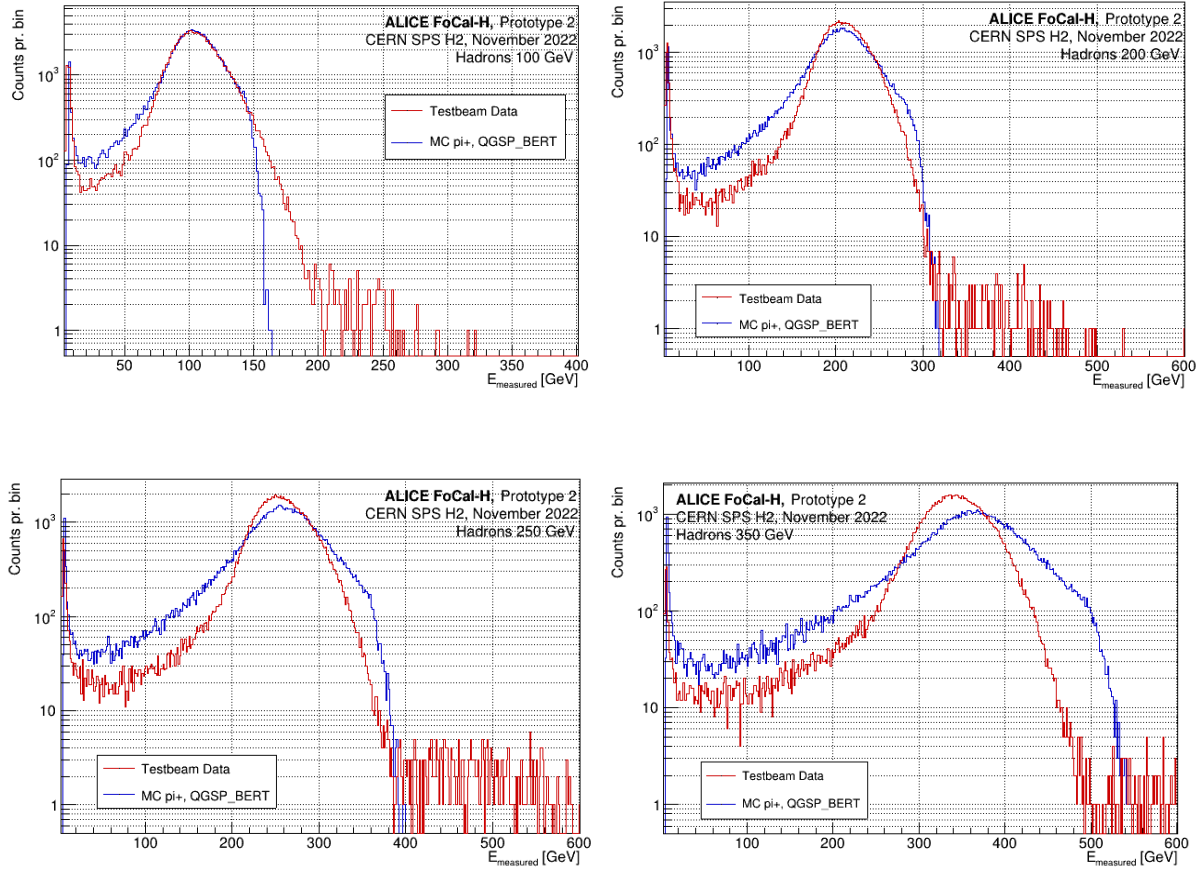


11.5.2.2 FTFP-BERT and Testbeam data



11.5.3 Saturation

This section shows results from the saturation study not included in section 8.3.2.1. The results in this section shows the response curves at a logarithmic scale for the testbeam data and the simulation using the QGSP-BERT physics list.



11.5.4 Punch through peak

This section shows results from the punch through peak study not included in section 8.3.3. The results in subsection 11.5.4.1 show comparisons of the punch through peak for the testbeam data and the simulations using the QGSP-BERT physics list (see figure 108), as well as a comparison between testbeam data, pion simulations using the QGSP-BERT physics list and muon simulations. The latter has been normalized with respect to the hadron peak, due to the different amount of simulated event between the pion and muon simulation.

The results in subsection 11.5.4.2 shows the corresponding comparison, as done in 11.5.4.1 for the QGSP-BERT physics list.

11.5.4.1 QGSP-BERT physics list

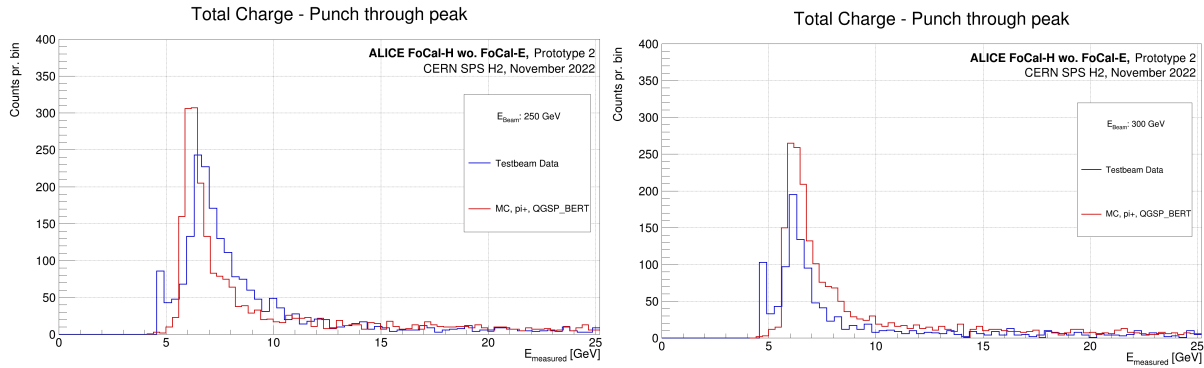


Figure 108: The figure shows two comparisons of the punch through peak of the testbeam data and a pion simulation, using the QGSP-BERT physics list. The left-side shows the comparison at 250 GeV, where the right-side figure shows the comparison at 300 GeV.

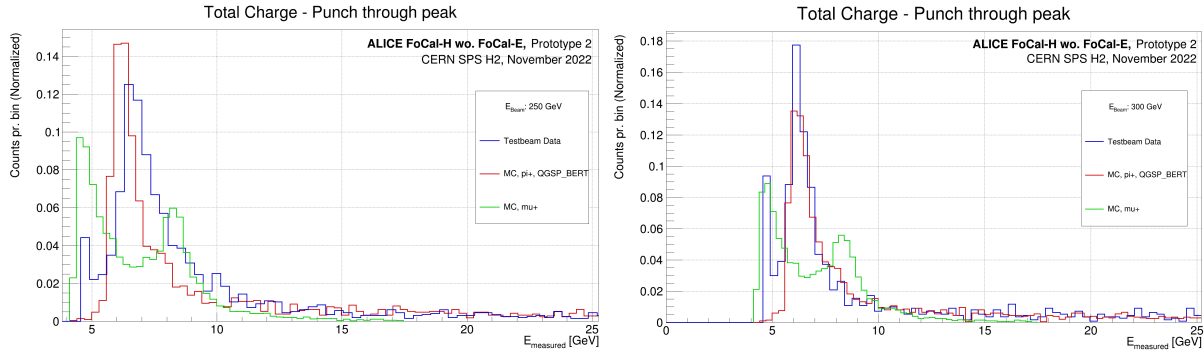
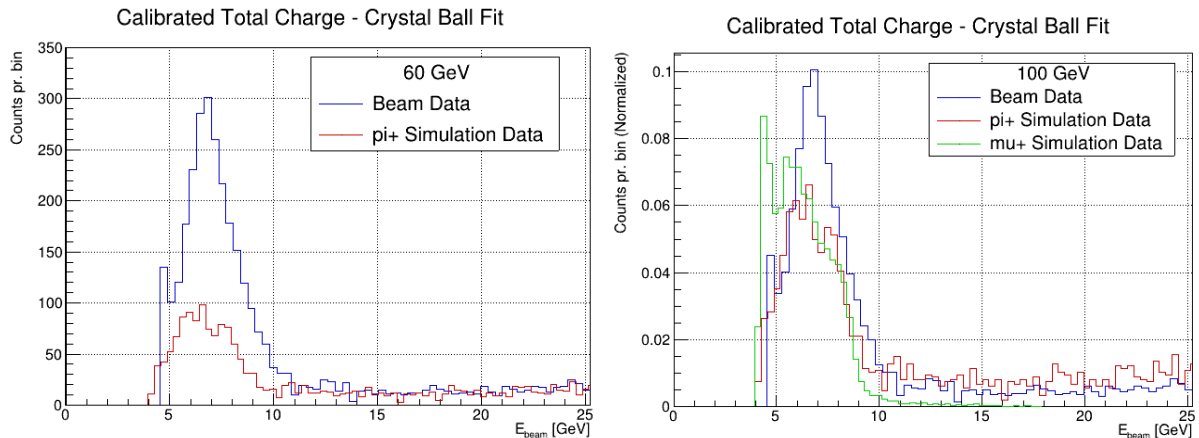
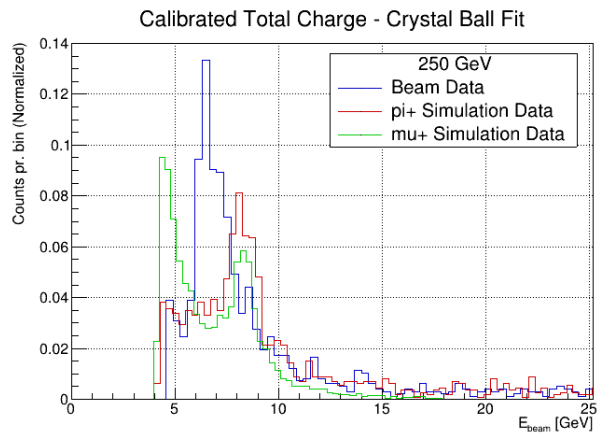
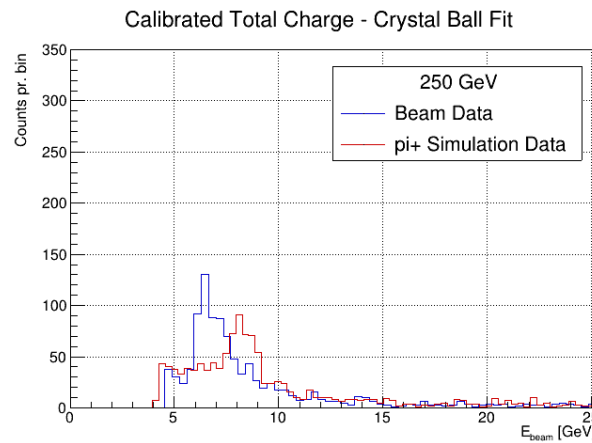
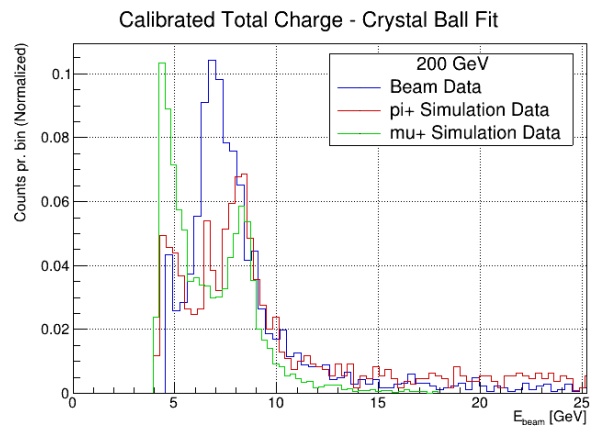
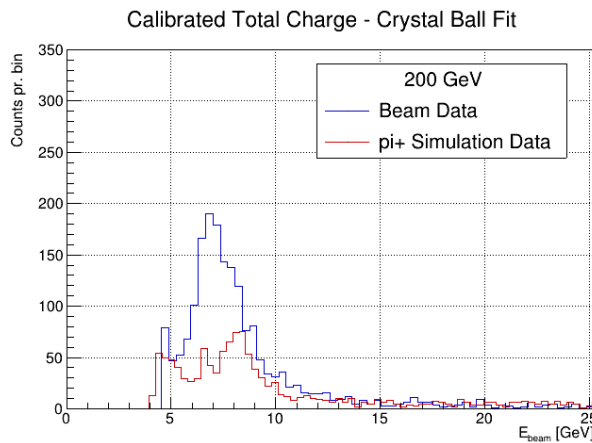
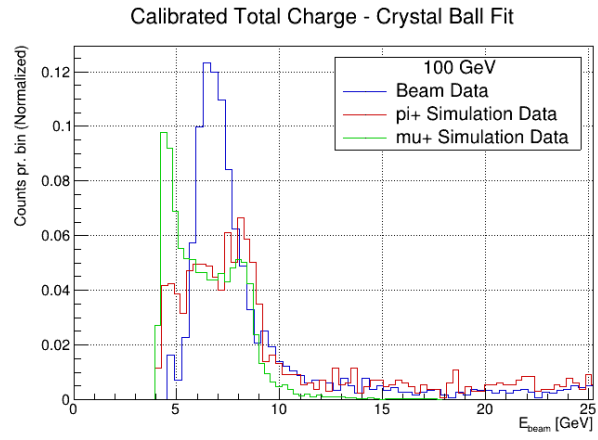
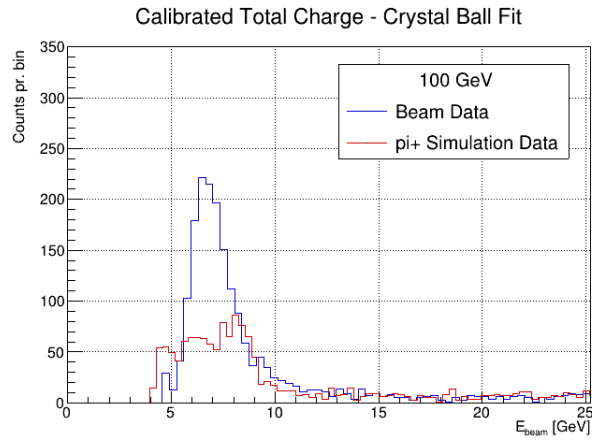
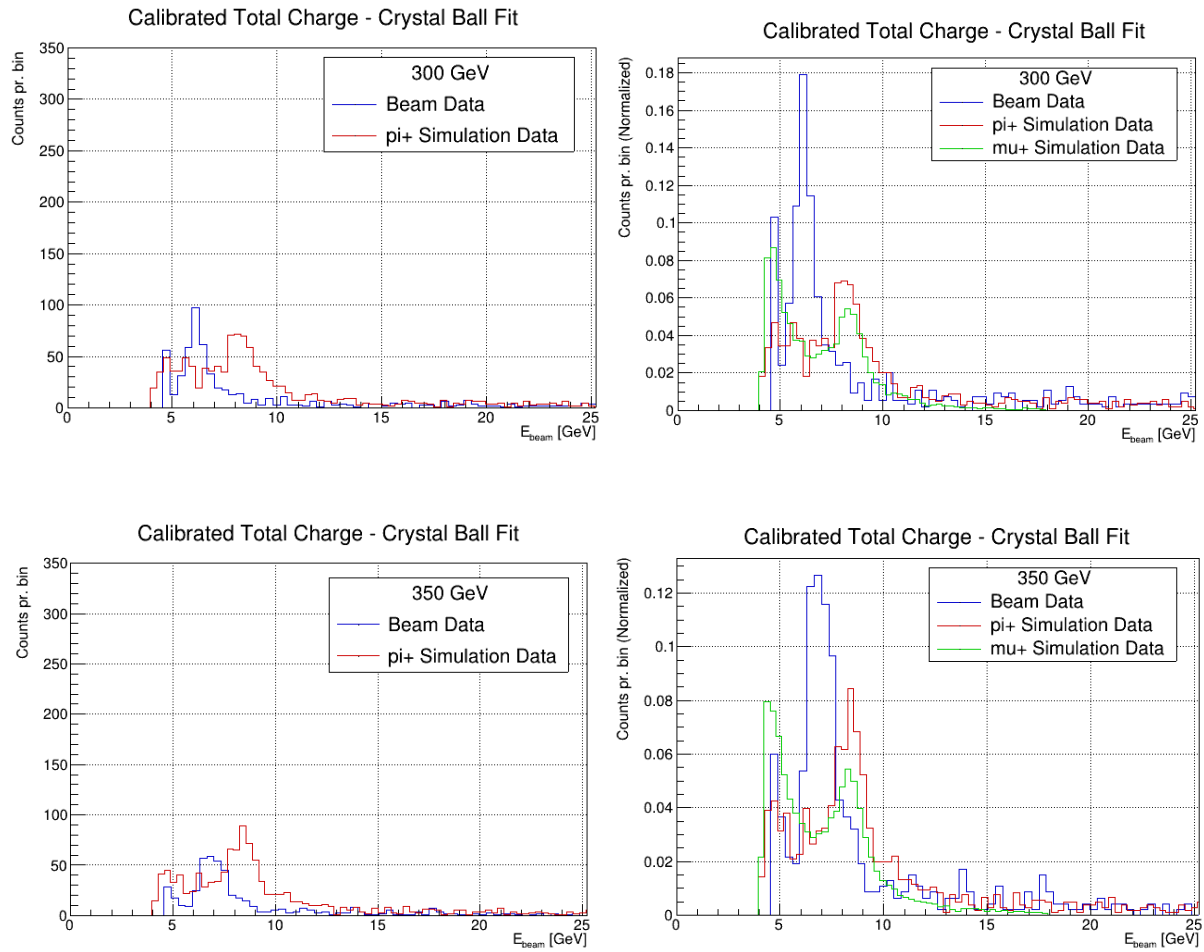


Figure 109: The figure shows two comparisons of the punch through peak of the testbeam data, a pion simulation using the QGSP-BERT physics list, and a muon simulation. The left-side shows the comparison at 250 GeV, where the right-side figure shows the comparison at 300 GeV

11.5.4.2 FTFP-BERT physics list







11.5.5 Rotation of FoCal-H

This section shows results not included in the study of the rotation of FoCal-H in section 8.3.3.1.

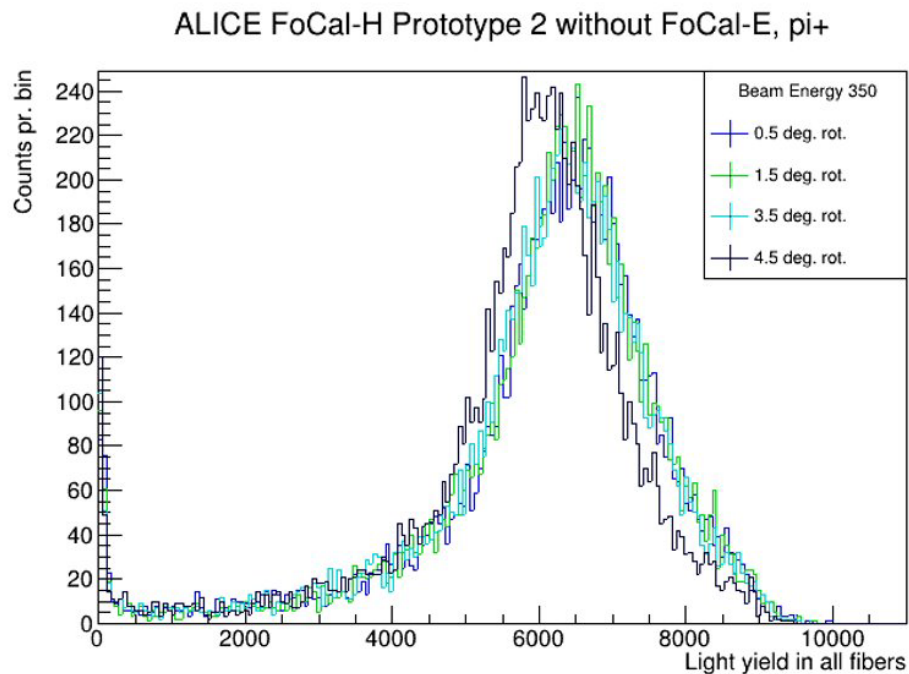
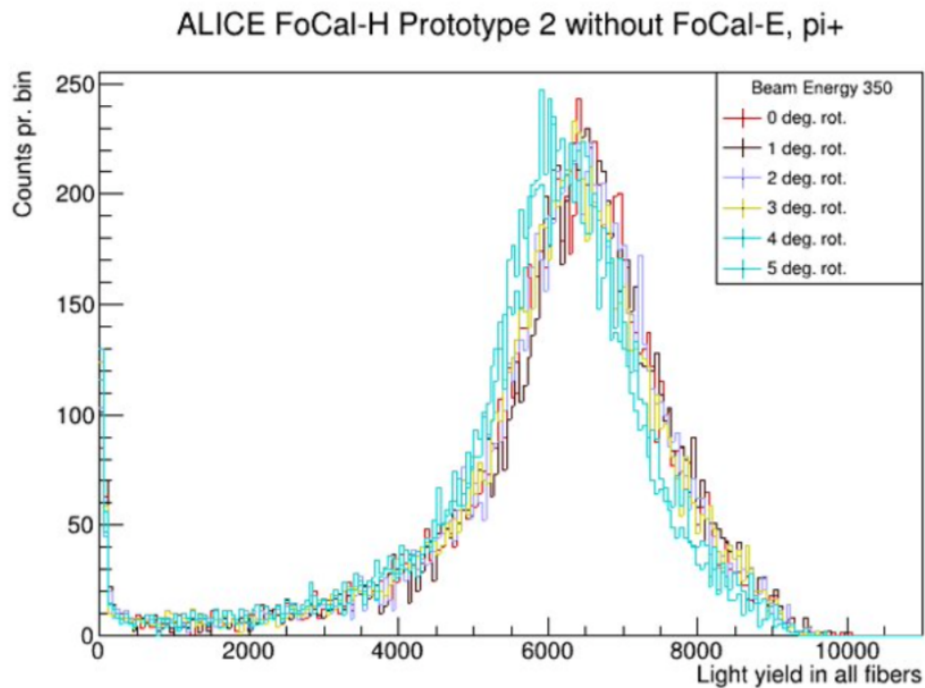


Figure 110: The figure shows a simulation using a 350 GeV pion beam with rotations of FoCal-H from 0 degrees to 5 degrees. The top figure shows the response in FoCal-H for rotations in intervals of 0.5 degrees, whereas the bottom figures shows the corresponding responses for intervals of 1 degree.

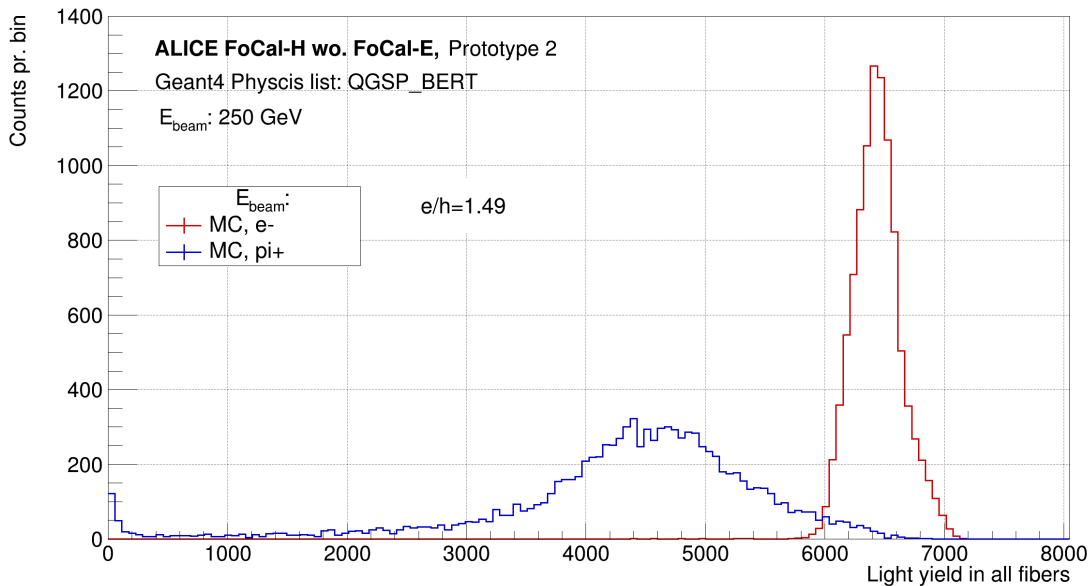
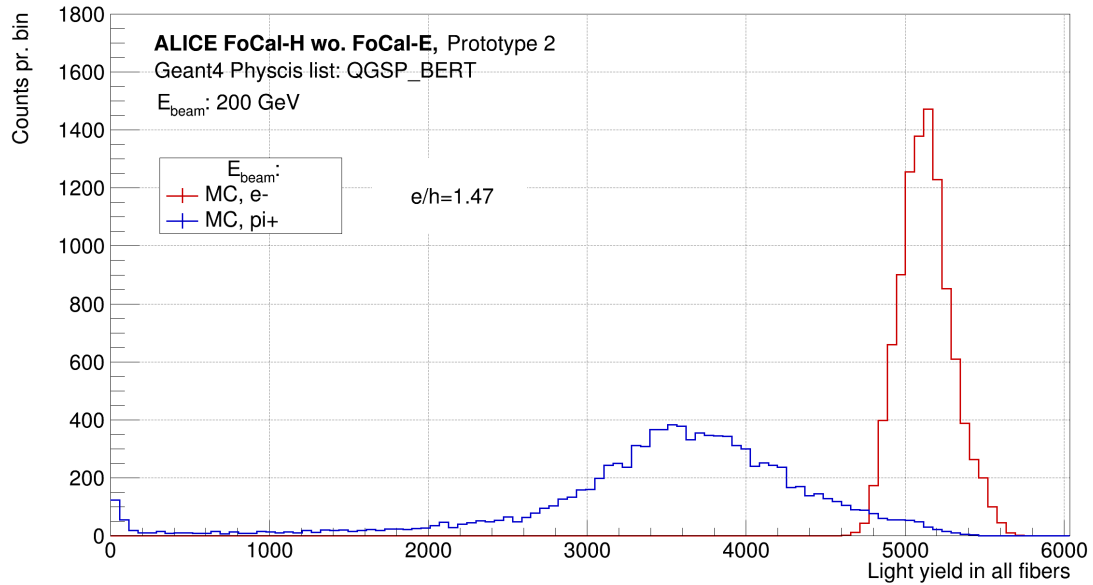
11.6 FoCal-H third prototype

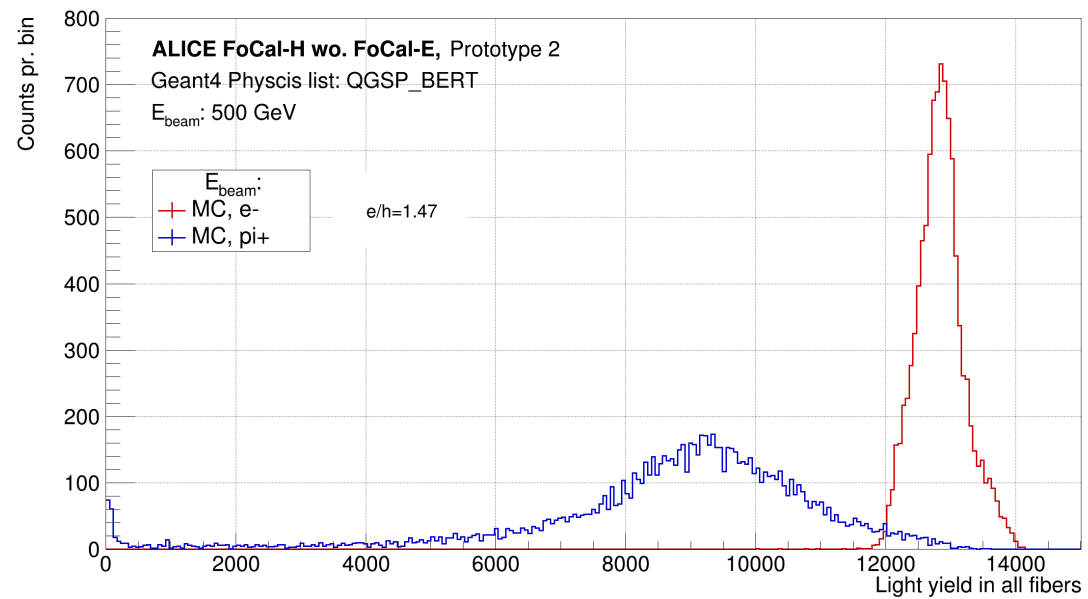
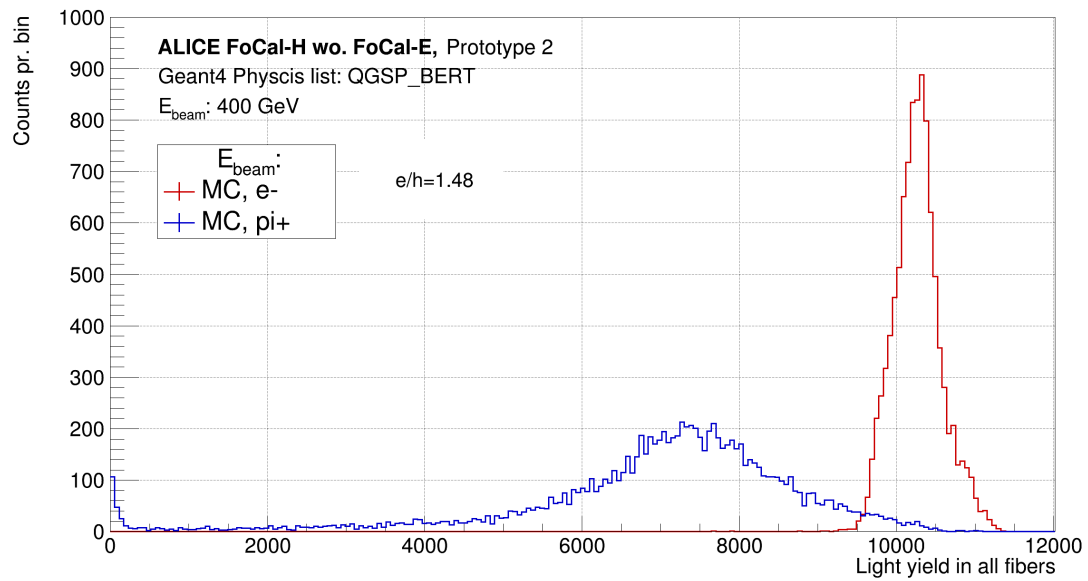
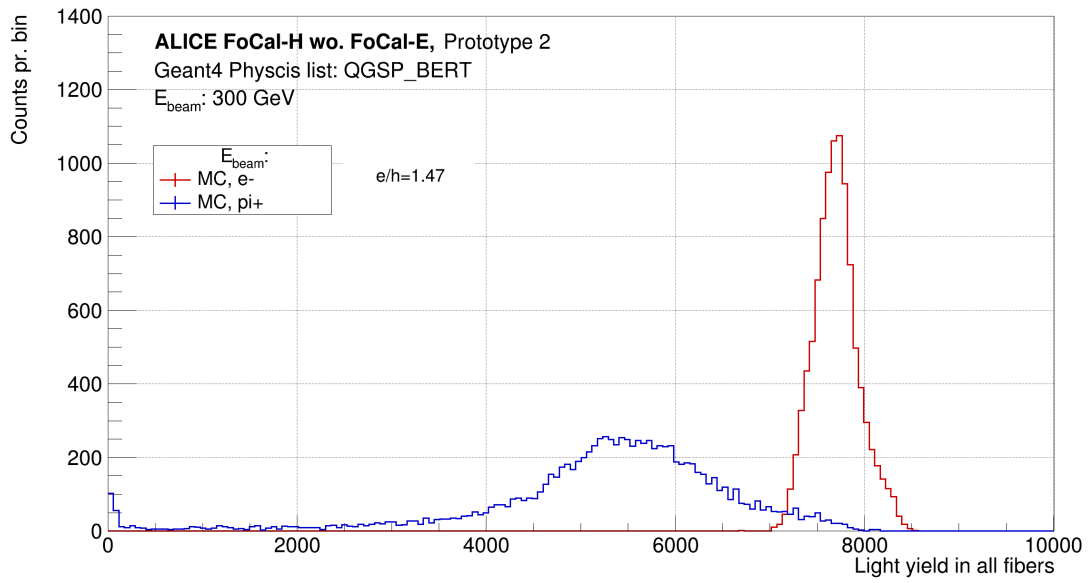
This section shows results from various studies performed for the FoCal-H third prototype not included in section 9.

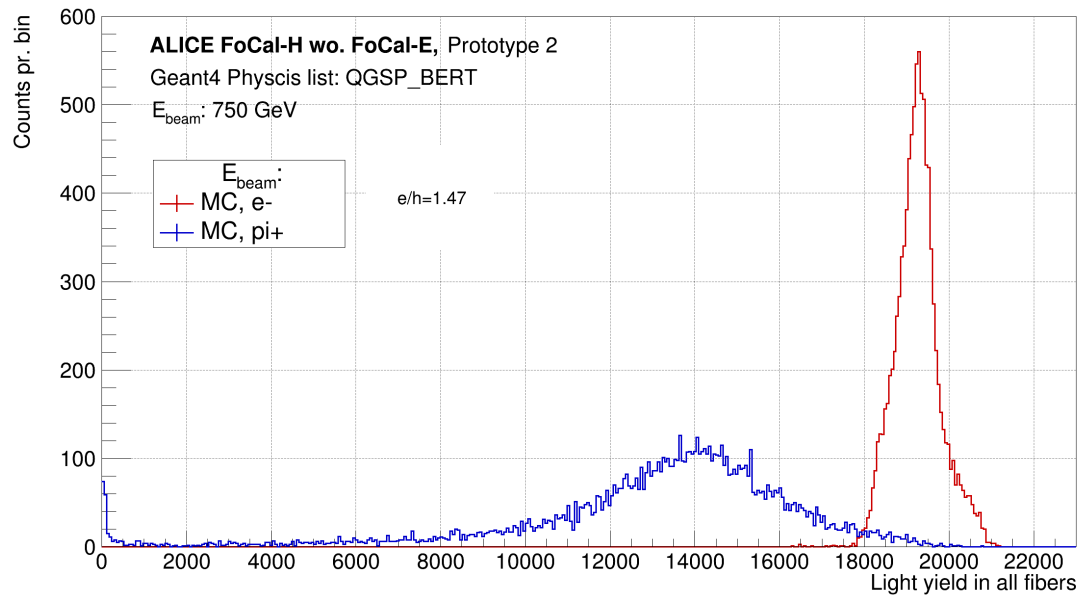
11.6.1 Compensation

This section shows results of compensation study performed for the FoCal-H second and third prototype not included in section 9.2.1. The results of the computed compensations for the FoCal-H second prototype can be seen in section 11.6.1.1 and for the third prototype in section 11.6.1.2.

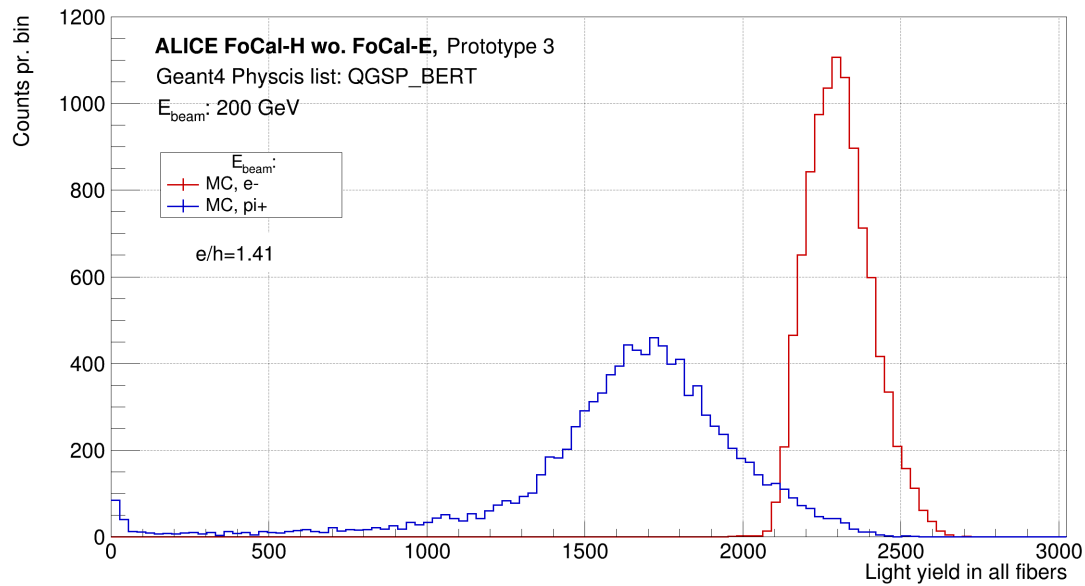
11.6.1.1 FoCal-H second prototype

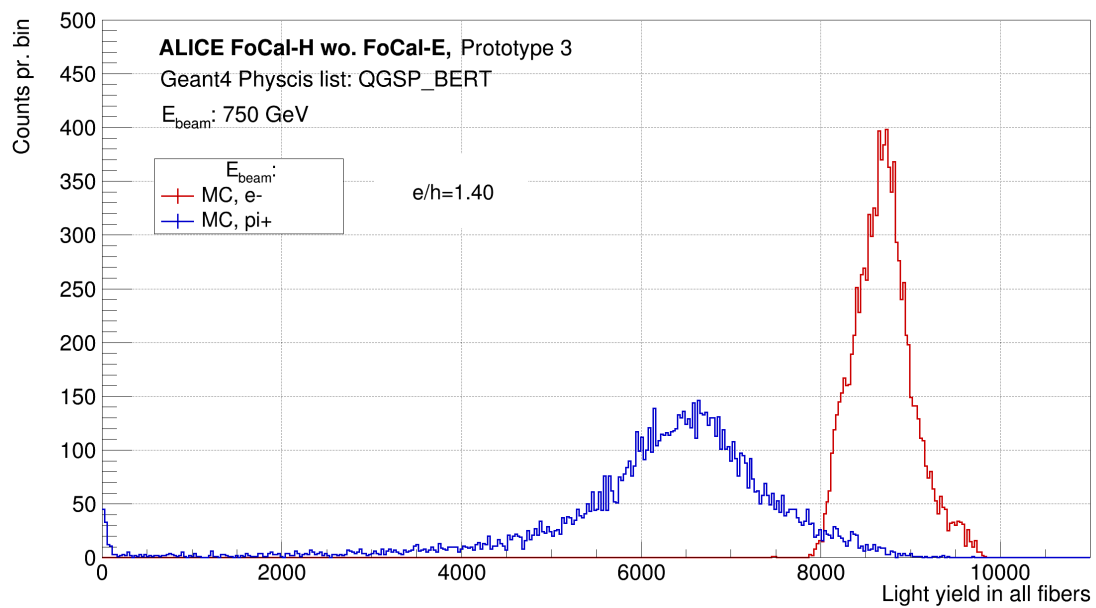
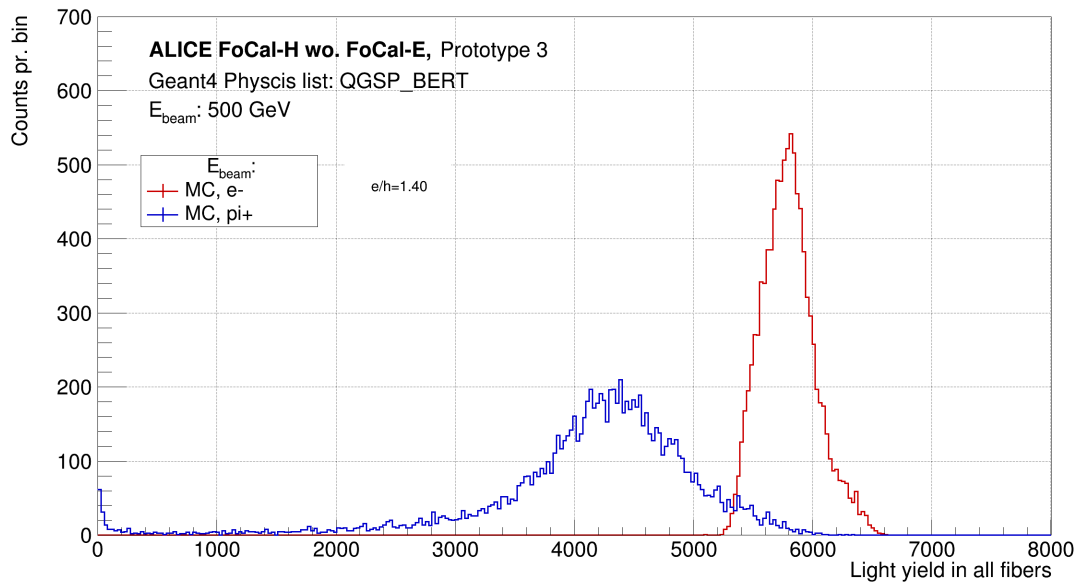
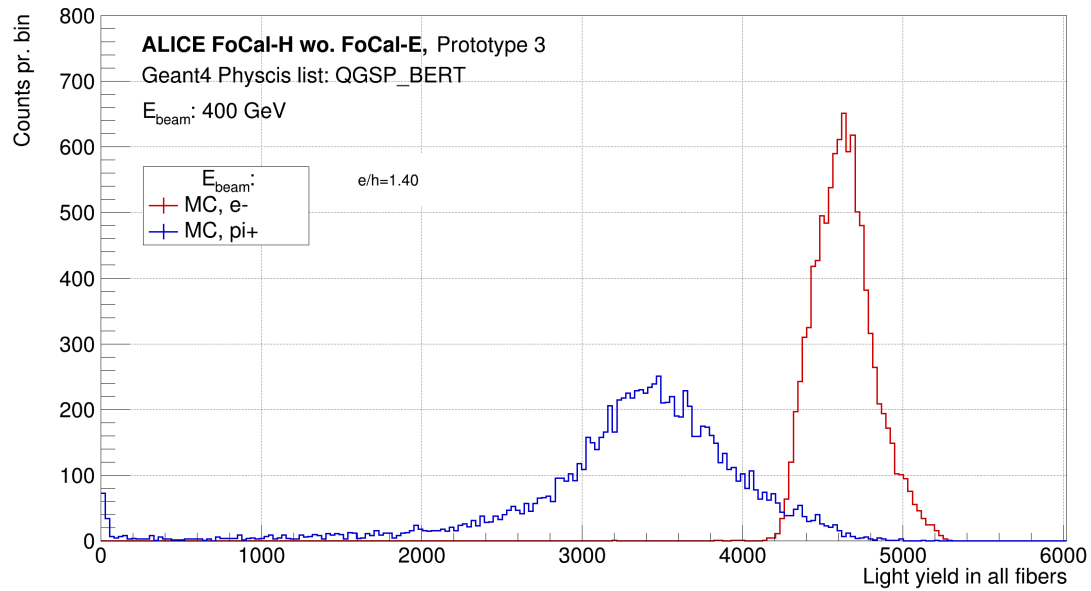






11.6.1.2 FoCal-H third prototype

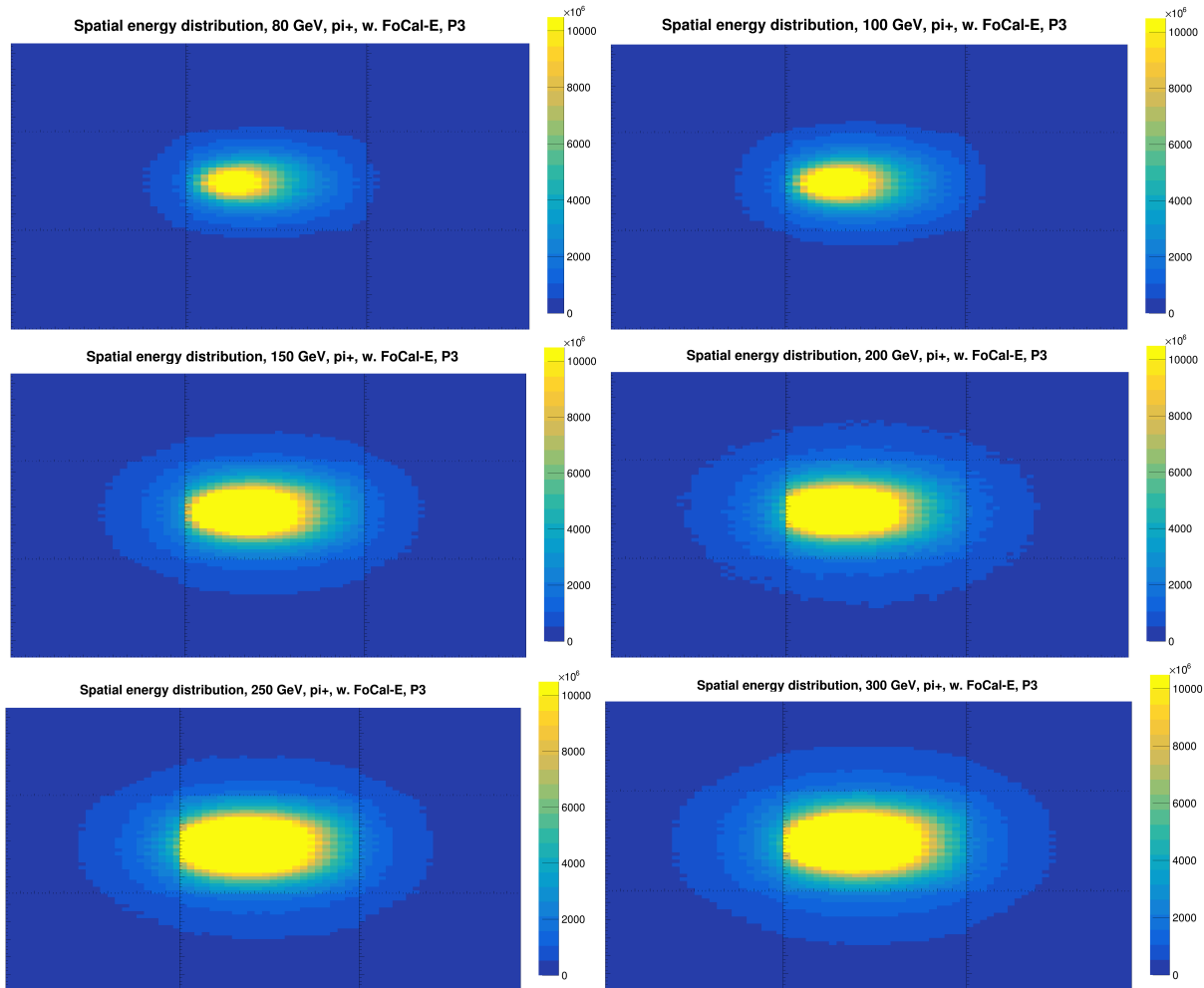




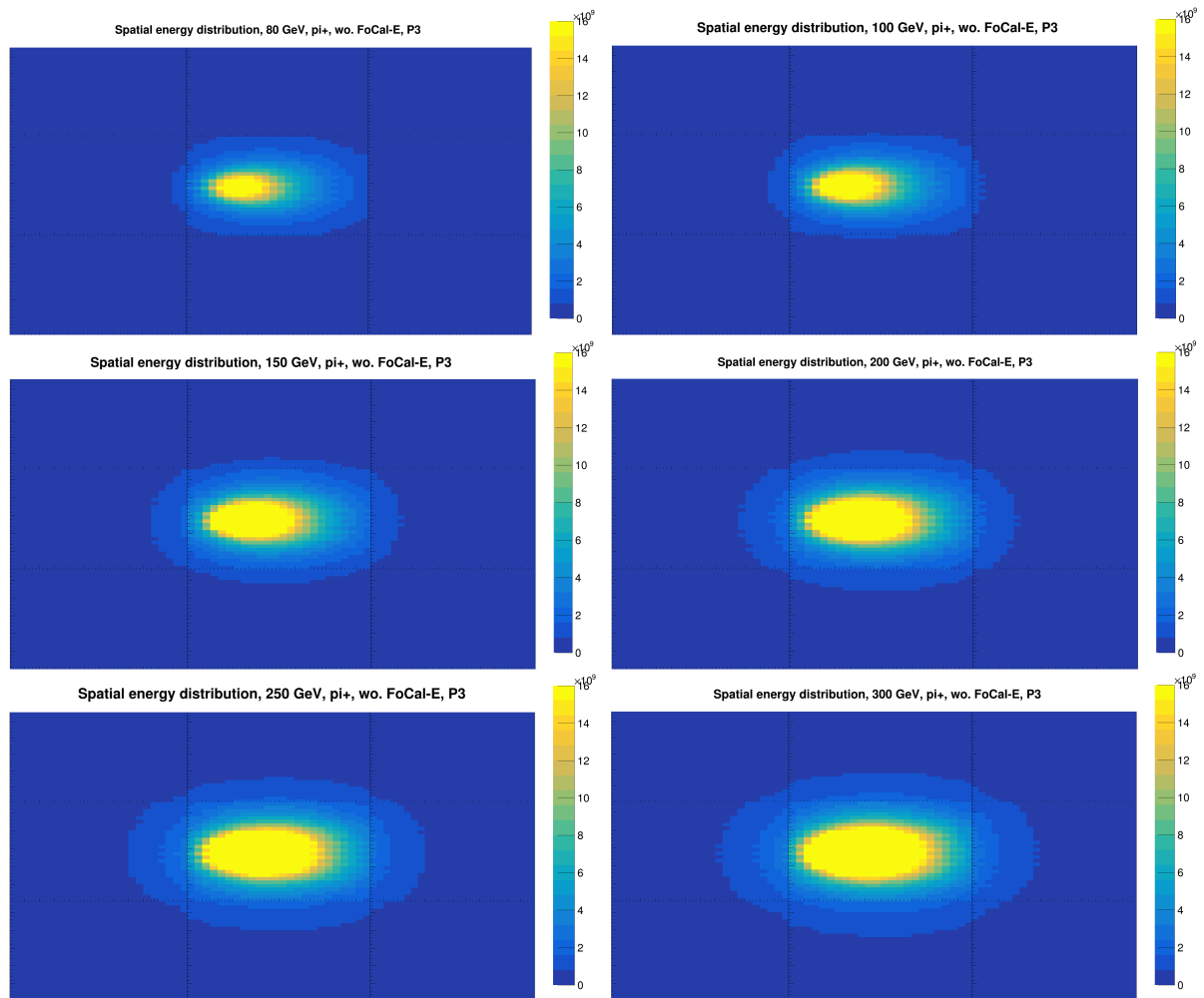
11.6.2 Shower containment

This section shows results of the simulations studies not included in the section 9.2.2 regarding the examination of lateral shower containment, of the FoCal-H third prototype. This section shows the spatial energy distribution, i.e. the particle shower size of an event, in the energy range from 80 GeV to 350 GeV, for the detector setup including and excluding FoCal-E in front of FoCal-H.

11.6.2.1 FoCal setup including FoCal-E



11.6.2.2 FoCal setup excluding FoCal-E



References

- [1] ALICE Collaboration, *Letter of intent: A forward calorimeter (FoCal) in the ALICE experiment*, CERN-LHCC-2020-009.
- [2] CERN, *WHAT IS CERN'S MISSION*, <https://home.cern/about/who-we-are/our-mission>(Seen 4/12-2022)
- [3] CERN, <https://home.cern/science/accelerators/accelerator-complex>(Seen 6/12-2022)
- [4] ALICE prepares for Run 3 after last new subdetector installation, *The ALICE apparatus and its various detector components*, <https://www.ibspe.com/news/alice-prepares-for-run-3-after-last-new-subdetector-installation>
- [5] CERN, *Immersive tour of the accelerator complex*, <https://home.cern/science/accelerators/accelerator-complex/panoramas>(Seen 6/12-2022) <https://en.wikipedia.org/wiki/CERN>(Seen 6/4-2022)
- [6] CERN, *The Low Energy Ion Ring*, <https://home.cern/science/accelerators/low-energy-ion-ring>(Seen 7/12-2022)
- [7] PhD Thesis - Valentina Zaccolo, *Charged-Particle Multiplicity Distributions over Wide Pseudorapidity Range in Proton-Proton and Proton-Lead Collisions with ALICE*.
- [8] CERN, *The Proton Synchrotron*, <https://home.cern/science/accelerators/proton-synchrotron> (Seen 19/5)
- [9] CERN, *Super Proton Synchrotron*, <https://home.cern/science/accelerators/super-proton-synchrotron>
- [10] CERN, *Facts and figures about the LHC*, <https://home.cern/resources/faqs/facts-and-figures-about-lhc>
- [11] ALICE collaboration, *ALICE ITS*, <https://alice-collaboration.web.cern.ch/node/34999>(Seen 14/12-2022)
- [12] ALICE collaboration, *ALICE TPC*, <https://alice-collaboration.web.cern.ch/node/34960>
<https://cds.cern.ch/record/451098/files/open-2000-183.pdf>(Seen 14/12-2022)
- [13] ALICE collaboration, *ALICE TRD*, <http://www-alice.gsi.de/trd/WorkingPrincipleOfTheALICETRD.gif> <https://cds.cern.ch/record/519145/files/cer-2275567.pdf>(Seen 14/12-2022)
- [14] ALICE collaboration, *ALICE Technical Design Report of the Time of Flight System (TOF)*, https://cds.cern.ch/record/430132/files/alice_toftdr.pdf(Seen 5/1-2023)
- [15] ALICE collaboration, *ALICE Technical Design Report of the High Momentum Particle Identification Detector*, https://alice-collaboration.web.cern.ch/sites/default/files/Documents/PROJECTS/HMPID/HMPID_TDR.pdf(Seen 5/1-2023)

- [16] ALICE collaboration, *ALICE EMCAL*, https://alice-collaboration.web.cern.ch/menu_proj_items/emcal(Seen 12/1-2023)
- [17] ALICE collaboration, *ALICE PHOS*, <https://alice-collaboration.web.cern.ch/node/34980>(Seen 12/1-2023)
- [18] The ACORDE collaboration, *ACORDE a Cosmic Ray Detector for ALICE* <https://cds.cern.ch/record/957722/files/0606051.pdf>(Seen 5/1-2023)
- [19] ALICE collaboration, *ALICE ZDC*, <https://alice-collaboration.web.cern.ch/node/34995>(Seen 12/1-2023)
- [20] ALICE collaboration, *ALICE Muon spectrometer*, <https://arxiv.org/pdf/hep-ex/0410061.pdf>(Seen 12/1-2023)
- [21] ALICE collaboration, *ALICE PMD*, <https://cds.cern.ch/record/451099/files/open-2000-184.pdf>(Seen 12/1-2023)
- [22] Brian R. Martin and Graham Shaw, *3rd edition, Nuclear and particle physics, an introduction*
- [23] Wikipedia, *Pseudorapidity* <https://en.wikipedia.org/wiki/Pseudorapidity>
- [24] Sketch of the jet quenching mechanism during heavy ion collision, https://www.researchgate.net/figure/Sketch-of-the-jet-quenching-mechanism-during-heavy-ion-collision_fig75_277669564
- [25] Lecture notes (Lecture 2) by You Zhou, *Particle Physics at the Density frontier and Energy frontier*.
- [26] Néstor Armesto, Nuclear shadowing <https://arxiv.org/pdf/hep-ph/0604108.pdf>
- [27] Michele Livan and Richard Wigmans, *Calorimetry for collider physics, an introduction*,
- [28] Christian W. Fabjan and Fabiola Gianotti, *Calorimetry for Particle Physics*, 31 October 2003, <https://cds.cern.ch/record/692252/files/ep-2003-075.pdf>
- [29] Michele Livan and Richard Wigmans, *Calorimetry for collider physics, an introduction*
- [30] CAEN - Tools for discovery, *CAEN A1702: 32 Channel SiPM Readout Board, Features and overview*, <https://www.caen.it/products/a1702/>
- [31] CAEN - Tools for discovery, *Desktop 64 Channel Citiroc unit for FERS-5200, Features and overview*, <https://www.caen.it/products/dt5202/>
- [32] Hamamatsu, *Multi-pixel photon counter for precision measurements*, https://www.hamamatsu.com/content/dam/hamamatsu-photonics/sites/documents/99_SALES_LIBRARY/ssd/s13360_series_kapd1052e.pdf
- [33] Hamamatsu, *Technical note - MPPC*, [mppc_kapd9008e.pdf](https://www.hamamatsu.com/content/dam/hamamatsu-photonics/sites/documents/99_SALES_LIBRARY/ssd/s13360_series_kapd1052e.pdf)
- [34] Bachelor project by Laura Dufke, *Characterization of SiPM for the ALICE forward calorimeter*
- [35] Saint-Gobain, *Scintillating optical fibers*, <https://ethz.ch/content/dam/ethz/special-interest/phys/particle-physics/precisionphysicsatlowenergy-dam/TeachingContent/ASL/bicronfiber.pdf>

- [36] Science Direct, *Scintillating Fibers*,
<https://www.sciencedirect.com/topics/physics-and-astronomy/scintillating-fibers>
- [37] D.E. Groom (LBNL) and S.R. Klein (NSD LBNL), *Passage of Particles Through Matter*, <https://pdg.lbl.gov/2019/reviews/rpp2018-rev-passage-particles-matter.pdf>
- [38] Geant4 Collaboration *Guide For Physics Lists, Release 10.6*, https://geant4.kntu.ac.ir/Dorsapax/Data/Sub_207/File/PhysicsListGuide.pdf
- [39] Thesis preparation project by Laura Marie Dufke, *Optimization of FoCal-H First Prototype*.
- [40] Saint-Gobain, *Radiation Detection Scintillators - fibers*, <https://www.crystals.saint-gobain.com/radiation-detection-scintillators/fibers>
- [41] ROOT histogram Library - TH1, *TH1 Class Reference*, <https://root.cern.ch/doc/master/classTH1.html#aefa4ee94f053ec3d217f3223b01fa014>
- [42] Master's thesis by Alexander Buhl, *Reading out a large SiPM array: Testing a readout system for ALICE FoCal-H*.
- [43] First year project by Caitlin Buch, Emil Hansen, Lillith Turner-Stone and Silas Schack, *Undersøgelse af data fra FoCal - en ny partikeldetektor til ALICE*
- [44] Bachelor thesis by Laura Dufke *Characterization of SiPM for the ALICE forward calorimeter*.